



NASA CR-1380

2.1



# NASA CONTRACTOR REPORT

NASA CR-1380

LOAN COPY: RETURN TO  
AFWL (WLIL-2)  
KIRTLAND AFB, N MEX

## STUDY OF AIR POLLUTANT DETECTION BY REMOTE SENSORS

*by C. B. Ludwig, R. Bartle, and M. Griggs*

*Prepared by*

GENERAL DYNAMICS CORPORATION

San Diego, Calif.

*for Electronics Research Center*

NASA CR-1380

TECH LIBRARY KAFB, NM



0060526

STUDY OF AIR POLLUTANT DETECTION  
BY REMOTE SENSORS

By C. B. Ludwig, R. Bartle, and M. Griggs

Distribution of this report is provided in the interest of information exchange. Responsibility for the contents resides in the author or organization that prepared it.

Issued by Originator as Report No. GDC-DBE68-011

Prepared under Contract No. NAS 12-630 by  
GENERAL DYNAMICS CORPORATION  
San Diego, Calif.

for Electronics Research Center

NATIONAL AERONAUTICS AND SPACE ADMINISTRATION

---

For sale by the Clearinghouse for Federal Scientific and Technical Information  
Springfield, Virginia 22151 - CFSTI price \$3.00



## FOREWORD

This report documents research performed under Contract NAS 12-630 between 28 March 1968 and 1 December 1968. The work was sponsored by the National Aeronautics and Space Administration, Electronic Research Center, Cambridge, Massachusetts and, in part, by General Dynamics research funds. The object of this program is to develop the capabilities of earth-oriented satellites in measuring air pollutant concentrations, geographical distribution, and dispersal rates.

The authors are indebted to the following personnel in Convair division's Space Sciences Laboratory for their respective contributions: Dr. W. Malkmus, for obtaining the spectral characteristics of the pollutants in the infrared from published laboratory data; Dr. S. Kaye, for the collection of pollutant data; Dr. E. Spargo, for assistance in the theoretical analysis of optical correlation methods; L. Acton and M. L. Streiff, for the laboratory development of optical correlation techniques; F. P. Boynton, for helpful discussions; and C. N. Abeyta, for assistance in the computations.

## ABSTRACT

In the present study the feasibility of detecting the major air pollutants by earth-oriented, satellite-borne sensors is investigated. The major pollutants considered are carbon monoxide, sulfur dioxide, ozone, ammonia, nitrogen dioxide, typical hydrocarbons, and peroxyacetyl nitrate (PAN). The spectral region considered extends from the ultraviolet to the microwave region. The detection is to be accomplished by observing the change in radiation level due to the presence of air pollutants. In the ultraviolet and visible region, the reflected sunlight provides the radiation, while in the infrared and microwave region the thermal emission from the earth and its atmosphere is the source of radiation. In the first case, the detection is adversely affected by Rayleigh and Mie scattering of the sunlight in the atmosphere, which is not readily accounted for, particularly for satellite observations. In the second case, the detection is influenced by meteorological conditions, which must be obtained by independent measurements either from the satellite directly or from the global weather-station network. Considerations of the number of species accessible to optical detection, the matter of day and night detection, and of specificity indicate that the infrared region extending from  $3.5\mu$  to  $13\mu$  is the most useful one.

In the first part of this report a discussion of the pollutant species, their occurrence, formation, chemistry, concentration levels, and distribution profiles through the atmosphere is given. The problems of detection in the UV and visible regions, in relation to aerosol and molecular scattering, are discussed. Calculations of signal changes expected for an ideal Rayleigh atmosphere are presented. Some considerations of aerosol (particulate) pollution detection are discussed. Then, the radiative transfer of the thermal emission of the earth and atmosphere under the influence of meteorological conditions is investigated. The spectral characteristics of the pollutants in the infrared are calculated from independent laboratory data (spectral absorption coefficients with a resolution of  $0.1\mu$  and band-averaged fine structure parameters). Signal changes arising from the difference in radiation levels due to "clean" and "polluted" atmospheres are calculated. It is found that under most atmospheric conditions, pollutant layers give rise to at least 1 percent signal changes.

In the second part of this report a performance evaluation of eight different spectroscopic instruments for the remote detection of pollutants is made. These include radiometers, grating spectrometers, Fourier-transform interferometer-spectrometers, three instruments based on optical correlation methods, microwave radiometers, and one active system — a satellite-based laser. It is found that two instruments, which are based on optical correlation methods (matched filter and selective chopper), have the greatest potential for near-future application. It is considered that, if present practical limitations can be overcome, interferometer-spectrometers offer great potential for future application.

## TABLE OF CONTENTS

<u>Section</u>		<u>Page</u>
	SUMMARY OF RESULTS AND CONCLUSIONS . . . .	xiii
1	INTRODUCTION . . . . .	1-1
2	CLASSIFICATION OF AIR POLLUTANTS . . . . .	2-1
2.1	IDENTIFICATION OF POLLUTANTS . . . .	2-1
2.1.1	List of Species . . . . .	2-1
2.1.2	Formation and Thermal Chemistry . . . .	2-1
2.1.2.1	Carbon Oxides . . . . .	2-1
2.1.2.2	Sulfur Compounds . . . . .	2-1
2.1.2.3	Nitrogen Compounds . . . . .	2-2
2.1.2.4	Intermediate Oxidation Products and Aerosols . . . . .	2-3
2.1.3	Photochemistry . . . . .	2-3
2.1.4	Sources . . . . .	2-4
2.2	CONCENTRATION AND DISTRIBUTION OF AIR POLLUTANTS . . . . .	2-6
2.2.1	Collection of Concentration Data . . . .	2-6
2.2.2	Estimates of Mean and Maximum Values . .	2-6
2.2.3	Height Distribution . . . . .	2-10
2.2.4	Difference Between Urban and Rural Concentrations . . . . .	2-11
3	RADIATIVE TRANSFER . . . . .	3-1
3.1	THE SUN AS THE SOURCE OF RADIATION . .	3-1
3.1.1	Calculation of the Signal Change in the UV and Visible Spectral Regions Between "Clean" and "Polluted" Atmospheres . . . . .	3-3
3.1.2	Discussion of Results . . . . .	3-4
3.1.3	Pollutant Detection in the Ultraviolet and Visible Regions . . . . .	3-7
3.1.4	Atmospheric Aerosols . . . . .	3-11
3.1.4.1	Aerosol Characteristics . . . . .	3-12
3.1.4.2	Optical Properties of Aerosols . . . . .	3-12
3.1.4.3	Calculations for Model Aerosol Layers . . .	3-13
3.1.4.4	Aerosol Absorption . . . . .	3-14
3.1.4.5	A Rayleigh Atmosphere Seen From a Satellite . . . . .	3-14
3.1.4.6	An Aerosol Atmosphere Seen From a Satellite . . . . .	3-14
3.1.4.7	Laser Probing of Aerosols From a Satellite . . . . .	3-14

## TABLE OF CONTENTS, Contd

<u>Section</u>	<u>Page</u>
3.1.4.8	Photographic Detection of Aerosols . . . . . 3-14
3.1.4.9	Concluding Remarks About Aerosol Detection . 3-15
3.2	THE EARTH AS THE SOURCE OF
	RADIATION . . . . . 3-15
3.2.1	Radiation Transfer Through the Atmosphere
	Computer Program . . . . . 3-15
3.2.1.1	Theory . . . . . 3-15
3.2.1.2	Atmospheric Transmission . . . . . 3-17
3.2.1.3	Comparison of Present Model With That of
	Wark et al. . . . . 3-17
3.2.1.4	Comparison of Model With Measurements . . 3-19
3.2.1.5	Computer Program for Calculating Signal
	Changes . . . . . 3-19
3.2.2	Influence of Meteorological Conditions Upon
	Air Pollution Detection . . . . . 3-22
3.2.2.1	General . . . . . 3-22
3.2.2.2	Diurnal Variations . . . . . 3-23
3.2.2.3	Seasonal Variations . . . . . 3-23
3.2.2.4	Atmospheric Moisture Content . . . . . 3-24
3.2.2.5	Low-Level Winds . . . . . 3-24
3.2.2.6	Surface Characteristics . . . . . 3-24
3.2.2.7	Spectral Inversion Procedures for
	Atmospheric Sounding . . . . . 3-25
3.2.2.8	Conclusions . . . . . 3-26
3.2.3	Spectral Characteristics of Pollutant Species
	in the Infrared . . . . . 3-26
3.2.3.1	Theoretical Background . . . . . 3-26
3.2.3.2	Extraction of Absorption Coefficients and Fine-
	Structure Parameters from Laboratory Data . 3-31
3.2.3.3	Accuracy of Determination of Mean Absorption
	Coefficients . . . . . 3-32
3.2.3.4	Comparison of Predicted Absorptivity With
	Experimental Data . . . . . 3-35
3.2.4	Calculated Signal Change Due to Pollutants in
	the IR . . . . . 3-38
3.2.4.1	Calculation for Confined Layers of Air
	Pollutants . . . . . 3-38
3.2.4.2	Calculation for Some Hypothesized Meteoro-
	logical Conditions . . . . . 3-41
3.2.4.3	Calculations Using Measured Pollution
	Profiles . . . . . 3-51

## TABLE OF CONTENTS, Contd

<u>Section</u>	<u>Page</u>
3.2.4.4	Conclusions from IR Region Calculations . . . 3-51
3.2.5	Measurement of Air Pollution in the Micro- wave Region . . . . . 3-54
3.3	CONCLUSIONS . . . . . 3-58
4	INSTRUMENTATION . . . . . 4-1
4.1	PERFORMANCE EVALUATION . . . . . 4-1
4.1.1	Radiometer . . . . . 4-5
4.1.1.1	Filter-Wheel Radiometer. . . . . 4-5
4.1.1.2	Polychromator-Radiometer . . . . . 4-6
4.1.2	Scanning Spectrometer . . . . . 4-8
4.1.3	Interferometer . . . . . 4-9
4.1.3.1	Single-Ended Michelson Interferometer- Spectrometer . . . . . 4-9
4.1.3.2	Advanced Development of Interferometers . . 4-15
4.1.4	Optical Correlation Instrument: Matched- Filter Type . . . . . 4-16
4.1.4.1	Physical Principle . . . . . 4-16
4.1.4.2	Theory and Optimization of the Matched-Filter Technique . . . . . 4-18
4.1.4.3	Airborne Matched-Filter Instrument . . . . 4-23
4.1.5	Optical Correlation Instrument: Selective Chopper Type . . . . . 4-26
4.1.5.1	Physical Principle . . . . . 4-26
4.1.5.2	Airborne Selective Chopping Instrument. . . 4-30
4.1.6	Optical Correlation Instrument: Fiber Optics Filter Type . . . . . 4-31
4.1.6.1	Physical Principle . . . . . 4-31
4.1.6.2	Theory . . . . . 4-34
4.1.6.3	Concluding Remarks on Fiber-Optics Filtering . . . . . 4-35
4.1.7	Laser Probing of Pollution . . . . . 4-36
4.1.7.1	Physical Principle . . . . . 4-36
4.1.7.2	Accuracy Considerations . . . . . 4-40
4.1.7.3	Tuning of Lasers . . . . . 4-41
4.1.7.4	Pulsing of Lasers . . . . . 4-42
4.1.7.5	Summary . . . . . 4-42
4.2	CONCLUSIONS . . . . . 4-42



## TABLE OF CONTENTS, Contd

<u>Section</u>		<u>Page</u>
5	RECOMMENDATIONS . . . . .	5-1
6	REFERENCES . . . . .	6-1
<u>Appendix</u>		
A	Tables of Rayleigh Atmosphere Intensities and Absorption Coefficients . . . . .	A-1

## LIST OF FIGURES

<u>Figure</u>		<u>Page</u>
1-1	Postulated Pollution Distribution Across U.S.A. . . .	1-2
1-2	Contributions of Sun and Earth to Earth Radiance . .	1-3
1-3	Schematic Representation of Energy Sources Seen by a Satellite . . . . .	1-4
2-1	Diurnal Variation of Pollutant Concentration . . . .	2-8
2-2	Frequency of Occurrence of Pollutant Concentrations .	2-9
2-3	Measured CH <sub>4</sub> Profiles (Reference 12) . . . . .	2-11
2-4	Measured SO <sub>2</sub> Profiles (References 14,15) . . . . .	2-11
3-1	Signal Change versus Wavelength . . . . .	3-6
3-2	Signal Change versus Sun Zenith Angle ( $\theta = 0^\circ$ , R = 0.2) . . . . .	3-8
3-3	Signal Change versus Look Nadir Angle ( $\theta_o = 30^\circ$ , R = 0.2) . . . . .	3-9
3-4	Signal Change versus Surface Albedo ( $\theta = 0^\circ$ , $\theta_o = 30^\circ$ ) . . . . .	3-10
3-5	Schematic of Sun and Look Angles . . . . .	3-11
3-6	Radiance Outside Atmosphere Compared with Wark et al. . . . .	3-20
3-7	Radiance Outside Atmosphere Compared with Wark et al. . . . .	3-20
3-8	Radiometric Temperature versus Altitude (Ocean 12/8/66) . . . . .	3-21
3-9	Surface Radiance versus Wavelength . . . . .	3-21
3-10	Partial Representation of the Line Intensities of CO <sub>2</sub> at 1500°K . . . . .	3-28
3-11	Collision-Broadened Curves of Growth for Various Intensity Distributions . . . . .	3-29
3-12	Methane Absorptivity Comparison ( $u = 0.052$ atm-cm, $P_e = 0.921$ atm) . . . . .	3-36

## LIST OF FIGURES, Contd

<u>Figure</u>		<u>Page</u>
3-13	Methane Absorptivity Comparison ( $u = 1.35$ atm-cm, $P_e = 1.001$ atm) . . . . .	3-36
3-14	Methane Absorptivity Comparison ( $u = 47.3$ atm-cm, $P_e = 0.987$ atm) . . . . .	3-36
3-15	Ammonia Absorptivity Comparison ( $u = 0.0772$ atm-cm, $P_e = 0.614$ atm) . . . . .	3-37
3-16	Ammonia Absorptivity Comparison ( $u = 1.617$ atm-cm, $P_e = 1.724$ atm) . . . . .	3-37
3-17	Ammonia Absorptivity Comparison ( $u = 47.1$ atm-cm, $P_e = 0.792$ atm) . . . . .	3-37
3-18	Vertical Temperature Profiles Used for the Results Summarized in Table 3-11 . . . . .	3-40
3-19	Temperature and $NH_3$ -Pollutant Concentration Pro- files for a Typical Mid-Day Atmosphere . . . . .	3-43
3-20	Temperature and $NH_3$ -Pollutant Concentration Pro- files for a Typical Mid-Night Atmosphere . . . . .	3-44
3-21	Temperature and $NH_3$ -Pollutant Concentration Pro- files for a Typical Day-Time Inversion Layer . . . . .	3-45
3-22	Temperature and $NH_3$ -Pollutant Concentration Pro- files for a Typical Upper-Level Inversion Layer . . . . .	3-46
3-23	Sensitivity to Varying $NH_3$ Pollution for Normal Day ( $T' = -2^\circ C/100$ m) . . . . .	3-48
3-24	Percent Radiance Changes Between Clean and Polluted Atmosphere . . . . .	3-50
3-25	Measured Temperature and $SO_2$ Profiles over Frankfurt, Germany . . . . .	3-52
3-26	Measured Temperature and $SO_2$ Profiles over Frankfurt, Germany and Chattanooga, Tennessee. . . . .	3-53
3-27	Atmospheric Transmission Windows in the Microwave Region (After Conway — Reference 67) and Air Pollu- tant Absorption Frequencies . . . . .	3-55

## LIST OF FIGURES, Contd

<u>Figure</u>		<u>Page</u>
4-1	Schematic of a Filter Wheel Radiometer . . . . .	4-5
4-2	Schematic of a Polychromator Radiometer . . . . .	4-7
4-3	Schematic of a Scanning Spectrometer . . . . .	4-8
4-4	Schematic of a Michelson Interferometer . . . . .	4-10
4-5	Schematic of IRIS Instrument. . . . .	4-11
4-6	Methane Correlation Signal Using Single and Multiple Entrance Slits . . . . .	4-19
4-7	Multiple Entrance Slit Effect on Discrimination . . .	4-19
4-8	Matched-Filter Instrument Configuration . . . . .	4-25
4-9	High Resolution Atmospheric Spectrum, Identifying Carbon Monoxide Lines Suitable for Matched-Filter Design . . . . .	4-25
4-10	Schematic of a Satellite-Borne Selective Chopper for Air Pollution Measurements . . . . .	4-27
4-11	Michelson's Theoretical Interferometer . . . . .	4-30
4-12	Schematic of Fiber-Optics Filter with Variable Transmission Resolution Elements . . . . .	4-32
4-13	Postulated Source, Background and Transmission Functions . . . . .	4-33
4-14	Oscilloscope Trace Illustrating Background Suppression . . . . .	4-34
4-15	Laser Probe Schematic . . . . .	4-37
4-16	Single Pass Transmission Through Clean Atmosphere (Surface to Satellite) versus Wavelength . . . . .	4-39
4-17	Signal-to-Noise Ratio as a Function of $\Delta E_{\lambda}$ . . . . .	4-45

## LIST OF TABLES

<u>Table</u>		<u>Page</u>
2-1	Survey of Pollutants by Groups . . . . .	2-2
2-2	Summary of Photochemical Primary Processes in Urban Air . . . . .	2-5
2-3	Comparison of "West Coast" and "London" Smog . .	2-7
2-4	CAMP Averages . . . . .	2-10
2-5	Typical Concentrations of Pollutants . . . . .	2-10
3-1	Intensities Seen by Satellite Looking Vertically Down (Surface Reflectivity 0.1) . . . . .	3-2
3-2	Maximum Signal Change as Function of Pollutant Con- centration and Sun Zenith Angle, for Surface Albedo of 0.2 and Looking Vertically Down . . . . .	3-5
3-3	Atmospheric Transmission Models . . . . .	3-18
3-4	Values of $a_0$ . . . . .	3-32
3-5	Comparison of Integrals of Absorption Coefficients with Experimentally Measured Band Intensities . . .	3-38
3-6	Signal Changes Between "Clean" and 1000-Foot-Thick, CO-Polluted Atmospheres for Various Atmospheric Temperature Profiles (ARDC, 1959) as Observed at 50 km and $\lambda = 4.6\mu$ (Surface Emissivity = 0.95) . .	3-41
3-7	Advantages and Disadvantages of Spectral Regions . .	3-59
3-8	Representative Signal Changes (SC) in the Infrared. .	3-59
4-1	Summary of Current Interferometer-Spectrometer Development . . . . .	4-17
4-2	Parameter Specified for Matched-Filter $\Delta S/N$ Calculation . . . . .	4-24
4-3	Parameters Specified for Selective Chopper $\Delta S/N$ Calculation . . . . .	4-31
4-4	Qualitative Comparison Among Spectroscopic Instru- ments for the Detection of Pollutants from Satellites .	4-44
5-1	High Resolution Atmospheric Spectra . . . . .	5-2
5-2	High Resolution Pollution Spectra . . . . .	5-2

## SUMMARY OF RESULTS AND CONCLUSIONS

In this study, techniques of detecting air pollution from an earth-oriented satellite were evaluated. The following factors were considered essential for reaching a decision as to the suitability of a given instrument:

- Sensitivity:** The signal-to-noise ratio, based upon realistic instrument parameters and calculated signal changes (the difference in radiation between "clean" and "polluted" atmospheres).
- Specificity:** Factors such as spectral characteristics of the pollutants, the overlap of atmospheric absorption lines, scattered sunlight, earth emission, and extraneous light sources (which limit discrimination among various pollutants and between pollutants and extraneous backgrounds).
- Complexity:** The weight, volume, and operational requirements of the different instruments.

The study was conducted in two phases.

- Phase I:** Classification, concentration, and distribution of pollutants; radiative transfer in the ultraviolet, visible, infrared, and microwave spectral regions; calculation of low-resolution signal changes due to pollutants; and detection of aerosols.
- Phase II:** Performance evaluation of specific instruments to detect air pollutants, viz., radiometer (filter and polychromator), scanning spectrometer, interferometer-spectrometer, matched-filter instrument, nondispersive ("selective chopper") instrument, fiber-optics instrument, and laser system.

The results of the study of Phase I and II are as follows:

### Phase I

Pollutants may be classified as primary emissions, and as secondary products formed during thermal and photochemical reactions. The principal pollutants are sulphur compounds ( $\text{SO}_2$ ), nitrogen compounds ( $\text{NO}$ ,  $\text{NO}_2$ ,  $\text{NH}_3$ ), oxygen compounds ( $\text{O}_3$ ,  $\text{CO}$ ,  $\text{CO}_2$ ), halogens, hydrocarbons, aldehydes, and particulates. The more important ones in characterizing the type and amount of man-made pollution include  $\text{CO}$ ,  $\text{SO}_2$ ,  $\text{NO}_2$ , and  $\text{O}_3$ . Representative pollutant concentrations in urban areas, based on CAMP values, are given in Table i.

Table i. Mean and Maximum Concentration of Pollutants

Pollutant	Mean ppm	Max ppm
SO <sub>2</sub>	0.05 to 0.10	1.5
NO	0.03 to 0.10	1.4
NO <sub>2</sub>	0.03 to 0.06	0.8
CO	5.00 to 10.00	70.0
O <sub>3</sub>	0.05 to 0.30	1.0
Total Oxidants	0.02 to 0.04	1.5
PAN	—	0.1
Total Hydrocarbons	2.00 to 3.00	20.0

Typical concentrations in rural areas are estimated to be less by one to two orders of magnitude. However, no extensive measurements have been made so far to corroborate this estimate.

The CO emission exceeds that of all other pollutants combined (except for CO<sub>2</sub>) and, thus, can be regarded as one of the prime indicators of air pollution. The observation of the large-scale dispersion of its day-time buildup during the night and particularly during early evening is important in reference to what may be referred to as Jaffe's paradox. Jaffe (Reference 1) has calculated that the known scavenging processes are inadequate to remove the world-wide addition of 200 million tons of CO per year, and that the atmospheric CO concentration should increase by 0.03 ppm/year. However, apparently this is not the case, as indicated by localized measurements in clean marine air.

Information about the vertical distribution of pollutants is scarce. However, theoretical considerations together with the evidence of a few measurements allow one to postulate representative vertical distributions near area sources or some distance away from strong point or line sources. Under normal lapse conditions, pollution will be distributed approximately uniformly through the troposphere, and, when a temperature inversion exists, most of the pollution will be confined near the earth's surface until the inversion breaks down.

In the spectral region from  $0.3\mu$  to  $3.5\mu$ , the sun acts as the primary radiation source for observing the absorption by pollutant species in the atmosphere. The solar radiation incident on the earth is backscattered by the atmosphere and reflected by the surface. The signal change due to pollutants as a function of wavelength and concentration was calculated using the atmospheric and surface conditions tabulated by Dave and Furukawa (Reference 2) and considering the transmission of the solar radiation passing twice through the pollution layer. The only species with significant absorption in the UV-visible region are  $O_3$ ,  $SO_2$ , and  $NO_2$ .

Theoretical signal changes of up to four percent in this spectral region have been estimated, but it is considered that in practice this will not be large enough to accurately measure a pollutant, due to the difficulty of separating the scattered and reflected contributions at the detector. In the presence of particulate (Mie) scattering and varying surface reflectivity, this separation is probably impossible.

At wavelengths longer than about  $3.5\mu$ , the thermal emission from the earth is greater than the energy due to reflected and scattered sunlight. Two reasons make this spectral region important for the detection of pollutants:

- Day and night observation is possible.
- All major pollutants have infrared absorption/emission bands.

The upper limits of the useful spectral region are given by the onset of the  $15\mu$   $CO_2$  absorption. In the microwave region ( $> 0.3$  cm) the rotational lines of the pollutants are broadened at 1 atmosphere pressure and overlap each other, so that no detailed information about single pollutants can be obtained.

The signal change in the infrared between "clean" and "polluted" atmospheres was calculated by modifying the "clean" atmosphere model of Green and Griggs (Reference 3) to include the presence of pollutants. Values of the absorption coefficients for most pollutants were calculated by fitting a statistical model, assuming a value of a band-averaged fine structure parameter, to the low resolution absorption data of Pierson et al. (Reference 4).

The calculated signal changes are strongly dependent upon the surface temperature and emissivity as well as the atmospheric temperature, which depends on meteorological conditions. As a result of many individual computations, the following general statements can be made:

- a. The difference between the earth's surface temperature and the effective temperature of the pollutants is the principal variable that affects the sensitivity of an instrument to changes in radiance, with and without the existence of air pollution. A knowledge of the temperature profile and of the pollutant concentration profile



is necessary to make detailed quantitative measurements. In general, the pollutant concentration profile may be related to the temperature profile. Methods of obtaining this knowledge either directly, or from a priori considerations must be further investigated.

- b. Significant measurable changes in radiance with and without even relatively small amounts of air pollution will exist under a variety of atmospheric conditions. However, these changes are less than linearly related to increasing pollutant concentrations. This appears to hold true independently of spectral resolution, at least for  $\Delta\lambda > 0.1\mu$ .
- c. Considerable spectral interference for a resolution of about  $0.1\mu$  exists between the individual species that normally are present in polluted atmospheres. This makes identification and quantitative measurement of specific pollutants difficult for conventional spectrometers and radiometers.
- d. Higher spectral resolution measurements would possibly alleviate the interference problem. In addition, with higher spectral resolution, larger values of pollutants' effective absorption coefficients would be obtained, thereby increasing the predicted radiance changes.

The results of one particular computation are given in Table ii for the conditions of a moderate air pollution level, uniformly mixed through the troposphere, and realistic meteorological conditions.

Table ii. Representative Signal Changes (SC) in the Infrared

Species	Concentration (ppm)	$\lambda$ ( $\mu$ )	SC(%)	Remarks
CO	2.5	4.6	27	Some interference by H <sub>2</sub> O
SO <sub>2</sub>	0.02	7.4	12	Some interference by H <sub>2</sub> O
NO <sub>2</sub>	0.02	6.3	5	Strong interference by H <sub>2</sub> O
O <sub>3</sub>	0.03	9.5	3	Strong interference by stratospheric O <sub>3</sub>
PAN	0.005	8.6	8	Some interference by H <sub>2</sub> O
NH <sub>3</sub>	0.05	10.8	5	Some interference by H <sub>2</sub> O and CO <sub>2</sub>

The optical properties of particulate (aerosol) pollution and the current theoretical knowledge of scattering (Rayleigh and Mie) within the real atmosphere were considered. It was concluded that quantitative measurements of the aerosol content of the lower atmosphere cannot presently be made from a satellite. Information on the aerosol content of the upper atmosphere may possibly be determined from occultation experiments.

## Phase II

Five general criteria are considered in the evaluation of instruments to detect air pollution from satellites:

- Sensitivity
- Specificity
- Required observation time
- Information content
- Complexity of the instrument

In general the sensitivity, specificity, and information content should be high, while the complexity should be low and the observation time short. A qualitative comparison of the instruments considered for passive systems is given in Table iii. In addition, active laser systems were investigated. It was found that it may be possible in principle to detect pollution in the visible region, but not in the infrared with present state-of-the-art laser devices.

**Table iii. Qualitative Comparison Among Spectroscopic Instruments for the Detection of Pollutants from Satellites**

	Radiometer (Filter Wheel or Many Single Filters)	Radiometer (Polychromator)	Scanning- Spectrometer	Optical Correlation Instrument	Interferometer- Spectrometer
Sensitivity	Medium	a. Low b. Medium	a. Low b. Medium	High	High
Specificity	Low	a. High b. Low	a. High b. Low	High	High
Complexity of Instrum.	Low	Medium	Medium	Medium	High
Observation Time	Short	a. Short b. Short	a. Long b. Medium	Short	Medium
Information Content	Medium	Medium	High	Medium	High
Remarks	Limit $\Delta\omega \sim 3$ $\text{cm}^{-1}$ ; many channels required	a. Assuming $\Delta\omega$ $< 1 \text{ cm}^{-1}$  b. Assuming $\Delta\omega$ $> 1 \text{ cm}^{-1}$ ; multiple detectors required	a. Assuming $\Delta\omega$ $< 1 \text{ cm}^{-1}$  b. Assuming $\Delta\omega$ $> 1 \text{ cm}^{-1}$	Matched filter with multiple entrance slits or nondisper- sive	Sampling time at least 10 sec; image motion compensation required; large information con- tent for wide spectral interval

Based on the above criteria, instruments employing correlation techniques, and interferometer-spectrometers appear to be most suitable. Ideally, a high-resolution interferometer-spectrometer with a short sampling time could detect air pollutants and also evaluate some meteorological parameters and earth surface conditions. Practically though, such an instrument becomes exceedingly complex and its development for near-term satellite application does not seem probable. Optical correlation instruments developed to monitor specific pollutants are considerably less complex than a suitable interferometer-spectrometer. The results of the quantitative evaluation of the sensitivity indicate that signal changes of one percent can be measured with an acceptable signal-to-noise ratio using optical correlation techniques or an ideal interferometer-spectrometer.

The conclusions, based on the results of Phases I and II, are as follows:

#### Selection of Spectral Region

The detection of pollutants in the infrared region of the spectrum is more advantageous than in the ultraviolet and visible regions for the following reasons:

- Day and night observations are possible.
- All pollutants have infrared absorption/emission bands, especially the important CO molecule.
- Scattered sunlight is not a problem, as it is in the ultraviolet and visible region.

The disadvantages as compared to the ultraviolet-visible regions are:

- The responsivity of infrared detectors is less than that of photomultipliers; however, this is not a serious drawback.
- For quantitative measurement of pollutants the surface temperature as well as the atmospheric temperature profile must be known.

The quantitative measurement of pollutants in the microwave region is not possible because of lack of specificity.

## Detectability of Pollutants in the Infrared

For the calculation of the signal change between "clean" and "polluted" atmospheres, the following factors must be considered:

- Pollutant optical thickness — concentration of the pollutant times thickness. The concentration alone can be obtained only through an independent knowledge of the thickness.
- Spectral characteristics of the pollutant, i.e., spectral absorption coefficients (line strength/line spacing) and fine structure parameters (line half-width/line spacing).
- In general, the transmission is not given by Beer's law.
- Interference by atmospheric absorption.
- Surface radiative temperature, i.e., the surface blackbody temperature and surface emissivity.

The effect of extraneous light sources, such as the reflection from sun, moon, and sky, is negligible. Also, city lights do not interfere because they do not emit significantly at wavelengths greater than  $3.5\mu$ . However, the presence of clouds in the line of sight makes the detection of air pollutants impossible.

## Dependence of Pollutant Detection in the Infrared on Meteorological Conditions

The signal change due to pollutant absorption/emission is dependent on the difference between the surface and low-level atmospheric (pollutant) temperatures, and on the relative pollutant profile through the atmosphere. Therefore, information about these parameters must be obtained independently. A measurement of the surface temperature can be made with a simple instrument already used on satellites. Atmospheric parameters will be obtained from satellites using radiance-inversion techniques and/or from the planned "World Weather Watch."

## Low Versus High Resolution Detection

No infrared absorption by pollutants is completely free from overlap of atmospheric lines and/or other pollutant lines and the continuum. To discriminate between the pollutant and interfering spectral lines, a knowledge of high resolution pollutant and atmospheric spectra is essential.

## Satellite Instrumentation

The following conclusions are drawn with regard to instruments to be used from a satellite platform:

- A high-resolution instrument with high sensitivity covering the infrared spectral region from  $3.5\mu$  to  $16\mu$  will have the greatest information content. Such an instrument is the Michelson interferometer-spectrometer. However, the present level of technology is not sufficiently advanced that such an instrument can be built for the present application.
- A high-resolution scanning spectrometer (grating, prism) does not have the necessary sensitivity for the detection of pollutants.
- A low- to medium-resolution radiometer requires a difficult data reduction procedure to correct for atmospheric and other pollutant interference.
- Instruments based on optical correlation techniques (selective chopper using absorption gas cells and matched filter) offer the greatest advantages for immediate development.

# 1

## INTRODUCTION

Air pollution is a problem of national and world-wide concern. To date, the detection and monitoring have been carried out on a local basis, where the methods employed consist mainly of gas sampling and subsequent chemical or spectroscopic analysis. The use of optical remote sensing techniques has been rare. No large-scale observations over urban areas are carried out at present, and the influence of the weather and diurnal and seasonal cycles on the large-scale patterns of pollution is not known. In addition, the effects of pollution on the meteorology and climatology of man's environment must be considered. It is not yet clear whether the mean atmospheric temperature is increasing, due to the "greenhouse effect" of carbon dioxide pollution, or whether it is decreasing, due to the addition of aerosol pollution, which reflects away more solar energy. It is apparent that day and night global coverage and more information about the concentration, spatial distribution, and dispersal rates under meteorological influences could be obtained economically using remote sensing techniques on earth-orbiting satellites. For detailed investigations of special local areas, these techniques could also be used on aircraft and balloons.

The importance of global coverage is further indicated by a conjecture given by Neiburger (Reference 5) concerning the pollution of an air mass moving around the earth. After a heavy buildup over the west coast of the United States, the pollution levels decrease over the deserts and Rocky Mountains down to background levels. Individual peaks then occur over large cities in the Midwest. Once the air enters the dense metropolitan areas toward the east coast, a general buildup can be expected, reaching its peak at the coastline (see Figure 1-1). This level will then decrease over the Atlantic Ocean before it starts to increase again over Europe. After completion of the circuit over the Pacific Ocean, the "clean" atmosphere enters the west coast pollution area. If in one revolution the natural cleaning processes are not sufficient to remove all pollutants from the atmosphere, the general "background" level will become higher at each circuit around the globe until it reaches lethal proportions.

The subject of air pollution inevitably involves atmospheric heating, hence radiation. In the ultraviolet and visible region the reflected sunlight is the source of radiation during daytime, while in the infrared and microwave region the thermal emission from the earth and its atmosphere is the source of radiation (during day- and night-time) (see Figure 1-2).

The total energy received at the entrance pupil of an instrument (aircraft - balloon - or satellite-based) is given by four individual components (see Figure 1-3), which are, of course, function of the wavelength,  $\lambda$ , and altitude,  $h$ :

$$E_{\text{tot}} = \int_{\lambda} \int_{z=0}^h (E_{\odot} \tau_{\text{clean}} \tau_{\text{poll}} \tau_{\text{sc}}^R + E_{\text{atm, sc}} + E_{\text{atm, th}} + E_{\oplus} \tau_{\text{clean}} \tau_{\text{poll}}) d\lambda dz \quad (1-1)$$

where  $E_{\odot}$  is the energy from the sun,

$\tau_{\text{clean}}$ ,  $\tau_{\text{poll}}$ , and  $\tau_{\text{sc}}$  represent the transmission resulting from absorption by the clean and polluted atmosphere, and by scattering, respectively, along a path passing through the atmosphere twice ( $\tau_{\text{sc}}$ ); and  $R$  is the albedo of the earth's surface.

A portion of the sun's energy scattered by the atmosphere is also received by the instrument and is indicated by  $E_{\text{atm, sc}}$ .

The thermal emission of the clean and polluted atmosphere is indicated by  $E_{\text{atm, th}}$ .

The last component of the energy equation is the thermal emission of the earth  $E_{\oplus}$ , which is attenuated by the transmission through the atmosphere ( $\tau_{\text{clean}} \times \tau_{\text{poll}}$ ).

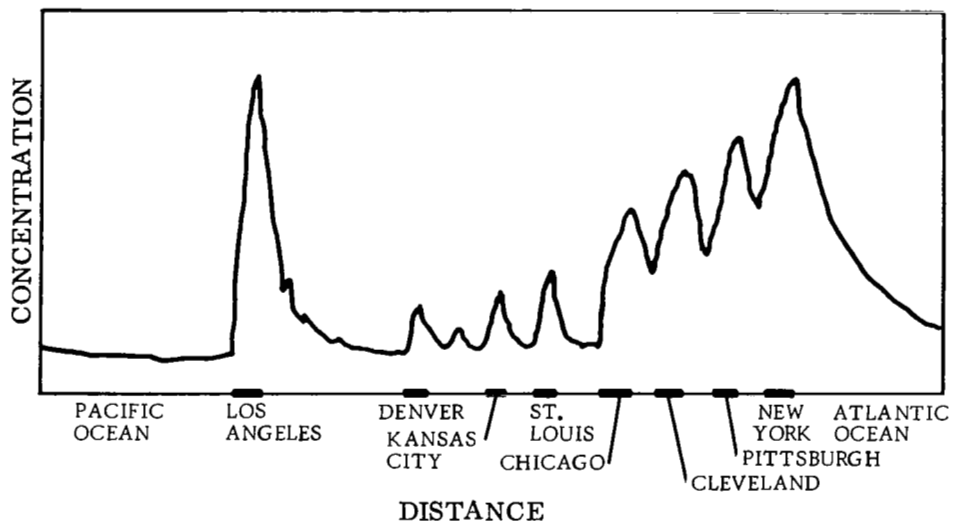


Figure 1-1. Postulated Pollution Distribution Across U.S.A. (Reference 5)

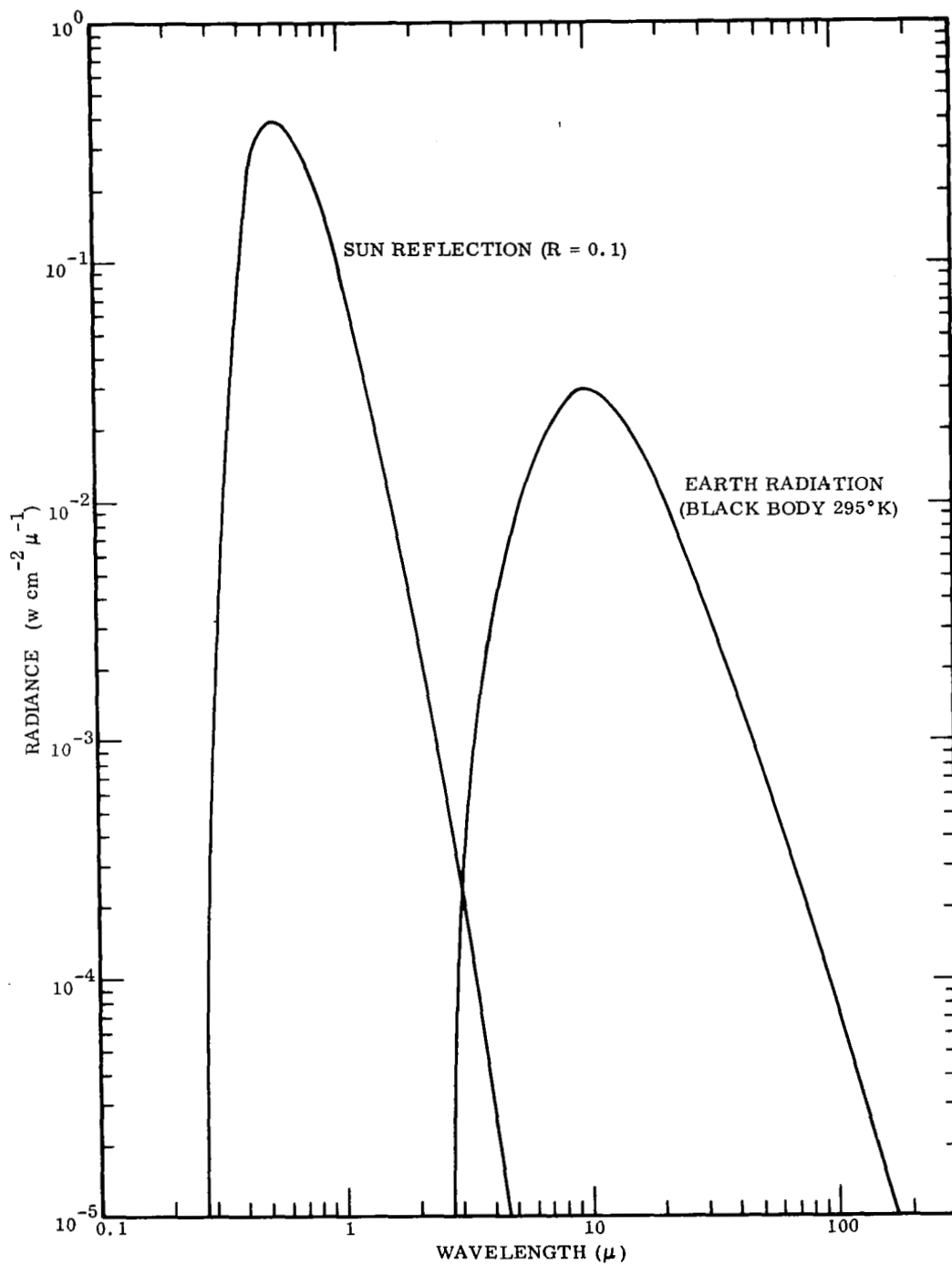


Figure 1-2. Contributions of Sun and Earth to Earth Radiance



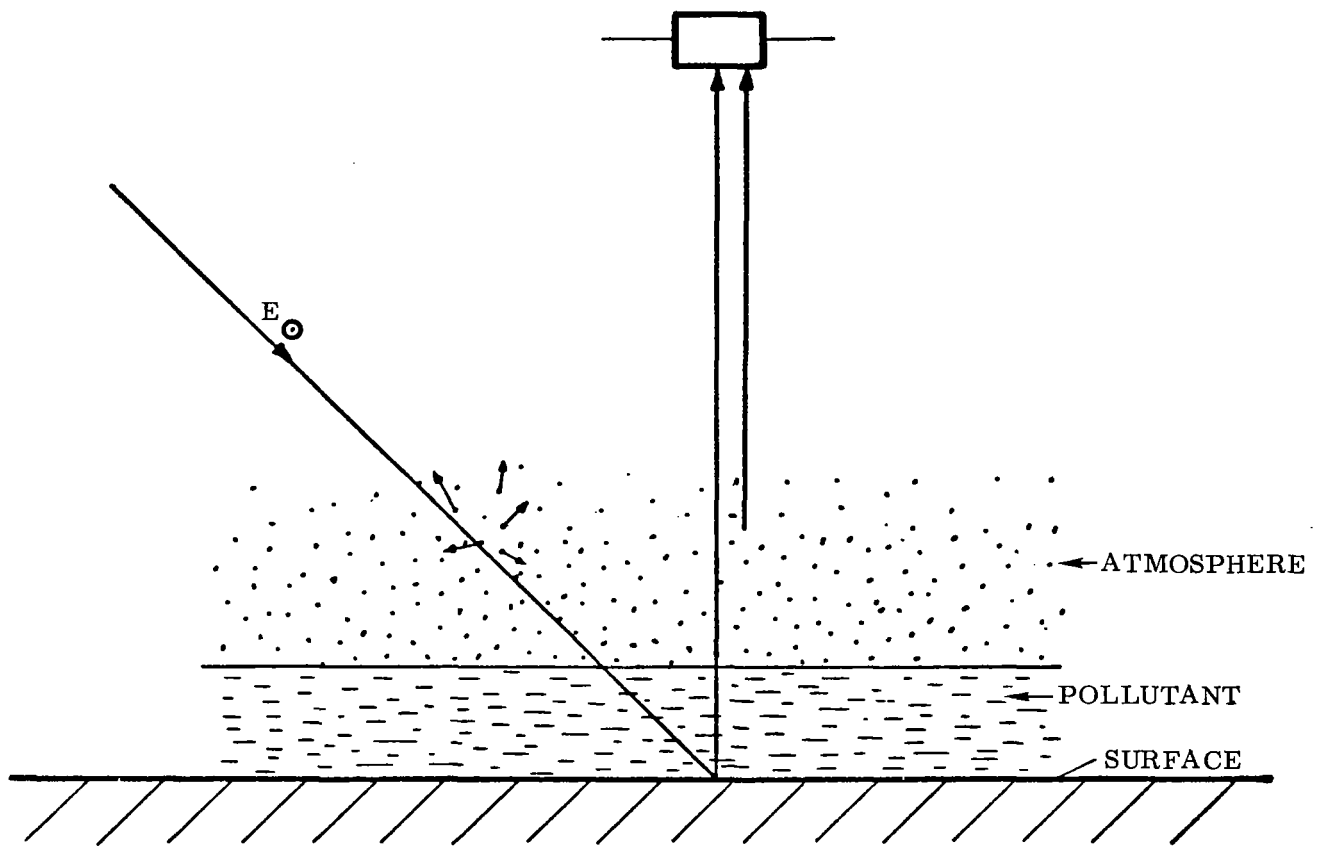


Figure 1-3. Schematic Representation of Energy Sources Seen by a Satellite

To determine the sensitivity of a given instrument to detect the presence of pollution, however, it is not the total energy but the energy difference between "clean" and "polluted" atmosphere which must be evaluated. In terms of signal-to-noise ratio, this fact is expressed as

$$\frac{\Delta S}{N} = D_{\text{SYS}} \Delta P$$

where

$D_{\text{SYS}}$  is the system detectivity, which is given by the inverse of the noise-equivalent-power and

$\Delta P$  is a function of the "throughput" or "étendue," spectral resolution, and energy difference.

In the ultraviolet and visible region the energy difference is given by

$$\begin{aligned} \Delta E_{UV} = & \iint (E_{\odot} \tau_{\text{clean}} \tau_{\text{sc}}^R + E_{\text{atm, sc}}) d\lambda dz \\ & - \iint (E_{\odot} \tau_{\text{clean}} \tau_{\text{poll}} \tau_{\text{sc}}^R + E_{\text{atm, sc}}) d\lambda dz \end{aligned} \quad (1-2)$$

Similarly, in the thermal region, we have

$$\begin{aligned} \Delta E_{IR} = & \iint (E_{\oplus} \tau_{\text{clean}} + E_{\text{atm, th}}) d\lambda dz \\ & - \iint (E_{\oplus} \tau_{\text{clean}} \tau_{\text{poll}} + E_{\text{atm, th}}) d\lambda dz \end{aligned} \quad (1-3)$$

It is seen that the computation of the energy differences reduces to the evaluation of the transmissivities of the radiative energy through "clean" and "polluted" atmospheres. The transmissivity is, in general, given by

$$\tau(\lambda, z) = \exp \{ -f [ k(\lambda); a(\lambda, p_i(z)); z; p(z); c(z) ] \} \quad (1-4)$$

where

$k(\lambda)$  is the "true" absorption coefficient of the molecular species, averaged over a specified wavelength interval,

$a(\lambda, p_i(z))$  is a parameter accounting for the spectroscopic fine structure of the molecule, as a function of  $\lambda$  and the partial pressure,  $p_i$ , of foreign gas-broadening species  $i$ ,

$p(z)$  is the total pressure and

$c(z)$  is the concentration at altitude  $z$ .

The functional relationship between these parameters can be expressed in several ways. In the case of the "clean" atmosphere, existing and experimentally verified models, which incorporate the conditions for standard atmospheres, were used. In the case of the "polluted" atmospheres, the statistical model was used. Here, the unknowns to be determined are the concentration as a function of altitude, and the spectral characteristics.

In Chapter 2, a brief survey of existing pollutants, their formation, sources, chemistry, estimated mean and maximum concentrations, and height distribution is given. In the first part of Chapter 3, Equation 1-2 is evaluated for the three pollutants active in the ultraviolet region, namely  $\text{SO}_2$ ,  $\text{NO}_2$ , and  $\text{O}_3$ . In the second part of Chapter 3, Equation 1-3 is evaluated for all of the important pollutants in the infrared region.

In the third part of Chapter 3, conclusions are drawn about the usefulness of the different spectral regions for the detection of pollutants.

In Chapter 4, spectroscopic instruments, in terms of sensitivity, specificity, information content, required observation time, and complexity are evaluated and conclusions drawn.

In the last chapter, recommendations for the future development of air pollutant detection from earth-oriented satellites are presented.

# 2

## CLASSIFICATION OF AIR POLLUTANTS

Air pollutants may be classified by physical state, by source, by chemical composition, by chemical or physiological effects, by relative abundance, etc. For our purposes, it is the optical properties which are important. These are the characteristics which differentiate the components of a polluted atmosphere and enable their detection, identification, and measurement by remote means. The optical properties arise as a consequence of the emission or absorption of rotational, vibrational, or electronic energy which is specific for particular chemical structures. The chemical structure is specific for each pollutant. It is therefore essential to know the elemental composition of pollutants, and the way in which the elements are joined together.

### 2.1 IDENTIFICATION OF POLLUTANTS

**2.1.1 LIST OF SPECIES.** When air pollution occurs it is marked by the appearance of distinctive chemical components which are absent or not detectable in a clean atmosphere because their concentration is low. Pollution arises typically from human endeavor in the fields of chemical, physical, or energy transformations. It is possible to classify the pollutants arising from each of these processes by their chemical constitution. Thus we have molecules in which nitrogen is combined with oxygen and with hydrogen. Halogens and their compounds constitute another important group. Finally, there are aerosols consisting of elements, compounds, and dust particles suspended in air. Table 2-1 lists these categories together with the important species involved.

### 2.1.2 FORMATION AND THERMAL CHEMISTRY

**2.1.2.1 Carbon Oxides.** Combustion of carbon compounds is the origin of perhaps 80 to 90 percent of all air pollutants. Of this amount, space heating contributes about 6 percent and the automobile from 60 to 80 percent. The pollutants are formed by the oxidation of coal, gas, and oil derivatives which are essentially carbon-hydrogen compounds. The major products are chiefly  $\text{H}_2\text{O}$  and  $\text{CO}_2$ , which are innocuous. However, because of poor mixing, insufficient oxygen, fast reaction times, and the  $\text{CO}_2 \rightleftharpoons \text{CO} + \frac{1}{2} \text{O}_2$  equilibrium, CO is an important by-product and a very toxic pollutant. In fact, the CO emission exceeds that of all other pollutants combined, and can be regarded as one prime indicator of air pollution.

**2.1.2.2 Sulfur Compounds.** Most coal and oil-base fuels contain about 2 percent sulfur. The sulfur is oxidized to  $\text{SO}_2$ , which in turn can be converted to  $\text{SO}_3$  in the atmosphere.  $\text{SO}_3$  reacts with  $\text{H}_2\text{O}$  in the air to form mists which impair visibility, and corrosive sulfuric acid,  $\text{H}_2\text{SO}_4$ . Because of the tremendous quantities of fuel burned,

Table 2-1. Survey of Pollutants by Groups

Group	Species
Nitrogen Compounds	NO, NO <sub>2</sub> , NO <sub>3</sub> , N <sub>2</sub> O <sub>3</sub> , N <sub>2</sub> O <sub>4</sub> , N <sub>2</sub> O <sub>5</sub> , HNO <sub>2</sub> , HNO <sub>3</sub>
Sulfur Compounds	SO <sub>2</sub> , SO <sub>3</sub> , H <sub>2</sub> S, RSH, RSR, H <sub>2</sub> SO <sub>4</sub>
Carbon Compounds, Inorganic	CO, CO <sub>2</sub>
Carbon Compounds, Organic	RH, RCHO, RR'CO, peroxides, polynuclear compounds, tars, NO derivatives
Halogen Compounds	HF, HCl, F, Cl, RX
Oxygen Compounds	O <sub>3</sub>
Elements and Particulates	As, Pb, carbon, fly ash, CaSiO <sub>3</sub> , ZnO, PbCl <sub>2</sub>

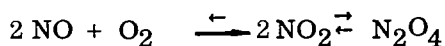
sulfur compounds assume great importance in air pollution. Ore roasting is also an important source in mining regions.

If the oxygen supply is inadequate, or if the atmosphere is a reducing one with a high hydrogen concentration, the sulfur compounds may be emitted in their reduced state, such as H<sub>2</sub>S, RSH, RSR, etc. These compounds of sulfur in a -2 valence state may be even more obnoxious to the senses and more toxic than the oxides.

**2.1.2.3 Nitrogen Compounds.** When air is used to oxidize fuel, some of the nitrogen in the air is oxidized to nitric oxide. An equilibrium exists between NO and its elements which favors the elements at low temperatures.

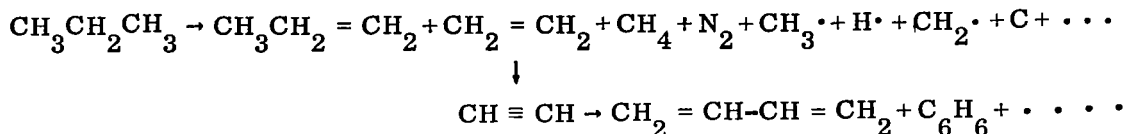


In high-temperature chambers, or when the reaction is quenched rapidly, more NO results. In air, further equilibrium reactions take place:

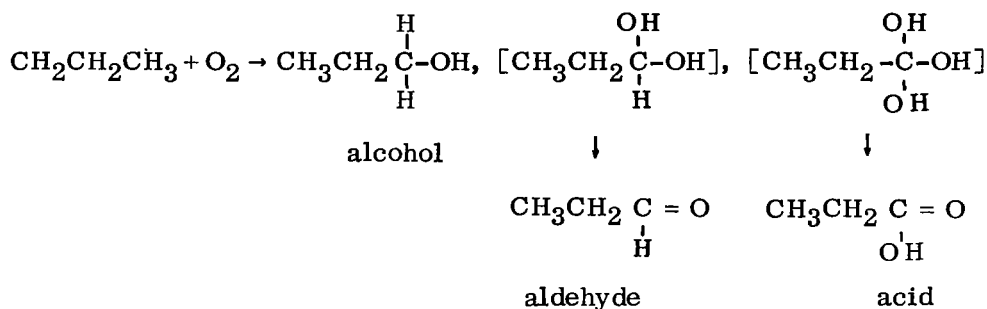


Oxidation to higher oxides such as N<sub>2</sub>O<sub>3</sub> and N<sub>2</sub>O<sub>5</sub> also occurs. In the presence of water, HNO<sub>2</sub> and HNO<sub>3</sub> are formed. Of every ton of fuel burned perhaps 20 pounds of N-oxides are formed. In the absence of high-temperature air as in refinery effluents, coke off-gases, stock yards, etc., nitrogen compounds in fuel appear as NH<sub>3</sub>.

**2.1.2.4 Intermediate Oxidation Products and Aerosols.** As long as fuels contain S, Pb, P, N, or halogen, it is inevitable that corresponding pollutants will be emitted as products. However, a significant 15 percent of the combustion products which are classified as pollutants are hydrocarbon derivatives that result from cracking processes, or insufficient oxidation. If air is insufficient or is not well-mixed with the fuel, unburned droplets or particles may be emitted to pollute the air and reduce visibility. A portion of the fuel may undergo thermal cracking in a local absence of air to produce organic fragments of higher and lower molecular weight. For example:

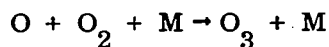
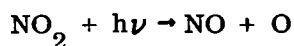


Alternatively, local insufficient concentrations of air or speedy reaction times may result in partially oxidized components. For example:



Finally, if the products are not volatile or have reacted with each other, they will be emitted as heavy tars, carbon particles, metal or metal oxide fumes, or other types of aerosols.

**2.1.3 PHOTOCHEMISTRY.** The obnoxious character of unburned fuel mists, carbon, cracked products, and partly oxidized products such as aldehydes are immediately evident wherever smoke and exhaust fumes prevail. An even greater problem may be the products of secondary reactions in the atmosphere. These secondary effects are photochemically induced. Haagen-Smit (Reference 6) in 1952 postulated that  $\text{NO}_2$  was the precursor for these reactions, which produced eye irritants and ozone, and reduced visibility. This has subsequently been confirmed by many investigators and given a theoretical basis by Leighton and Perkins (Reference 7). The postulated mechanism is



The oxygen atom, the NO, and the ozone are highly energetic as well as irritating substances which then may undergo further reactions with aldehydes, alkenes, alkynes, etc. to form peroxides, other aldehydes, and peroxyalkyl nitrates and nitrites (PAN). Leighton (Reference 8) has summarized the reactions and products of primary and secondary photochemical processes in air, and discusses the possible absorbers which lead to the products. In Table 2-2 a brief resumé of important reactions is given by equations showing processes which give rise to NO, O<sub>3</sub>, peroxides, aldehydes, alkyl nitrites and nitrates, and acids. A comparison between the photochemical smog and London-type air pollution is shown in Table 2-3.

2.1.4 SOURCES. It is estimated that 142,000,000 tons of air pollutants are discharged each year in the United States. Industry and refuse disposal are responsible for 20 percent of the total. Industrial sources consist essentially of chemical processing operations and metal and oil refining. The emissions usually consist of solvent vapors, S, H<sub>2</sub>S, sulfur oxides, CO, ammonia, acids, and dusts of metal, metal oxides, silica, etc. Power plants generate about 15 percent of the pollutants in the form of nitrogen and sulfur oxides and fly-ash. The most important source of air pollution in the United States is the automobile, which accounts for 60 percent of the total air pollutants. Eighty-six million tons of air pollutants can be ascribed to motor vehicles. They are distributed as follows:

<u>Pollutant</u>	<u>Tons/Year</u>
CO	66,000,000
NO <sub>2</sub>	6,000,000
Hydrocarbons	12,000,000
SO <sub>2</sub>	1,000,000
Pb	190,000
Particulates	1,000,000

In some areas, natural sources of pollution may assume importance. These consist of salt particles from the sea; sulfur gases from volcanoes; smoke and particulates from forest fires; and dusts consisting of soil, volcanic ash, bacteria and pollens.

Table 2-2. Summary of Photochemical Primary Processes in Urban Air

Absorber	Primary Photochemical Process in Air
$\text{NO}_2$	$\text{NO}_2 \rightarrow \text{NO} + \text{O} (^3\text{P})$
$\text{O}_3$ 4500-7500 Å	$\text{O}_3 \rightarrow \text{O}_2 + \text{O} (^3\text{P})$
$\text{O}_3$ 2900-3500 Å	$\text{O}_3 \rightarrow \text{O}_2 + \text{O} (^1\text{D})$
$\text{SO}_2$	Probably $\text{SO}_2 + \text{O}_2 \rightarrow \text{SO}_4$
Alkyl Nitrites	$  \begin{array}{c}  \text{RCH}_2\dot{\text{O}} + \text{NO} \\  \nearrow \\  \text{RCH}_2\text{ONO} \\  \searrow \\  \text{RCHO} + \text{HNO}  \end{array}  $
Acyl and Peroxyacetyl Nitrates (PAN)	Not known (see text)
Nitroalkanes	Same as alkyl nitrites
Alkyl Nitrates	$\text{RONO}_2 \rightarrow \text{R}\dot{\text{O}} + \text{NO}_2$
Diketones (glyoxal, biacetyl)	$  \begin{array}{c}  2\text{R}\dot{\text{C}}\text{O} \\  \nearrow \\  (\text{RCO})_2 \\  \searrow \\  \text{R}_2\text{CO} + \text{CO}  \end{array}  $ $(\text{RCO})_2 + \text{X} \rightarrow ?$
Olefinic Aldehydes (acrolein, crotonaldehyde)	$\text{RCH} = \text{CHCHO} + \text{O}_2 \rightarrow ?$
Formaldehyde	$  \begin{array}{c}  \text{H} + \text{H}\dot{\text{C}}\text{O} \\  \nearrow \\  \text{HCHO} ? \\  \searrow \\  \text{H}_2 + \text{CO}  \end{array}  $
Aliphatic Aldehydes	$\text{RCHO} \rightarrow \dot{\text{R}} + \text{H}\dot{\text{C}}\text{O}$
Aliphatic Ketones	$\text{RRCO} \rightarrow \dot{\text{R}} + \text{R}\dot{\text{C}}\text{O}$



Table 2-2. Summary of Photochemical Primary Processes in Urban Air, (Contd)

Nitrous Acid	$\begin{array}{c} \text{HONO} \begin{array}{l} \nearrow \text{OH} + \text{NO} \\ \searrow \text{H} + \text{N}_2 \end{array} \end{array}$
Nitric Acid	$\text{HONO}_2 \rightarrow \text{OH} + \text{NO}_2$
Hydrogen Peroxide	$\text{H}_2\text{O}_2 \rightarrow 2\text{OH}$
Organic Peroxides and Hydroperoxides	$\text{ROOR} \rightarrow \text{RO} + \text{OR}$

## 2.2 CONCENTRATION AND DISTRIBUTION OF AIR POLLUTANTS

**2.2.1 COLLECTION OF CONCENTRATION DATA.** Air pollution measurements have been performed on a systematic basis since 1818 in London and since the early 20th century in the United States. These studies related to climatology. Early in this century, systematic studies associated with smoke abatement and smelter fumes resulted in reports on particulate matter. About 1930, the advent of automatic instrumentation led to the establishment of networks of analyzers to obtain overall pollution measurements. A National Air Sampling Network was set up by the U.S. Public Health Service in 1963 to determine the trends in pollution levels of urban and non-urban areas of the United States. This was extended to the establishment of a Continuous Air Monitoring Program (CAMP) by the U. S. Congress when it was realized that gases from motor vehicles seriously affected health and that available data were inaccurate. The problem was first recognized and studied by the Air Pollution Control District in Los Angeles and by the California Air Resources Board. At present the data are being collected, organized, analyzed and disseminated by the Public Health Center at Cincinnati, Ohio. It is expected that this systematization of data will lead to broad generalizations concerning maximum, average, and minimum pollutant concentrations, diurnal variations, height distribution, meteorological effects, differences between urban and rural concentrations, and similar relationships.

**2.2.2 ESTIMATES OF MEAN AND MAXIMUM VALUES.** It would be desirable ideally to obtain instantaneous values of concentration which could then be integrated and evaluated for average, mean, and total concentration. This condition of ideality does not yet prevail because all instantaneous values represent some degree of integration of spectroscopic or wet chemical analyses. Actually, fluctuations occur because of variations in emission strength related to numbers of vehicle sources, changes in atmospheric ventilation and meteorology, proximity to sources, seasonal variations, solar radiation, etc.

Table 2-3. Comparison of "West Coast" and "London" Smog

Characteristic	West Coast	London
Temperature prevailing	75 to 90° F	30 to 40° F
Relative humidity	< 70%	85% (+ fog)
Type of temperature inversion	Subsidence	Radiation
Wind speed	< 5 mph	Calm
Visibility prevailing	< 0.5 to 1 mile	< 100 yards
Months of most probable occurrence	August - September	December - January
Major fuels involved	Petroleum	Coal and petroleum products
Principal constituents	O <sub>3</sub> , NO, NO <sub>2</sub> , CO, organic matter	Particular matter, CO, S compounds
Types of atmospheric reactions	Photochemical plus thermal	Thermal
Type of chemical reactions	Oxidative	Reductive
Time of maximum occurrence	Midday	Early morning
Principal biological effects	Temporary eye irritation	Bronchial irritation; coughing

It can be anticipated that computer analysis will eventually allow automatic calculation and presentation of running five-minute, hourly, daily, weekly, seasonal, etc., averages.

Two-year averages of hourly samples of the average pollutant concentration of six cities are shown in Figure 2-1 (Reference 9). Concentrations of several gaseous pollutants range from maximum values of from 7 to 30 times the mean levels to minimum values below the sensitivity of instruments. Table 2-4 and Figure 2-2 summarize some of the results for seven major cities with CAMP stations (Reference 9).

However, the instantaneous measurements of concentration obtained at recording stations, as shown in Table 2-5, may show an order of magnitude increase over average concentrations.

The observation and analysis of such wide ranging results await the establishment of a computer network that can handle and supply the information necessary for interpreting the massive amount of data in a reasonable period of time.

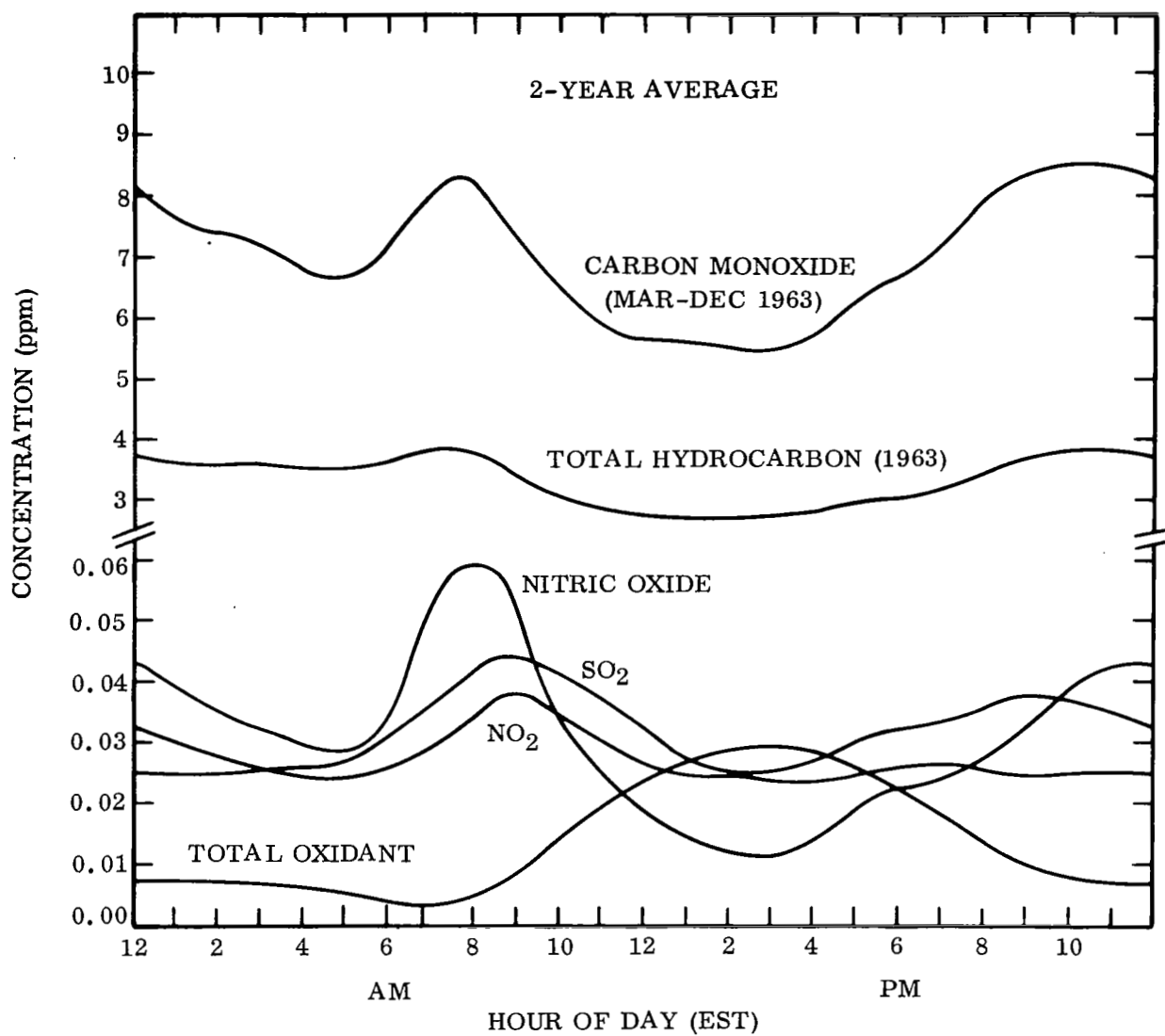


Figure 2-1. Diurnal Variation of Pollutant Concentration

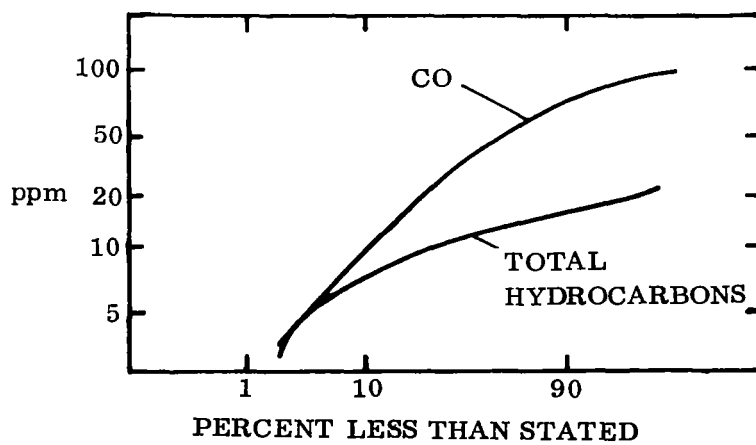
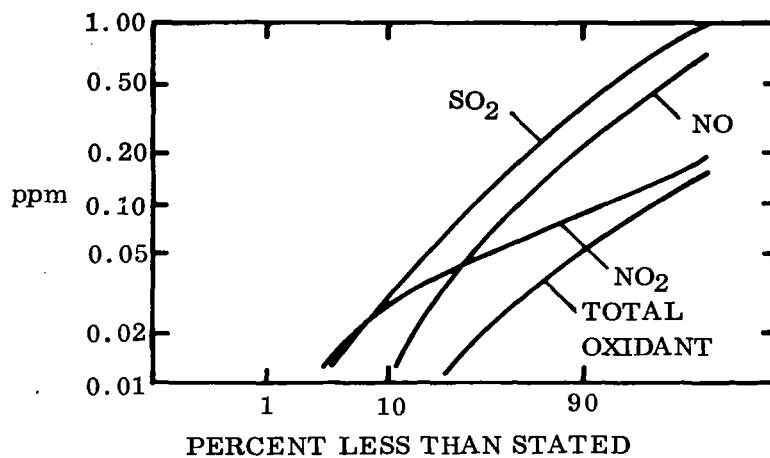


Figure 2-2. Frequency of Occurrence of Pollutant Concentrations

Table 2-4. CAMP Averages

Pollutant	Monthly Average (ppm)	Average Daily Maximum(ppm)
CO	6.8	32.1
NO	0.053	0.282
NO <sub>2</sub>	0.037	0.152
SO <sub>2</sub>	0.065	0.789
Hydrocarbons	2.7	10.0
Oxidants	0.028	0.093

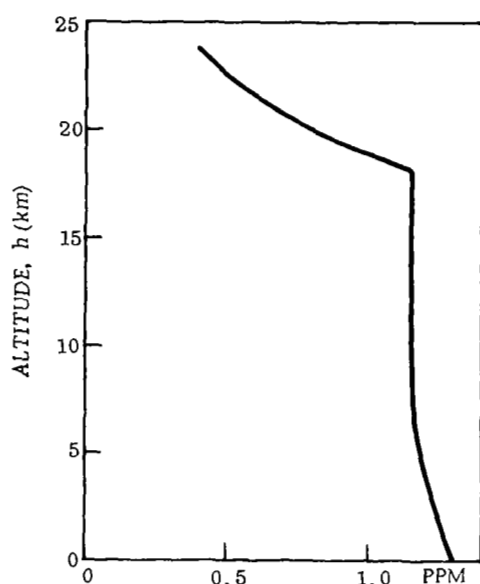
Table 2-5. Typical Concentrations of Pollutants

Pollutant	Range of Concentrations(ppm)
Aldehyde	0.02 - 2.0
Ammonia	0.02 - 3.0
Carbon Monoxide	2.0 - 300
Hydrogen Fluoride	0.001 - .08
Hydrogen Sulfide	0.002 - 1.0
Nitrogen Oxide	0.02 - 3.5
Ozone	0.009 - 1.0
Sulfur Dioxide	0.001 - 3.2

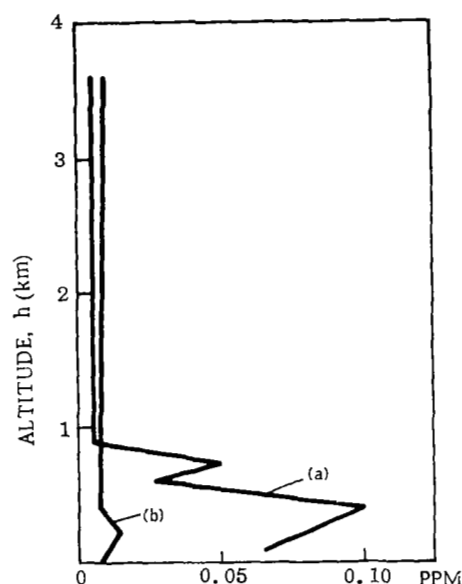
**2.2.3 HEIGHT DISTRIBUTION.** The extent of pollution dispersion in a vertical direction is important in establishing harmful concentrations. If pollutants were evenly distributed by natural mixing processes and diffusion, a ten-fold increase in the load could be tolerated. However, when the temperature decrease with height is less than 5.4°C per 1000 feet, the atmosphere is stable and mixing is suppressed. At night and particularly in autumn and winter, radiation cooling of the earth is frequent (Reference 10). This radiation cooling produces temperature inversions that form earlier in the evening and last longer in the fall and winter than in the spring and summer. The atmosphere under these conditions is very stable, mixing is poor, and the pollution potential is high.

Only a small quantity of data are available regarding the vertical distribution of pollutants. Some ozone and SO<sub>2</sub> data related to stations a few meters from the surface may be

obtained from observations in which the height of the station was specified (Reference 11). Enhalt (Reference 12) used aircraft and balloons to measure vertical profiles of methane concentration at levels from 0 to 30,000 feet. Bainbridge and Heidt (Reference 13) measured the methane concentration profile to 25 kilometers. These investigators found a high variability in methane concentration with both time and altitude, with an average value of about 1.2 ppm at lower altitudes (see Figure 2-3). German workers have measured  $\text{SO}_2$  concentrations to heights of 3600 meters above ground level (see Figure 2-4). Inversions trap the pollutants below the inversion level so that above it the concentration averages about 1 pphm. Below the inversion level, which varies from 400 to 1200 meters, concentrations vary greatly about a range of 1 to 15 pphm. Similar profiles, but with about 10 percent of the concentration level, were found in New York (Reference 16).



NOTE:  
NORMAL LAPSE CONDITIONS



NOTE:  
(a) TEMPERATURE INVERSION AT  
900 METERS.  
(b) NORMAL LAPSE CONDITIONS.

Figure 2-3. Measured  $\text{CH}_4$  Profiles      Figure 2-4. Measured  $\text{SO}_2$  Profiles

**2.2.4 DIFFERENCE BETWEEN URBAN AND RURAL CONCENTRATIONS.** Since the atmosphere is continually changing and all parts interacting, it must be studied on a global scale at all heights. Vertical stability of the air is the chief factor in dispersion, and depends on wind shear and temperature gradients. Winds can change the pollutant concentrations by factors of 1000 or 10,000 from day to day.

In urban areas and within given geographical locations, dispersion may be hindered, so that concentrations of pollutants build up. These urban pollutants are sometimes characteristic of the area. In Los Angeles, there is a marked existence of oxygen compounds, acids, and water-soluble compounds. Philadelphia is marked by a high prevalence of aromatics, and Cincinnati by hydrocarbons. New York and London have high SO<sub>2</sub> concentrations in the atmosphere. Their atmospheres contain nonspecific materials which act as irritants.

Topography is important. One region may be free of pollutants which collect in another. Valleys are bad, as witnessed by the Donora (1948) and Meuse Valley (1930) incidents. Observations from aircraft show that ground level pollution varies with area. Urban centers are characterized by an overlying smoke pall that is almost always present. Pollution varies diurnally in cities according to recurrent traffic peaks and industrial activity.

In addition to accumulating and showing diurnal cycles of concentration, the higher concentration of pollutants in urban air affects plants, animals, and human beings. Plants show leaf lesions and growth impairment at very low levels of concentrations. Lung damage to animals and human beings is evident at autopsy. Urban inhabitants exhibit darkened tissue and damage, predisposing to emphysema.

# 3

## RADIATIVE TRANSFER

### 3.1 THE SUN AS THE SOURCE OF RADIATION

At wavelengths below about  $3\mu$  the solar energy reflected from the surface of the earth is greater than the thermal emission from the earth and atmosphere. The exact wavelength at which the energies are equal depends on the sun elevation, surface reflectivity and emissivity, and surface temperature. However, in general, the thermal radiation may be neglected below about  $2\mu$  and the reflected solar energy above about  $4\mu$ .

Thus, the sun acts as a source from the UV through the visible to the near IR, although below about 3000 Å the energy available at the surface is greatly reduced due to absorption by the stratospheric ozone. There is no significant pollutant absorption between 6550 Å and  $2\mu$ , and we consider absorption of solar radiation only by the pollutants  $O_3$ ,  $SO_2$ ,  $NO_2$ , and PAN. These absorb between 3000 Å and 6550 Å, and in this region, sensing of surface phenomena from a satellite is considerably handicapped by Rayleigh and Mie scattering within the atmosphere, in addition to absorption by the Huggins and Chappuis ozone bands.

The relative contributions of the surface reflection and of the atmosphere to the intensity seen by a satellite looking vertically down are shown in Table 3-1 as a function of sun zenith angle. The values are for a surface reflectivity of 0.1. The surface contribution is approximately proportional to the reflectivity, while the atmospheric portion increases only slightly with increasing reflectivity. The mean surface reflectivity over polluted areas such as cities will generally be low (0.1 to 0.2), except when snow-covered. The data in Table 3-1 are taken from Dave and Furukawa (Reference 2) and account for both ozone (present in the normal clean atmosphere), absorption, and multiple scattering.

These discussions have ignored the effect of aerosol scattering, which is described by the complicated Mie theory. Aerosols are always present in the normal atmosphere and extend from the surface to the stratosphere. The effects of aerosol scattering are not readily included in a complete atmospheric model, as discussed later in Subsection 3.1.4. The presence of aerosols in the atmosphere will increase the ratio of atmospheric to surface contributions, so that detection of surface pollution is more difficult. But, a greater problem is the fact that quantitative calculations of the aerosol influence are impossible, even if the theory is satisfactory, since the type of aerosol and its size distribution is not known and cannot be determined with present remote sensing techniques. Thus, quantitative determination of pollution amounts from a satellite will be very difficult, if not impossible, in the scattering regions, i.e., UV and visible.



Table 3-1. Intensities Seen by Satellite Looking Vertically  
Down (Surface Reflectivity 0.1)

Wavelength	Upward Radiation (Specific Intensity)		Sun Zenith ( $\theta$ )
	Atmosphere	Surface	
3025 Å	$7.6 \times 10^{-3}$	$1.9 \times 10^{-4}$	30°
	$2.8 \times 10^{-3}$	$1.4 \times 10^{-5}$	60°
	$1.4 \times 10^{-3}$	$5.2 \times 10^{-7}$	75°
3125 Å	$9.3 \times 10^{-2}$	$9.4 \times 10^{-3}$	30°
	$3.7 \times 10^{-2}$	$2.6 \times 10^{-3}$	60°
	$1.1 \times 10^{-2}$	$4.2 \times 10^{-4}$	75°
3225 Å	$1.8 \times 10^{-1}$	$2.5 \times 10^{-2}$	30°
	$9.2 \times 10^{-2}$	$9.7 \times 10^{-3}$	60°
	$3.9 \times 10^{-2}$	$2.7 \times 10^{-3}$	75°
3600 Å	$1.8 \times 10^{-1}$	$5.0 \times 10^{-2}$	30°
	$1.1 \times 10^{-1}$	$2.4 \times 10^{-2}$	60°
	$6.8 \times 10^{-2}$	$9.8 \times 10^{-3}$	75°
4950 Å	$5.1 \times 10^{-2}$	$7.2 \times 10^{-2}$	30°
	$3.4 \times 10^{-2}$	$4.0 \times 10^{-2}$	60°
	$2.6 \times 10^{-2}$	$1.8 \times 10^{-2}$	75°
6150 Å	$1.9 \times 10^{-2}$	$7.4 \times 10^{-2}$	30°
	$1.3 \times 10^{-2}$	$4.0 \times 10^{-2}$	60°
	$1.0 \times 10^{-2}$	$1.8 \times 10^{-2}$	75°

These values, multiplied by  $I_{\lambda}/\pi$  (where  $I_{\lambda}$  is solar irradiance at wavelength  $\lambda$ ), give actual intensities observed by the satellite.

**3.1.1 CALCULATION OF THE SIGNAL CHANGE IN THE UV AND VISIBLE SPECTRAL REGIONS BETWEEN "CLEAN" AND "POLLUTED" ATMOSPHERES.** Calculations of signal changes available at a satellite due to pollution at the earth's surface may be calculated for an ideal Rayleigh scattering atmosphere. The calculations do not include aerosol scattering, which would reduce the values of signal changes presented below.

To determine the signal change due to the presence of a pollution layer at the surface of the earth, we may consider that only the surface contribution is modified by the pollution layer. Thus, the fractional signal change, SC, is given by

$$SC = \frac{\Delta I_{\lambda}}{I_{\lambda}} = \left[ 1 - \frac{I_{\lambda}(A) + \tau_{\lambda} I_{\lambda}(S)}{I_{\lambda}(A) + I_{\lambda}(S)} \right] \quad (3-1)$$

where

$I_{\lambda}$  is the total intensity at wavelength  $\lambda$  seen at the satellite,

$I_{\lambda}(A)$  is the atmospheric contribution,

$I_{\lambda}(S)$  is the surface contribution, and

$\tau_{\lambda}$  is the transmission of the solar radiation passing twice through the pollution layer.

The values of  $I_{\lambda}(A)$  and  $I_{\lambda}(S)$  are determined from the data tabulated by Dave and Furukawa (Reference 2) for a plane-parallel atmosphere. In the UV and visible it may be assumed that the absorption by the pollutants follows Lambert's Law:

$$\ln \tau_{\lambda} = -k\ell (\sec \theta + \sec \theta_o)cp \quad (3-2)$$

where

$k$  is the absorption coefficient,

$\ell$  is the thickness of the pollution layer,

$c$  is the pollutant concentration,

$p$  is the atmospheric pressure,

$\theta$  is the satellite observation nadir angle,

$\theta_o$  is the sun zenith angle.

Using the mean absorption coefficients for 100 Å intervals tabulated by Leighton (Reference 8) the signal change was calculated as a function of wavelength ( $\lambda$ ),  $\theta$ ,  $\theta_o$ ,  $c$ , surface albedo ( $R$ ) and a uniformly mixed pollutant layer 1000 feet thick.

Calculations were made for the following cases

$$\theta = 0^\circ \text{ with } \theta_o = 0^\circ, 30^\circ, 60^\circ, 75^\circ, 85^\circ$$

$$\theta_o = 30^\circ \text{ with } \theta = 30^\circ, 60^\circ, 85^\circ, \text{ Antisolar side}$$

$$\theta_o = 85^\circ \text{ with } \theta = 30^\circ, 60^\circ, 85^\circ, \text{ Antisolar side}$$

$$\theta_o = 30^\circ \text{ with } \theta = 30^\circ, \text{ Solar side}$$

In each case, R took the values 0.1, 0.2, 0.4, 0.8;

c took the values 0.05, 0.5, 1.0, 5.0 ppm for  $O_3$

0.001, 0.01, 0.1, 1.0 ppm for  $NO_2$

0.005, 0.05, 0.5, 5.0 ppm for  $SO_2$

0.001, 0.01, 0.1, 1.0 ppm for PAN;

and  $\lambda$  varied from 2875 Å to 6550 Å. The values of  $\lambda$ ,  $\theta$ , and  $\theta_o$  are restricted to those tabulated by Dave and Furukawa (Reference 2) but intermediate values may be obtained by interpolation. R, c, and the pollutant layer thickness may assume any values.

**3.1.2 DISCUSSION OF RESULTS.** The values of  $I_\lambda(S)$ ,  $I_\lambda(S)/I_\lambda(A)$ , and  $I_\lambda(S) + I_\lambda(A)$ , which were calculated from the data of Dave and Furukawa, are presented in Tables A-1 to A-5 (Appendix) for  $\theta = 0$  as a function of  $\lambda$ , R,  $\theta_o$ . The values  $I_\lambda(A)$  and  $I_\lambda(S)$  are the intensities for an atmosphere illuminated by unidirectional solar radiation of  $\pi$  units per unit area normal to the incident direction. In order to obtain absolute intensities these quantities are multiplied by  $I_{o\lambda}/\pi$ , where  $I_{o\lambda}$  is the absolute specific irradiance of the sun outside the earth's atmosphere. The total intensity seen from a satellite, i.e.,  $[I_\lambda(S) + I_\lambda(A)] I_{o\lambda}/\pi$ , is shown in units of  $w \text{ cm}^{-2} \mu^{-1} \text{ sr}^{-1}$ . These tables are included to clearly show the relative values of the scattered atmospheric and reflected surface components, and the total intensity available for detection at the satellite.

The computed maximum signal changes for reasonable values of concentration, surface albedo, sun zenith angle, and viewing angle are presented in Table 3-2. It appears that the values for PAN are probably too small for detection. The variation of the signal change as a function of wavelength is shown for low spectral resolution (100 Å) in Figure 3-1. It is seen that atmospheric ozone absorption precludes detection of surface pollutants below about 3000 Å. General observations of the dependence of the signal change on the various parameters deduced from comprehensive computer

Table 3-2. Maximum Signal Change as Function of Pollutant Concentration and Sun Zenith Angle, for Surface Albedo of 0.2 and Looking Vertically Down

Albedo 0.2 $\theta = 0$					
$\theta_o = 0$			$\theta_o = 75^\circ$		
Conc. (ppm)	$\lambda_{\max}$ (Å)	Max SC(%)	$\lambda_{\max}$ (Å)	Max SC(%)	
O <sub>3</sub>	0.5	3075	1.7	3175	1.5
	5.0	3075	10.4	3300	9.6
NO <sub>2</sub>	0.01	4000	0.44	4000	0.83
	0.1	4000	4.3	4000	7.9
SO <sub>2</sub>	0.05	3075	0.28	3175	0.14
	0.5	3075	2.57	3175	1.31
PAN	0.1	3075	0.003	3075	0.001
	1.0	3075	0.026	3075	0.010

calculations are presented below. Some understanding of the observations may be obtained by rewriting Equation 3-1:

$$\frac{\Delta I}{I} = (1 - \tau) \frac{I_S}{I_A + I_S} \quad (3-3)$$

Now,

$$\tau = \exp(-k\ell cp) \quad (3-4)$$

Approximating (3-4) for small exponent:

$$\tau = 1 - k\ell cp \quad (3-5)$$

Thus in (3-3):

$$\frac{\Delta I}{I} = k\ell cp \frac{I_S}{I_A + I_S} \quad (3-6)$$

at short  $\lambda$ , when  $I_A \gg I_S$ :

$$\frac{\Delta I}{I} \approx k\ell cp \frac{I_S}{I_A} \quad (3-7)$$

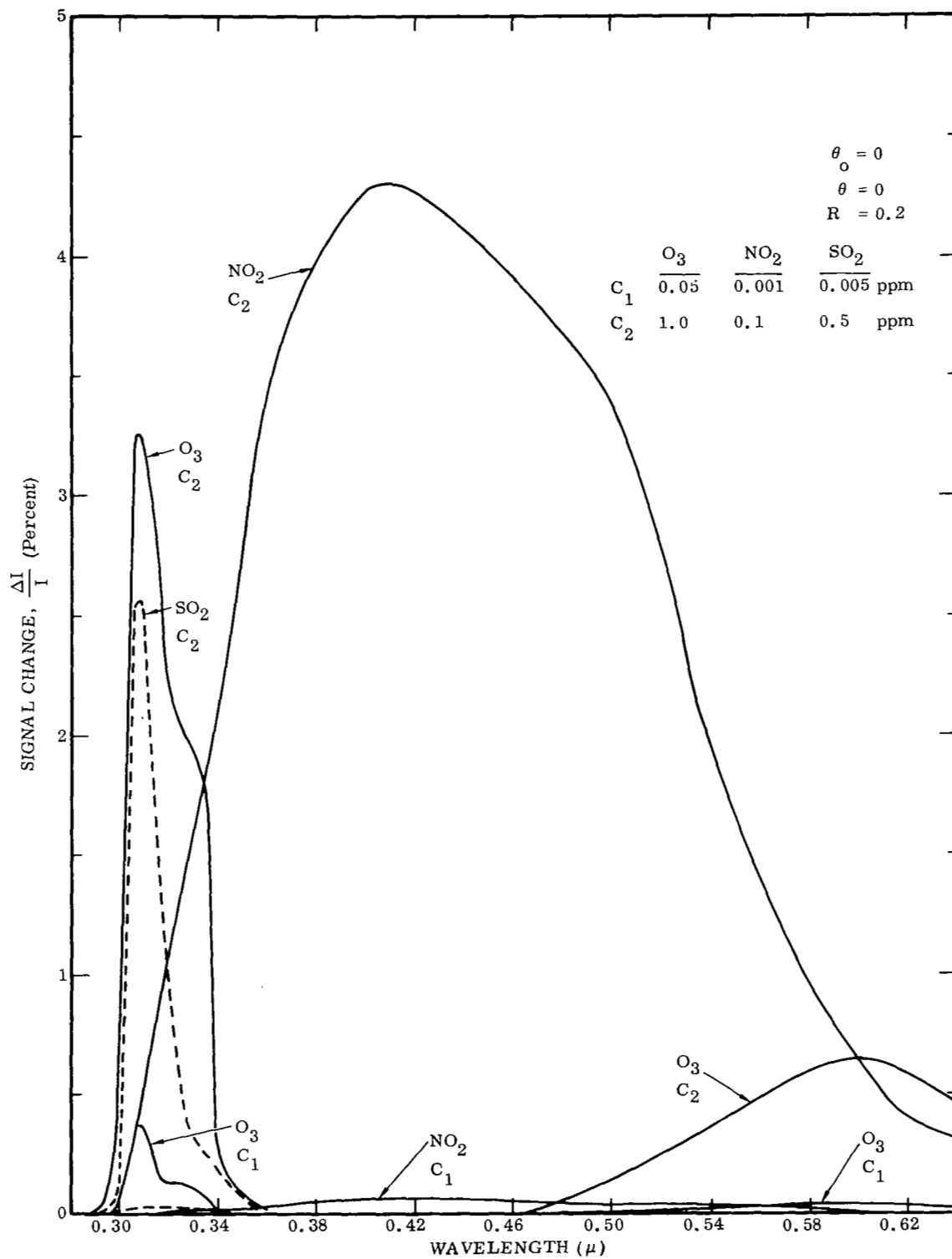


Figure 3-1. Signal Change versus Wavelength

at long  $\lambda$ , when  $I_A \ll I_S$ :

$$\frac{\Delta I}{I} \approx k l c p \quad (3-8)$$

#### Signal Change Dependence on Parameters

- a. Variation of sun zenith angle ( $\theta_o$ ); other parameters constant: In the UV, where atmospheric ozone absorption is strong, SC decreases with increasing  $\theta_o$ . In the visible and near UV, where the atmospheric absorption is weak, SC increases with increasing  $\theta_o$ . Figure 3-2 shows some sample results to illustrate the dependence on  $\theta_o$ .
- b. Variation of look nadir angle ( $\theta$ ); other parameters constant: In the UV, SC decreases with increasing  $\theta$ . In the visible, SC generally increases with increasing  $\theta$ , except for large  $\theta_o$ , when SC decreases with increasing  $\theta$ . Figure 3-3 shows the dependence of SC on  $\theta$  for  $\theta_o = 30^\circ$ .
- c. Variation of Surface Albedo (R); other parameters constant: In the UV where the surface contribution is small, SC is roughly proportional to R. This follows from Equation (3-3), since  $I_S$  is approximately proportional to R. In the visible where  $I_S > I_A$ , SC increases only slightly with increasing R. Typical results are shown in Figure 3-4.
- d. Variation of Pollutant Concentration (c); other parameters constant: At all wavelengths SC is approximately proportional to c, particularly at small c (following approximation to Equation 3-4).

The increase of SC in the visible and near UV with increasing sun or look angle (except when both are large) is due to the fact that the optical thickness of the pollutant layer, which is proportional to  $(\sec \theta + \sec \theta_o)$ , increases more rapidly than the ratio  $I_A/I_S$ . Thus, there appears to be a possible advantage in using non-vertical observation angles. However, the calculations assume a plane-parallel atmosphere, and the conclusions for large sun zenith angles or observer's nadir angles are probably not applicable to the real atmosphere. At larger look angles, the larger atmospheric scintillation (noise) may offset the advantage of an increased signal change.

The calculations discussed above were made for the sun, surface target, and satellite being coplanar, and for  $\theta$  on the antisolar side as shown in Figure 3-5. For the same value of  $\theta$  on the solar side, SC is slightly greater. This is due to the reduced atmospheric background and increased  $I_S/I_A$  when  $\theta$  is on the solar side.

#### 3.1.3 POLLUTANT DETECTION IN THE ULTRAVIOLET AND VISIBLE REGIONS.

The UV and visible regions do not appear suited to pollutant detection from a satellite platform due to the difficulty of accounting for the scattering in a real spherical atmosphere, which includes aerosols. However, these problems are reduced, although not

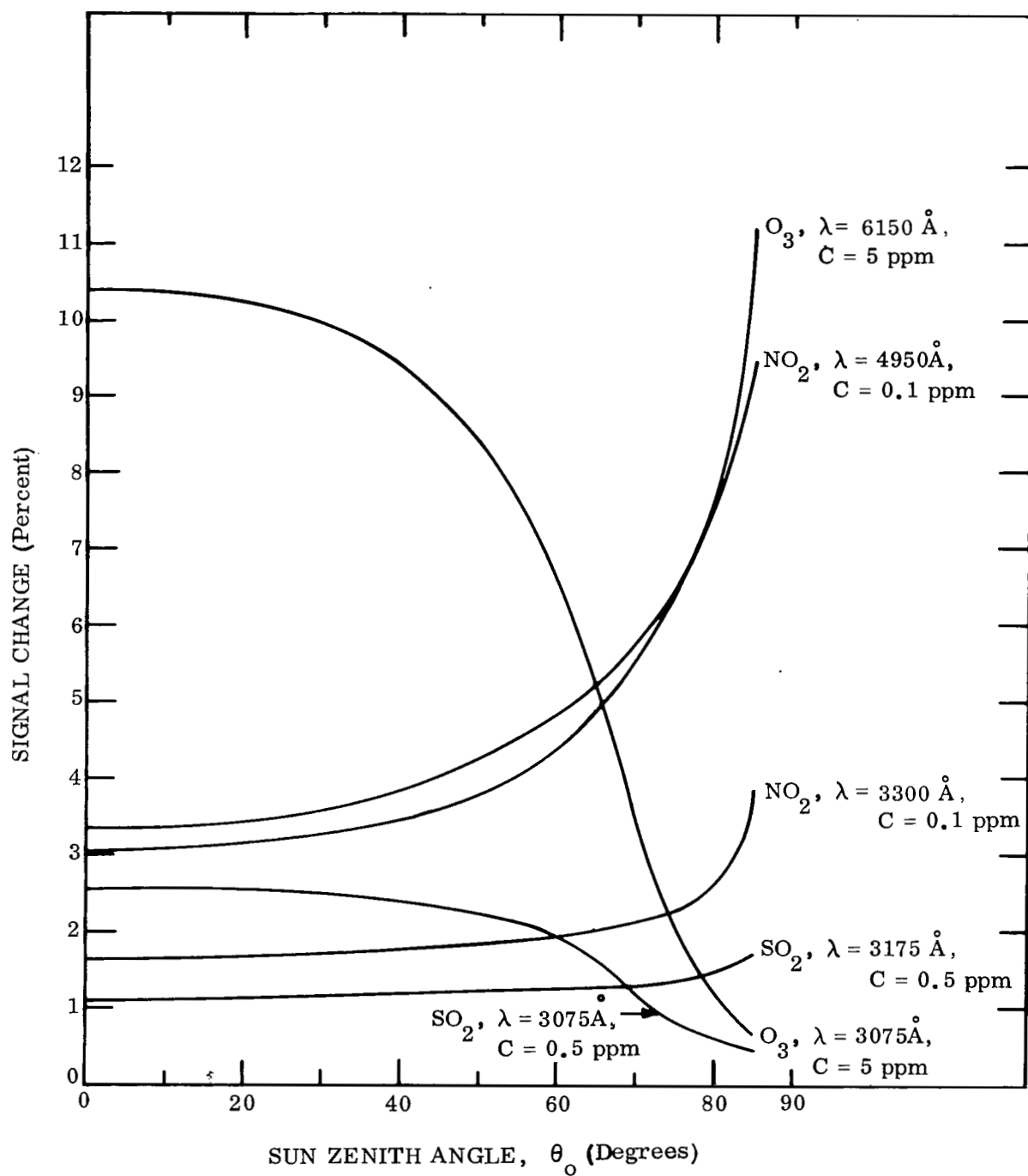


Figure 3-2. Signal Change versus Sun Zenith Angle ( $\theta = 0^\circ$ ,  $R = 0.2$ )

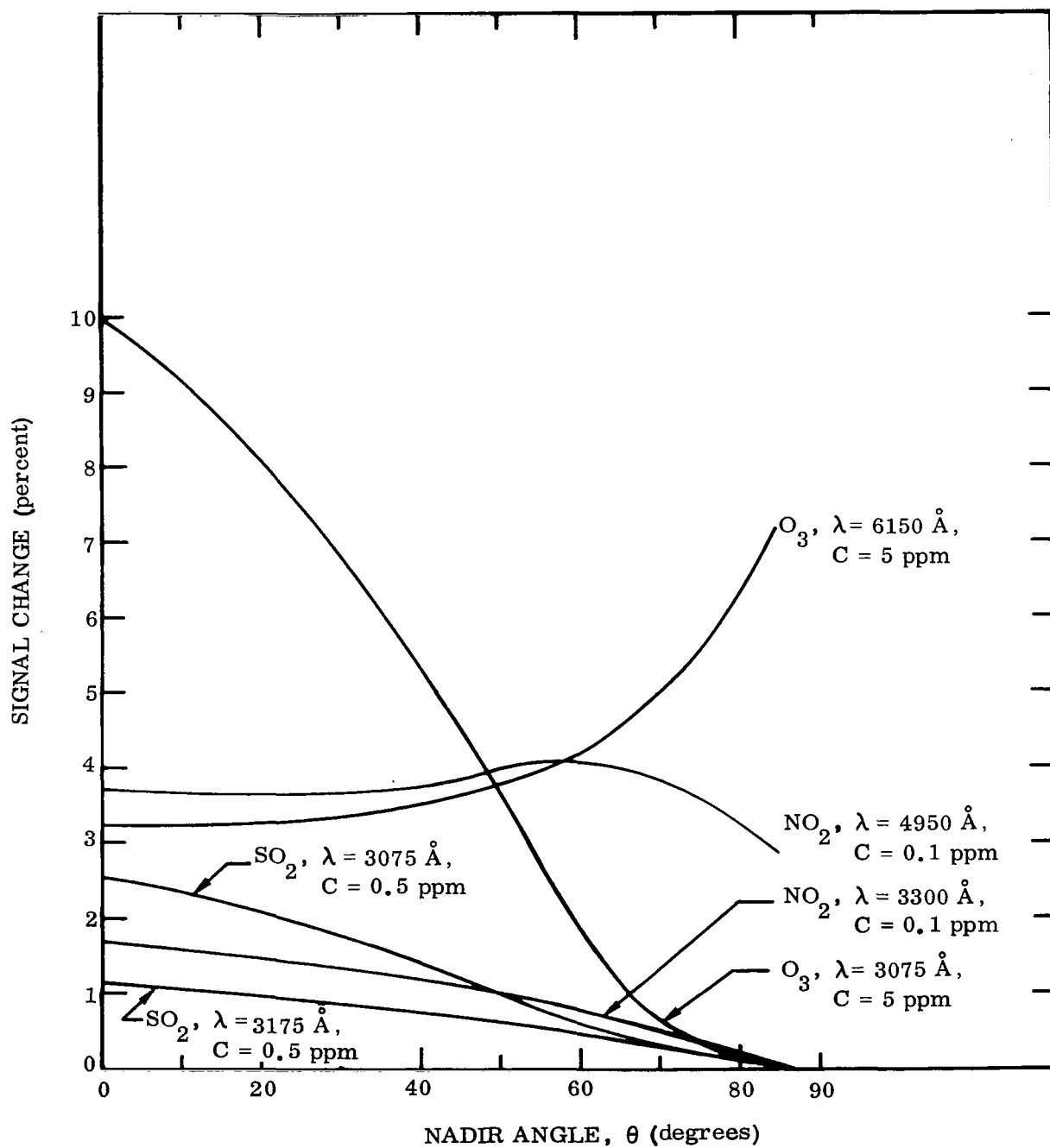


Figure 3-3. Signal Change versus Look Nadir Angle ( $\theta_0 = 30^\circ$ ,  $R = 0.2$ )



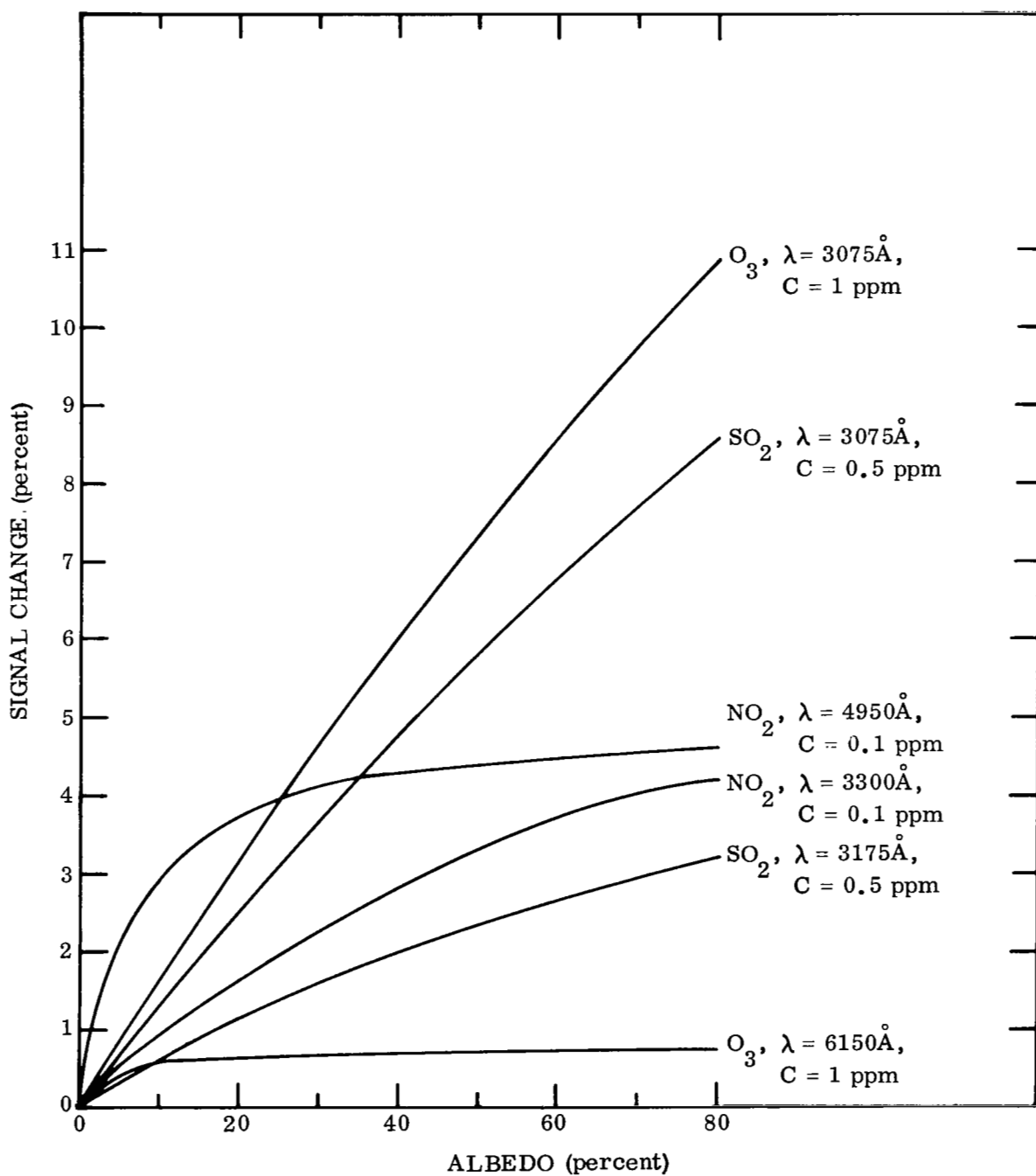


Figure 3-4. Signal Change versus Surface Albedo ( $\theta = 0^\circ$ ,  $\theta_o = 30^\circ$ )

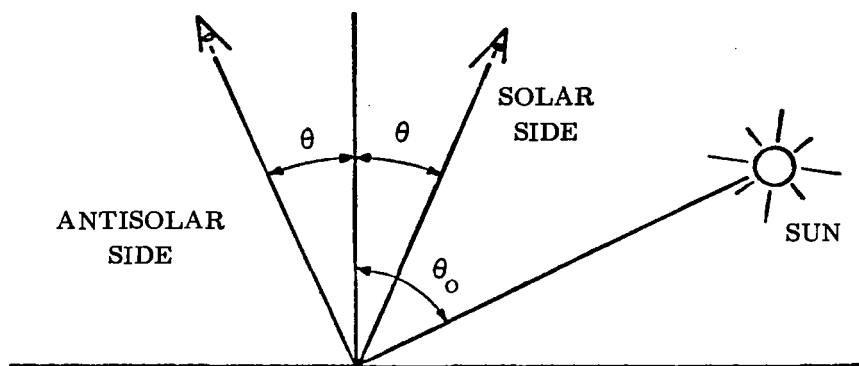


Figure 3-5. Schematic of Sun and Look Angles

completely eliminated, for observations from an aircraft platform. Barringer (Reference 17) has been very active in this field, developing the optical correlation technique and using it for aircraft observations of  $\text{SO}_2$  and  $\text{NO}_2$  pollutants. His measurements have been very successful in tracking movements of these pollutants in urban areas and show good qualitative agreement with ground-based in situ measurements of the pollutant concentration. However, from our considerations of the scattering problem, it is not clear that accurate quantitative values of the pollutant optical thickness are possible even at low altitudes.

Barringer is also developing a correlation interferometer for pollutant detection using reflected and scattered sunlight as the source (Reference 18). This technique would have the advantage of a larger energy throughput than the spectrometer, but is considerably more complex.

**3.1.4 ATMOSPHERIC AEROSOLS.** In addition to gaseous pollutants in the atmosphere, we must also consider particulate and aerosol pollutants. From analysis of atmospheric measurements, McCormick and Ludwig (Reference 19) suggest that there is evidence of a worldwide buildup of atmospheric aerosol pollution. An increase of aerosol content will produce an increased earth albedo, which in turn will produce a decrease in mean temperature of the earth-atmosphere system. This will counteract the postulated increase of temperature due to the "greenhouse effect" of the increased

CO<sub>2</sub> emissions by human activities. Indeed, the aerosol pollution may already be producing a greater effect than the CO<sub>2</sub>; a decrease in mean annual air temperature is reported (Reference 20) to have started between 1940 and 1950.

**3.1.4.1 Aerosol Characteristics.** In considering the remote detection of aerosols from a satellite, we must understand the characteristics of the aerosol in relation to its optical properties, i.e., how it scatters and absorbs radiation. Thus, it is important to know the size distribution of the particles and their composition in order to estimate their refractive index, which is an essential input parameter to scattering calculations by the Mie theory.

Junge (Reference 21) found that the natural aerosol content of the atmosphere can be represented for radii from 0.1 $\mu$  to 10 $\mu$ , by:

$$dn(r) = \gamma r^{-\nu} d(\log r) \quad (3-9)$$

where

$n(r)$  is the number of particles with radii between  $r$  and  $r + dr$ ,

$\gamma$  is a constant depending on the total particle concentration,

$\nu$  characterizes the size distribution.

Junge found that on the average the natural continental aerosol distribution was best described by  $\nu = 3$ .

The composition of the particulates is variable (Reference 22) and will vary considerably with location. Bullrich (Reference 23), in considering natural aerosols, decided that a refractive index of  $m = 1.55$  is most suitable for calculations of Mie scattering by the aerosols. However, it is not clear that this value is the best for all aerosol types, e.g., continental, maritime, industrial and natural vegetation hazes.

In a clean atmosphere the vertical distribution of the natural aerosol density varies with the meteorological conditions, but on the average it decreases, with a scale height of about 1.25 km (Reference 23) in the troposphere. The measurements of Chagnon and Junge (Reference 24) showed a peak in the distribution in the stratosphere at about 20 km. This peak is  $10^{-3}$  times the surface density.

**3.1.4.2 Optical Properties of Aerosols.** The problem of light scattering in the atmosphere due to Rayleigh and Mie scattering are discussed in a review article by Rosenberg (Reference 25) and in greater depth by Bullrich (Reference 23). Both authors emphasize that it is impossible to calculate backward from experimental measurements in the atmosphere to obtain quantitative aerosol information. This is due to the complicated scattering processes.

The scattering function and polarization function may be calculated by the Mie theory for a single spherical particle of known refractive index. However, in the real atmosphere the particles are not necessarily spherical and vary in size and composition. Thus the results obtained with the theory as applied to real aerosol distributions can be only approximate.

In addition to the approximations in the theory, the aerosol scattering is coupled with Rayleigh scattering by the molecules in the atmosphere. This coupling is very complicated due to multiple scattering.

Thus, to analyze experimental measurements, it is necessary to compare the results with calculations for various model aerosol atmospheres. In the case of satellite observations it is necessary to consider the effects of the intervening Rayleigh atmosphere, although it is not apparent that the two types of scattering will be separable.

**3.1.4.3 Calculations for Model Aerosol Layers.** Bullrich (Reference 23) makes calculations of the scattering and polarization functions for various size distributions of aerosols and suggests that the polarization function, which describes the degree of polarization as a function of scattering angle, is a sensitive indicator for the aerosol composition. The degree of polarization increases with  $\nu$  (the size distribution parameter), i.e., with a relative increase of small particles. Deirmendjian (Reference 26) shows results of calculations for different haze and cloud models and points out that for small samples of a polydisperse suspension the concentration of particles is directly proportional to the intensity scattered in the scattering angle  $\theta = 40$  degrees, regardless of size distribution and maximum size of the particles, provided the distribution is continuous and the refractive index is real.

Thus, observations of the degree of polarization of the atmosphere and its scattering function (near  $\theta = 40$  degrees), using the sun as a source, may allow satellite determinations of the aerosols. This possibility should be further investigated, particularly with regard to the separation of the Rayleigh and Mie scattering effects on the observations.

Other results of the theoretical calculations which might be used in remote detection of aerosols are outlined below:

- a. The ratio of forward to backscatter increases as  $\nu$  decreases, i.e., large particles effect a stronger forward scattering.
- b. The scattering functions for Rayleigh and for haze atmospheres are similar in shape, but the degree of polarization is much greater for the Rayleigh scattering. Both Rayleigh and Mie scattering exhibit a maximum degree of polarization near  $\theta = 100$  degrees.
- c. The degree of polarization for aerosols is independent of wavelength, whereas in

Rayleigh scattering it is strongly dependent, being large at small optical thickness and small in large optical thickness. The latter may be attributed to the depolarizing effect of multiple scattering.

- d. The polarization function may be used to distinguish haze from fog, according to the calculations of Bullrich. The transition from haze to fog occurs as the visibility falls below 400 m, and the polarization maximum shifts to about  $\theta = 145$  degrees for fog.

**3.1.4.4 Aerosol Absorption.** In addition to scattering radiation, aerosols may absorb radiation. This is indicated by the early measurements of Waldram (Reference 27) in the visible region. More recent work (Reference 28) has identified possible dust absorption bands in the infrared, although it is not clear that these could be identified in the real atmosphere.

At the present time the scattering properties, rather than the absorption properties of the aerosols, appear more useful for remote detection of particulates.

**3.1.4.5 A Rayleigh Atmosphere Seen from a Satellite.** Calculations of the intensity and polarization of radiation emerging from the top of the earth's atmosphere, assumed to be a pure nonabsorbing molecular atmosphere, have been made by Coulson (Reference 29) and Sekera and Viezee (Reference 30). These workers assumed that the earth's surface was a perfect diffuse reflector and nonpolarizing. However, Coulson (Reference 31) in a later work demonstrates that the earth's surface has directional reflectance properties and is polarizing, and that these properties strongly affect the outgoing radiation of the planet earth. Thus, quantitative observations would be very difficult for even a Rayleigh atmosphere without detailed knowledge of the surface characteristics.

**3.1.4.6 An Aerosol Atmosphere Seen from a Satellite.** Recent work (References 32, 33), using the Monte Carlo method for atmospheric modeling, has coupled Rayleigh and Mie scattering to determine the radiance and polarization seen from a satellite, assuming a Lambertian earth's surface. These are the first calculations to account for both types of scattering without significant approximation. However, experimental results again can be analyzed only by comparison with various model atmospheres, and knowledge of the surface characteristics is still necessary. The Monte Carlo technique is presumably capable of handling non-Lambertian surfaces.

**3.1.4.7 Laser Probing of Aerosols from a Satellite.** The use of a laser as a LIDAR to detect aerosol layers from a satellite does not seem feasible at the present time due to the low return signals backscattered from the layer. These signals would be less than those from the surface discussed in Subsection 4.1.7.

**3.1.4.8 Photographic Detection of Aerosols.** It would seem that a simple method of taking photographs from space of the earth's surface and measuring the contrast of

known features might provide a qualitative measure of the total aerosol content in the atmosphere, so long as the haze does not completely obscure the surface. The theory (Reference 34) of visual range and contrast attenuation by the atmosphere should allow an estimate of the aerosol optical thickness to be made. In the case of total obscuration the haze brightness could be related to its thickness. Examples of smoke pollution and dust storms (Reference 35) and industrial haze (Reference 36) have been observed in satellite photographs taken with cameras held by astronauts.

**3.1.4.9 Concluding Remarks About Aerosol Detection.** With the present theoretical knowledge of scattering (Rayleigh and Mie) within the real atmosphere, it seems unlikely that quantitative measurements of aerosol content in the lower atmosphere can be made from a satellite. However, it may be possible to estimate the aerosol content of the upper atmosphere using occultation techniques (Reference 37).

## **3.2 THE EARTH AS THE SOURCE OF RADIATION**

At wavelengths longer than about  $3.5\mu$ , the thermal emission from the earth is larger than the energy due to reflected and scattered sunlight. This thermal emission will be attenuated by pollutants in the atmosphere. A detector located in a satellite will receive this modulated thermal emission from the earth, and the thermal emission from the atmosphere. This radiation may be used to determine the pollution present in the atmosphere. There are two reasons for the importance of this spectral region in the detection of pollutants:

- Day and night observations are possible and
- All major pollutants have infrared absorption/emission bands.

A computer program was used to determine, at satellite altitudes, the level of radiation and the sensitivity of this radiation to the presence of pollutants. In this subsection we describe (1) the computer program, (2) some influences of meteorological conditions, (3) the interaction of radiation with pollutants, (4) some calculated radiance changes when air pollution exists, and (5) the detection possibilities in the microwave region.

### **3.2.1 RADIATION TRANSFER THROUGH THE ATMOSPHERE (COMPUTER PROGRAM)**

**3.2.1.1 Theory.** In determining the signal seen by the instrument, it is necessary to calculate the effects of the atmosphere on the radiation emitted by the earth, and the self-emission from the atmosphere.

The basic equation for the calculation of the energy,  $E_\lambda(h, T_o)$ , at a wavelength,  $\lambda$ , received at an altitude,  $h$ , from a surface with a temperature,  $T_o$ , may be expressed as:

$$E_\lambda(h, T_o) = \epsilon_\lambda N_\lambda(T_o) \tau_\lambda(0, h) + \int_0^h N_\lambda(T_z) \frac{d\tau_\lambda}{dz} dz \quad (3-10)$$

where

- $\epsilon_\lambda$  is the emissivity of the surface at wavelength  $\lambda$
- $N_\lambda(T)$  is the blackbody radiance at temperature  $T$  at wavelength  $\lambda$
- $T_o$  is the surface temperature
- $T_z$  is the atmospheric temperature at height  $z$
- $\tau_\lambda(0, h)$  is the atmospheric transmission at  $\lambda$  from the surface to  $h$
- $\tau_\lambda$  is the atmospheric transmission from altitude  $z$  ( $< h$ ) to  $h$ .

The first term on the right-hand side corresponds to the emission from the earth's surface, and the second term gives the integrated emission from the atmospheric gases. This may be simplified by dividing the atmosphere into a series of isothermal layers and replacing the integral term by a sum of terms representing the contribution of each individual layer:

$$E_\lambda(h, T_o) = \epsilon_\lambda N_\lambda(T_o) \tau_\lambda(0, h) + \sum_{i=1}^n N_\lambda(T_i) \Delta\tau_{\lambda i} \quad (3-11)$$

where

- $T_i$  is the mean temperature of atmospheric layer  $i$
- $\Delta\tau_{\lambda i}$  is the difference in transmission from the top of layer  $i$  to the observation level,  $h$ , and the bottom of the layer to  $h$ .

The units of the radiance,  $E_\lambda(h, T_o)$ , in Equation 3-11 are determined by those of  $N_\lambda(T)$ :

$$N_\lambda(T) = \frac{C_1}{\lambda^5 \left[ \exp\left(\frac{C_2}{\lambda T}\right) - 1 \right]}$$

where

$$C_1 = 1.1908 \times 10^4 \text{ w cm}^{-2} \text{ sr}^{-1} \mu^{-1}$$

$$C_2 = 1.4388 \times 10^4 \mu - ^\circ\text{K}$$

Thus, the radiance,  $E_\lambda(h, T_o)$ , is in units of watts  $\text{cm}^{-2} \mu^{-1} \text{sr}^{-1}$ .

**3.2.1.2 Atmospheric Transmission.** The value of the transmission,  $\tau_\lambda$ , used in the radiance calculations is the resultant transmission for all the species absorbing at that wavelength and is given by the product of the transmission of each individual species, e.g.,

$$\tau_\lambda = \tau(\text{H}_2\text{O}) \times \tau(\text{CO}_2) \times \tau(\text{N}_2\text{O}) \times \tau(\text{O}_3) \times \tau(\text{CH}_4) \times \tau(\text{pollutant}) \quad (3-12)$$

The validity of this assumption for overlapping absorption bands has been verified experimentally for atmospheric conditions, and for the low spectral resolution of the data used for these calculations. Aerosol attenuation is ignored in these calculations.

The gases  $\text{CO}_2$  and  $\text{N}_2\text{O}$  are considered to be uniformly mixed in the atmosphere and to be of constant concentration from day to day.  $\text{CH}_4$ ,  $\text{H}_2\text{O}$ , and  $\text{O}_3$  are variable gases and their distribution is an input variable in the computer program.

The transmission for each species is calculated using the methods of Green and Griggs (Reference 3) and Green et al. (Reference 38) in which empirical fits to laboratory data were made and applied to the atmosphere. In this study, the transmission model was updated using recent laboratory and theoretical absorption data and has been modified and extended to include the effects of pollutants. A summary of the specific transmission models for the various species is presented in Table 3-3. Details of the method for calculating the absorption coefficients of the pollutants are given separately (see Subsection 3.2.3).

**3.2.1.3 Comparison of Present Model With That of Wark Et Al.(Reference 40).** The present model is used to compute the spectral radiance as seen from a satellite looking vertically down through the same atmosphere used by Wark et al., with the exception of the ozone distribution. However, it was verified by computation that the small difference from our ozone distribution (total ozone 0.277 atm-cm) has a negligible effect on the spectral radiance. The comparison is made for two cases considered by Wark et al., namely, Number 31 (total ozone 0.273 atm-cm) and Number 43 (total ozone 0.289 atm-cm) in their reports. Number 31 is for Barter Island, Alaska, 1 January 1958, and is representative of a cold target and a cold dry atmosphere; Number 43, (Albuquerque, New Mexico, 11 July 1958) represents a warm target and a warm, moist atmosphere.



Table 3-3. Atmospheric Transmission Models

$\tau = \tau(\text{CO}_2) \times \tau(\text{Pol}) \times \tau(\text{H}_2\text{O}) \times \tau(\text{ROT}) \times \tau(\text{cont.}) \times \tau(\text{O}_3) \times \tau(\text{CH}_4)$				
Species	$\ln \tau$		$u(\text{atm-cm})$	
$\text{CO}_2$	$-k_\lambda u^{c_\lambda}$	$y_2 \int_{y_1}^{\frac{P}{P_S}} \left( \frac{T_S}{T} \right)^{1/2} \rho dy =$	$252 \left( e^{-0.313 y_1} - e^{-0.313 y_2} \right) \quad y > 12 \text{ km}$ $151 \left( e^{-0.226 y_1} - e^{-0.226 y_2} \right) \quad 0 - 12 \text{ km}$	
Pollutants and $\text{CH}_4$	$\frac{-k_\lambda u}{\sqrt{1 + \frac{k_\lambda u}{c}}}$	$y_2 \int_{y_1}^{\frac{P}{P_S}} \left( \frac{T_S}{T} \right)^{1/2} \rho dy =$	$7.64 \times 10^5 \sum_{i=1}^{19} \left[ f_{pi} \left( e^{-0.313 y_1} - e^{-0.313 y_2} \right) \right] \quad y > 12 \text{ km}$ $4.58 \times 10^5 \sum_{i=1}^{19} \left[ f_{pi} \left( e^{-0.226 y_1} - e^{-0.226 y_2} \right) \right] \quad 0 - 12 \text{ km}$	
$\text{H}_2\text{O}$	$\frac{-1.73 \frac{u}{u_{o\lambda}}}{\left( 1 + 5.24 \frac{u}{u_{o\lambda}} \right)^{1/2}}$	$m \int_{y_1}^{\frac{P}{P_S}} \left( \frac{T_S}{T} \right)^{1/2} \rho dy =$	$0.589 \sum_{i=1}^{19} \left[ m_i \left( e^{-0.226 y_1} - e^{-0.226 y_2} \right) \right] \quad 0 - 12 \text{ km}$ $0.985 \sum_{i=1}^{19} \left[ m_i \left( e^{-0.313 y_1} - e^{-0.313 y_2} \right) \right] \quad y > 12 \text{ km}$	
$\text{H}_2\text{O} (\text{ROT})$	$-k_\lambda u^{n_\lambda}$	$m \int_{y_1}^{\frac{P}{P_S}} \left( \frac{T_S}{T} \right)^{1/2} \rho dy =$	$0.589 \sum_{i=1}^{19} \left[ m_i \left( e^{-0.226 y_1} - e^{-0.226 y_2} \right) \right] \quad 0 - 12 \text{ km}$ $0.985 \sum_{i=1}^{19} \left[ m_i \left( e^{-0.313 y_1} - e^{-0.313 y_2} \right) \right] \quad y > 12 \text{ km}$	
Continuum	$-k_\lambda u$	$y_2 \int_{y_1}^{\frac{P}{P_S}} m \rho dy =$	$0.973 \sum_{i=1}^{19} \left[ m_i \left( e^{-0.127 y_1} - e^{-0.127 y_2} \right) \right] \quad 0 - 12 \text{ km}$ $0.787 \sum_{i=1}^{19} \left[ m_i \left( e^{-0.157 y_1} - e^{-0.157 y_2} \right) \right] \quad y > 12 \text{ km}$	
$\text{O}_3$	Reference 39			

LEGEND

$u$	is the optical thickness of species	$e$	is density of absorbing species at pressure $P$
$u_{o\lambda}$	is wavelength-dependent constant for water vapor	$P$	is pressure at altitude $y$
$c$	is a constant dependent on species	$P_S$	is pressure of experimental data
$n_\lambda$	is a wavelength-dependent constant for $\text{H}_2\text{O}$ rotational band	$T_S$	is temperature of experimental data
$m$	is water vapor mixing ratio	$T$	is temperature at altitude $y$
$m_i$	is mean water vapor mixing ration in $i$ th layer	$f_{pi}$	is pollutant mole fraction in $i$ th layer
$y_1, y_2$	are altitudes above surface		

The comparison of the models is shown in Figures 3-6 and 3-7. The agreement is generally very good, even though the present model uses only nineteen layers, in contrast to the two hundred used by Wark et al.

To satisfactorily compare different models it is necessary to consider the contribution of each absorbing species to the radiance. However, a direct comparison with measured data in the atmosphere is the final determination of the merit of a model. A comparison of the integrated radiance — calculated with the present model — with the measured radiance is made below and suggests that the present model satisfactorily describes absorption and emission properties.

**3.2.1.4 Comparison of Model With Measurements.** In the course of the Convair aircraft measurement program (Reference 41), measurements of the earth-atmosphere radiance as a function of altitude were made from the surface to 20,000 feet.

Typical results of the comparison of the model and the measurements are presented to further illustrate the validity of the present theoretical model.

Figure 3-8 shows a comparison of results of the calculations with radiance measurements made with a Barnes PRT-4 radiometer (8-14 $\mu$ ) over the ocean. The calculated results agree very closely with the measured values of surface radiometric temperatures.

Figure 3-9 shows a comparison of spectral calculation results with spectral measurements made with a Block I6T Interferometer Spectrometer 3,000 feet over the ocean. Again, the agreement is very good. The fluctuations on the measured data are due to instrument noise and not spectral features.

**3.2.1.5 Computer Program for Calculating Signal Changes.** The calculations have been programmed for the computer so that the signal changes due to pollutants may be readily determined as a function of wavelength for any altitude of observation, any clear meteorological conditions, and any concentration of pollutants. The computations were made using a CDC 6400 computer. Printouts of both the first and second terms of the right-hand side of Equation 3-11 are given as a function of wavelength. Also, the percent difference between "clean" and polluted atmospheres is printed as a function of wavelength; this, of course, is representative of the signal change an instrument would sense with and without pollution present.

Preliminary calculations showed that the signal change sensed by a satellite-borne sensor with and without air pollutants present is strongly dependent upon the difference between the earth's surface temperature and the effective temperature of the pollutants. In turn, this temperature difference is governed by the prevailing meteorological conditions. A survey of meteorological conditions that are likely to prevail, and their effect upon the temperature difference between the earth's surface and the pollutants is given in Subsection 3.2.2.

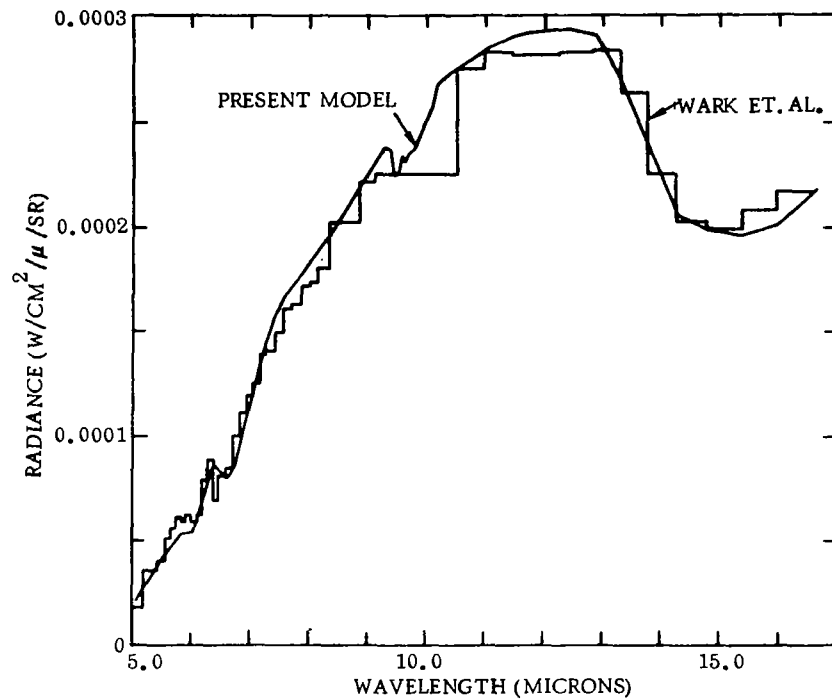


Figure 3-6. Radiance Outside Atmosphere Compared with Wark et al. (Reference 40) Model 31

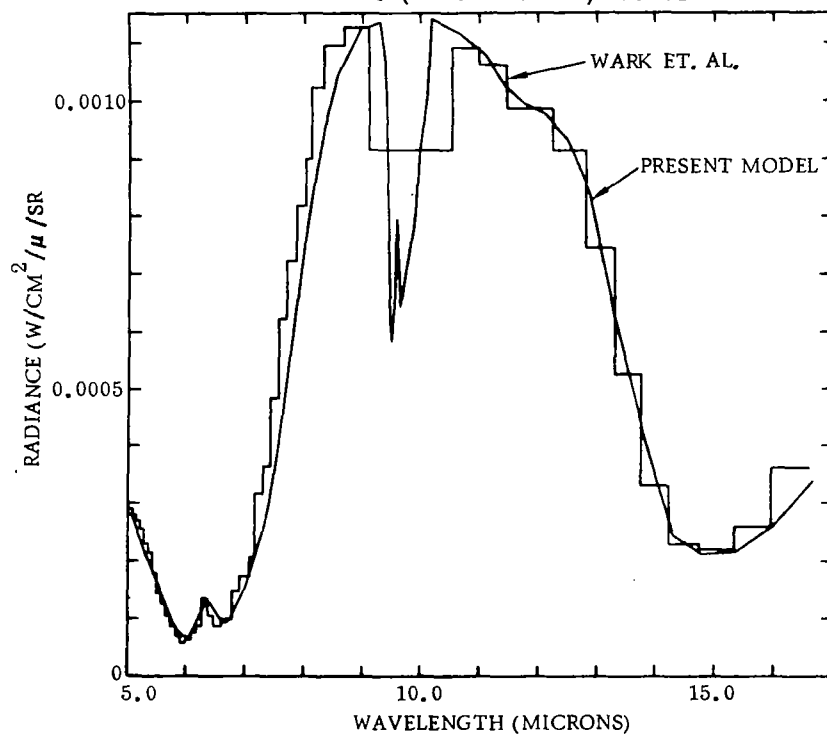


Figure 3-7. Radiance Outside Atmosphere Compared with Wark et al. (Reference 40) Model 43

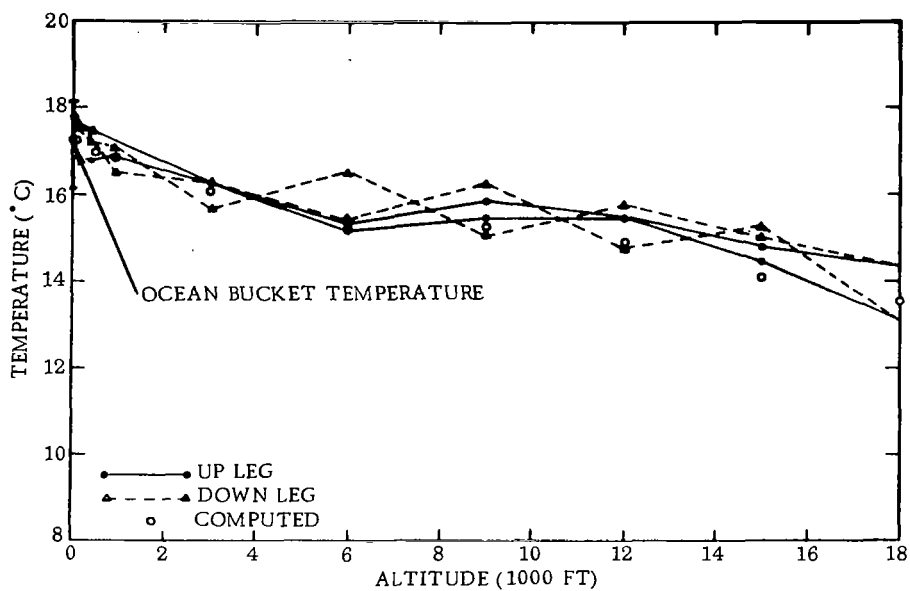


Figure 3-8. Radiometric Temperature versus Altitude (Ocean 12/8/66)(Reference 41)

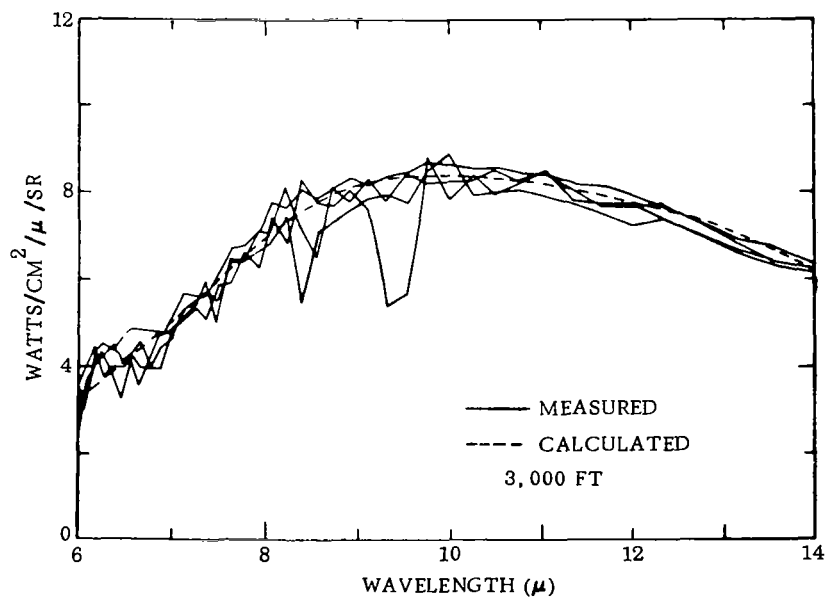


Figure 3-9. Surface Radiance versus Wavelength (Reference 41)

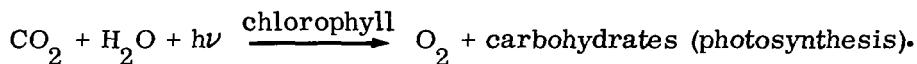
### 3.2.2 INFLUENCE OF METEOROLOGICAL CONDITIONS UPON AIR POLLUTION DETECTION

**3.2.2.1 General.** The results presented in this section were, in general, extracted from References 42 - 48. The most striking feature of near-earth meteorology is the pronounced diurnal effect normally exhibited by the vertical temperature profile. Under normal clear-weather conditions the near-earth vertical temperature profile is approximately isothermal shortly before sunset and after dawn. During daylight hours when the sun is 10 to 15 degrees above the horizon, incoming solar radiation exceeds outgoing terrestrial radiation, and the earth's surface warms; the air temperature decreases with height, rapidly in the lowest level and more slowly at the greater heights. This condition is characterized by a low level temperature lapse rate,  $dT/dh$ , ranging from the dry adiabatic ( $dT/dh = -1^\circ\text{C}/100\text{ m}$ ) to super-adiabatic ( $dT/dh < -1^\circ\text{C}/100\text{ m}$ ); at various times it may have a constant vertical density (isopycnic) profile ( $dT/dh = 3.4^\circ\text{C}/100\text{ m}$ ). At night, an inversion ( $dT/dh > 0$ ) forms; again, the largest temperature gradients are at the lowest heights. From thermodynamic equilibrium considerations the atmosphere is stable for  $dT/dh \geq -1^\circ\text{C}/100\text{ m}$  and unstable for  $dT/dh < -1^\circ\text{C}/100\text{ m}$ .

Under normal conditions, surface air pollution will not normally build up since pollutants emanating from the surface or near the surface will diffuse fairly rapidly both horizontally and vertically during the day-time hours when emissions are normally the largest. The night-time inversion layer will tend to trap emitted pollutants, but these are generally much less than the day-time emissions. Also, the normal night inversion is generally not very strong; typically, it extends to several hundred meters, and the air temperature,  $\overline{T}_a$ , is usually only a few  $^\circ\text{C}$  higher than the surface temperature,  $T_s$ . For these reasons low level night-time buildup of near-surface air pollution is usually small. However, locally generated pollution is eventually spread throughout the atmosphere and a global buildup of atmospheric pollution may be occurring.

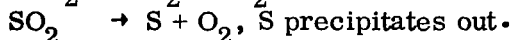
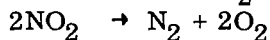
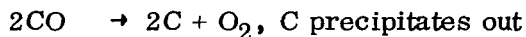
In general, pollutants distributed in the atmosphere are removed by the following mechanisms:

- a. Precipitation and condensation phenomena.
- b. Absorption and adsorption after contact with earth surface features.
- c. Chemical reactions after contact with earth surface features, e.g.,



Various oxidizing reactions.

- d. Escape to upper atmosphere where reducing reactions may occur,



At the present time it is not clear whether natural pollution removal methods are keeping pace with the steadily increasing amounts of pollutants being injected into the atmosphere, but many scientists are afraid that they are not. For example, estimates of CO<sub>2</sub> buildup range from 5 to 10 percent over the last 50 years. Jaffe (Reference 1) has investigated the paradox of CO being dumped into the atmosphere and, using known CO removal mechanisms, finds the removal mechanisms grossly inadequate to remove the total amount of CO being deposited; yet, local ground measurements do not indicate a buildup of CO. Global measurements of air pollutants are needed before the seriousness of global-scale air pollution can be evaluated.

If any significant amounts of air pollutants are accumulated at altitudes above 2 to 3 km there will generally exist sufficient temperature difference between  $T_s$  and  $\bar{T}_a$  to permit quantitative determinations of the pollutant concentration using infrared-sensitive instruments. On the other hand, if the pollutants are confined to the lower levels of the atmosphere, the temperature differential will be too small under some meteorological conditions to permit measurements. However, there are many factors that influence low-level vertical temperature profiles. Some of these factors will create sufficient differences between  $T_s$  and  $\bar{T}_a$  so that the detection of air pollution using infrared sensors will be feasible. In the following discussion we shall outline those factors which have a strong influence on near-earth atmospheric vertical temperature profiles.

**3.2.2.2 Diurnal Variations.** As mentioned previously the normal low-level temperature profile has a strong diurnal variation. Typically, the average night-time inversion will have a maximum  $\Delta T \equiv T_s - \bar{T}_a \approx -3^\circ\text{C}$  for  $h \approx 200$  m at about 22:00 hours, the day-time lapse temperature gradient will have a maximum  $\Delta T \approx 10^\circ\text{C}$  for  $h \approx 500$  m at about 13:00 hours; and at about 1 hour after sunrise and at about sunset  $\Delta T \approx 0$  for  $h \approx 200$  m. Thus, on the average, measurements of air pollution by remote, infrared sensors would best be made at about 13:00 and 22:00 hours, and no measurements would be possible near the times of sunrise and sunset. It must be stressed, however, that these values are only on the average. In reality, most severe low-level pollution builds up during occasions when day-time temperature inversions exist and the lower atmosphere is stable. Under these conditions, a typical low-level inversion with  $\Delta T \approx -10^\circ\text{C}$  may exist from 0 to 500 or 1000 m, and local air pollution will be confined within this inversion layer. In other cases two inversion layers may develop sequentially (one with  $\Delta T \approx -8^\circ\text{C}$  from 0 to about 500 m and a second with  $\Delta T \approx -4^\circ\text{C}$  from about 1000 to 1500 m) and air pollution will be trapped in two layers.

**3.2.2.3 Seasonal Variations.** The principal effect of seasonal changes is that temperature excursions are generally less in the winter than in the summer, but the same diurnal cycling occurs with respect to the times of sunrise and sunset. Likewise, the vertical temperature gradients near the earth's surface are usually smaller in the winter than in the summer. However, day-time thermal inversions do not occur as frequently in the winter as in the summer; but, when they do, serious buildups of local air pollution may occur due to increased pollutant emissions created by heating requirements.

**3.2.2.4 Atmospheric Moisture Content.** The presence of increased moisture in the atmosphere decreases the cooling rate of the earth's surface by terrestrial radiation, and smaller temperature gradients will exist. If the moisture content increases sufficiently to cause precipitation, an effective scavenging of pollutants occurs.

**3.2.2.5 Low-Level Winds.** The primary role of winds is to increase the mixing rates, which reduces temperature gradients. However, the increased atmospheric mixing disperses the air pollutants more rapidly. Over large-scale rough surfaces (like cities), increased low-level winds particularly enhance the vertical mixing, and smaller temperature gradients exist. However, the sudden occurrence of low-level winds will influence the atmospheric temperature profile more rapidly than the temperature of the earth's surface, and a very large temperature gradient may exist within a few centimeters of the surface.

**3.2.2.6 Surface Characteristics.** The characteristics of the portion of the earth's surface being used as a background may strongly influence the local temperature profile. Among the more influential factors are the surface color, vegetation, if any, roughness, slope with respect to the sun, moisture content, and state (liquid or solid).

Dark surfaces (low albedo) warm rapidly due to solar heating, and large  $\Delta T$ 's (in excess of  $20^{\circ}\text{C}$  in a cm) will arise. An example of this is asphalt paving, which becomes much hotter than the air above it. Typically, urban areas exhibit a higher surface temperature than the surrounding open countryside, partly for this reason.

Several studies (Reference 48) have shown that both surface and air temperatures in urban areas are generally considerably greater, and the diurnal range smaller, than those of the surrounding rural areas. This is undoubtedly due not only to the color effect, but also due to locally generated heat and the greater mixing due to the wind-buildings effect.

Surveys (Reference 48) of the San Francisco Bay area have indicated that the temperature near an urban center may be as much as  $11^{\circ}\text{C}$  higher than the surrounding area and, on the average,  $6^{\circ}\text{C}$  higher. These values may be compared with the Tiros II data (Reference 49), which indicated a  $10^{\circ}\text{C}$  higher temperature over San Francisco than over the ocean. It was suggested (Reference 49) that the Tiros II results might be only an apparent temperature increase due to a "hot" ozone pollution layer. From the above, this would not appear to be a necessary conclusion.

The effect of vegetation growing on the earth's surface is to retard the solar heating of the terrestrial surface. This creates a peak in the temperature profile located near the top of the vegetation (the crest for trees). For a sensor looking downward upon dense vegetation, the apparent surface becomes the top of the vegetation and the pertinent temperature difference is the one between  $\overline{T}_a$  and the temperature of the top of the vegetation. The temperature profiles extending from the top of the vegetation are similar to those of temperature profiles over bare ground.

The slope of the surface with respect to the sun's elevation is an important parameter. If the attitude of the surface is such that the sun's rays become normal to it, very high surface temperatures may exist with relatively cool temperatures in the near air layers. In these cases  $\Delta T$ 's in excess of  $20^{\circ}\text{C}$  within a meter distance have been observed.

Evaporation of moisture from the ground will tend to retard terrestrial heating, and air temperature gradients will generally be less than for drier soils. The same applies over large bodies of water such as oceans. However, a sharp temperature difference usually exists at the earth-air boundary due to the evaporation effects which create a thin, saturated boundary layer. Thus, one expects  $\Delta T$ 's of up to  $\pm 4^{\circ}\text{C}$  within a one-meter vertical path.

**3.2.2.7 Spectral Inversion Procedures for Atmospheric Sounding.** Since the determination of vertical concentration profiles of atmospheric pollutants is important, the possible application of spectral inversion techniques to this problem is outlined.

The equation for radiative transfer through the atmosphere (e.g., Equation 3-10) expresses a measurable function of wavelength (viz., the spectral radiance in a vertical direction) as an integral of the product of the local radiance and the derivative of the transmissivity over the vertical path. This suggests the approach of measuring the radiance as a function of wavelength and then inverting the integral equation to determine the local radiance (and hence, temperature) or transmissivity (and hence, concentration), if one quantity is known, as a function of altitude.

By making various simplifying assumptions, it is possible to convert this equation into a Fredholm integral equation of the first kind. There are established procedures for performing this inversion process, which is known to be unstable; i.e., an infinite number of "solutions" can be found which satisfy the equation to arbitrary accuracy.

Obvious physical limitations can be used to restrict the number of "solutions," and standard procedures have been developed for selecting optimum solutions. If statistical information on local mean temperature profiles is available, this can also be used in the inversion process. (See References 50, 51, 52).

A conventional approach is to make spectral radiance measurements in the  $15\text{-}\mu$  band of  $\text{CO}_2$  and invert these measurements to produce a vertical temperature profile. The distribution of  $\text{CO}_2$  in the atmosphere is assumed known and constant, and the transmissivity of atmospheric  $\text{CO}_2$  is assumed not to vary significantly from a standard set of values.

In general, deviations from the above assumptions are systematic and do not affect the results of the inversion procedure seriously. The major difficulty is introduced by random errors of measurement. These random errors magnify the inherent instability of the inversion process greatly. Considerable care in taking of measurements is required to obtain acceptable accuracy.



Once the temperature profile has been established, a similar set of measurements on a selected absorption band of a molecule whose vertical concentration profile is unknown could, in principle, be used to infer some information on its vertical concentration profile by a subsequent inversion process. Because of the compounding of uncertainties in the inferred temperature profile with the experimental error in the new set of measurements, this approach does not presently appear to be a feasible means of accurately determining concentration profiles of trace constituents.

**3.2.2.8 Conclusions.** To summarize, the temperature difference between the earth's surface and the lower atmosphere is the major parameter governing the detection of air pollution by infrared-sensitive instruments. In turn, this temperature difference is affected by many factors which can create, under most conditions, sufficiently large differences (either positive or negative) that the measurement of air pollution by remote, infrared sensors becomes feasible.

### **3.2.3 SPECTRAL CHARACTERISTICS OF POLLUTANT SPECIES IN THE INFRARED**

**3.2.3.1 Theoretical Background.** The molecular emission spectrum in the infrared consists of the superposition of a large number of individual spectral lines. This complex fine structure is normally not apparent in most measured spectra because of the finite spectral resolution of the spectrometers used. However, its importance is indicated if the measured transmission,  $\tau$ , of a uniform volume of gas is found not to obey Beer's law. Beer's law may be written in the form

$$-\frac{d}{d\ell} \ln(\bar{\tau}) = \text{constant} \quad (3-13)$$

This relationship is satisfied for the monochromatic function,  $\tau$ ; however, it may or may not be satisfied for the mean transmissivity,  $\bar{\tau}$ . If  $k_{\lambda} \ell$  is small ( $\ll 1$ ) or does not vary greatly over the interval  $\Delta\lambda$ , corresponding to the spectrometer resolution, then  $\exp(-k_{\lambda} \ell)^{\Delta\lambda}$  can be closely approximated by  $\exp(-\bar{k}_{\lambda}^{\Delta\lambda} \ell)$ . If  $k_{\lambda} \ell$  does vary greatly and is large somewhere in the interval, this approximation cannot be made, and Beer's law (Equation 3-13) is not satisfied. Thus Equation 3-13 may be used to extrapolate thin-gas emissivity measurements to any thickness if  $k_{\lambda}$  is a slowly varying function of wavelength (such as for solid carbon particles). However, a different approach is normally required for molecular emission.

Approximate theoretical techniques for treating molecular emission have been developed for isothermal gas volumes. These techniques directly evaluate the average or "smeared" emissivity which the spectrometer measures. These are the so-called band model procedures (statistical model, regular model, etc.). They treat large groups of spectral lines as regular or random arrays and carry out the wavelength averages of the transmission or emissivity analytically.

In a random band model, the transmission function ( $\bar{\tau}$ ) may be written as a product of the transmission  $\bar{\tau}_i$  of the individual line sequences which result from transitions having different upper vibrational states:

$$\bar{\tau} = \prod_i \bar{\tau}_i \quad (3-14)$$

In Figure 3-10 a schematic breakdown of the CO<sub>2</sub> spectrum into individual sequences is shown. Here  $\bar{\tau}_i$  is related to the ratio of the mean equivalent width,  $W_i$ , to the mean line spacing,  $d_i$ , of the  $i$ th sequence:

$$\bar{\tau}_i = \exp(-W_i/d_i) \quad (3-15)$$

It is convenient to express the ratio  $W_i/d_i$  in terms of the smeared absorption coefficient,  $\bar{k}_i$  ( $= S_i/d_i$ , where  $S_i$  is the mean line intensity of the  $i$ th sequence) and the ratio  $a_i$  of the line half-width to mean line separation ( $a_i = \gamma_i/d_i$ ):

$$W_i/d_i = a_i f(\bar{k}_i u/a_i) \quad (3-16)$$

Here  $u$  is the path length. The dimensionless function ( $f$ ) is the curve of growth for the  $i$ th sequence. For equally intense randomly distributed Lorentz lines,  $2\pi f(x/2\pi)$  is the Ladenburg-Reiche function (Reference 53).

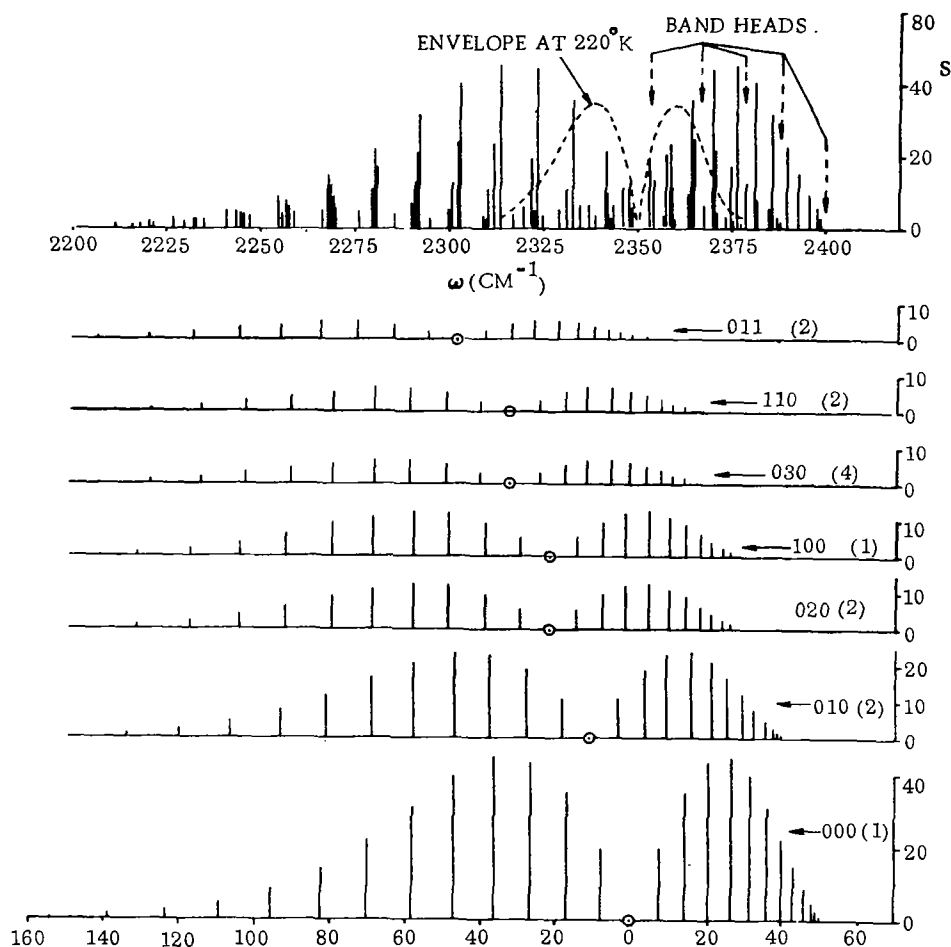
$$f_{LR}(x) = x e^{-x/2\pi} \left( J_0\left(\frac{ix}{2\pi}\right) - iJ_1\left(\frac{ix}{2\pi}\right) \right) \quad (3-17)$$

Within 10 percent, this function may be approximated by the somewhat simpler form (see Figure 3-11):

$$f_1(x) = x/\sqrt{1+x/4} \quad (3-18)$$

This curve of growth is exact for an exponential distribution of line intensities.

When the total number of branches contributing to the emission of a particular wavelength is relatively small, and not too many evaluations of  $\bar{\tau}$  are required, it is feasible to compute the contribution ( $\bar{\tau}_i$ ) from each fundamental sequence individually and multiply the individual terms together. However, in general, the simplest method is to assign all the lines to one group and approximate the curve of growth by a single universal temperature- and pressure-independent function, such as the Ladenburg-Reiche function or that corresponding to an exponential or  $1/S$  intensity distribution (Reference 54). In this approximation the transmission properties can be specified in terms of two parameters at each wavelength and temperature: the mean absorption coefficient,  $\bar{k}$ , and the mean value of the line width to spacing ratio,  $a$ . For homogeneous gases at high pressures, where Doppler broadening is not important, this has been found to yield reasonably accurate results when the line spacing is chosen so that



The total spectrum is a superposition of a number of individual sequences or branches corresponding to transitions between different vibrational levels (of which only a few are shown). The lower state of the transition is denoted by vibrational quantum numbers ( $v_1, v_2, v_3$ ) to the right of each sequence. The bracketed value is the number of sequences which have the same values of  $v_1, v_2, v_3$  in the lower state. For clarity only every fifth rotational line is shown.

Figure 3-10. Partial Representation of the Line Intensities of  $\text{CO}_2$  at  $1500^\circ\text{K}$

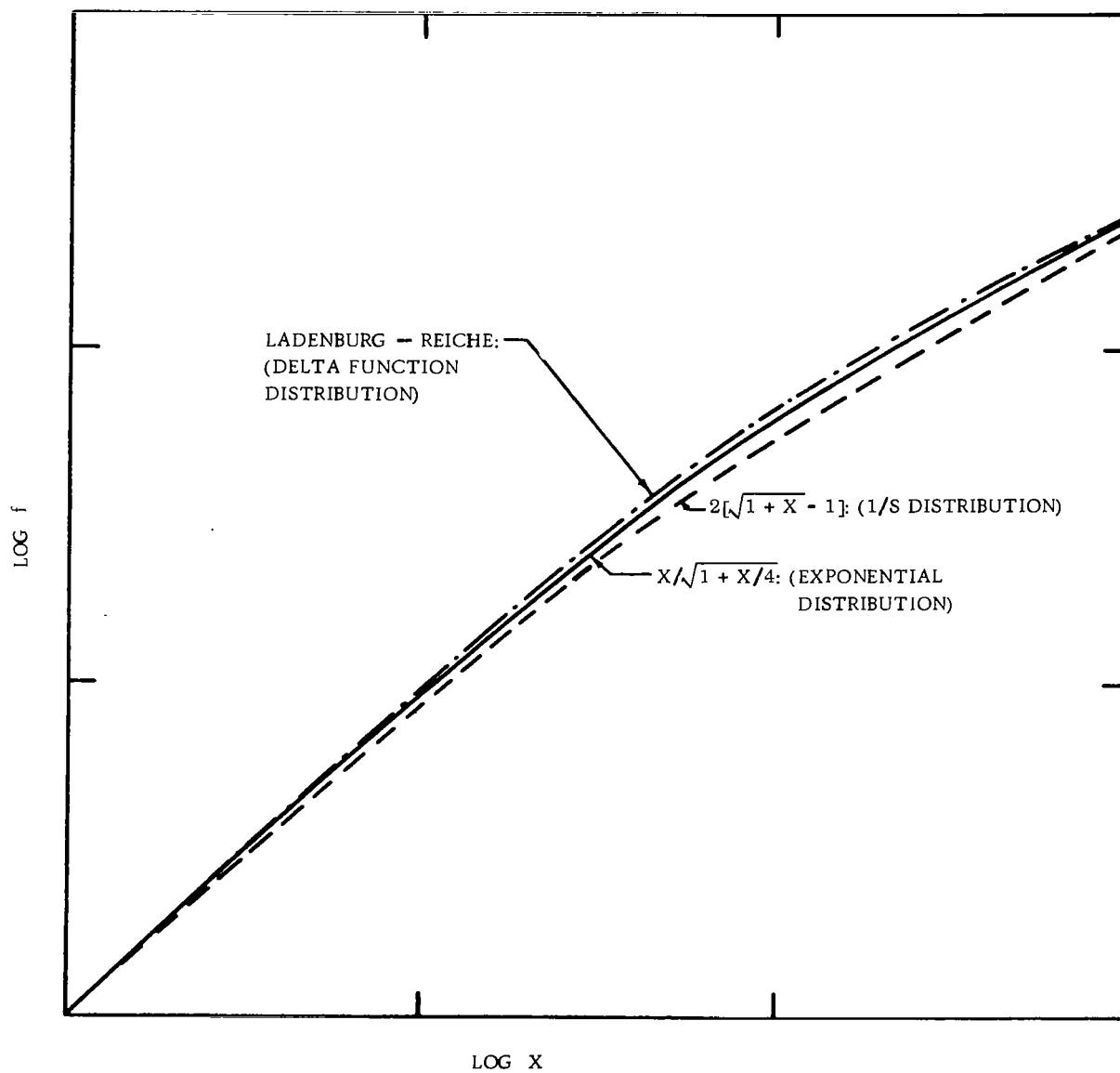


Figure 3-11. Collision-Broadened Curves of Growth for Various Intensity Distributions

the correct limiting values are obtained in the square root region. This is due to the fact that, for Lorentz lines, the curves of growth are relatively insensitive to the intensity distribution functions. For example, the curve of growth for a delta function distribution,  $\delta(S-\bar{S})$ , differs from that for a  $(1/S)e^{-S/\bar{S}}$  distribution by less than 25 per cent throughout the entire range of optical depth. (See Figure 3-11).

In general, the mean emissivity may be represented as a two-parameter function of the gas thickness

$$\bar{\epsilon} = 1 - \exp \left( -f[\bar{k}(\lambda)\ell, a(\lambda)] \right) \quad (3-19)$$

where both  $\bar{k}(\lambda)$  and  $a(\lambda)$  are functions of temperature,  $T$ , wavelength,  $\lambda$ , and partial pressure,  $p_i$ , of the various species. The form of the function  $f(x,a)$  depends on the assumed line intensity probability distribution function, but calculations have shown that largely different distribution functions result in very similar functions  $f(x,a)$ . When more than one species is present the emissivity has the form

$$\bar{\epsilon} = 1 - \exp \left( -\sum_i f_i [k_i(\lambda)\ell, a_i(\lambda)] \right) \quad (3-20)$$

For example, the random exponential model for collision-broadened lines yields an emissivity function of the form

$$\bar{\epsilon} = (1 - \bar{\tau}) = 1 - \exp \left\{ -\frac{\bar{k}\ell}{\sqrt{1 + \frac{1}{\pi} \frac{\bar{k}\ell}{a}}} \right\} \quad (3-21)$$

Here  $\bar{k}$  is the true mean absorption coefficient and may be evaluated from the emissivity of a very thin sample of gas ( $\ell$  small). The parameter  $a$  is the ratio of the line half-width to the mean line spacing. Note that, for this case

$$-\frac{d}{d\ell} (\ln \bar{\tau}) \propto \ell^{-1/2} \quad (3-22)$$

where  $\ell$  is large (this is the so-called square root region).

In an inhomogeneous gas (pressure and/or temperature not constant along the line of sight), the Curtis-Godson approximation is used to replace a multi-layered medium (in each layer of which a given spectral line may have a different intensity and half-width) by a homogeneous medium with an equivalent line intensity and an equivalent half-width. These two equivalent values are determined by the condition that the approximation be exact in the linear and square-root regions (Reference 55).

This approximation has been extended to the use of band models by similar defining relations between the mean absorption coefficient,  $\bar{k}$ , and the fine-structure parameter,  $a$ , which expresses this ratio of mean line half-width to mean line spacing.

The error introduced by the use of the Curtis-Godson approximation has been investigated by Thomson (Reference 56) and is found to be large only when great differences of temperature or line widths occur.

**3.2.3.2 Extraction of Absorption Coefficients and Fine-Structure Parameters from Laboratory Data.** The parameter "a" in the equation for the curve of growth of a random exponential Lorentz band model is defined as the ratio of the half-width to the effective mean line spacing. In applying this model to a particular molecule, sufficiently extensive observations should be made to evaluate the parameters  $\bar{k}$  and a separately, while verifying the applicability of the model to the molecule.

In the absence of observations extensive enough to evaluate  $\bar{k}$  and a uniquely, it may be necessary to estimate a in advance, and determine  $\bar{k}$  based on this assumed value. The exponential intensity distribution is not derived from any physical properties of the molecule, hence any theoretical relationship between a and the molecular parameters is necessarily tenuous. However, in the region where the strongest lines dominate the properties of the spectrum, some approximate relationship can be obtained. In the spectrum of a diatomic molecule, the separation of the lines in the fundamental band is given by  $2B$ , where  $B$  is the rotational constant of the molecule. For a rigid symmetric-top molecule, a similar expression is valid, at least for the parallel bands. For perpendicular bands, and bands of asymmetric-top molecules, appropriate effective rotation constants can be chosen to give reasonable estimates of the mean line spacing. Additionally, where sufficiently high resolution spectra are available, the number density of intense lines can be determined by counting. Reasonably consistent results have been obtained from these two procedures.

The line width can also be estimated with reasonable accuracy. For a nonpolar molecule, the air-broadened half-width can be taken to be about  $0.05 \text{ cm}^{-1}$ . For highly polar molecules higher values are appropriate. Sophisticated methods of calculating line widths exist, but are probably not justified for this purpose.

We note that in no case does the parameter a enter into the expression for absorptivity with more than a square-root dependence; generally it is less. The results of the procedure described may be quite insensitive to the particular value of a which was chosen.

In general, the procedure is to select a quantitative spectral measurement, assume an "a", and determine an effective  $\bar{k}$  based on this value of a. This set of values is used to extrapolate to other values of path length. If the measurements are in the linear region,  $\bar{k}$  (as well as absorptivity) is completely insensitive to the value of a. On the other hand, in the square-root region the absorptivity is dependent only on the product  $\bar{k} a$ , so that while the individual values of  $\bar{k}$  and a may be in considerable error, the product is unaffected. In the intermediate region, an error in "a" will have some effect on the predicted absorptivities. The largest inaccuracies will result from extrapolations to largely different conditions, using parameters determined from restricted and insufficient measurements.

Values of  $\bar{k}$  and  $a_o$  ( $=a/p$ ) have been extracted for the molecules CO, NO, HCl, HF, SO<sub>2</sub>, NO<sub>2</sub>, O<sub>3</sub>, NH<sub>3</sub>, CH<sub>4</sub>, C<sub>2</sub>H<sub>4</sub>, C<sub>6</sub>H<sub>6</sub>, and PAN and are presented in Table A-6 (Appendix A) and Table 3-4, respectively. The data for the diatomic molecules were taken from the theoretical calculations of Malkmus and Thomson (Reference 57). The data for most of the other molecules were based on Pierson, Fletcher, and Gantz (Reference 4). Walshaw (Reference 58) was used for O<sub>3</sub>, and Leighton (Reference 8) for PAN. Further discussion of the reliability of these coefficients is given in Subsections 3.2.3.3 and 3.2.3.4.

Table 3-4. Values of  $a_o$

	$a_o$	Spectral Interval
CO	0.015	2.3-5.1 $\mu$
SO <sub>2</sub>	0.15	3.8-10 $\mu$
NO <sub>2</sub>	0.12	3.1-6.5 $\mu$
PAN	0.5	7.4-13.2 $\mu$
C <sub>2</sub> H <sub>4</sub>	0.027	2.1-12.3 $\mu$
NH <sub>3</sub>	0.042	4.9-6 $\mu$
NH <sub>3</sub>	0.21	6-6.3 $\mu$
NH <sub>3</sub>	0.042	6.3-10.1 $\mu$
NH <sub>3</sub>	0.21	10.1-10.8 $\mu$
NH <sub>3</sub>	0.042	10.8-15 $\mu$
C <sub>6</sub> H <sub>6</sub>	0.08	0.1-9.9 $\mu$

3.2.3.3 Accuracy of Determination of Mean Absorption Coefficients. Spectral absorption measurements are generally available over a more restricted range of parameters (path length, pressure) than one might hope for. In fact, such data may be available for only one pressure and path length. If such a spectrum is known to be in the linear region of the curve of growth (e.g., if it is fully pressure-broadened), the spectral absorption coefficient,  $\bar{k}$ , can be derived from it. If it is known to be in the square-root region, the product  $a\bar{k}$  of the fine-structure parameter and the spectral absorption coefficient can be determined (but not the two separately). If, as is quite likely, the measurement is in some intermediate region (or is not known to be in the linear or square-root region), some assumption regarding the value of the fine-structure parameter may be made to determine an absorption coefficient.

If, for example, the measurement happens to be in the square-root region, any assumed value of "a" will yield a corresponding value of  $\bar{k}$ . If these values are used to

extrapolate to other points in the square-root region, since only the product  $\bar{a}\bar{k}$  is involved, no error results even if  $\bar{k}$  and  $a$  are separately in considerable error. If an extrapolation is made to other regions of the curve of growth, some degree of error is introduced, which will be examined quantitatively later. A similar argument holds for measurements and extrapolations within the linear region of the curve of growth.

We are using the assumed curve of growth

$$-\ln \bar{\tau} = \frac{\bar{k}u}{\sqrt{1 + \bar{k}u/4a}} = \frac{\bar{k}pc\ell}{\sqrt{1 + \bar{k}c\ell/4a_0}} \quad (3-23)$$

where

$$u = pc\ell \quad (3-24)$$

and

$$a = a_0 p \quad (3-25)$$

which has been derived theoretically for a random Lorentz band model with an exponential line intensity distribution function. It has been shown that random Lorentz band models with widely different intensity distribution functions have curves of growth which are only slightly different.

The asymptotic (linear and square-root) regions of Equation 3-23 are given by

$$-\ln \bar{\tau} = \bar{k}pc\ell \quad (3-26)$$

and

$$-\ln \bar{\tau} = \sqrt{4a_0 \bar{k}p^2 c\ell} \quad (3-27)$$

Equation 3-23 can be rewritten

$$-\ln \bar{\tau} = \frac{\sqrt{4a_0 \bar{k}p^2 c\ell}}{\sqrt{1 + 4a_0/\bar{k}c\ell}} \quad (3-28)$$

The error in absorptivity,  $\alpha$ , is less than or equal to the error in  $-\ln \bar{\tau}$ . We will examine the error in Equation 3-28 resulting from an error in  $a$ . If we consider Equation 3-28 a function of the two parameters  $a_0$  and  $a_0 \bar{k}$ , we can write it as

$$-\ln \bar{\tau}(a_0, a_0 \bar{k}) = \frac{\sqrt{4a_0 \bar{k}p^2 c\ell}}{\sqrt{1 + 4a_0^2/a_0 \bar{k}c\ell}} \quad (3-29)$$



If we denote an alternate choice of  $a_o$  by  $a_o'$ , then we have

$$\frac{\ln \bar{\tau}(a_o', a_o' \bar{k}')}{\ln \bar{\tau}(a_o, a_o \bar{k})} = \sqrt{\frac{1 + 4a_o'^2/a_o \bar{k} c \ell}{1 + 4a_o'^2/a_o' \bar{k}' c \ell}} \times \frac{a_o' \bar{k}'}{a_o \bar{k}} \quad (3-30)$$

We identify  $a_o'$  and  $\bar{k}'$  here with the "correct" values of the parameters, and  $a_o$  with the assumed value used in determining  $\bar{k}$ . If the measurement was made in the square-root region of the curve of growth, Equation 3-27 shows that the product  $a_o \bar{k}$  is determined, and therefore,  $a_o \bar{k} = a_o' \bar{k}'$ . Thus we have

$$\frac{\ln \bar{\tau}(a_o', a_o \bar{k})}{\ln \bar{\tau}(a_o, a_o \bar{k})} = \sqrt{\frac{1 + 4a_o'^2/a_o \bar{k} c \ell}{1 + 4a_o'^2/a_o \bar{k} c \ell}} \quad (3-31)$$

Therefore, the fractional error in the mean absorptivity,  $\bar{\alpha}$ , is bounded by

$$\left| \frac{\bar{\alpha}(a_o', a_o \bar{k})}{\bar{\alpha}(a_o, a_o \bar{k})} - 1 \right| \leq \left| \frac{\ln \bar{\tau}(a_o', a_o \bar{k})}{\ln \bar{\tau}(a_o, a_o \bar{k})} - 1 \right| = \left| \frac{1 + 4a_o'^2/a_o \bar{k} c \ell}{1 + 4a_o'^2/a_o \bar{k} c \ell} - 1 \right| \quad (3-32)$$

As an example, we have determined independently that the Pierson spectrum of  $\text{CH}_4$  at  $3100 \text{ cm}^{-1}$  is completely in the square-root region. Since  $a_o \bar{k} = 0.0170 \text{ atm}^{-2} \text{ cm}^{-1}$ , an assumed value of  $a_o = 0.013 \text{ atm}^{-1}$  leads to a value of  $\bar{k} = 1.31 \text{ atm}^{-1} \text{ cm}^{-1}$ .

Then we have

$$\left| \frac{\alpha(a_o', 0.0170)}{\alpha(0.013, 0.0170)} - 1 \right| \leq \left| \sqrt{\frac{1 + 0.0398/c \ell}{1 + 23.5 a_o'^2/c \ell}} - 1 \right| \quad (3-33)$$

or (if  $a_o$  is too large, i.e.,  $a_o' \leq a_o$ ):

$$\frac{\alpha(a_o', 0.0170)}{\alpha(0.013, 0.0170)} - 1 \leq \sqrt{1 + 0.0398/c \ell} - 1 \quad (3-34)$$

an even more conservative estimate, which is independent of  $a_o$ . Thus, from Equation 3-34, if  $c \ell > 0.19 \text{ cm}$  (e.g.,  $c = 10^{-6}$ ,  $\ell = 2 \text{ km}$ ), the error in  $\bar{\alpha}$  is less than 10 percent, independent of how much smaller  $a_o'$  is than the assumed value,  $a_o$ . Similarly, if  $c \ell > 0.032 \text{ cm}$ , the error in  $\bar{\alpha}$  is less than 50 percent.

A closer limit on the error in  $\alpha$  may be obtained from Equation 3-33 if a bound can be placed on the error in  $a_0$ . For example, if  $a_0$  is believed correct within a factor of two, the error in  $\alpha$  for  $cl > 0.032$  cm is less than 31 percent if  $a_0$  is too large ( $a_0' \geq 1/2 a_0$ ), and less than 39 percent if  $a_0$  is too small ( $a_0' \leq 2 a_0$ ).

**3.2.3.4 Comparisons of Predicted Absorptivity with Experimental Data.** As was stated previously, experimental data are frequently available over a much more restricted range of conditions than would be desired to check the applicability of the assumed band model and to determine the parameters accurately and uniquely. At one extreme, the absorption coefficients for PAN have been developed from one spectrum taken at a low pressure (where Doppler broadening introduces additional uncertainty) and from an assumed value of  $a_0$  based on the assumed molecular structure. Absorptivities which are calculated at atmospheric pressure near the linear region of the curve of growth must be considered quite uncertain.

However, for some molecules such as  $\text{CH}_4$  and  $\text{NH}_3$  there are extensive laboratory measurements (References 59, 60). A comparison is shown in Figures 3-12 through 3-14 of predicted values of absorptivity for  $\text{CH}_4$  (using the coefficients tabulated in the Appendix) with laboratory measurements of Burch et al (Reference 59). These comparisons cover a range of three orders of magnitude in optical path (from 0.05 to 50 atm-cm). Equivalent pressures of about 0.5 to 1 atm were chosen as being most relevant to the intended usage of the coefficients. The comparison is considered to be very good.

A similar comparison is made in Figures 3-15 through 3-17 for  $\text{NH}_3$  (Reference 60). The range of optical path is about the same as for  $\text{CH}_4$ . Because of the very sharp Q peaks in the ammonia band, the peak value registered by a spectrometer of moderate resolution is slit-width-dependent. Since the structure in the P and R branches is not fully smeared out, the computed points should be compared with a running mean value of the measured absorptivity. Again, the comparison is good.

To further illustrate the validity of the calculated absorption coefficients, Table 3-5 shows a comparison of the calculated band intensities and measured values. The calculated band intensities presented in Table 3-5 were obtained by a number of slightly different methods, each appropriate to the choice of data available for the particular molecule.

For example, for PAN, the data consisted of one absorption spectrum taken at one pressure and path length (Reference 8). In this case, a value of "a" was assumed (based on the molecular geometry), and values of "k" extracted as previously described.

For  $\text{CH}_4$ , several sources were available (Reference 4), containing extensive absorption spectra and measured band intensities; (Reference 59, containing several absorption spectra; and Reference 61, which presents mean absorption coefficients for one absorption band). The absorption coefficients in the  $7.7\text{-}\mu$  region were derived by

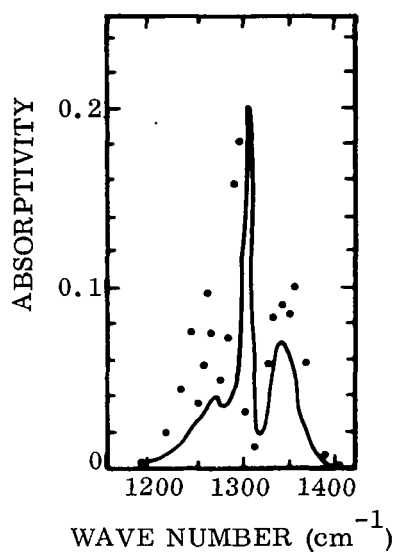


Figure 3-12. Methane Absorptivity Comparison ( $\mu = 0.052$  atm-cm,  $P_e = 0.921$  atm)

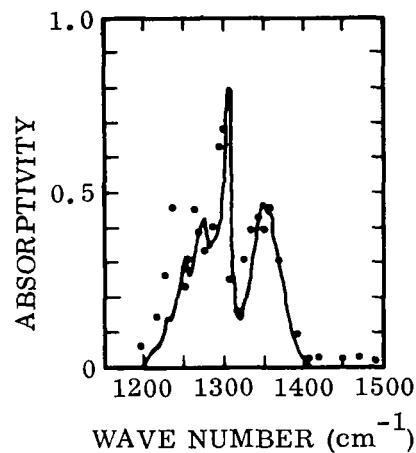


Figure 3-13. Methane Absorptivity Comparison ( $\mu = 1.35$  atm-cm,  $P_e = 1.001$  atm)

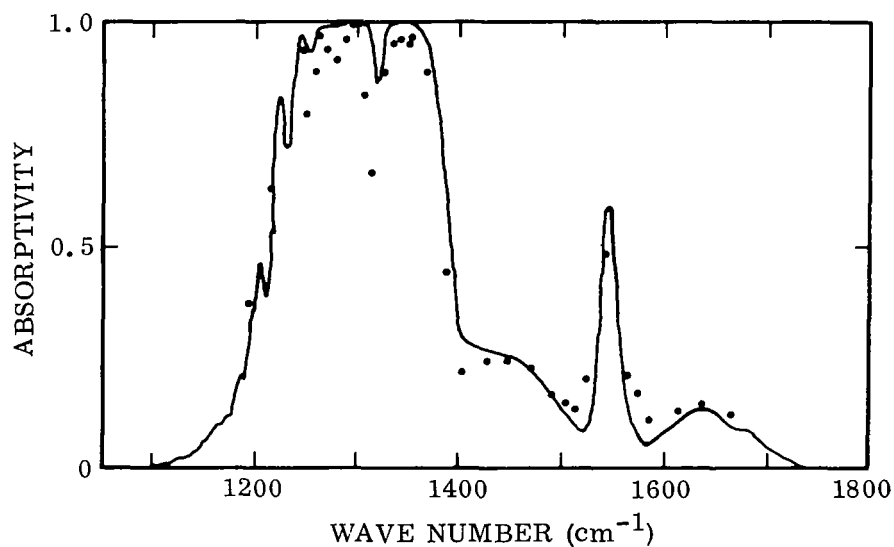
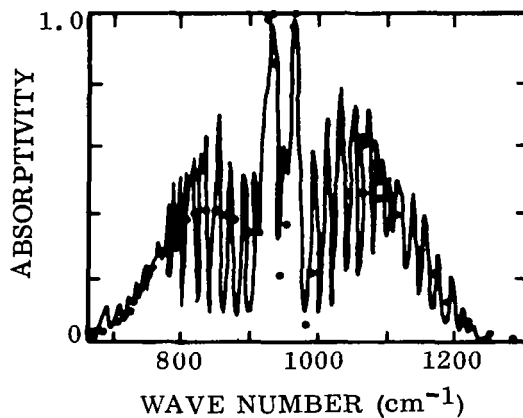
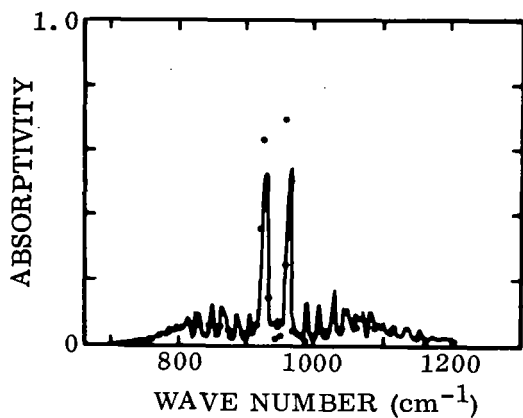


Figure 3-14. Methane Absorptivity Comparison ( $\mu = 47.3$  atm-cm,  $P_e = 0.987$  atm)

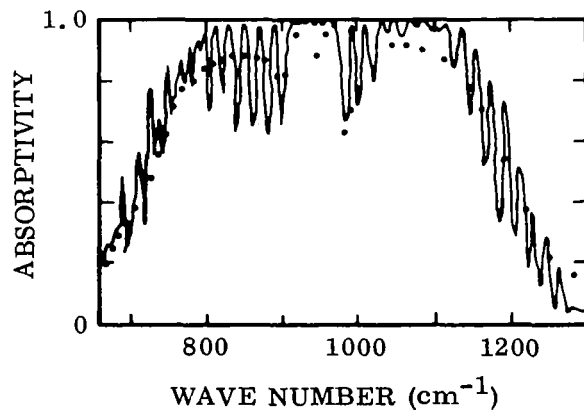
Dots are calculated values.



Dots are calculated values.

Figure 3-15. Ammonia Absorptivity Comparison ( $\mu = 0.0772$  atm-cm,  $P_e = 0.614$  atm)

Figure 3-16. Ammonia Absorptivity Comparison ( $\mu = 1.617$  atm-cm,  $P_e = 1.724$  atm)



Dots are calculated values.

Figure 3-17. Ammonia Absorptivity Comparison ( $\mu = 47.1$  atm-cm,  $P_e = 0.792$  atm)

Table 3-5. Comparison of Integrals of Absorption Coefficients  
With Experimentally Measured Band Intensities

Band	$\int k du$ (cm <sup>-2</sup> atm <sup>-1</sup> )STP	Measured Intensity (cm <sup>-2</sup> atm <sup>-1</sup> )STP	Reference
SO <sub>2</sub> 4.0μ ( $\nu_1 + \nu_3$ )	23	24	62
CH <sub>4</sub> 7.7μ ( $\nu_4$ )	418	185	59
CH <sub>4</sub> 3.3μ ( $\nu_3$ )	270	320	59
NH <sub>3</sub> 10.5μ ( $\nu_2$ )	607	790	60
NH <sub>3</sub> 6.1μ ( $\nu_4$ )	126	150	60
CO 4.7μ ( $\nu$ )	260	260	59
HCl 3.5μ ( $\nu$ )	143	143	63
O <sub>3</sub> 9.7μ ( $\nu_3$ )	365	455	58
NO <sub>2</sub> 6.2μ ( $\nu_3$ )	16000	2250	64
NO <sub>2</sub> 3.4μ ( $\nu_1 + \nu_3$ )	290	67	64

reduction of data from Reference 59. Values of "a" were adjusted to provide consistency with the data of Reference 4. In the 3.3-μ region, absorption coefficients were based on Reference 61. As a check, comparisons were made with conditions of Reference 4 over a wide range of optical path lengths (see Figures 3-12 through 3-14).

The absorption coefficients must be considered provisional, and subject to change as more data become available. The large apparent differences in the case of NO<sub>2</sub> reflect various uncertainties such as the concentration of NO<sub>2</sub> and the effect of self-broadening. Additionally, the band intensities presented in Reference 64 are believed to be too low, based on an examination of the data presented therein.

### 3.2.4 CALCULATED SIGNAL CHANGE DUE TO POLLUTANTS IN THE INFRARED

3.2.4.1 Calculations for Confined Layers of Air Pollutants. Using the computer program (Subsection 3.2.1) together with the deduced values of the pollutants' absorption coefficients (Subsection 3.2.3), a number of calculations have been performed. The signal change, SC, (defined as the percent difference between the radiances,

without and with air pollutants present, received by a space-borne sensor) was computed for a number of vertical distributions of temperature and pollutant concentrations as a function of wavelength. For radiances received by a satellite-borne sensor, the top of the atmosphere was considered to be at 50 km. Negligible atmospheric attenuation occurs above 50 km.

Preliminary calculations were made assuming an  $O_3$  pollution layer of 0.5 ppm extending to 0.305 km (1000 feet) with  $T_s = 317^\circ K$  and  $\epsilon_s = 0.92$ . This low level  $O_3$  distribution was superimposed upon an hypothesized normal  $O_3$  concentration of 0.02 ppm extending from the ground to 12 km, and reaching a maximum of 0.16 ppm at 23 km and 0.02 ppm above 40 km; the total  $O_3$  optical depth was 0.292 atm-cm. The results show that only a 0.9 percent signal change will occur above 50 km due to the masking effect of the stratospheric  $O_3$ . At 6.3 km, an airborne detector would sense a 2.8 percent signal change for the above conditions. Thus, even at an observation altitude of 6.3 km a large amount of near-surface  $O_3$  pollutant ( $1.6 \times 10^{-2}$  atm-cm) is necessary before any substantial change in total radiance would be observed. This is due to the counteracting effects discussed previously, namely, that the  $O_3$  pollution layer both absorbs the radiation from the earth's surface and emits radiation. Thus, for  $\epsilon_s \approx 1$  and for  $\bar{T}_a \approx T_s$  the net change in radiation received above the  $O_3$  pollution layer is relatively small. For these calculations the pollutant layer temperature was linearly decreased by  $12^\circ C$  to the top of the pollutant layer (1000 feet).

Similar sets of calculations were performed assuming a 1000-foot-thick layer of CO with concentrations of 1, 10, and 100 ppm. These correspond to negligible, moderate, and very strong amounts of CO pollution, respectively. For the pertinent spectral region, namely, the  $4.6\mu$  band of CO, the earth's surface emissivity was assumed equal to 0.95. Various atmospheric temperature profiles were used in this set of calculations. The profiles selected are representative of typical temperature profiles that would be encountered during global surveillance. Specifically, they were taken from Reference 42 and are the 1959 ARDC Model Atmosphere, the Artic Winter Atmosphere, and the Tropical Atmosphere. These temperature distributions are shown in Figure 3-18. The vertical pressure distributions used for these calculations were also taken from Reference 42 for each model atmosphere. Also, two additional surface temperatures were used to represent the extremes that might be encountered during the day and night. The temperatures noted in Table 3-6 are the earth surface temperature,  $T_s$ , and the average temperature of the pollution layer,  $\bar{T}_a$ . The results show the maximum percentage change in radiance, SC, as would be observed by a low spectral-resolution instrument located at an altitude of 50 km. Examination of the results shown in Table 3-6 indicate that significant changes (either positive or negative) in radiance due to CO air pollution occur under several conditions.

These results are encouraging as CO is a good candidate for monitoring global build-up of air pollution, CO being a representative emission from all combustion processes.

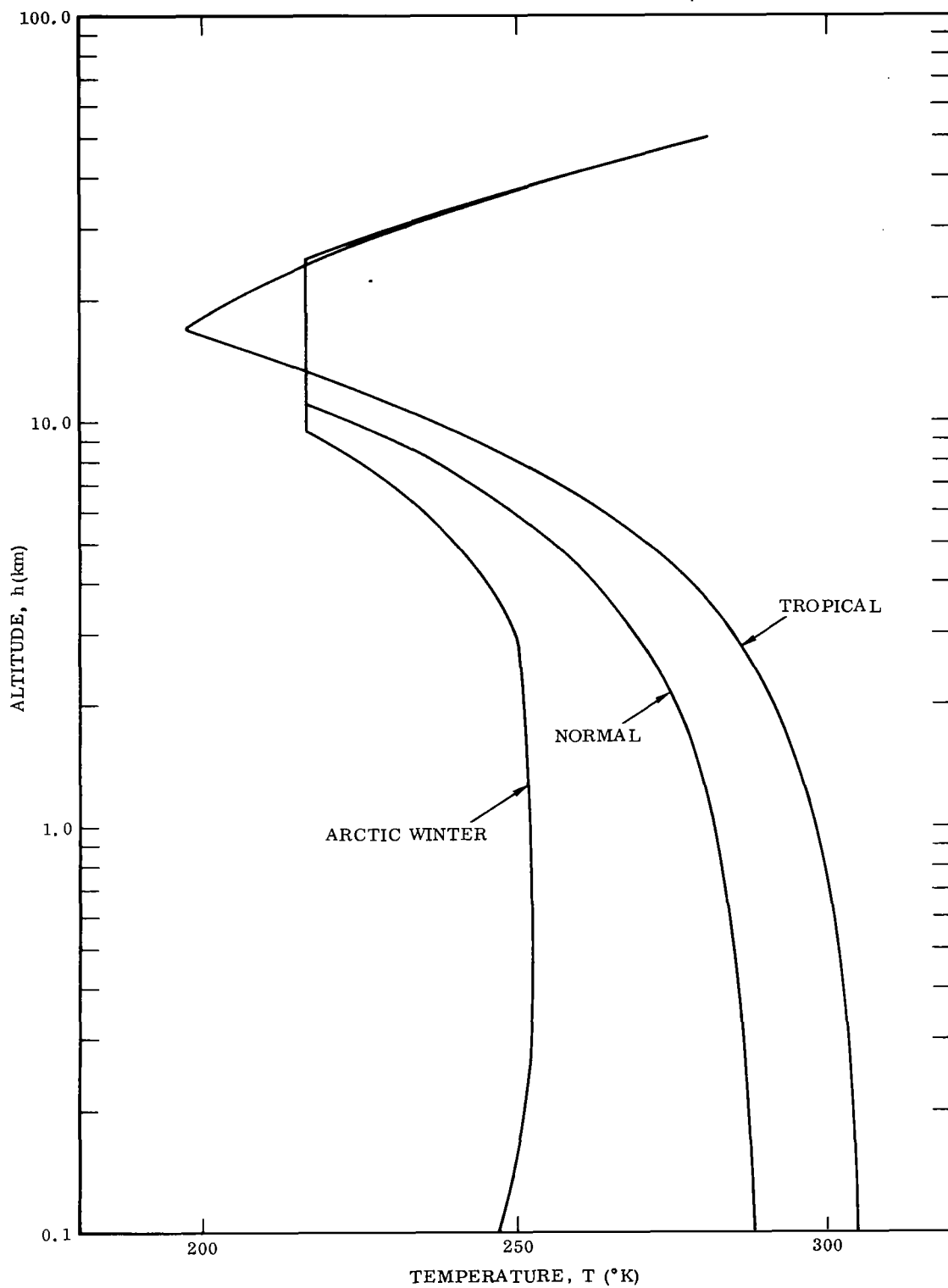


Figure 3-18. Vertical Temperature Profiles Used for the Results Summarized in Table 3-11

Table 3-6. Signal Changes Between "Clean" and 1000-Foot-Thick, CO-Polluted Atmospheres for Various Atmospheric Temperature Profiles (ARDC, 1959) as Observed at 50 km and  $\lambda = 4.6\mu$  (Surface Emissivity = 0.95)

Atmosphere	CO (ppm)	SC (%)
Normal	1	0.05
$T_s = 288^\circ\text{K}$	10	0.26
$\bar{T}_a = 287^\circ\text{K}$	100	0.80
Normal	1	1.85
$T_s = 298^\circ\text{K}$	10	6.56
$\bar{T}_a = 287^\circ\text{K}$	100	16.63
Normal	1	-2.65
$T_s = 278^\circ\text{K}$	10	-9.20
$\bar{T}_a = 287^\circ\text{K}$	100	-22.96
Tropical	1	0.02
$T_s = 305^\circ\text{K}$	10	0.06
$\bar{T}_a = 304^\circ\text{K}$	100	0.32
Arctic Winter	1	-1.74
$T_s = 247^\circ\text{K}$	10	-6.49
$\bar{T}_a = 251^\circ\text{K}$	100	-16.98

3.2.4.2 Calculations for Some Hypothesized Meteorological Conditions. We have previously noted that any remote measurement of air pollutants obtained by sensing changes in radiance will be strongly dependent upon the temperature difference between that of a pollutant and that of the source (the earth's surface in the infrared region). This conclusion resulted from radiance calculations assuming a uniform thin layer of pollution. In addition, we have postulated several different pollutant concentration profiles that might exist for a given temperature profile, and have performed radiance calculations using  $\text{NH}_3$  as a pollutant. These profiles and the resulting percent radiance changes between clean and  $\text{NH}_3$ -polluted atmospheres are shown



in Figures 3-19 through 3-22. In all these cases we have assumed the integrated

pollution to be the same, i.e.,  $\int_0^{\infty} (\text{NH}_3) dh = \text{const.}$  In other words, we considered

that a fixed amount of pollution was emitted at the earth's surface and that it was then distributed throughout the atmosphere in a manner that depended upon the general meteorological conditions (as represented by the temperature profile that exists). For all of the calculations the surface emissivity was assumed to be 0.97. Ammonia was chosen as the pollutant since it is an air pollutant that possesses a typical absorption coefficient and thereby provides representative signal changes. Also,  $\text{NH}_3$  seems to be becoming an increasingly important air pollutant since it is associated with the presence of a large population. The results, indicated by Figures 3-19 through 3-22, are discussed in more detail in the following paragraphs.

Figure 3-19: We have hypothesized for this case that the pollutant distribution remains essentially constant throughout the lower troposphere under conditions in which good atmospheric mixing occurs, i.e.,  $dT/dh = T' < 0$ . This pollutant concentration profile may be compared with the measured  $\text{CH}_4$  and  $\text{SO}_2$  profiles that were discussed in Section 2. The same pollutant concentration profile was used for two different low-level (extending from 0 to 1 km) temperature lapse rates,  $T' = -10$  and  $-20^\circ\text{C}/1000$  m; and the respective maximum radiance changes,  $\text{SC}_{\text{max}}$ , are 3.85 and 5.42 percent respectively. These values occur at  $\lambda \approx 10.8\mu$ , the wavelength at which the absorption coefficient of  $\text{NH}_3$  is maximum. It is interesting to note that for this case, when the pollutant is considered to extend far outward from the surface, the integrated emission from the air pollutant (c.f. 2nd term, Equation 3-5) is larger for  $T' = -10^\circ\text{C}/1000$  m, thereby giving a smaller value for  $\text{SC}_{\text{max}}$  than for  $T' = -20^\circ\text{C}/1000$  m. Most important though is the observation that relatively large values of SC are obtained when even very small amounts of pollution are present in the upper portion of the troposphere where the temperature is much lower than the temperature of the surface.

Figure 3-20: Here we have postulated the conditions that may exist typically during the middle of the night. At this time, a very low-level temperature inversion, which is relatively weak, usually exists. When this occurs, pollutants emitted near the surface are retarded from mixing into the upper levels of the atmosphere, and surface concentrations may become relatively high. The calculations for this case result in  $\text{SC}_{\text{max}} = 1.47$  percent for  $T' = +3^\circ\text{C}/300$  m, and  $\text{SC}_{\text{max}} = 1.25$  percent for  $T' = +6^\circ\text{C}/300$  m.

Figure 3-21: Three typical day-time temperature inversion profiles extending to 1 km are presented with the same pollutant concentration profile for all three temperature profiles. Under these conditions, typical of smoggy days in the Los Angeles basin, a high pollutant concentration tends to be trapped within the inversion layer. For two of these temperature profiles, the same surface temperature is used, and the calculations give  $\text{SC}_{\text{max}} = -1.44$  percent for  $T' = +10^\circ\text{C}/1000$  m, and  $\text{SC}_{\text{max}} = -3.55$  percent for  $T' = +20^\circ\text{C}/1000$  m. For the third case, using a  $10^\circ\text{C}$  higher surface temperature and

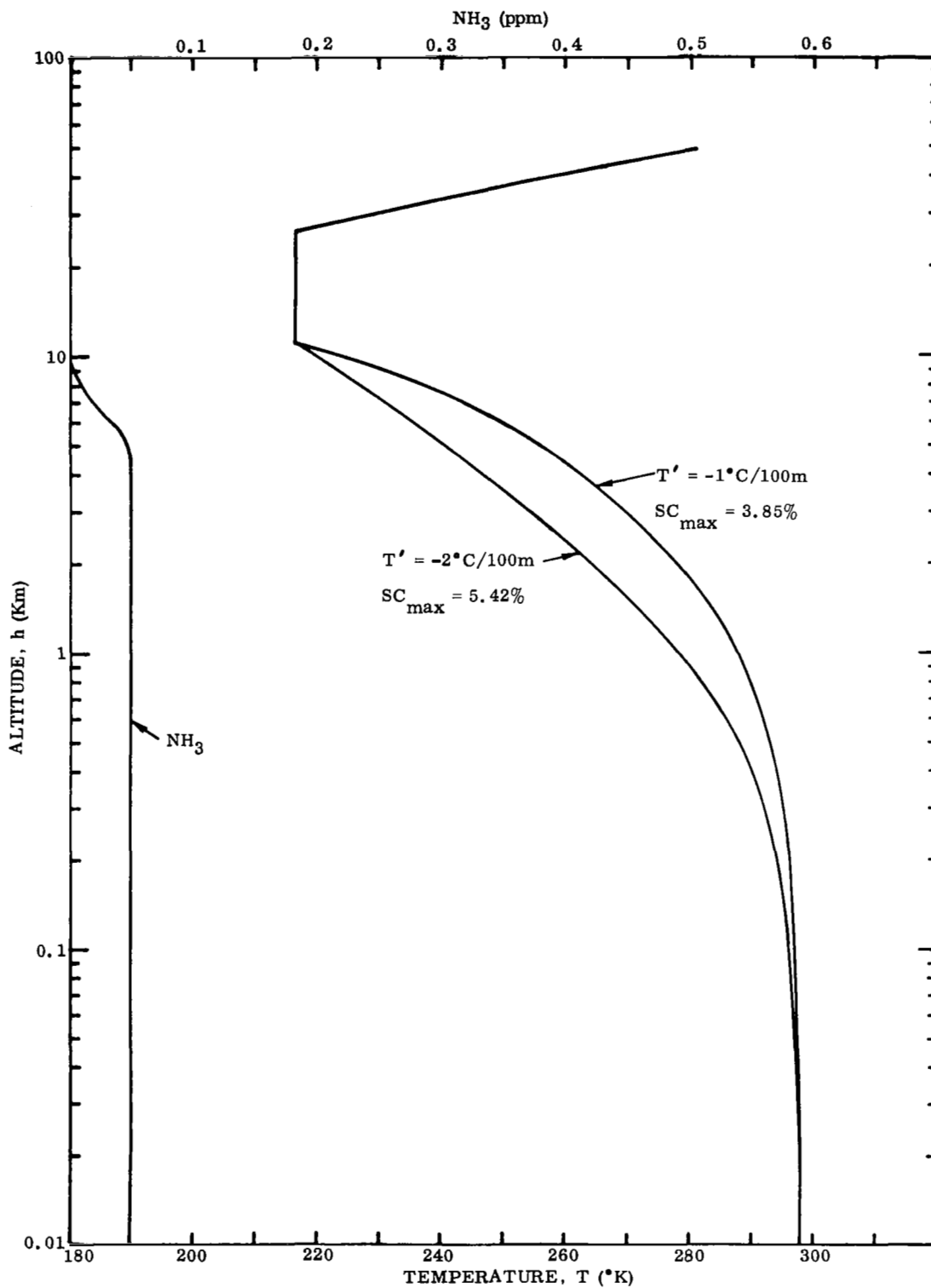


Figure 3-19. Temperature and  $\text{NH}_3$ -Pollutant Concentration Profiles for a Typical Mid-Day Atmosphere

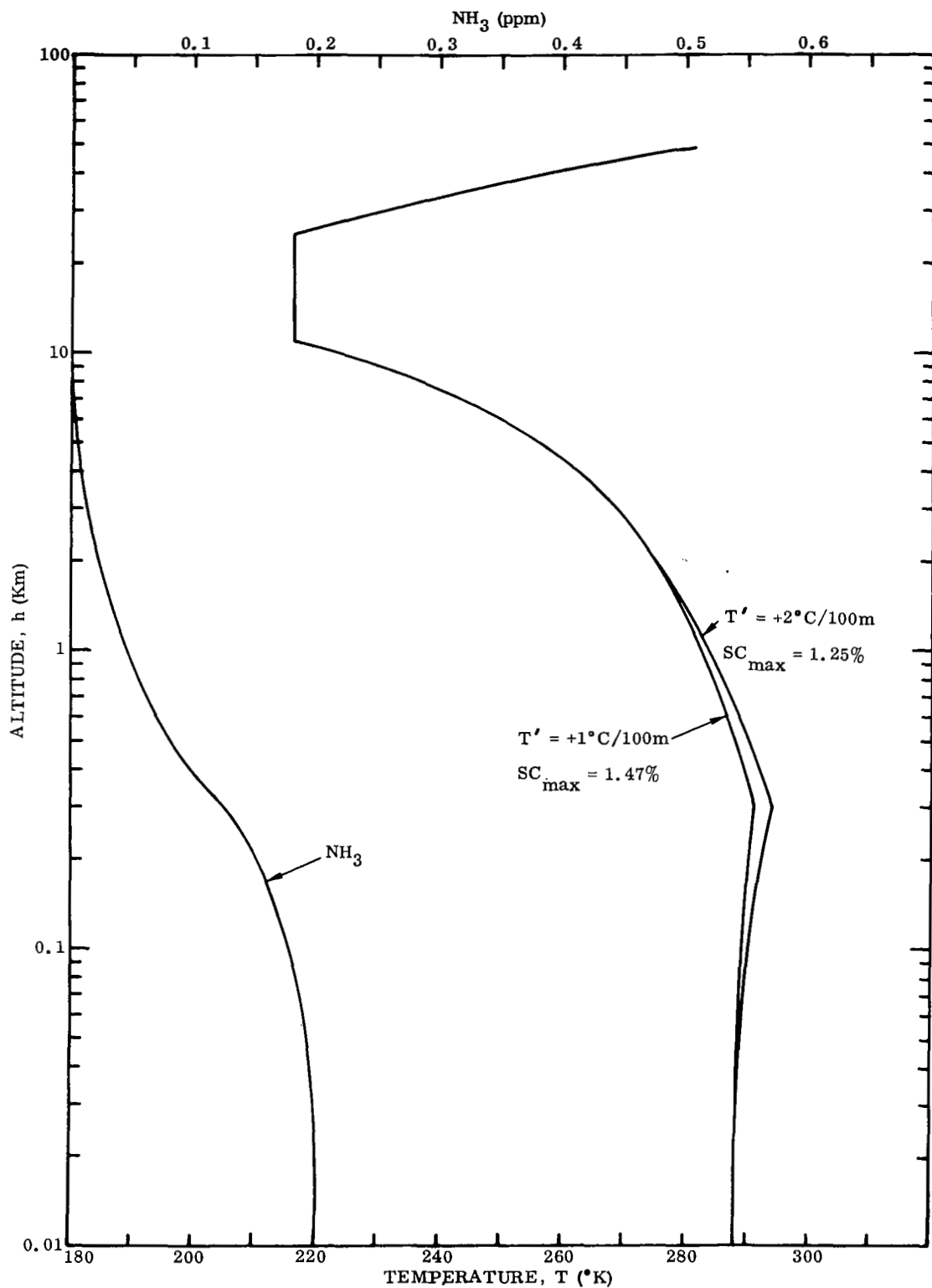


Figure 3-20. Temperature and  $NH_3$ -Pollutant Concentration Profiles for a Typical Mid-Night Atmosphere

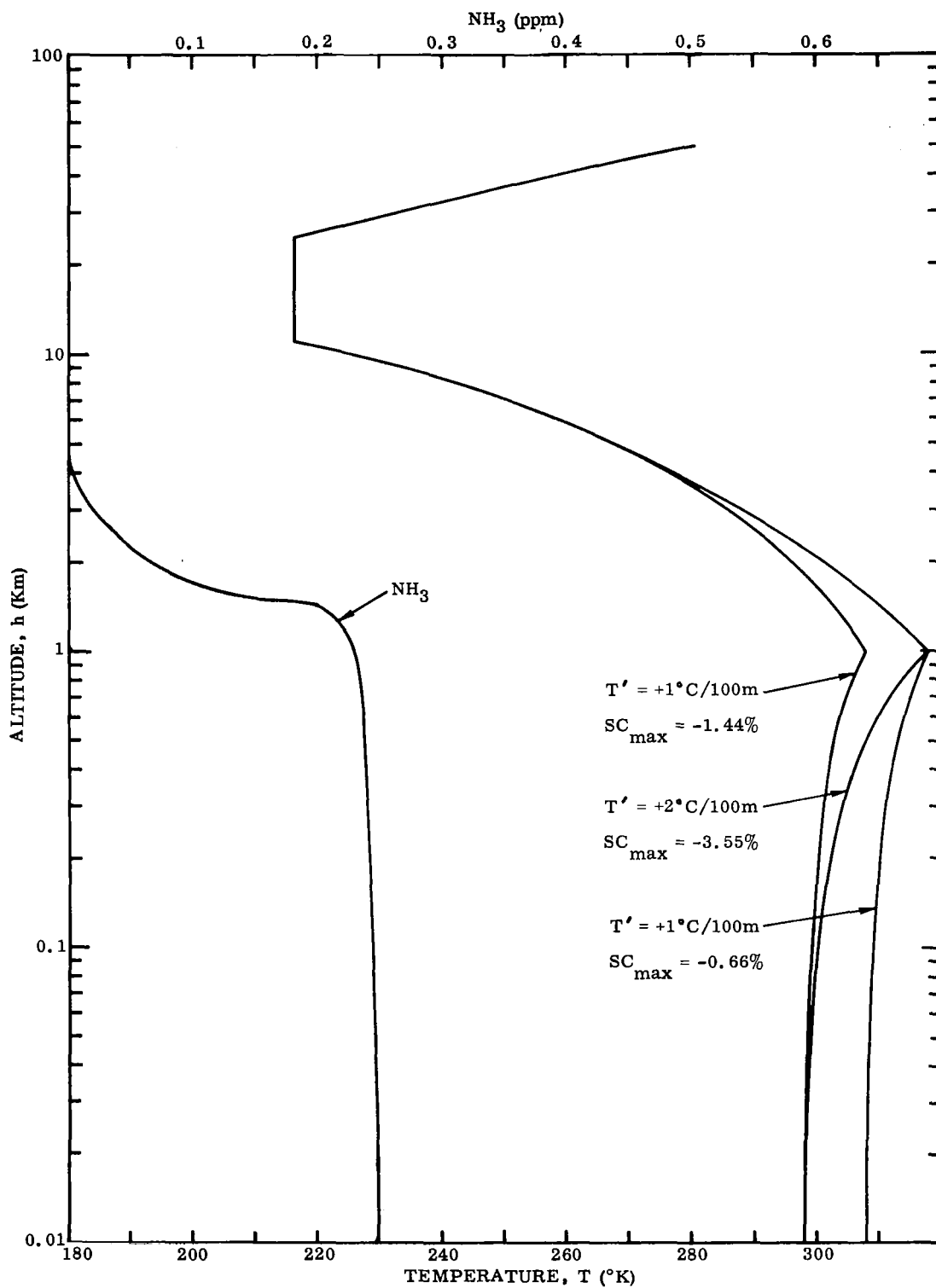


Figure 3-21. Temperature and NH<sub>3</sub>-Pollutant Concentration Profiles for a Typical Day-Time Inversion Layer

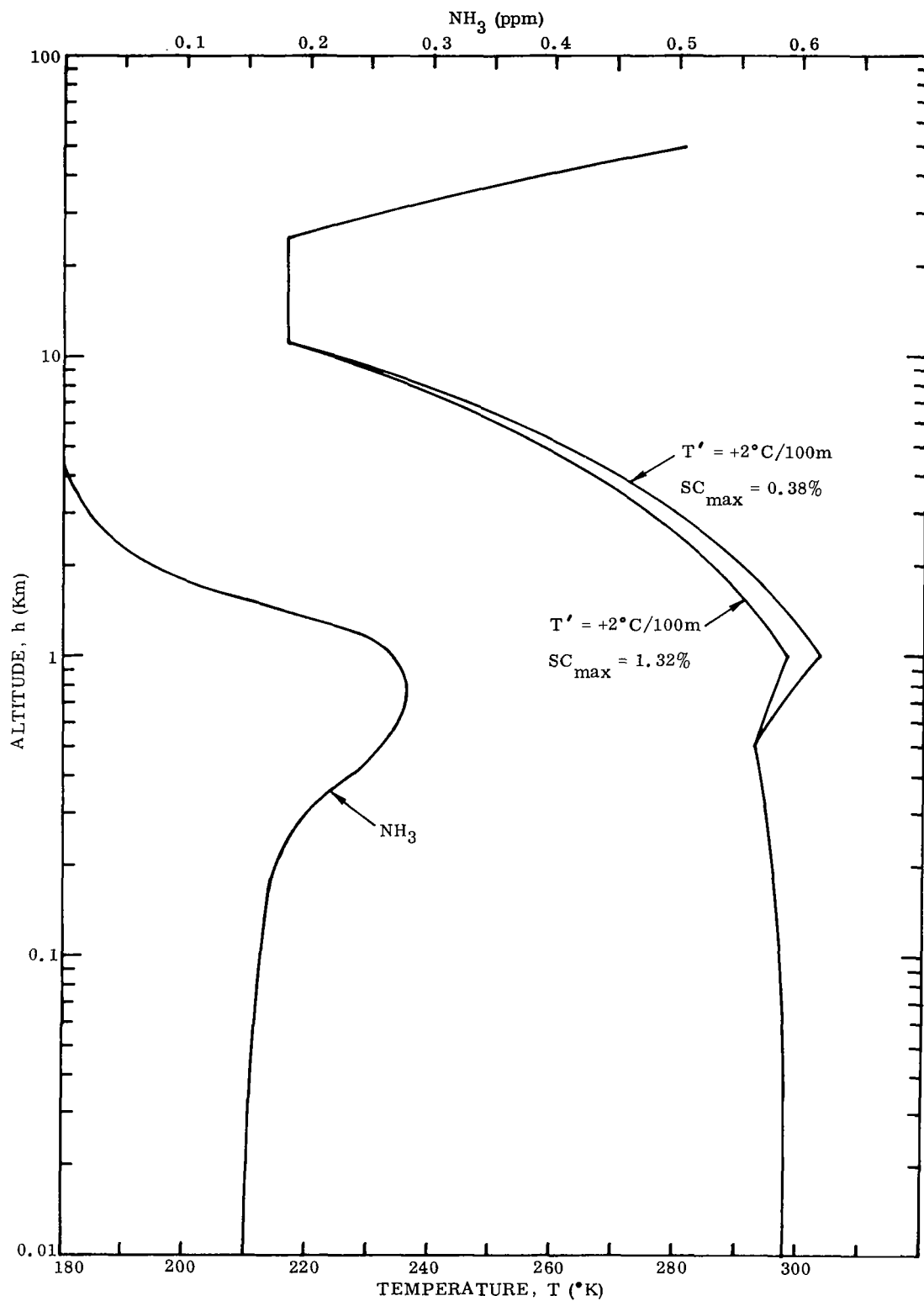


Figure 3-22. Temperature and NH<sub>3</sub>-Pollutant Concentration Profiles for a Typical Upper-Level Inversion Layer

$T' = +10^{\circ}\text{C}/1000\text{ m}$ ,  $SC_{\text{max}} = -0.66$  percent. For these cases the pollutant layers' thermal emission dominates ( $SC < 0$ ).

**Figure 3-22:** We imposed the condition of an upper altitude thermal inversion layer extending from 0.5 to 1.0 km. Again, in this case pollution tends to build up within the stable inversion layer. The results for the two different inversion layers are  $SC_{\text{max}} = 1.32$  percent for  $T' = +5^{\circ}\text{C}/500\text{ m}$  and  $SC_{\text{max}} = 0.38$  percent for  $T' = +10^{\circ}\text{C}/500\text{ m}$ . These results follow the same general trend as for the lower-level temperature inversion layer results.

From these and previous results it is clear that, although the presence of air pollution may significantly change the radiance from that observed with no air pollution present, interpretation of the signals received by a remote sensor will be complicated. This is true since, for a particular distribution of air pollutants throughout the atmosphere, large changes in signal, dependent upon the temperature profile through the atmosphere, will exist. Likewise, for a particular temperature profile, the distribution of pollutants as well as the integrated amount of pollutants will affect the change in signals.

Two additional computer calculations were made using two different amounts of  $\text{NH}_3$  as a pollutant. The profiles selected were the same as in Figure 3-19, using the  $T' = -2^{\circ}\text{C}/100\text{ m}$  case. The same pollutant distribution was used as is shown in Figure 3-19, but the maximum  $\text{NH}_3$  concentrations used were 0.02 and 0.10 ppm, whereas the first calculation used  $(\text{NH}_3)_{\text{max}} = 0.05\text{ ppm}$ . These values of  $(\text{NH}_3)_{\text{max}}$  may be compared with the value  $(\text{NH}_3)_{\text{max}} = 0.2\text{ ppm}$  which may exist in a heavily polluted atmosphere; this value was obtained from the National Center for Air Pollution Control, Cincinnati, Ohio. The results of all three calculations are shown in Figure 3-23. We calculated values of  $SC_{\text{max}} = 2.31, 5.42,$  and  $9.88$  percent for values of  $(\text{NH}_3)_{\text{max}} = 0.02, 0.05,$  and  $0.10\text{ ppm}$ , respectively. These results are for a spectral resolution of  $0.1\mu$ . Higher spectral resolution calculations were not possible due to the lack of higher resolution absorption coefficient data, both for the natural air constituents and pollutants. However, it should be noted that a higher resolution ( $< 0.1\mu$ ) instrument would indicate much greater signal changes than the present calculations show, due to increased values of the pollutant's absorption coefficient. From these results a cross-plot of  $SC$  versus  $(\text{NH}_3)_{\text{max}}$  is presented in the insert of Figure 3-23. Note that the percent signal change is nonlinear with  $\text{NH}_3$  concentration. It may also be noted that when the values of  $SC$  are integrated over the entire absorption band, the same form of nonlinearity is exhibited.

The same case (Figure 3-19) with  $T' = +1^{\circ}\text{C}/100\text{ m}$  was used to investigate the situation when multiple pollutants are present in the atmosphere. Calculations for eight pollutants, both individually and all together, were made. These pollutants and their maximum concentrations are:

Carbon Monoxide,	$(\text{CO})_{\text{max}}$	$= 2.5\text{ ppm}$
------------------	----------------------------	--------------------

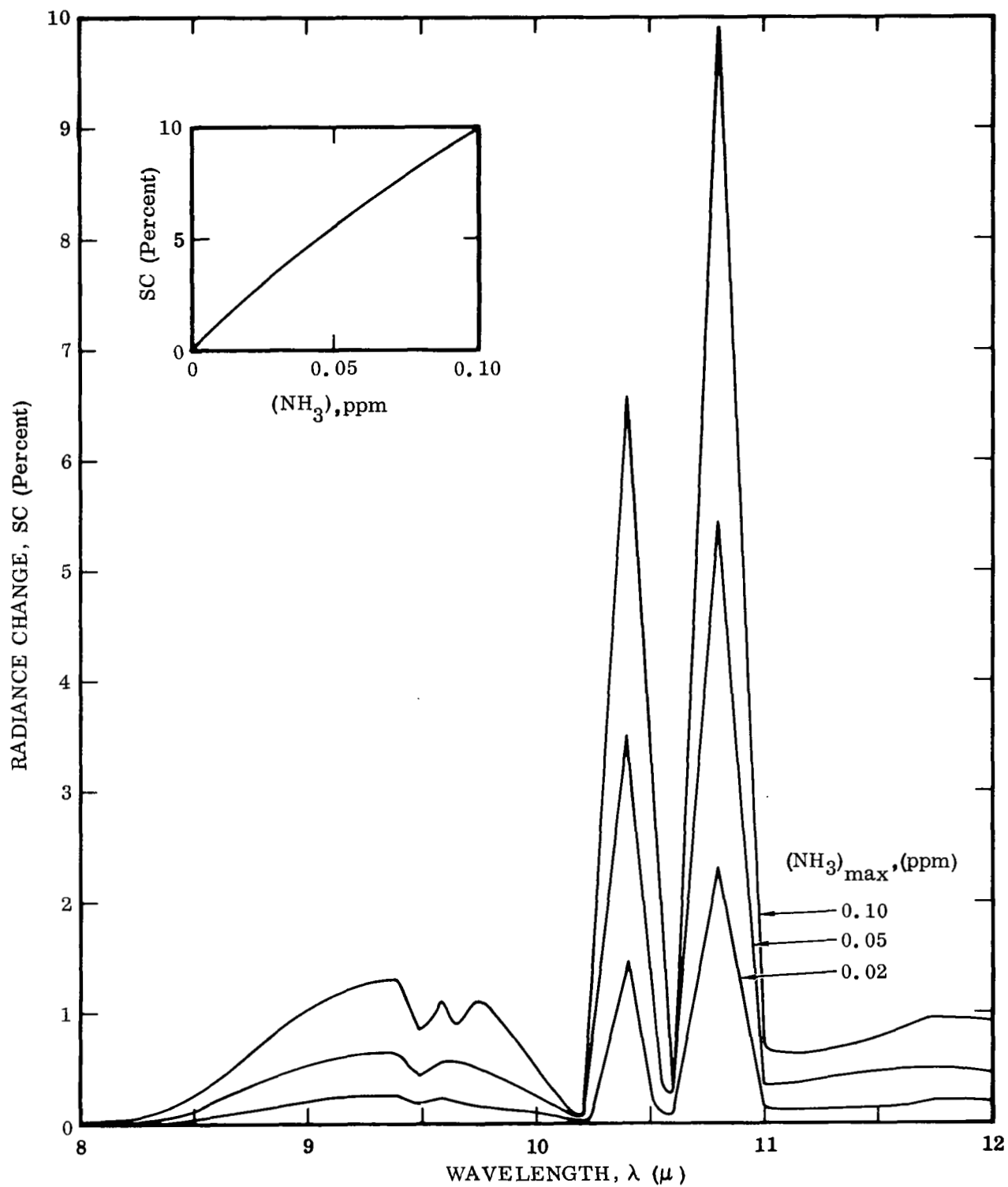


Figure 3-23. Sensitivity to Varying  $\text{NH}_3$  Pollution for Normal Day ( $T' = -2^\circ\text{C}/100\text{ m}$ )

Sulfur Dioxide,	$(\text{SO}_2)_{\text{max}}$	= 0.02 ppm
Nitrogen Dioxide,	$(\text{NO}_2)_{\text{max}}$	= 0.02 ppm
Ozone,	$(\text{O}_3)_{\text{max}}$	= 0.03 ppm
Peroxyacetyl Nitrate,	$(\text{PAN})_{\text{max}}$	= 0.005 ppm
Ethylene,	$(\text{C}_2\text{H}_4)_{\text{max}}$	= 0.01 ppm
Ammonia,	$(\text{NH}_3)_{\text{max}}$	= 0.05 ppm
Benzene,	$(\text{C}_6\text{H}_6)_{\text{max}}$	= 0.005 ppm

These concentrations are one-tenth of typical ground level concentrations that have been observed during moderate to heavy air pollution attacks. The two hydrocarbons,  $\text{C}_2\text{H}_4$  and  $\text{C}_6\text{H}_6$ , were selected as representative of the hydrocarbon pollution resulting from burned and unburned automobile fuels and other combustion processes.

The results of these calculations are shown in Figure 3-24. Again, the percent change in radiance, with and without pollution, SC, is presented as a function of wavelength. The upper curve represents the radiance changes which occur when all the pollutants are present simultaneously; the lower curves represent the individual pollutant contributions to the radiance changes. Examination of these results indicates that interferences between pollutant absorption bands will have to be carefully considered before any degree of specificity can be obtained. It should be noted that the superposition of the signal change due to different pollutant bands is not simply additive.

The region  $\lambda = 4.6\mu$  indicates the largest percent change in radiance and is uniquely due to the CO pollution. This seems to be potentially a good region to monitor air pollution; however, it may be somewhat deceiving, as illustrated by the following table:

$\lambda, \mu$	$E_c$	$E_p$	$E_s (\tau = 1)$	SC (%)
4.6	1.408	1.025	1.600	27.2
10.8	8.968	8.168	9.381	8.9

In this table,  $E_c$ ,  $E_p$ , and  $E_s(\tau = 1)$  refer to clean, polluted, and surface radiances transmitted through the atmosphere; the units of all are  $10^{-4} \text{ w cm}^{-2} \mu^{-1} \text{ sr}^{-1}$ . From the table we observe that at the shorter wavelengths the total radiances are smaller than at the longer wavelengths. (Actually from a  $300^\circ\text{K}$  surface the radiance peaks at about  $10\mu$  and falls off at both longer and shorter wavelengths.) For this reason small values of  $\Delta E = E_c - E_p$  give larger values of  $\Delta E/E (= \text{SC})$  at the shorter wavelength.



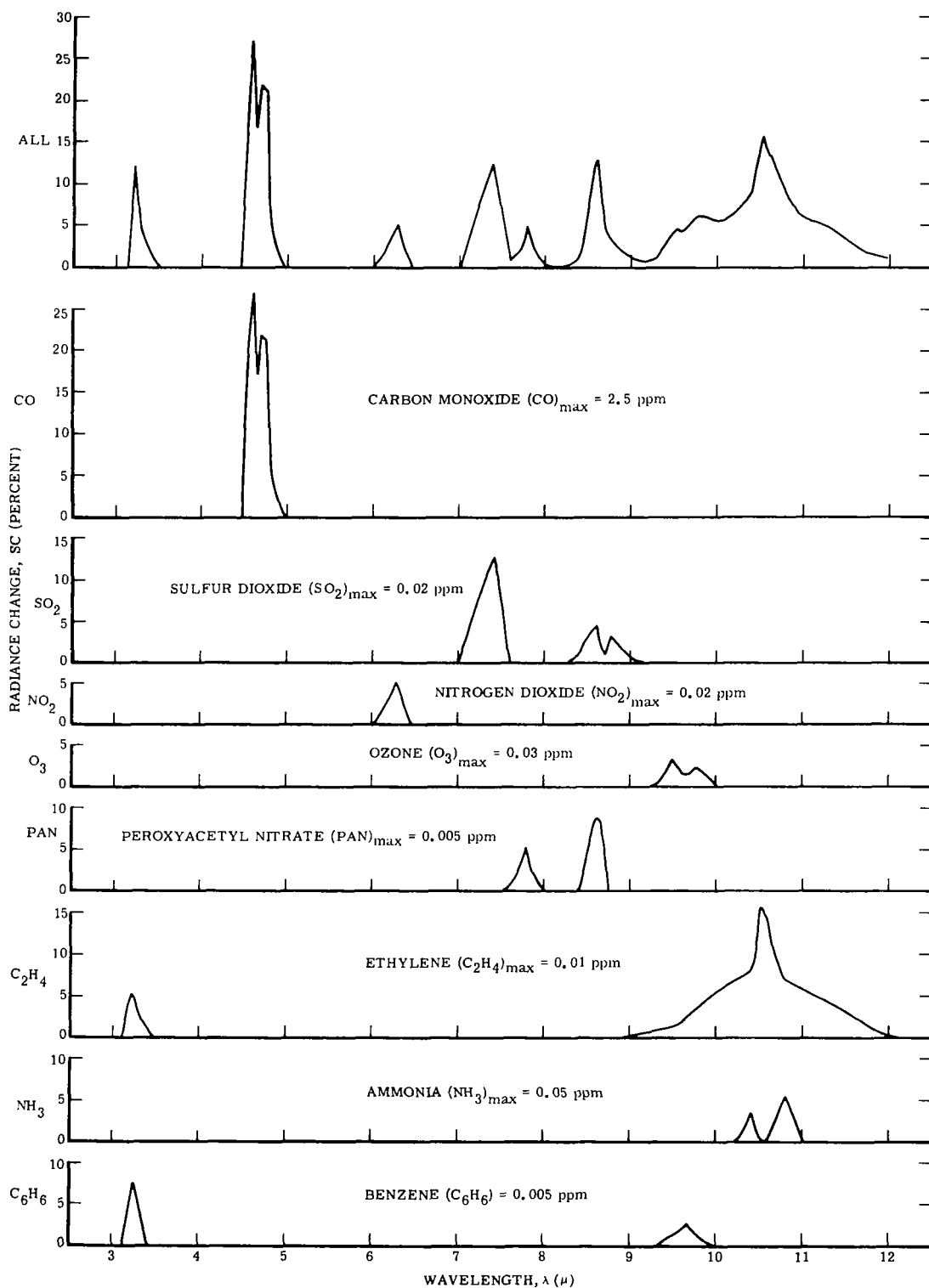


Figure 3-24. Percent Radiance Changes Between Clean and Polluted Atmosphere

Also, in this region,  $\lambda = 4.6\mu$ , the normal, clean atmosphere attenuates the radiance more than at  $\lambda = 10.8\mu$  (compare the values for  $E_c$  and  $E_s$  ( $\tau = 1$ )). This leads to potentially much larger variation in general background, depending upon the  $H_2O$  vapor concentration in the atmosphere.

**3.2.4.3 Calculations Using Measured Pollution Profiles.** We have performed three additional calculations of infrared radiance changes between clean and polluted atmospheres using measured values of  $SO_2$  concentration profiles (Reference 14, 15). These profiles, their corresponding temperature profiles, and the results of the calculations are shown in Figures 3-25 and 3-26.

In Figure 3-25 an upper-level temperature inversion existed, which confined the  $SO_2$  to the lower level with a characteristic relatively large increase in  $SO_2$  to the lower level with a characteristic relatively large increase in  $SO_2$  just below the inversion. In this case the maximum computed radiance change between the clean and  $SO_2$ -polluted atmospheres is 1.30 percent. This profile is very similar to the one we hypothesized earlier for this particular meteorological condition.

The third calculation was performed using the  $SO_2$  profile presented by H. H. Slater of NAPCA during a workshop held at NASA-ERC (Reference 16). Slater stated that this  $SO_2$  profile existed over Chattanooga, Tennessee during a normal lapse condition, but no details of the temperature profile were available. This  $SO_2$  profile, which has a maximum value of 0.5 ppm, is also presented in Figure 3-26 and, lacking details on the temperature profile, the same temperature profile as was used for the Frankfurt, Germany calculation was used in this case. With these two profiles the maximum calculated radiance change between clean and  $SO_2$ -polluted atmospheres is 5.49 percent. It would be somewhat surprising to find the large maximum in this  $SO_2$  profile if a normal lapse condition were present. We would expect this to occur only if an upper-level temperature inversion were present.

Further qualitative  $SO_2$  profiles, together with temperature profiles received later from Slater (Reference 16), in general support the types of profiles used in the calculations.

**3.2.4.4 Conclusions from IR Region Calculations.** From these calculations the following conclusions can be drawn with respect to the remote measurement of air pollutants in the infrared region.

- a. The difference between the earth's surface temperature and the effective temperature of the pollutants is the principal variable that affects the sensitivity of the instrument to changes in radiance with and without the existence of air pollution.
- b. Since the atmospheric temperature changes with altitude, a knowledge of this temperature profile and of pollutant concentration profile shape is necessary to make quantitative measurements. Methods of obtaining this knowledge either directly or from a priori considerations should be investigated.

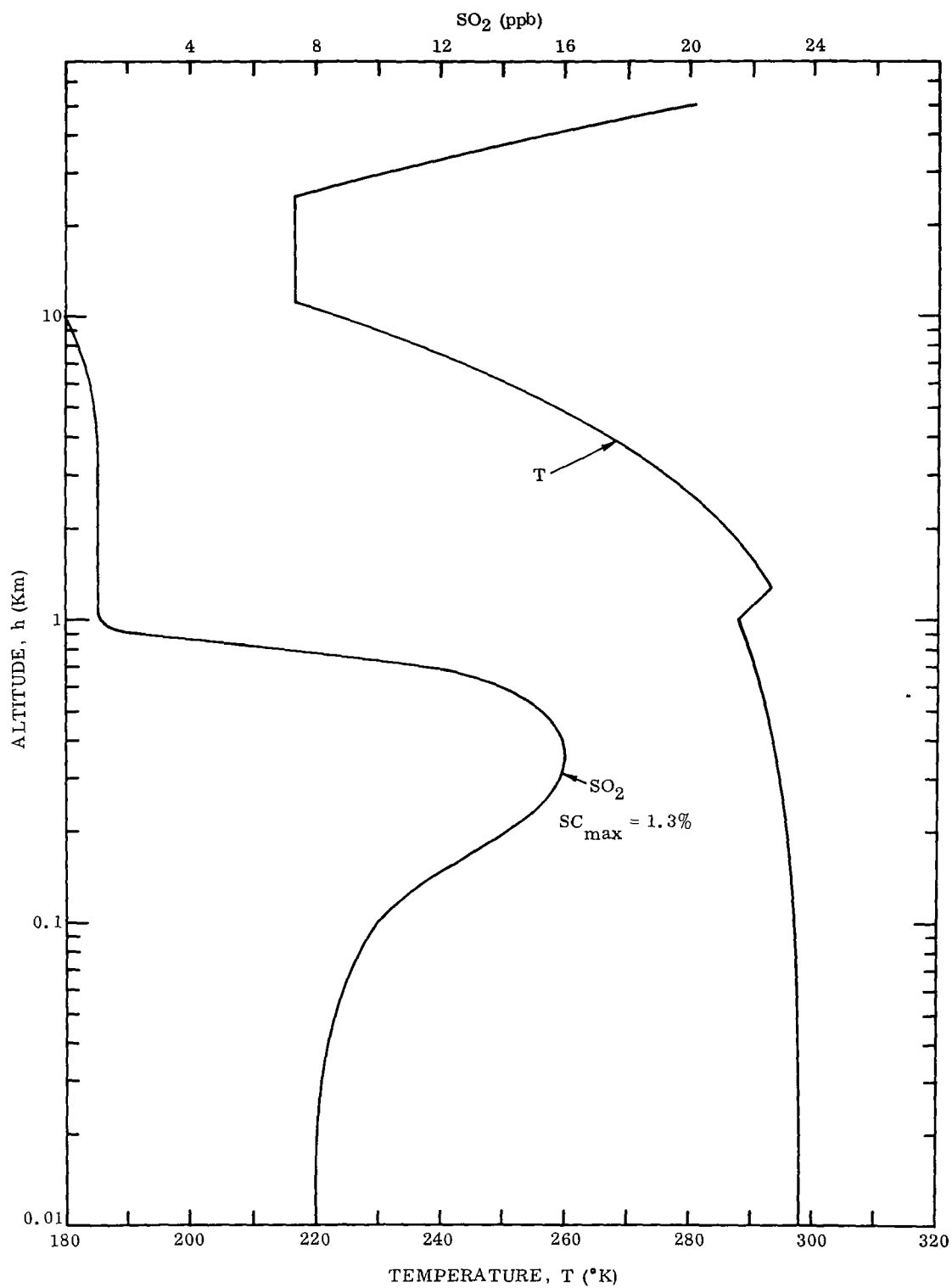
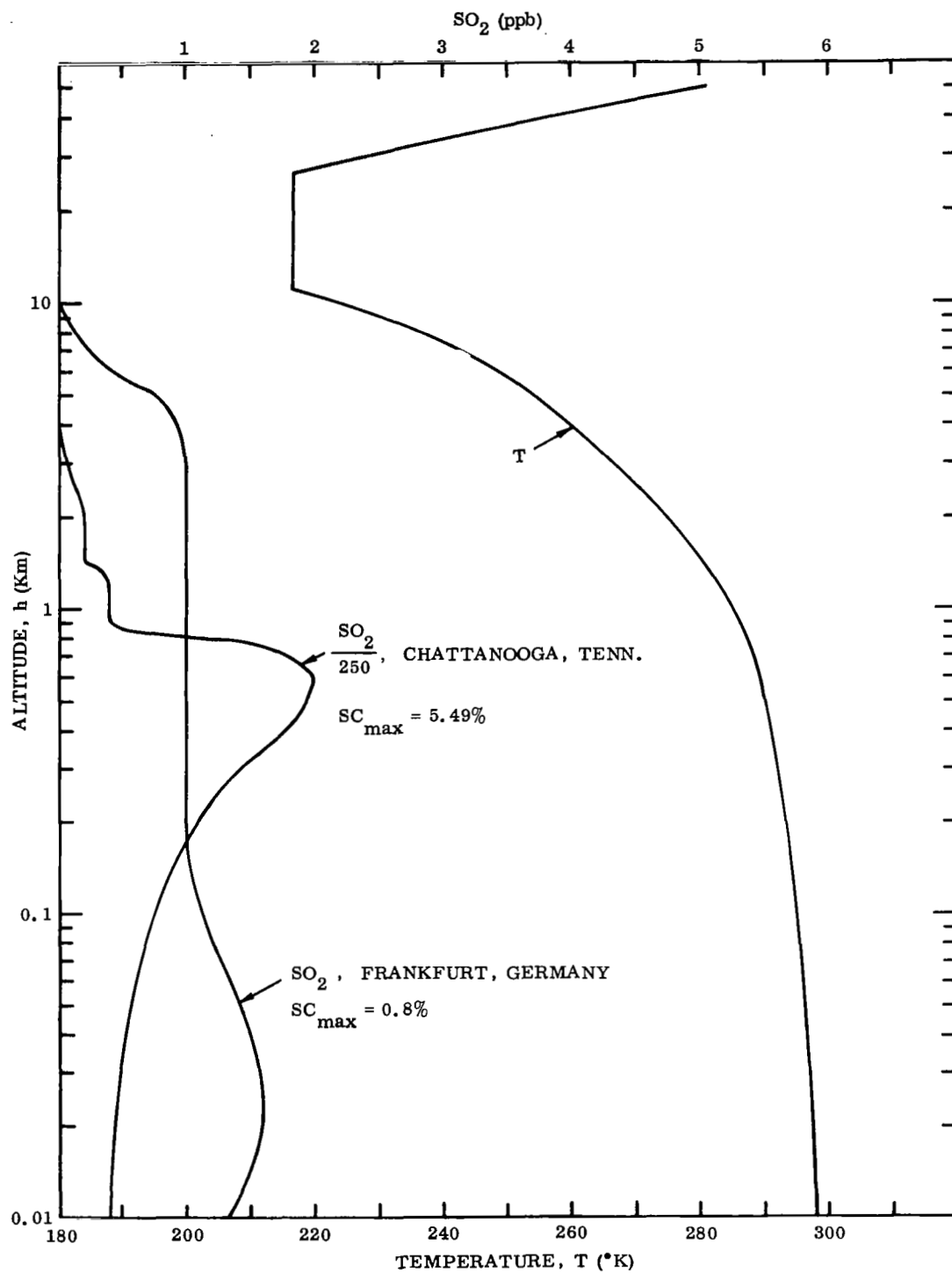


Figure 3-25. Measured Temperature and SO<sub>2</sub> Profiles over Frankfurt, Germany



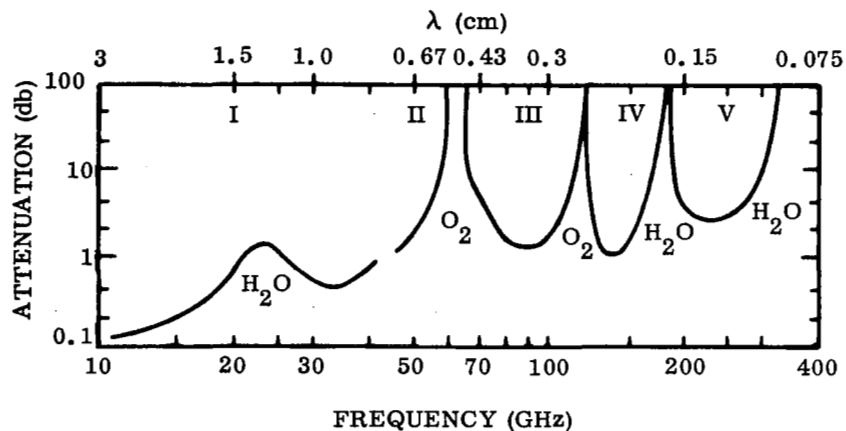
**Figure 3-26.** Measured Temperature and SO<sub>2</sub> Profiles over Frankfurt, Germany and Chattanooga, Tennessee

- c. In general, the pollutant concentration profile shape is related to the temperature profile. Further studies on this relationship are required.
- d. Significant, measurable changes in radiance, with and without even relatively small amounts of air pollution, will exist under a variety of atmospheric conditions. However, these changes are less than linearly related to increasing pollutant concentrations. This appears to hold true independent of spectral resolution, at least for  $\Delta\lambda \geq 0.1\mu$ .
- e. Considerable spectral interference exists between the individual pollutants that normally are present in polluted atmospheres for spectral resolutions of about  $0.1\mu$ . This makes identification and quantitative measurements of specific pollutants difficult for conventional type spectrometers or radiometers.
- f. Higher spectral resolution measurements would possibly alleviate the interference problem to obtain specificity. In addition, with higher spectral resolution, larger values of pollutant's absorption coefficients would be obtained, thereby increasing the observed radiance changes. Further studies are required in this general area.

**3.2.5 MEASUREMENT OF AIR POLLUTION IN THE MICROWAVE REGION.** In this section we consider the application of passive microwave spectroscopic techniques to the remote measurement of air pollution. Microwave spectroscopy has proved to be a powerful laboratory tool for qualitative measurements of gases. At low pressures, on the order of  $10^{-3}$  to 1 mm Hg, microwave spectra are so specific that observations of a single frequency are usually adequate to identify a particular species.

As was indicated in Subsection 3.2.2, the value of the earth's surface emissivity has a pronounced effect upon the radiance changes, detectable at satellite altitudes, with and without air pollutants present. The microwave region has the advantage of possessing lower surface emissivities than the IR region. Typically, these are  $\epsilon_s \approx 0.85$  for most land surfaces and  $\epsilon_s \approx 0.55$  for water surfaces at  $\nu \approx 20$  GHz ( $1.5$  cm), whereas, in the IR region  $\epsilon_s \approx 1$  at  $\lambda \approx 10\mu$ . Another advantage of the microwave region is that it possesses windows where atmospheric transmission losses may be small, even in the presence of clouds. These windows are shown in Figure 3-27, in which the total atmospheric attenuation as estimated by Conway et al. (Reference 65) for normal atmospheric conditions is presented. The principal sources of atmospheric attenuation are the absorption due to  $H_2O$  vapor and  $O_2$  (see Figure 3-27). Other contributions to the total attenuation are due to aerosol scattering and absorption by minor atmospheric constituents, such as  $O_3$  and liquid  $H_2O$  (Reference 78).

In Figure 3-27 five windows in the microwave region were noted where radiation from the surface will penetrate through the atmosphere. Three of these — I (10-40 GHz), IV (120-160 GHz), and V (200-300 GHz) — are limited by the  $H_2O$  vapor bands and their accompanying continuum; the other two — II (40-50 GHz) and III (70-100 GHz) — are limited by  $O_2$  absorption. Since the precise degree of attenuation during any measurement is due to the amount of  $H_2O$  vapor and  $O_2$  in the atmosphere, observations in



		FREQUENCY (GHz)	REF.
<div> <div>VERY WEAK</div> <div> <div>73</div> <div>115</div> <div>230</div> </div> <div>CO</div> </div>		73	66
		115	67
		230	68
<div> <div>150</div> <div>NO</div> </div>		150	69
<div> <div>15</div> <div>3941</div> <div>NO<sub>2</sub></div> </div>	all		70
<div> <div>25</div> <div>N<sub>2</sub>O</div> </div>	25		71
<div> <div>169</div> <div>H<sub>2</sub>S</div> </div>	169		72
<div> <div>38</div> <div>102</div> <div>96</div> <div>118</div> <div>O<sub>3</sub></div> </div>	all		73
<div> <div>20 - 30</div> <div>54</div> <div>70</div> <div>SO<sub>2</sub></div> </div>	20-30 all		74 75
<div> <div>18 - 29</div> <div>NH<sub>3</sub></div> </div>	18-29		76
<div> <div>HYDRO-CARBONS</div> </div>	all		77

Figure 3-27. Atmospheric Transmission Windows in the Microwave Region (After Conway — Reference 65) and Air Pollutant Absorption Frequencies

Since we conclude that quantitative pollutant measurements would be quite difficult in the microwave region due to lack of specificity, we will not discuss the application and/or selection of potential microwave spectrometers and radiometers. Guidelines for the selection of microwave instruments have been laid out in detail in References 78, 80.

### 3.3 CONCLUSIONS

The detection of air pollutants by remote sensing in the spectral range from the ultraviolet to the microwave region has been investigated. It is found that

- The ultraviolet-visible region has more disadvantages than advantages (see Table 3-7)
- The infrared region ( $3.5 - 13\mu$ ) has more advantages than disadvantages, (see Table 3-7)
- The microwave region ( $0.1 - 3$  cm) is not useful because of lack of specificity, and
- The quantitative measurements of aerosol content in the lower atmosphere probably cannot be made from a satellite.

For the calculation of the signal change in the infrared region, the following factors must be considered:

- a. Pollutant Optical Thickness (Concentration of the Pollutants Times Thickness). The concentration alone can be obtained only through an independent knowledge of the thickness.
- b. Spectral Characteristics of the Pollutant, i.e., Spectral Absorption Coefficients (Line Strength/Line Spacing) and Fine Structure Parameter (Line Half Width/Line Spacing). In general, the transmission is not given by Beer's law.
- c. Interference by Atmospheric Absorption. No infrared absorption by pollutants is completely free from overlap of atmospheric lines and/or other pollutant lines and the continuum. It is relatively easy to account for the overlap by the continuum by making an independent measurement of the continuum. To account for the overlap due to other lines, high-resolution observations must be made.
- d. Dependence on the Difference Between the Surface and Low-Level Atmospheric (Pollutant) Temperatures, and on the Pollutant Concentration Profile through the Atmosphere. Information about these parameters must therefore be obtained independently. A measurement of the surface temperature can be made with a simple instrument already used on satellites. Atmospheric parameters can be obtained from satellites using radiance-inversion techniques and/or from the global network of weather stations.

- e. Effect of Extraneous Light Sources. The effect of extraneous light sources, such as the reflection from sun, moon, and sky radiation, is negligible. Also, city lights do not interfere because they do not emit significantly at wavelengths greater than  $3.5\mu$ .

The results of the calculation of typical signal changes in the infrared for representative concentration distributions and meteorological conditions are summarized in Table 3-8.

Table 3-7. Advantages and Disadvantages of Spectral Regions

		Spectral Range	
		0.3 - $3.5\mu$	$3.5 - 13\mu$
a)	Time of observation	Day-time	Day- and night-time
b)	Factors affecting observation	Rayleigh and Mie scattering from the atmosphere	Meteorological conditions such as surface temperature and temperature profile through the atmosphere
c)	Methods of over-coming affecting factors	Not possible by direct measurement; maybe through theoretical calculations	Possible by direct measurements from satellite and/or through global weather-station network
d)	Radiative active species	$\text{NO}_2$ , $\text{SO}_2$ , $\text{O}_3$ (weak)	All molecules

Table 3-8 . Representative Signal Changes (SC) in the Infrared

Species	Concentration (ppm)	$\lambda$ ( $\mu$ )	SC(%)	Remarks
CO	2.5	4.6	27	Some interference by $\text{H}_2\text{O}$
$\text{SO}_2$	0.02	7.4	12	Some interference by $\text{H}_2\text{O}$
$\text{NO}_2$	0.02	6.3	5	Strong interference by $\text{H}_2\text{O}$
$\text{O}_3$	0.03	9.5	3	Strong interference by stratospheric $\text{O}_3$
PAN	0.005	8.6	8	Some interference by $\text{H}_2\text{O}$
$\text{NH}_3$	0.05	10.8	5	Some interference by $\text{H}_2\text{O}$ and $\text{CO}_2$



# 4

## INSTRUMENTATION

### 4.1 PERFORMANCE EVALUATION

The following criteria are considered in evaluation of spectroscopic instruments to detect air pollutants from a satellite:

- a. Sensitivity of the instrument to the signal arising from the presence of pollutants. The computed quantity is the signal-to-noise ratio.
- b. Specificity of the instrument; i.e., its ability to discriminate against an interfering background and other radiating species. The determining quantity is the spectral resolution.
- c. Required observation time for the instrument to sample and integrate the received signal, which must be consistent with the satellite speed and desired ground coverage.
- d. Information content of the signal received by the instrument. Since additional knowledge about the surface temperature and the meteorological condition of the atmosphere is required for interpretation of the data, instruments able to give this information are considered to have a high information content.
- e. The complexity of the system, including weight, volume, power, and cooling requirements.

The first four criteria are expressed in terms of the signal-to-noise (S/N) ratio of the system. The S/N ratio is proportional to the system detectivity and the available radiant power, integrated over the wavelength interval:

$$\frac{S}{N} = \int_{\Delta\lambda} D_{\text{SYS}}(\lambda) P(\lambda) d\lambda$$

In the following, S/N is evaluated only over small wavelength intervals in which  $D_{\text{SYS}}$  and  $P$  are independent of the wavelength. Thus,

$$\frac{S}{N} = D_{\text{SYS}, \lambda} P_{\lambda} \Delta\lambda$$

or in terms of wavenumber  $\omega$ :

$$\frac{S}{N} = D_{\text{SYS}, \omega} P_{\omega} \Delta\omega \quad (4-1)$$

The system detectivity is inversely proportional to the noise-equivalent power and is expressed in terms of specific detectivity  $D_{\omega}^*$ , detector area  $A_d$ , and noise-equivalent-band width  $\Delta f$ :

$$D_{\text{SYS}, \omega} = \frac{1}{(\text{NEP})_{\omega}} = \frac{D_{\omega}^*}{\sqrt{A_d \Delta f}} \quad (4-2)$$

For a Class I detector,  $D^*$  is independent of the value of the detector time constant (photoemissive tubes, ideal heat detectors, photoconductive cells), and  $D^*$  is given only as a function of  $\lambda$ .

For a Class II detector, the specific detectivity is proportional to the square root of the detector time constant  $\tau_D$  (thermocouples, bolometers, photographic film, the human eye, and most PbS cells). Thus,  $D^* = D_c^* \sqrt{\tau_D}$ , where  $D_c^* \approx 10^9 - 10^{10} \text{ Hz}^{1/2} \text{ cm watt}^{-1} \text{ sec}^{-1/2}$  is representative for modern thermistor bolometers.

For cooled detectors,  $D^* \approx 10^{10} \text{ Hz}^{1/2} \text{ cm watt}^{-1}$  is a representative (although conservative) value. The upper limit of the specific detectivity at the cut-off wavelength is given by  $D_{\text{BLIP}}^*(T_B, 2\pi)$ , where  $T_B$  is the effective background temperature. For  $T_B = 295^\circ\text{K}$  and a cut-off wavelength of  $10\mu$ ,  $D_{\text{BLIP}}(295^\circ\text{K}, 2\pi) = 3 \times 10^{10} \text{ cm Hz}^{1/2} \text{ watt}^{-1}$ . For less than  $2\pi$  steradians exposure (assuming cooled instrument), this value is improved by

$$D_{\text{BLIP}}^*(\Theta) = D_{\text{BLIP}}^*(2\pi) \text{CSC}(\alpha)$$

where  $\alpha$  is half-angle field of view.

Thus, the theoretical specific detectivity of a cooled detector may be as high as  $6 \times 10^{12} \text{ cm Hz}^{1/2} \text{ watt}^{-1}$  for  $\alpha = 5 \text{ mrad}$ . At  $3.5\mu$ ,  $D_{\text{BLIP}}^*$  is higher by another order of magnitude. In practice, however,  $D^* \lesssim 2 \times 10^{10} \text{ cm Hz}^{1/2} \text{ watt}^{-1}$  for germanium doped or Hg  $T_e$  - Cd  $T_e$  detectors and  $D^* \lesssim 10^{11} \text{ cm Hz}^{1/2} \text{ watt}^{-1}$  for InSb detectors have been achieved. Further improvement is possible by limiting the spectral range the detector is seeing at any time.

The available radiant power (watts) originating from an extended source<sup>†</sup> at the detector is proportional to the "étendue" of the instrument (aperture  $A_o$  times solid angle  $\Omega$ ), the efficiency of system  $\eta$  and the spectral radiance  $N_{\omega} (\text{w cm}^{-2} \text{ sr}^{-1} (\text{cm}^{-1})^{-1})$  as seen by the detector:<sup>††</sup>

<sup>†</sup> Assuming that the pollution layer fills the field-of-view.

<sup>††</sup> The symbol for spectral radiance is  $N_{\omega}$  in contrast to the symbol for the noise voltage,  $N$ , which has no subscript.

$$P_{\omega} \Delta\omega = \eta A_o \Omega N_{\omega} \Delta\omega.$$

To establish the sensitivity of the instrument to small changes in radiance levels, produced by the absorption/emission of pollutants in the atmosphere, the radiance is substituted with the radiance change (SC), calculated in the previous section. Therefore,

$$\Delta N_{\omega} = \left[ \frac{N_{\omega}^{\text{CLEAN}} - N_{\omega}^{\text{POLL}}}{N_{\omega}^{\text{CLEAN}}} \right] N_{\omega}^{\text{CLEAN}} = \text{SC} \times N_{\omega}^{\text{CLEAN}}$$

and the available power becomes

$$P_{\omega} \Delta\omega = \eta A_o \Omega \Delta N_{\omega} \Delta\omega \quad (4-3)$$

The collector area  $A_o$  and the detector area are related through the "étendue" of the instrument:

$$A_o \Omega = A_d \Omega_d \quad (4-4)$$

where  $\Omega_d$  is the solid angle under which the detector is illuminated, which can be expressed in terms of an f-number (f/no) at the detector:

$$\Omega_d = \frac{A_o}{f^2} = \frac{C}{(f/\text{no})^2} \quad (4-5)$$

where f is the focal length and C determines the ratio of the "effective radius" to the geometrical diameter of the collector. Thus, substituting Equations (4-2) through (4-5) into Equation (4-1), and substituting  $\Delta S$  for S, indicating the difference in the signal voltage

$$\frac{\Delta S}{N} = \eta C^{1/2} \sqrt{\frac{A_o \Omega}{\Delta f}} \frac{D_{\omega}^* \Delta N_{\omega} \Delta\omega}{(f/\text{no})} \quad (4-6)$$

This is the basic equation which will be evaluated for the different instruments. The range of  $\Delta N_{\omega}$  is determined by the range of signal changes considered (1 percent to 30 percent)

$$0.01 < \text{SC} < .3$$

and the blackbody energy at 300°K from 3 to 13  $\mu$  in  $\omega \text{ cm}^{-2} \text{ sr}^{-1} (\text{cm}^{-1})^{-1}$

$$0.5 \times 10^{-8} < N_{\omega} < 0.14 \times 10^{-4}.$$

Thus, we have, since  $\Delta N_{\omega} = SC \times N_{\omega}$ :

$$0.5 \times 10^{-10} < \Delta N_{\omega} < 0.5 \times 10^{-5} \quad (4-7)$$

The satellite system parameters which were chosen correspond to those given by the University of Michigan study (Reference 80):

Orbit altitude  $h = 200$  n. mi.

Velocity  $v = 4$  n. mi. /sec

$v/h = 0.02$  rad/sec<sup>-1</sup>

A reasonable ground resolution (if not otherwise noted) of  $10 \times 10$  miles was assumed, resulting in a field-of-view  $2\alpha = 0.05$  rad. For a square entrance slit (or detector), the solid angle becomes  $\Omega = 4 \sin^2 \alpha \approx (2\alpha)^2 = 2.5 \times 10^{-3}$  sterad. For a circular ground resolution with a diameter of 10 miles, the solid angle becomes  $\Omega = \pi \sin^2 \alpha \approx \pi \alpha^2 = 2 \times 10^{-3}$  sterad.

In this general discussion, one more consideration regarding the spectral resolution must be made. As stated before, the calculation of the signal change was based upon relatively low spectral resolution ( $\Delta\lambda \sim 0.1\mu$ ). This was necessary because the information required for a high resolution atmospheric transmission model as well as high resolution absorption spectra of most of the molecular pollutants do not yet exist. However, it is believed that this fact does not necessarily constitute a serious handicap in the present evaluation, because two physical effects tend to compensate. This can be understood by observing Equation (4-6), in which the  $\Delta S/N$  is proportional to the energy  $\Delta N_{\omega}$  and the spectral band pass  $\Delta\omega$ . In low resolution, the spectral absorption coefficients of the molecular pollutants are averaged with the result that the peak absorption at the center of the lines are considerably lower than in high resolution, thus reducing the signal difference  $\Delta N_{\omega}$ . On the other hand, the band pass  $\Delta\omega$  is larger in low resolution. In high resolution,  $\Delta N_{\omega}$  increases while  $\Delta\omega$  decreases. In a first approximation, an increase in resolution by a factor of 10 ( $\Delta\omega = 1 \text{ cm}^{-1}$ ) might, depending upon the molecule, increase  $\Delta N_{\omega}$  by a factor of 2 to 10. In only two of the detection methods investigated here is the exact knowledge of high resolution atmospheric transmission and pollutant absorption/emission important: optical correlation techniques and active laser techniques. For these cases, special considerations were made.

The following evaluation analysis of the different instruments is restricted to the electro-optical sensitivity. The thermal control, dynamic range of the electronics, analog-digital conversion (12-bit word is considered sufficient for the actual data and housekeeping), tape storage, and telemetry are considered to be well within the present state-of-art for satellite systems.

**4.1.1 RADIOMETER.** A radiometer consists basically of a collecting lens (or mirror), a detector, filter, chopper, and reference calibration source. For the observation of several spectral intervals, either one dispersing unit and several detectors (polychromator) for simultaneous measurements, or one detector and several filters (filter-wheel) for sequential measurements can be used. For a detailed observation of many pollutants, together with the simultaneous determination of the temperature and water vapor profile through the atmosphere and the surface temperature, a large number of spectral intervals have to be employed. However, practical considerations limit the total number which can be used.

**4.1.1.1 Filter-Wheel Radiometer.** The schematic of a filter-wheel radiometer is shown in Figure 4-1. In the evaluation of  $\Delta S/N$  as a function of  $\Delta N_{\omega}$  according to Equation (4-6), a spectral bandwidth of  $10 \text{ cm}^{-1}$  is assumed. It should be noted that the maximum spectral resolution in interference filters is currently about  $3 \text{ cm}^{-1}$ . The collecting area is taken to be  $(10 \times 10) \text{ cm}^2$ , and the field of view  $\Omega$  to be  $0.0025$  steradians, giving an "étendue" of  $0.25 \text{ sterad cm}^2$ . With a focal length of  $10 \text{ cm}$ , the square detector area ( $C = 1$ ) becomes  $0.25 \text{ cm}^2$ . The use of a field lens may be considered to relax the requirement of high precision for a fast-speed instrument, because the detector size is reduced by approximately the ratio of the f-number of the field lens to the f-number of the collecting optics, while the effective f-number of the instrument becomes that of the field lens. However, the theoretical limit of an unimmersed field lens detector assembly is an f-number of  $0.5$  and the detector size in the above example can be reduced by only a factor of  $2$ . A further improvement is possible by immersing the detector in a high-index material. However, these gains are partly offset by high transmission losses in the field lens configuration. Therefore, the use of a field lens will not be explicitly included in the present considerations.

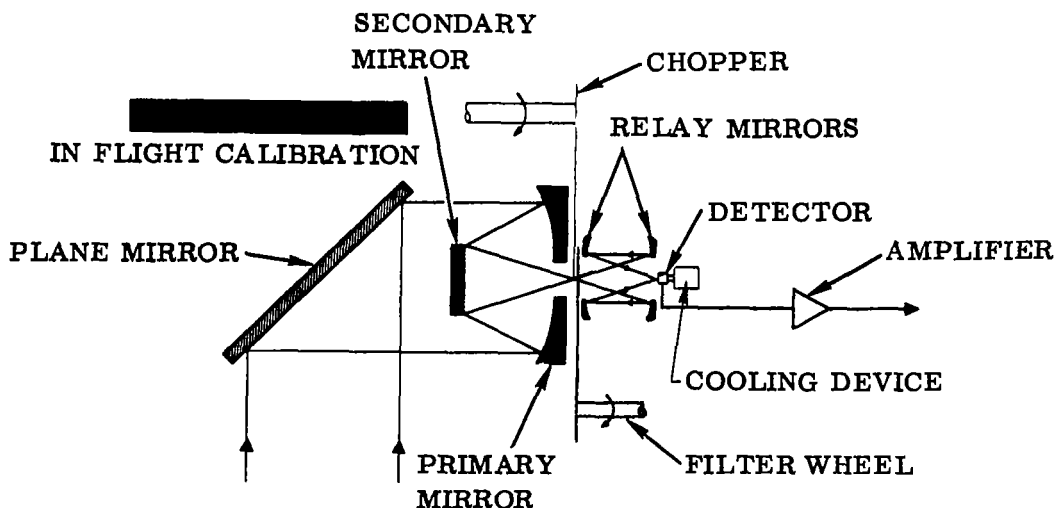


Figure 4-1. Schematic of a Filter Wheel Radiometer

The total observation time (without image motion compensation) is given by the time in which the field-of-view will have traversed a complete field-of-view on the ground, thus

$$t_{\text{obs}} = \frac{\sqrt{\Omega}}{v/h} = 2.5 \text{ sec} \quad (4-8)$$

Assuming that the individual signals per spectral channel are integrated over this time, the noise-equivalent-bandwidth becomes

$$\Delta f = \frac{1}{2t_{\text{obs}}} = 0.2 \text{ Hz} \quad (4-9)$$

The individual "look-time" through each optical filter is given by the rotation time of the filter wheel and the number and size of filters. If 10 filters are used and the rotation is 1 RPS, the time becomes  $1/2 \times 100 \text{ ms}$ . The one-half is introduced due to the chopper. The actual look-time will be less because the edge of the chopper needs a finite time to cross the optical beam. The chopping frequency should be high in order to avoid noise contribution from the  $1/f$  detector. However, if a thermistor-bolometer is used it is desirable to keep the chopping frequency down to maximize the specific detectivity. For an unimmersed thermistor bolometer, a chopping frequency of 10 Hz is outside the range of severe  $1/f$  noise. A representative value for the specific detectivity is  $\sim 10^9 \text{ Hz}^{1/2} \text{ cm/watts}$ .

The efficiency  $\eta$  is determined by the following factors. Assuming the use of 10 filters, the total observation time per channel is 250 msec. However, both the signal and noise are integrated during the actual look-time for each channel. Thus,  $\sqrt{0.05/0.25} = 0.45$ . An additional degradation due to the detector time constant is given by the ratio of the average to peak signal, which for a square wave is  $\sqrt{2}/\pi = 0.35$ . The noise factors of the detector bias supply and amplifier are assumed to be proportional to  $1/\sqrt{2}$  each. A reflectivity of 0.95 for each of the mirrors and a transmissivity of 0.4 for the filter results in a net optical efficiency of 0.29. Therefore, the total efficiency of the system becomes  $\eta = 0.45 \times 0.35 \times (1/\sqrt{2})^3 \times 0.38 = 0.021$ .

Substituting all other terms into Equation (4-6), we have

$$\begin{aligned} \frac{\Delta S}{N} &= 0.021 \sqrt{\frac{0.25}{0.2}} 10^9 \times 10 \Delta N_{\omega} \\ &\approx 2 \times 10^8 \Delta N_{\omega} \end{aligned} \quad (4-10)$$

**4.1.1.2 Polychromator-Radiometer.** This system uses a dispersing element (prism, grating) and a bank of detectors at the exit plane of the spectrometer (Figure 4-2). The obvious advantage is that all channels are observed simultaneously and the integration time for each channel is increased over that of the sequential observation. Using 10

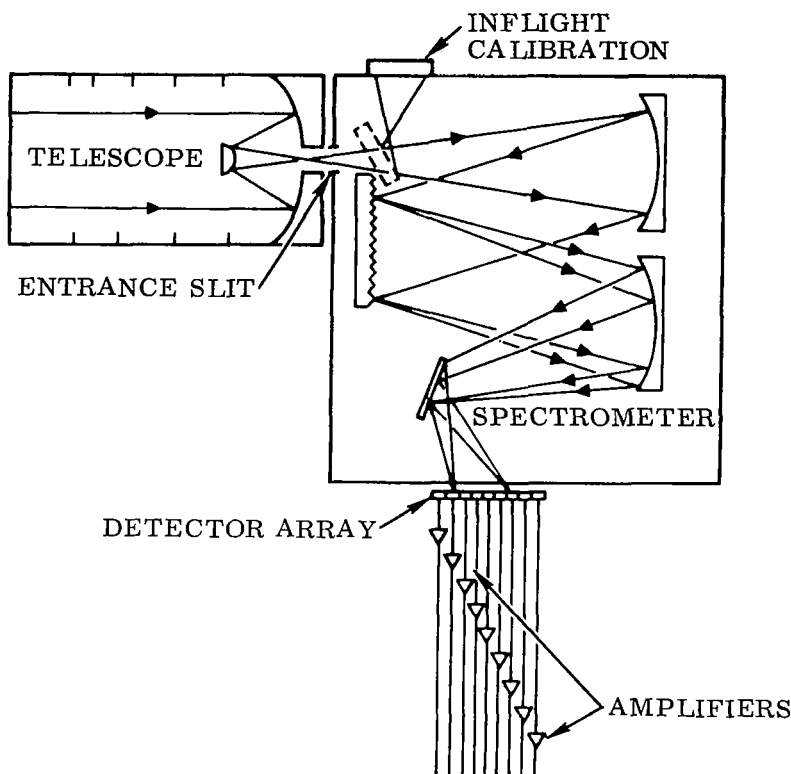


Figure 4-2. Schematic of a Polychromator Radiometer

channels as in the filter-wheel radiometer, the improvement is a factor of  $\sim 3$ . In using individual detectors for each spectral interval, higher specific detectivities can be obtained. For Hg CdTe and doped Ge detectors, an average of  $D^* = 10^{10} \text{ Hz}^{1/2} \text{ cm}^2/\text{watt}$  can be assumed, resulting in an improvement of a factor of 10. However, it is not possible to utilize the very fast optical system at the detectors as was the case for the filter-wheel radiometer. Thus, a reduction in f-number of about 5 has to be made. A further reduction in solid angle is necessary if a spectral resolution of  $10 \text{ cm}^{-1}$  is to be maintained. For a grating spectrometer,  $\Omega \leq 0.17 \frac{\Delta\omega^\dagger}{\omega}$ , which results (at  $5\mu$ ) in  $\Omega \leq \frac{0.17 \times 10}{2000} = 8.5 \times 10^{-4} \text{ sterad}$ , which is a reduction of  $\sqrt{1/3}$ . Thus,

$$\begin{aligned} \frac{\Delta S}{N} &\approx \left( \frac{\Delta S}{N} \right)_{\text{FILTER WHEEL}} \times 10 \times 3 \times 0.2 \times 0.6 \frac{\Delta N}{\omega} \\ &\approx 6 \times 10^8 \frac{\Delta N}{\omega} \end{aligned} \quad (4-11)$$

† This expression can be derived considering the angular height of the slit and the angle of incidence on the grating.

However, the slight improvement in  $\Delta S/N$  is offset by greater system complexity. It is necessary to monitor the sensitivity in every channel very closely in order to account for the slightest shift, because absolute values are to be compared, while only relative values are compared in the filter wheel radiometer.

In addition, a heavy weight penalty has to be paid in the case of the polychromator radiometer. The operational "Satellite Infrared Spectrometer (SIRS)" used in TIROS and NIMBUS, (Reference 81) weighed approximately 90 pounds, while the filter-wheel radiometer is estimated to weigh approximately nine pounds.

4.1.2 SCANNING SPECTROMETER. The evaluation of a spectrally scanning spectrometer (Figure 4-3) is accomplished in a manner similar to that for the filter-wheel radiometer, except that the same limitation in spatial resolution used for the polychromator-radiometer has to be applied. Thus, for a spectral resolution of  $10 \text{ cm}^{-1}$ , a reduction of  $S/N$  of  $\sqrt{1/3}$  applies, and for observing 10 spectral intervals with  $\Delta\omega = 10 \text{ cm}^{-1}$ , the signal-to-noise ratio becomes

$$\frac{\Delta S}{N} \approx 10^8 \Delta N_{\omega}, \quad (4-12)$$

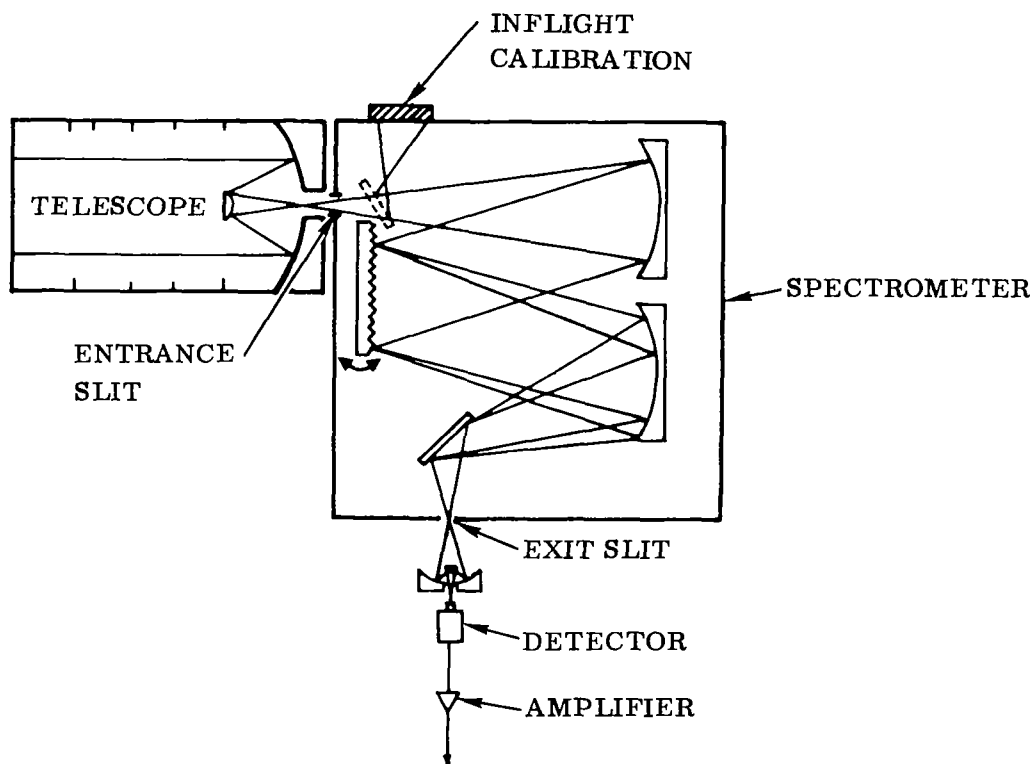


Figure 4-3. Schematic of a Scanning Spectrometer



which is essentially equal to the value of the filter-wheel radiometer. Since a scanning spectrometer is capable of much higher resolution than a filter-wheel radiometer, an estimate of the signal-to-noise is made for an instrument with a resolution of  $0.5 \text{ cm}^{-1}$ . In that case, the reduction in  $\Delta\omega$  is  $1/20$  and in  $\Omega$  is  $\sqrt{1/60}$ , which results in  $\Delta S/N \approx 10^6 \Delta N_\omega$ . In contrast to the filter-wheel radiometer, it is, of course, possible (and desirable) to increase the number of spectral intervals to be observed. However, a correspondingly larger noise-equivalent band pass  $\Delta f$  is required.

**4.1.3 INTERFEROMETER.** Developments in the last few years indicate the possibility of employing interferometer-spectrometers on satellites for the observation of air pollutants. If spectra over a large spectral interval with high resolution can be observed with high enough sensitivity, the greatest information content will be obtained. One spectrum can give information about the pollutants, surface temperature, atmosphere water content, and the temperature profile needed for the interpretation of the pollutant signal. The following parameters are deemed desirable:

Spectral range:	$3\text{--}15\mu$
Spectral resolution:	$0.1 \text{ to } 0.5 \text{ cm}^{-1}$
Observation time:	$\sim 10 \text{ sec}$

Such an instrument does not exist at present, but the development activity by industry may lead to such an instrument in a few years. The following paragraphs describe the standard Michelson interferometer-spectrometer (as it is used at present for space application), and advanced development being pursued at the Jet Propulsion Laboratory (JPL) and in France.

**4.1.3.1 Single-Ended Michelson Interferometer-Spectrometer.** In the Michelson interferometer, the incoming energy is divided by a beam splitter into two equal components, which are recombined at the detector after reflection from mirrors (Figure 4-4). A phase difference is introduced by a movable mirror in one of the two paths, and the output signal  $I(x)$  from the detector is given as a function of mirror movement  $(x)$  by:

$$I(x) = \int_{\omega_1}^{\omega_2} E(\omega) \cos(2\pi \omega x) d\omega, \quad (4-13)$$

which is called the interferogram, being the Fourier cosine transform of the spectrum  $E(\omega)$ . The spectrum is reconstructed by taking the inverse transform through a digital or analog computation.

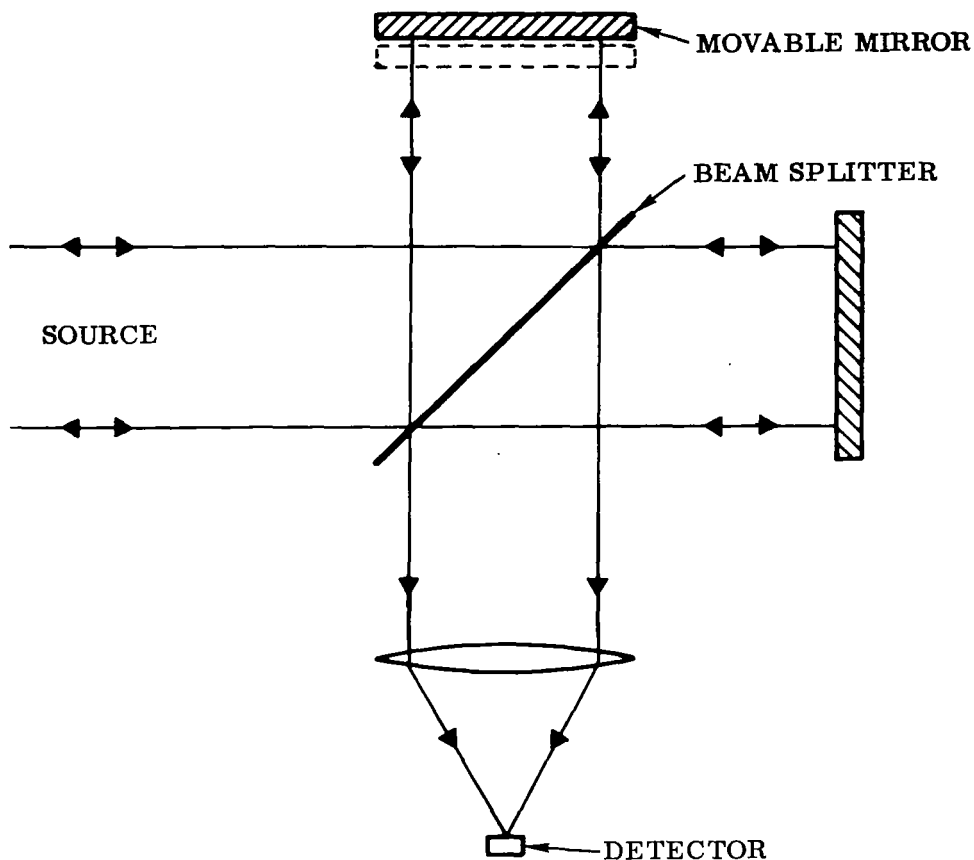


Figure 4-4. Schematic of a Michelson Interferometer

The theoretical limitations imposed upon the system are given by the finite mirror travel and the finite solid angle, while practical limitations are given by variations of the mirror movement.

For the derivation of the signal-to-noise ratio for a Michelson interferometer, Hanel and Chaney are followed (Reference 82) who described the satellite-borne IRIS instrument (Figure 4-5) to be flown on NIMBUS for the measurement of the temperature and humidity profiles. The signal power in the spectral interval  $\Delta\omega$  on the detector is given by

$$P_{\Delta\omega} = \frac{1}{2} \Delta N_{\omega} A_o \Omega \eta \Delta\omega \quad (4-14)$$

where the factor  $1/2$  accounts for the beam splitting; i.e., half of the energy is reflected back to the source.

In an interferometer, the NEP is inversely proportional to  $\sqrt{n/2}$  where  $n$  is the number of samples taken per interferogram; thus

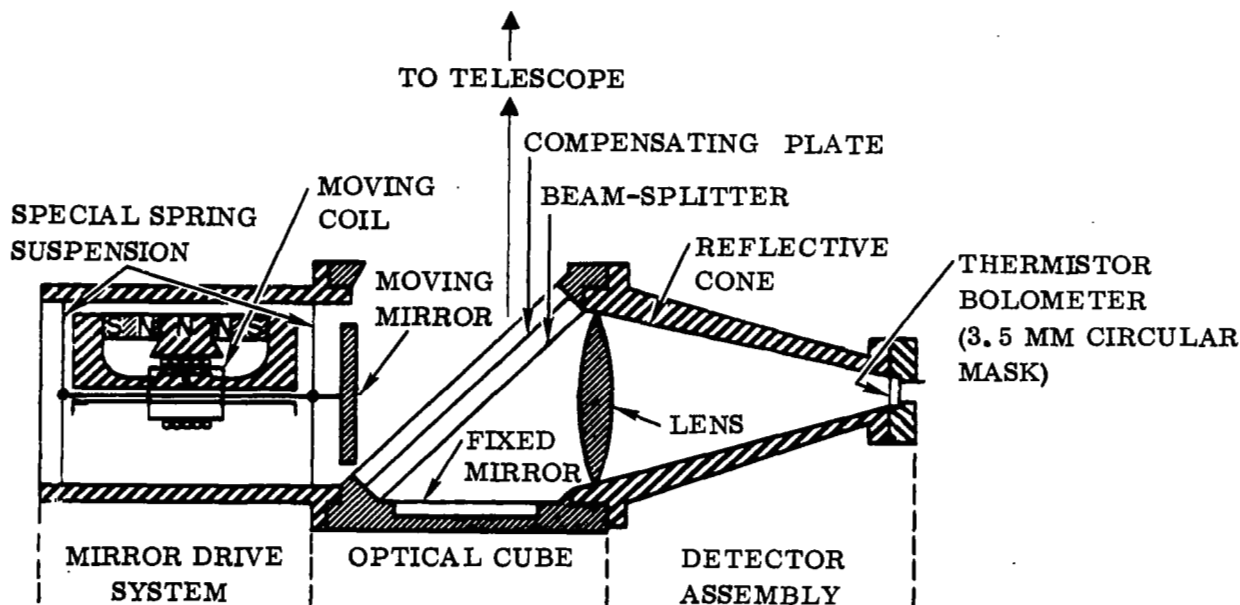


Figure 4-5. Schematic of IRIS Instrument (From Reference 82)

$$\text{NEP} = \frac{1}{D^*} \sqrt{\frac{2A_d \Delta f}{n}} \quad (4-15)$$

The band pass and number of samples are related to the total observation time by

$$\tau_{\text{obs}} = \frac{n}{2\Delta f} \quad (4-16)$$

The minimum number of samples must be at least twice the number of resolution elements at the highest wavenumber of interest, i.e.

$$n = 2 \frac{\omega_{\text{max}}}{\Delta\omega} \quad (4-17)$$

The maximum number of samples must be consistent with the relationship in Equation (4-17). It is desirable to sample close to the upper limit in order to remove undesirable high-frequency components. The noise-equivalent-bandwidth  $\Delta f$  must be large enough to pass the output frequencies of the detector, the maximum and minimum of which are given by

$$\begin{aligned} f_{\text{max}} &= 2 \nu \omega_{\text{max}} \\ f_{\text{min}} &= 2 \nu \omega_{\text{min}} \end{aligned} \quad (4-18)$$

where  $v$  is the velocity of the moving mirror. The mirror velocity determines the time required for one interferogram:

$$\tau = \delta/v \quad (4-19)$$

The mirror deflection  $\delta$  is determined by the desired spectral resolution:

$$\delta = (\Delta\omega)^{-1} \quad (4-20)$$

Usually, a mirror deflection larger than that given by Equation (4-20) is desirable to apply apodization for eliminating side lobes of the instrument function.

In practice it is found (Reference 83) that the minimum observation time should be at least five seconds to obtain acceptable S/N ratios (Reference 83). Therefore, if the time required for one interferogram  $\tau$  is smaller than five seconds, several interferograms of the same target should be obtained. If  $\tau$  is greater than five seconds,  $\tau_{\text{obs}}$  can be set equal to  $\tau$ . Of course, long observation times require image motion compensation (IMC). The IRIS instrument has a total observation time of 11 seconds (Reference 82). Within this time, the orbital motion of NIMBUS corresponds to about 80 km, or one-half of the field-of-view. The IMC is accomplished by a slowly rotating mirror, which images an area two degrees ahead of the satellite subpoint. At the end of 11 seconds, the mirror points two degrees behind the satellite and advances to the starting position within the five-seconds time interval between interferograms.

The remaining instrument parameter to be determined is the solid angle  $\Omega$ , which is related to the resolution by

$$\Omega = 2\pi \frac{\Delta\omega}{\omega} \quad (4-21)$$

Thus, the equation for the  $\Delta S/N$  becomes

$$\frac{\Delta S}{N} = \frac{\eta}{2} \frac{D^*}{(f/\text{no})} \sqrt{A_o \Omega t_{\text{obs}} \Delta N_{\omega} \Delta\omega} \quad (4-22)$$

From this equation, the advantages of an interferometer as compared to a conventional grating spectrometer become apparent:

- a. Étendue  $A_o \Omega$  — The change in power at the detector,  $\Delta P$ , for a given change in source radiance  $\Delta N$ , (i.e., for a given change in spectral radiance,  $N_{\omega}$ , integrated over a spectral bandwidth  $\Delta\omega$ ) can be written

$$\frac{\Delta P}{\Delta N} = A_o \Omega \eta$$

The change in power is proportional to a characteristic area of the instrument, the solid angle subtended at that area by the boundaries of the beam, and to the overall optical transmission of the instrument. If the characteristic area is taken to be that of the disperser or interferometer plate the solid angle involved is that subtended by the slits in the case of the classical dispersion instrument, or by a limiting field aperture in the case of the interferometric instrument.

One of the practical advantages of all of the interferometric devices is the increased solid angle of acceptance over that of classical prism or grating instruments. Expressed in terms of the solid angle-resolution product

$$\Omega R = 2\pi \quad \text{interferometer}$$

$$\Omega R = 2\beta \sin i \quad \text{grating}$$

where  $\beta$  is the angular height of the slit and  $i$  is the angle of incidence on the grating.

The value of this product for the grating might range approximately from a typical value of 0.02 to a maximum value of 0.17. Thus, for equal resolution, area, and transmission, the power on the detector per unit radiance for the interferometer is roughly 40 to 300 times that of the grating.

- b. Multiplexing — The signals from all of the spectral elements are recorded in parallel instead of being recorded sequentially as in most other instruments. If the noise is independent of the signal, the signal-to-noise ratio is improved by the "multiplex advantage" and is proportional to  $\sqrt{m}$  for a band containing  $m$  spectral elements, because

$$t_{\text{obs}} = m t_{\omega} \quad (4-23)$$

Another advantage of the Michelson interferometer is its independence of optical surface imperfections and its simplicity in optical layout, although great demands are made for the mechanical mirror drive.

In order to compare the performance of an interferometer spectrometer with the performance of the spectrometer described in Section 4.1.2, the  $\Delta S/N$  is calculated from Equation (4-22) with the following values. The efficiency is given by the optical transmission times the noise figures of the detector, preamplifier, power supply, and the error in the encoding process. Hanel and Chaney give a value of 0.2 for the optical transmission, and  $1/\sqrt{2}$  each for the three noise sources and the encoding process (one coding step is set equal to the rms value of the noise in the interferogram). Thus,  $\eta = 0.05$ . The entrance area is kept at  $A_0 = 100 \text{ cm}^2$ . In this comparison, a continuous coverage of 10 spectral intervals of  $10 \text{ cm}^{-1}$  is maintained. We select  $\Delta\lambda = 9.54\mu$  to  $10.5\mu$ . Thus,  $\omega_{\text{max}} = 1055 \text{ cm}^{-1}$  and  $\omega_{\text{min}} = 955 \text{ cm}^{-1}$ . The solid angle is given by  $\Omega = 2\pi \cdot 10/1055 = 0.06 \text{ sterad}$ . The specific detectivity is  $10^{10} \text{ Hz}^{1/2} \text{ cm watt}^{-1}$ . The

total observation time is kept at 2.5 seconds and the f-number at the detector is equal to 1. Thus,  $\Delta S/N = 10^{10} \Delta N_\omega$  which is two orders of magnitude better than the corresponding filter-wheel radiometer or scanning spectrometer.

The preceding calculation was tailored to match the systems and instrument parameters of those used previously for the radiometer and spectrometer. The following paragraph provides a comparison of Michelson's spectrometer characteristics with those of the operational IRIS instrument (which covers a larger spectral range with better spectral resolution).

The spectral range is from  $500 - 2000 \text{ cm}^{-1}$ , the resolution is  $5 \text{ cm}^{-1}$ . The number of spectral intervals, therefore, is 300. The travel of the drive mirror is 4 mm, twice the required minimum displacement. The velocity of the mirror is  $0.24 \text{ mm/sec}$ . The total observation time is equal to the time for one interferogram. The frequency range of the detector is from 20 to 80 Hz and the equivalent-noise-band width is 136 Hz. The number of samples per total observation time is 3400, giving a sampling rate of  $300 \text{ sec}^{-1}$ . The detector used is a thermistor-bolometer with a specific detectivity of  $6 \times 10^9 \sqrt{t_D}$  and a time constant of 1 msec. The areas of the collector and detector are  $10 \text{ cm}^2$  and  $0.1225 \text{ cm}^2$ , respectively. The usable solid angle is  $0.0157 \text{ sterad}$ . The optical efficiency is quoted as 0.2 and the degradation due to instrument noise and encoding process is  $(\sqrt{2})^{-4} = 0.25$ . Introducing these values into Equation (4-15)

$$NEP = \frac{1}{1.8 \times 10^8} \sqrt{\frac{0.245 \times 136}{3400}}$$

and Equation (4-14)

$$P_\omega \Delta\omega = 0.05 \times 10 \times 0.0157 \times 5 \times \Delta N_\omega$$

results in

$$\frac{\Delta S}{N} = 3 \times 10^7$$

The corresponding value for a scanning spectrometer, using the IRIS parameters, would be approximately  $10^5$ .

Extending the evaluation of a Michelson type interferometer to a desired range from  $800 - 3000 \text{ cm}^{-1}$  and spectral resolution of  $0.5 \text{ cm}^{-1}$ , we find that such an instrument would have a very low signal-to-noise ratio, demanding at the same time an impractically high mirror velocity, and sampling rate, and, subsequently, very high mechanical stability. Thus, different approaches in interferometer design are indicated.

The disadvantages of the "simple" Michelson interferometer-spectrometer are the following:

- a. The instrument is "single-ended," which means that half of the energy is returned to the source.
- b. The requirements of the system stability is far greater than for a conventional spectrometer, in order to avoid errors arising from misaligned mirror movement and inaccurate sampling procedure.
- c. The instrument is susceptible to intensity fluctuations, which can degrade the quality of the interferogram to such a degree that the multiplex advantage is nullified.
- d. Since the output (interferogram) has to be converted into a spectrum, an additional device such as a wave analyzer or a high-speed computer is necessary. Either device can introduce additional errors and "Fourier spectroscopy is as full of pitfalls on the mathematical side as on the experimental." (Reference 84)

Most of the disadvantages are being overcome in advanced models of laboratory interferometers. It is believed that it will take several years before these devices can be placed on satellites.

4.1.3.2 Advanced Development of Interferometers. All disadvantages discussed previously can be overcome by employing certain techniques. The modern development is based on the work by Fellgett, (Reference 85) Mertz, (Reference 86) R. Beer, (Reference 87) J. and P. Connes, (Reference 88) and many others. The results of their work is described briefly in the following paragraphs.

Greater system stability is achieved by using retroreflectors instead of plane mirror surfaces. These retroreflectors (either cube-corners or cat's-eyes) eliminate the sensitivity to tilts, but introduce a sensitivity to lateral displacement. This can be eliminated by double-passing the radiation. An additional advantage is gained, because the maximum retroreflector deflection is only one-fourth of the path difference required for a given resolution. However, the system is still single-ended like the "conventional" Michelson interferometer-spectrometer, thus losing 50 percent of the incident radiation. Nevertheless, the great advantage of the double-passed retroreflector interferometer is its inherent stability, thus making it more adaptable to severe environmental conditions, such as created by rocket launching for satellite operation. A laboratory prototype as described by Beer (Reference 87) is capable of a resolution of better than  $1 \text{ cm}^{-1}$  in the spectral interval from  $1.2$  to  $5 \mu$ .

In using double entrance and exit apertures, a single-passed retroreflecting cat's-eye interferometer utilizes both the usual interferogram as well as the complimentary one, thus doubling the sensitivity of the instrument. In this case, there are higher demands on the mechanical drive and the instrument is better adapted for observations

from the ground, or at best, from a balloon. The requirements are especially critical for the near IR region.

The other great difficulty of overcoming the effect of intensity fluctuations is being solved by applying the Mertz (Reference 86) "jitter modulation". This replaces the monitoring of the incoming radiation by another detector, which has been found to be impractical because of the strong nonuniformities of different detectors. Good results with the jitter modulation have been obtained by Connes (Reference 88) for the observation of planetary spectra from ground-based observatories.

A summary of the three basic designs of interferometers-spectrometers is given in Table 4-1.

#### 4.1.4 OPTICAL CORRELATION INSTRUMENT — MATCHED-FILTER TYPE

**4.1.4.1 Physical Principle.** Prior knowledge of the relative strengths and spectral locations of lines of particular species permits modification of the entrance and exit slits of a spectrometer to produce an instrument slit function which has a high degree of correlation with the spectral contribution from a particular gas, and a low degree of correlation with all other overlapping spectral structure. The previous approach has been to make a spectrographic plate of the emission lines of the species of interest (Reference 89, 90), to insert a negative of this plate in the focal plane of the spectrometer, and to focus the entire dispersed spectrum onto a single detector. Thus, if the radiation falling on the entrance slit of the spectrometer contains absorption/emission lines of the specie from which the spectrographic plate was obtained, a correlation function is obtained by scanning the spectrum over the plate. This function has large changes (indicated by a large signal change) when the lines of the plate are aligned with the lines in the radiation due to that specie. Oscillation of the spectrum about this point produces an a-c signal which can be related to the concentration of the particular gas.

In the infrared region where spectrographic plates cannot be made, the plate has been replaced by Convair with a series of slits etched in an opaque metal (the positions of the slits correspond to the positions of the lines of the particular gas). In effect, an instrument slit function which has a high cross-correlation with the particular species is produced. This mask is referred to as a matched-filter. While achieving a high degree of specificity, the throughput of the instrument is increased by using multiple exit slits. Another Convair development provides a further increase in "étendue" by using multiple entrance slits. This is possible because the line separation for most gases is a slowly varying function. Thus, a correlation spectrometer is an instrument with both high specificity and high "étendue"; it also has the advantage that the output is a "real time" measure of the species concentration as opposed to some instruments (e.g., interferometers which have transform outputs).



Table 4-1. Summary of Current Interferometer-Spectrometer Development

	Manufacturer	Platform	Status	Spectral Range $\mu$	Spectral Resolution $\text{cm}^{-1}$	Single or Double Ended	Plane Mirror or Retro- reflector	Continuous or Step Drive	"Jitter Modulation"
Conventional Michelson interferometer	Block FTS-12	Ground/ Balloon	Operational	0.8-3 2.5-16 1-4,5 4-40	40 40 40	Single	Plane Mirror	Step	No
	Block FTS-14	Laboratory	Operational	1-40	$\leq 1$	Single	Plane Mirror	Step	No
	Block FTS-16	Laboratory	Operational	25-3000	0.1 - 0.5	Single	Plane Mirror	Step	No
	IRIS(Goddard/ Texas Instr)	Satellite	Operational	5-18	5	Single	Plane Mirror	Continuous	No
	Goddard/Idea Lab.	Ground	Operational	8-12	0.6	Single	Plane Mirror	Continuous	No
	JPL	Balloon	Operational	10-125	0.4 - 0.8	Single	Plane Mirror	Continuous	No
Double-passed retroreflector interferometer	JPL (Connes, Beer)	Balloon Satellite	1970	1.25-5	$\leq 1 \text{ cm}^{-1}$	Single	Cat's eye	Step	No
Single-passed retroreflector interferometer	JPL (Connes, Beer)	Balloon	?	10-100	0.03	Double	Cat's eye	Step	Yes
	Connes	Ground	Operational	1.25-5	0.03	Double	Cat's eye	Step	Yes
	Imperial College, London	Balloon	Operational	12-40	0.25 ?	Double	Corner Cube	Step	No

**4.1.4.2 Theory and Optimization of the Matched-Filter Technique.** Extensive laboratory tests have demonstrated the validity and usefulness of coupling a matched filter with multiple entrance slits (see Figures 4-6 and 4-7). In order to apply this technique to field problems, one needs to optimize general design parameters. We have developed a theory for a multiple entrance and multiple exit slit instrument in sufficient generality to demonstrate how design parameters can be adjusted to obtain optimized results. From the same considerations, those situations where the "matched-filter" technique is advantageous become evident. This theory is described in the following.

The power accepted by a spectrometer with several entrance slits of equal dimensions is:

$$S = m \int_{\lambda_1}^{\lambda_2} E_{\lambda} A_o \Omega d\lambda, \quad (4-24)$$

where  $m$  is the number of entrance slits,  $E_{\lambda}$  is the source radiance,  $A_o$  the slit areas, and  $\Omega$  the solid angle of acceptance. The power transmitted by a single entrance and exit combination is

$$S_{ij} = A_o \Omega \int_{-\Delta\lambda_g}^{+\Delta\lambda_g} E_{\lambda} g_{ij}(\lambda, \lambda_o) d\lambda, \quad (4-25)$$

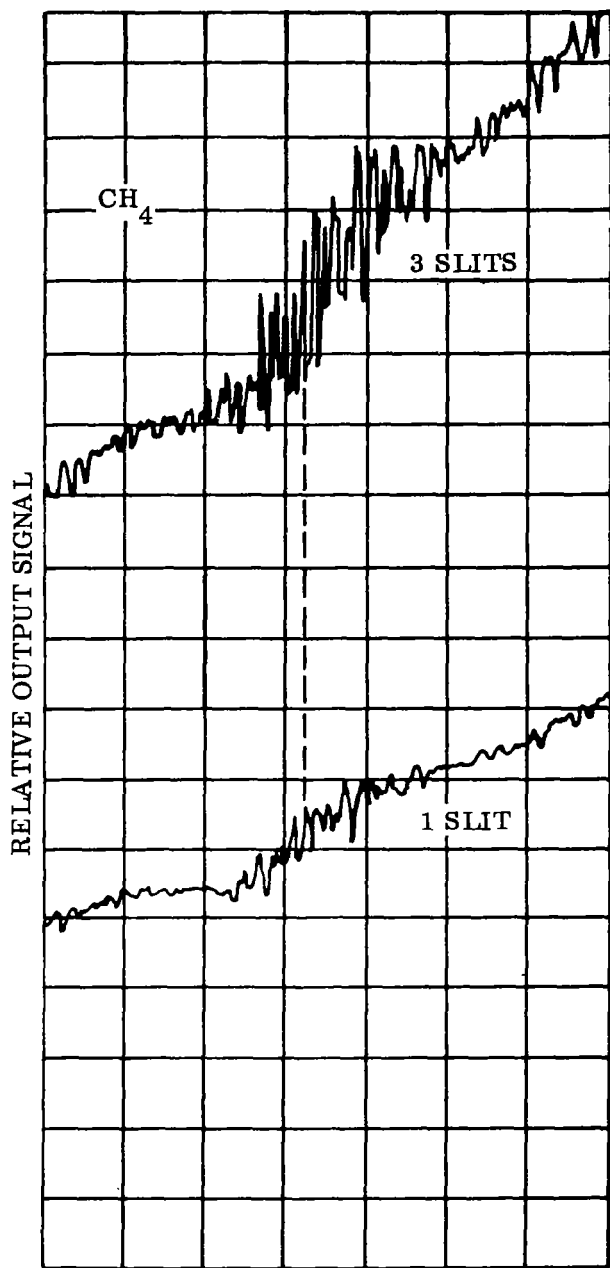
where  $g_{ij}(\lambda, \lambda_o)$  is the slit function and the indices  $i$  and  $j$  refer to the entrance and exit slits, respectively. For equal entrance and exit slit widths, the slit function is triangular, viz.

$$g_{ij} = g_o \left(1 - \left| \frac{\lambda - \lambda_{ij}}{\Delta\lambda_g} \right| \right), \quad |\lambda - \lambda_{ij}| \leq \Delta\lambda_g \quad (4-26)$$

where  $g_o$  is the maximum and  $\Delta\lambda_g$  is the slit function half-width.

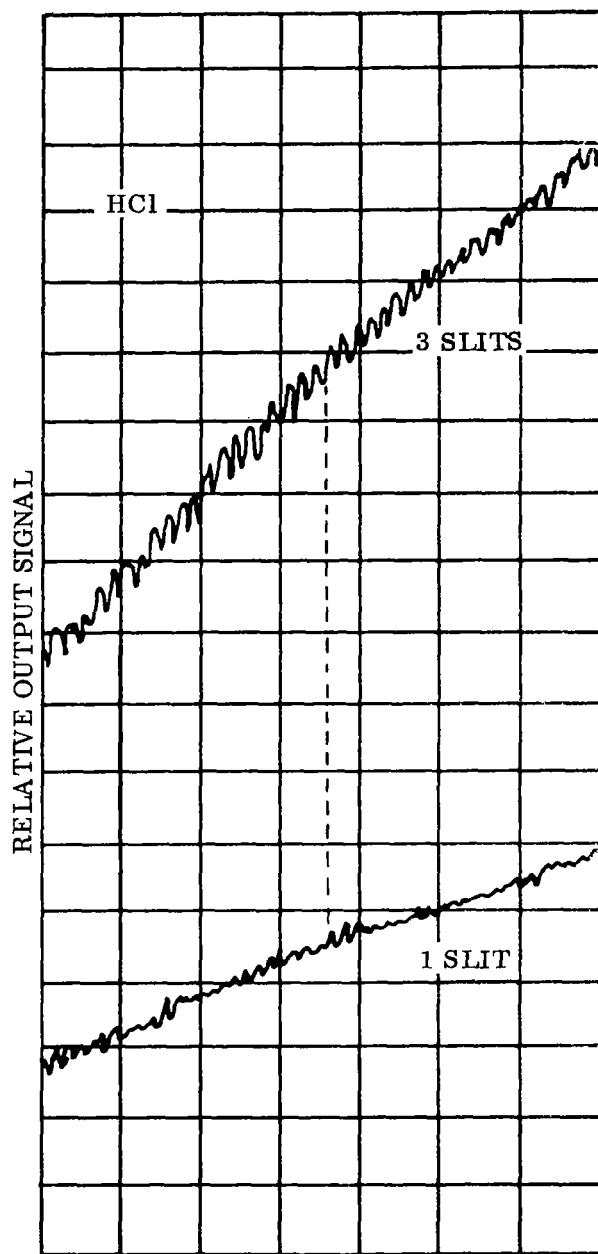
A spectrum composed of a slowly varying spectral term,  $E_o(\lambda)$ , and which also has sharp-line structure due to lines associated with the molecule of interest and overlapping lines from other species can be defined by:

$$E_{\lambda} = E_o(\lambda) + \sum_{k=1}^p E_k \delta(\lambda - \lambda_k) + \sum_{\ell=1}^q E_{\ell} \delta(\lambda - \lambda_{\ell}), \quad (4-27)$$



Mask Position Relative to Spectrum

Figure 4-6. Methane Correlation Signal Using Single and Multiple Entrance Slits



Mask Position Relative to Spectrum

Figure 4-7. Multiple Entrance Slit Effect on Discrimination

where the first summation is due to the background structure and the second summation is due to the species of interest and  $\delta$  signifies the delta function. The total power transmitted by the instrument is:

$$S = A_o \Omega \sum_{i,j}^{m,n} \left[ \int_0^\infty E_o(\lambda) g_{ij}(\lambda) d\lambda + \int_0^\infty \sum_{k=1}^p E_k \delta(\lambda - \lambda_k) g_{ij}(\lambda) d\lambda + \int_0^\infty \sum_{\ell=1}^q E_\ell \delta(\lambda - \lambda_\ell) g_{ij}(\lambda) d\lambda \right], \quad (4-28)$$

where  $m$  and  $n$  represent the total number of entrance and exit slits, respectively. Equation (4-28) can be reduced to:

$$S = A_o \Omega \sum_{i,j}^{m,n} \left\{ \int_0^\infty E_o(\lambda) g_{ij}(\lambda) d\lambda + \sum_{k=1}^p E_k g_{ij}(\lambda_k) + \sum_{\ell=1}^q E_\ell g_{ij}(\lambda_\ell) \right\}. \quad (4-29)$$

The refractor plate or exit mask oscillation effectively shifts the instrument slit function by some amplitude,  $\Delta\lambda$ , such that

$$g_{ij}'(\lambda_{ij}) = g_{ij}(\lambda_{ij} + \Delta\lambda). \quad (4-30)$$

Then the change in signal becomes:

$$\Delta S = A_o \Omega \sum_{i,j}^{m,n} \left\{ \int_0^\infty E_o(\lambda) [g_{ij}(\lambda) - g_{ij}'(\lambda)] d\lambda + \sum_{k=1}^p E_k [g_{ij}(\lambda_k) - g_{ij}'(\lambda_k)] + \sum_{\ell=1}^q E_\ell [g_{ij}(\lambda_\ell) - g_{ij}'(\lambda_\ell)] \right\} \quad (4-31)$$

From the first term of this relation we see that if  $E_o(\lambda)$  is not a constant there is a contribution to the signal change from any continuum background. Thus, the greater the slope of the continuum and the greater the spectral oscillation ( $\Delta\lambda$ ), the larger this term becomes. This limits the smallest measurable  $\Delta S$ .

The entrance and exit slits should be designed such that the signal obtained from the species of interest dominates; i.e.,  $g_{ij}$  and  $g'_{ij}$  are adjusted so that the change in signal:

$$\Delta S_{\alpha} = A_o \Omega \sum_{i,j,\ell}^{m,n,q} E_{\ell} [g_{ij}(\lambda_{\ell}) - g'_{ij}(\lambda_{\ell})] \quad (4-32)$$

dominates the change in background signal:

$$\Delta S_{\beta} = A_o \Omega \sum_{i,j,k}^{m,n,p} E_k [g_{ij}(\lambda_k) - g'_{ij}(\lambda_k)]. \quad (4-33)$$

There are three parameters to be considered in this optimization; the slit function centers ( $\lambda_{ij}$ ), the slit function half width ( $\Delta\lambda_g$ ), and the spectral oscillation amplitude ( $\Delta\lambda$ ).

Van Cittert (Reference 91) has shown that the product of the slit width measured in wavelength units and the angular divergence of the beam accepted by the spectrometer collimator should be approximately one. Increasing the slit width under these conditions reduces the instrument resolution without appreciably increasing the intensity of the line center. This criterion for the slit width may be compromised somewhat using the "matched filters" technique since discrimination then is based on both resolution and correlation.

For a single entrance slit (fixed  $i$ ) the slit function centers ( $\lambda_{ij}$ ) are dictated by line structure of the particular spectrum of interest. An autocorrelation of the spectrum of interest results in a series of peak and valleys. This is especially true when the line spacing is nearly uniform. The separation between these correlation peaks correspond to the spectral shifts required between entrance slit locations. This completely fixes the slit function centers. Thus, the spectral differences between the peaks and valleys of this correlation function are the required  $\Delta\lambda$  for the oscillation of the slit functions to produce the signal  $\Delta S_{\alpha}$ . (If  $\Delta\lambda$  varies, some compromise is necessary.) Thus,  $\Delta S_{\alpha}$  is optimized and all of the parameters ( $\Delta\lambda$ ,  $\Delta\lambda_g$ ,  $\lambda_{ij}$ ) have been fixed in so doing.

The background signal,  $\Delta S_{\beta}$  is now considered. Since both the entrance and exit slit combination, and the oscillation amplitude correspond to the auto-correlation peaks of the species of interest, as opposed to the background lines, the  $\Delta S_{\beta}$  is expected to be small. To further reduce  $\Delta S_{\beta}$ , a phase-lock detector system may be employed so that only signals with proper phase are amplified. If the background structure is known to some extent, cross-correlation data,  $\phi_{\alpha\beta}(\lambda)$ , could be used to ensure that the shifts in the entrance slits do not correspond to peaks in the cross correlation spectra.

The change in signal-to-noise ratio for a detector-noise-limited system may be written

$$\frac{\Delta S}{N} = \frac{A_o \Omega \sum_{i,j,\ell}^{m,n,q} E_{\ell} [g_{ij}(\lambda_{\ell}) - g_{ij}'(\lambda_{\ell})]}{(1/D^*) \sqrt{A_d \Delta f}} \quad (4-36)$$

The basic effect of employing multiple entrance and exit slits is to modify the areas,  $A_o$  and  $A_d$ . Assuming that the lines of interest are separated by more than  $2\Delta\lambda_g$ , that they are uniform in strength and spacing, and that the entrance and exit slits are equal in size, it is found from geometrical considerations that  $A_o$  is effectively increased by the factor  $F_1$ :

$$F_1 = 2(1 + 2 + 3 + \dots + n) - n$$

where the number of entrance slits equals the number of exit slits (i.e.  $m = n$ ), and that  $A_d (= A_o)$  is effectively increased by the factor

$$F_2 = (1 + a)n,$$

where  $a$  is the ratio of the opaque area to the open area of the mask ( $a \geq 1$ ). Thus, if the lines are separated by more than  $2\Delta\lambda_g$ , and are uniform in strength and spacing, Equation (4-36) may be rewritten to obtain

$$\begin{aligned} \frac{\Delta S}{N} &= \frac{D^* A_o \Omega E_{\ell} \left[ 2 \sum_{q=1}^n (q) - n \right]}{\sqrt{(1+a)n A_o \Delta f}} \\ &= \frac{D^* \Omega E_{\ell} \left[ 2 \left\lfloor \frac{n(n+1)}{2} \right\rfloor - n \right]}{\sqrt{(1+a)n \Delta f / A_o}} \end{aligned}$$

and finally

$$\frac{\Delta S}{N} = \frac{D^* \Omega E_{\ell} n^2}{\sqrt{(1+a)n \Delta f / A_o}} \quad (4-37)$$

For the best case possible,  $a = 1$ , we can see that there is a maximum gain over a single slit system of  $(n^3/2)^{1/2}$ . This demonstrates the expected gain for a highly idealized case. In actual practice the  $\Delta S/N$  gain achieved by using a multiple slit instrument depends on the varying strengths of  $E_\lambda$ , the uniformity of line spacing, and the line separation in terms of slit width.

4.1.4.3 Airborne Matched-Filter Instrument. From the preceding considerations, a general signal-to-noise equation can be written for a matched-filter instrument.

$$\frac{\Delta S}{N} = \left[ \frac{n^3 A_o}{(1+a) \Delta f} \right]^{1/2} \Omega D^* I \Delta \lambda (\Delta I/I), \quad (4-38)$$

where  $\Delta I/I$  is the modulation due to the spectral oscillation (the fractional change between clean and polluted atmospheres). In this form,  $A_o$ ,  $\Omega$ , and  $\Delta \lambda$  are values for a single slit combination. Replacing  $(1+a)$  by the ratio of the line spectral separation,  $\delta$ , to the spectral half width,  $\Delta \lambda$ , Equation 4-38 can be rewritten in terms of instrument parameters,  $f/no$  (instrument f-number),  $\eta$  (over-all instrument efficiency factor),  $M$  (magnification factor of the exit slit image onto the detector),  $\ell$  (slit length), and  $d$  (slit width), viz,

$$\frac{I}{\Delta I} \times \frac{\Delta S}{N} = \left[ \frac{n^3 d \ell \Delta \lambda^3}{\delta \Delta f} \right]^{1/2} \frac{\eta D^* I}{M (f/no)^2} \quad (4-39)$$

This equation assumes a square detector such that  $\Omega = 1/(f/no)^2$ .

The best compromise between resolution and transmission for a spectrometer has been shown to exist (Reference 91) when

$$d = \lambda (f/no) . \quad (4-40)$$

Technique currently used to construct masks limits  $d$  to be no smaller than 20 to 25  $\mu$ . Thus for  $\lambda = 5\mu$  (as for CO) the optimum  $f/no$  of the instrument should be 4 to 5, and since the signal-to-noise ratio of the instrument is inversely proportional to  $(f/no)^2$  an  $f/4$  instrument would be preferred.

Furthermore, it is apparent that  $\Delta S/N$  increases with  $\Delta \lambda$ . However, for  $\Delta \lambda > \delta/2$  the system deteriorates since the shift of the slit function would overlap an adjoining line in this case. Moreover, increasing  $\Delta \lambda$  reduces the specificity of the instrument. Thus, for a given source, it is necessary to compromise specificity and  $\Delta S/N$ , but, by correlating many lines, losses in specificity may be minimized.

From the linear dispersion relation we have

$$d = R(f/no)\Delta\lambda, \quad (4-41)$$

where R is the resolution of the grating. Due to practical considerations the selection of R is based upon available stock gratings.

All of the parameters necessary to design a matched-filter instrument are selected based upon a CO detection instrument. For CO in particular, a grating blazed at  $4\mu$  with  $R = 9600$  (150 lines/mm with an aperture of 65 mm) may be obtained. Since  $\delta$  for CO is about  $10^{-2}\mu$ , the value  $\Delta\lambda = 2 \times 10^{-3}\mu$  and  $d = 75\mu$  could be selected. These values, and realistic values for the remaining parameters specified by the  $\Delta S/N$  equation, are tabulated in Table 4-2.

Table 4-2. Parameters Specified For Matched-Filter  $\Delta S/N$  Calculation

Spectrometer f-number	$f/4$
Number of equally strong spectral lines	$n = 15$
Spectral wavelength of the band	$\lambda = 4.8\mu$
Spectral line separation	$\delta = 0.01\mu$
Slit function half width	$\Delta\lambda = 2 \times 10^{-3}\mu$
Slit width	$d = 75\mu$
Slit length	$\ell = 1 \text{ cm}$
Resolution of the instrument	$R = 9,600$
Instrument efficiency	$\eta = 2 \times 10^{-2}$
Detector specific detectivity (InSb)	$D^* = 10^{11} \text{ cm Hz}^{1/2} \text{ w}^{-1}$
Magnification of exit mask on to detector	$M = 10^{-1}$
Electronic band width	$\Delta f = 4.5 \text{ Hz}$
Clean atmosphere radiance ( $T_s = 300^\circ\text{K}$ )	$I = 1.5 \times 10^{-4} \text{ w-cm}^{-2}\text{-sr}^{-1}\text{-}\mu^{-1}$

Using the values listed in Table 4-2, a  $\Delta S/N$  of about 5 results for a one percent change in radiance between clean and polluted atmospheres. A schematic diagram of a possible instrument configuration using the matched-filter technique is shown in Figure 4-8.



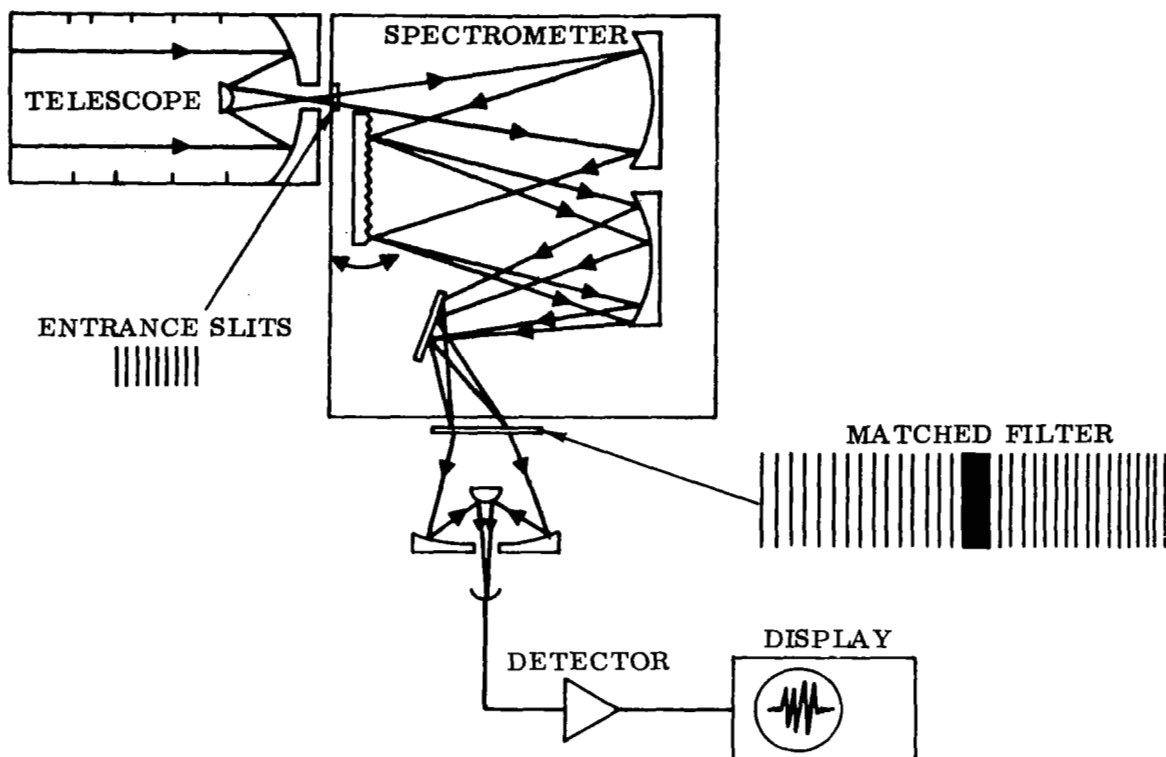


Figure 4-8. Matched-Filter Instrument Configuration

To illustrate the suitability of the matched-filter method for measuring carbon monoxide, Figure 4-9 shows a high resolution ( $0.5 \text{ cm}^{-1}$ ) atmospheric spectrum (Reference 92) in which carbon monoxide lines may be identified. Most of them do not overlap with normal atmospheric lines; those that do overlap would not be used in the matched filter. The lines which would be used are shaded in the figure.

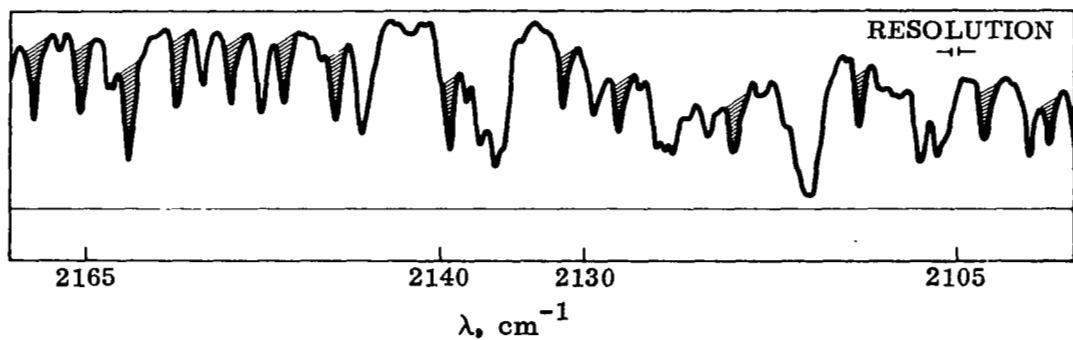


Figure 4-9. High Resolution Atmospheric Spectrum, Identifying Carbon Monoxide Lines Suitable for Matched-Filter Design

The design of a correlation instrument is such that it may be readily adapted to other pollutants of interest, such as SO<sub>2</sub>, and the final design of the system may include a built-in capability for detecting different pollutants.

#### 4.1.5 OPTICAL CORRELATION INSTRUMENT - SELECTIVE CHOPPER TYPE

4.1.5.1 Physical Principle. Two non-dispersive instruments for the remote detection of air pollutants are discussed in this section. Normally, this type of instrument uses a reference cell containing a particular pollutant gas, and the radiation is modulated only at wavelengths at which the pollutant gas absorbs. Depending upon the path length and pressure of the pollutant gas in the cell, the transmission, as a function of wavelength, through the reference cell may be adjusted to values between 0 and 1. More important, this type of system results in exceptionally high spectral resolution by instrument standards. That is, the pollutant gas in the reference cell will very closely match the spectral characteristics of the pollutant to be detected, differing only by the minor effects of their respective temperatures, optical depths, and collisional broadening species. In instrument terms, resolution of better than 0.1 cm<sup>-1</sup> may be expected; i.e., the effective spectral resolution is of the order of the width of spectral lines.

The two instruments described here differ primarily in their methods of modulation. In the first (selective-chopper, Reference 93), the incoming radiation is chopped by rotating a split cylindrical cell containing the reference gas in one-half and a vacuum in the other half. In the second (cross-correlating spectrometer, Reference 94), the incoming radiation is modulated by passing it through a cell containing the reference gas which is pressure-modulated by about 8 percent at 13.5 cps. In both of these techniques a cross-correlation is obtained between the spectral structure of the reference gas, and of the gas to be detected. Ideally, no cross-correlation is obtained between the spectrum of the reference gas and the spectrum of other species; i.e., background spectral structure is suppressed. Thus, using this technique, high specificity is attained for the remote detection of a particular pollutant.

Therefore, a selective chopper, the simplest instrument, possesses the following advantages:

- a. High spectral resolution and a corresponding high degree of specificity.
- b. Large étendue. In contrast to a conventional spectrometer or radiometer, the selective chopper is a multiplex type of instrument, and since it does not require a narrow entrance slit, large apertures may be employed. Both the multiplex operation and the use of relatively large circular apertures contribute to the high energy gathering efficiency.
- c. Small size and weight. Its simplicity leads to a compact instrument which would be substantially smaller and lighter than a conventional spectrometer.

- d. **Mechanical stability.** Both spectrometers and interferometers require a high degree of mechanical stability for proper operation, particularly with respect to spectral calibration. In contrast, a selective chopper may only require a rotating cell and band-pass filters for spectral selection.

In the following, a potential satellite-borne instrument using the selective chopping technique, is considered. Peckham et al (Reference 95) have developed a selective chopper radiometer, based upon the results of Reference 93, for remote sensing of the atmospheric temperature. A prototype instrument was tested via balloon flights, and a refined instrument was on-board the ill-fated NIMBUS D satellite. The same technique may be applied to monitoring specific gaseous pollutants in the atmosphere.

A split cylindrical cell containing a specific pollutant in one half and a vacuum in the other half is used as a chopper. The self emission from the chopper may be eliminated by chopping the radiation received between earth and space as is done on the Tiros radiometer (Reference 96). This system is shown schematically in Figure 4-10. The effective signal received by the detector for this system may be expressed by

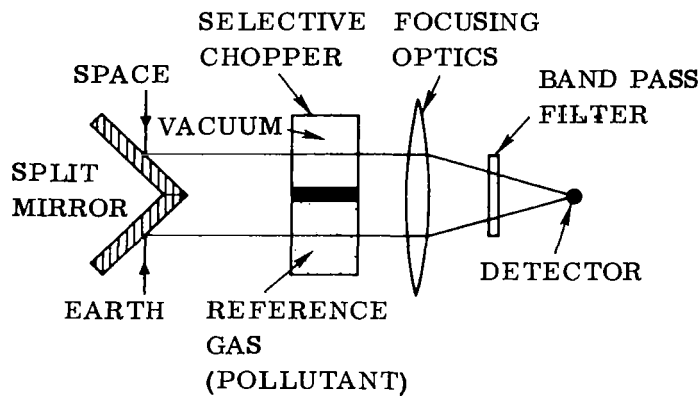


Figure 4-10. Schematic of a Satellite-Borne Selective Chopper For Air Pollution Measurements

$$S \propto N_{\text{earth}} (1 - \tau_{\text{sc}}) \quad (4-42)$$

where  $N_{\text{earth}}$  is the radiance from the earth modified by the absorption and emission of the earth's atmosphere, and  $\tau_{\text{sc}}$  is the transmission, through the reference pollutant, in the selective chopper.  $N_{\text{earth}}$  is equivalent to  $E_{\lambda}(h, T_0)$ , c.f. Equation (3-11).

Equation (4-42) may be verified by noting that during the first half cycle of the chopper, the signal received,

$$S_1 \propto N_{\text{chopper}} + N_{\text{earth}} \tau_{\text{sc}} + N_{\text{space}} \quad (4-43)$$

and during the second half cycle the signal received,

$$S_2 \propto N_{\text{chopper}} + N_{\text{earth}} + N_{\text{space}} \tau_{\text{sc}}. \quad (4-44)$$

Since  $N_{\text{space}}$  is small compared to  $N_{\text{earth}}$ , the modulated signal expressed by Equation (4-42) results.

In the following, a simplified analysis is made of the sensitivity of a selective chopper to the change in radiance between clean and polluted atmospheres. If the earth's surface is "hot" relative to a polluted atmosphere, the radiance received by the instrument will effectively be attenuated by the clean and polluted atmospheric transmission functions  $\tau_c$  and  $\tau_p$ , respectively. In this case, the signal,

$$S_p \propto N_{\text{surf}} \tau_c \tau_p (1 - \tau_{\text{sc}}). \quad (4-45)$$

That is, to a first approximation it is assumed that the first term of Equation (3-11) is much larger than the second term and that  $N_{\text{surf}} = \epsilon_{\lambda} N_{\lambda}^0(T_{\odot})$ . Thus, the change in signal between clean and polluted atmospheres (Equation (4-42) minus Equation (4-45)) is

$$\Delta S = S_c - S_p \propto N_{\text{surf}} \tau_c (1 - \tau_p)(1 - \tau_{\text{sc}}) \quad (4-46)$$

Likewise, it can be readily seen that if the earth's surface is "cool" relative to the atmospheric pollution,

$$\Delta S \propto N_{\text{atm}} (1 - \tau_c) \tau_p (1 - \tau_{\text{sc}}) \quad (4-47)$$

where the second term of Equation (3-11) has been represented by  $N_{\text{atm}}(1 - \tau_c)(1 - \tau_p)$ .

It is clear from Equations (4-46) and (4-47), therefore, that maximum sensitivity is achieved if  $\tau_{\text{sc}} = 0$ . However, the cross-correlation function for this system is defined by

$$\phi_{\tau_p \tau_{\text{sc}}}(\lambda) = \Delta\lambda \lim_{\Delta\lambda \rightarrow \infty} \frac{1}{2\Delta\lambda} \int_{-\Delta\lambda}^{+\Delta\lambda} \tau_p(\lambda) \tau_{\text{sc}}(\lambda) d\lambda. \quad (4-48)$$

Since it is also desirable to maximize this function, maximum correlation is obtained for both  $\tau_p$  and  $\tau_{\text{sc}} = 1$ . Goody (Reference 94) attempted to analyze these conflicting requirements and concluded that optimization would probably be obtained if  $0 < \tau_p = \tau_{\text{sc}} < 1$ .

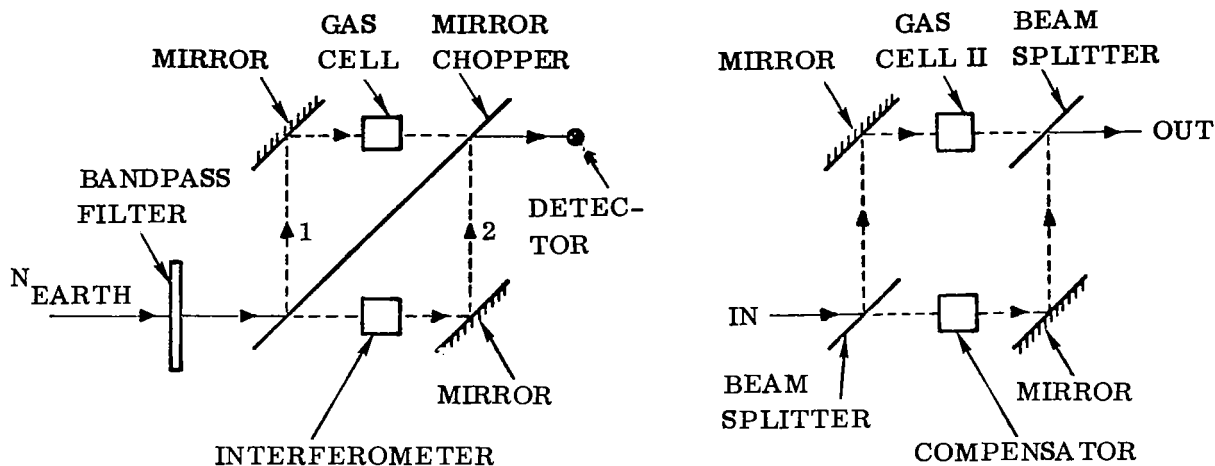
The signal-to-noise ratio for this system may be related to a conventional radiometer in terms of the parameters,  $D_o$ ,  $\ell$ ,  $\theta$ ,  $f/\text{no}$ , etc. The major difference arises in considering the spectral bandwidth,  $\Delta\lambda$ . In the case of the selective chopper, the effective spectral bandwidth becomes the sum of the halfwidths of the spectral lines of the pollutant over the entire band pass used. Normally, an interference filter (see Figure 4-10) would be employed to limit the total spectral band pass to only the spectral region where the pollutant has relatively strong absorption.

For example, the CO fundamental band has 60 primary absorption lines with a half-width of about  $1.5 \times 10^{-4}$  microns (Reference 97) each between  $\lambda \approx 4.461$  and  $4.967$  microns (Reference 98). Thus, if this region were used, the effective  $\Delta\lambda$  for the S/N calculation would be about 0.009 micron. Thus, the S/N is about an order of magnitude lower than the S/N for a conventional radiometer with  $\Delta\lambda = 0.1$  micron.

However, the selective chopper would have a high specificity whereas the conventional radiometer would have little or none. Also, of course, the selective chopper, being a high-spectral-resolution instrument, will operate using much larger values for the pollutant's absorption coefficient, and, hence, larger changes in radiance with and without pollution present,  $\Delta E$ , will occur than for a radiometer with 0.1 micron resolution. It has been estimated that this change in  $\Delta E$  will be about one order of magnitude higher using high resolution values for the absorption coefficient. Therefore, the S/N for a selective chopper of this type will typically be as great as those indicated for a conventional radiometer.

There is one major drawback to the selective chopper type of instrument. Namely, since the line halfwidth-to-line spacing may be quite small (0.016 for CO), a d.c. level of uncorrelated signal will be present. This is 60 ( $=1/0.016$ ) times larger than that of a masked filter type of optical correlation instrument. This drawback limited the accuracy to which Goody (Reference 94) was able to measure the atmospheric content of nitrous oxide. To measure  $\sim 0.3$  atm-cm of  $N_2O$  required electronic processing of modulations  $10^{-5}$  times that of the carrier signal.

One possible way to overcome this problem has been proposed by Goody (Reference 94). This hypothetical instrument is shown in Figure 4-11(a). The incoming radiant energy is confined to the spectral region of interest for a particular pollutant by the band-pass filter. The mirror chopper alternately divides this radiant energy into paths 1 and 2. In path 1, a gas cell, containing a particular pollutant gas, absorbs energy at wavelengths where the pollutant gas has absorption lines. Conversely in path 2, an interferometer is placed, and passes only the energy at the center of the absorption lines. The two paths may be balanced when none of the wanted gas is in the path of  $N_{\text{earth}}$  so that no signal is received. Then when a pollutant gas exists in the path, a correlation signal will be obtained due to the energy modulated only at the absorption lines of the pollutant.



(a) Possible non-dispersive instrument

(b) Detail of interferometer (after Reference 94)

Figure 4-11. Michelson's Theoretical Interferometer

The detail of the interferometer which passes only the radiant energy at absorption lines is shown in Figure 4-11(b). The net effect of this system is effectively the reverse of the selective chopper previously described. Further details of this proposed instrument may be found in Reference 94. Although this instrument appears to be theoretically an ideal instrument for the detection of specific pollutants, considerable laboratory work would be required to verify its performance, and even more work would be necessary before it could be developed into a flight instrument.

**4.1.5.2 Airborne Selective Chopping Instrument.** A general signal-to-noise equation may be written for a selective chopping instrument, viz,

$$\frac{I}{\Delta I} \frac{\Delta S}{N} = \frac{\eta D^* (n \Delta \lambda_\ell) I}{\sqrt{\Delta f / A_d (f/no)^2}} \quad (4-49)$$

This equation differs from that for a conventional radiometer in that the spectral band pass is equal to the number ( $n$ ) of spectral lines being utilized times the effective half-width of a line ( $\Delta \lambda_\ell$ ). Typical values selected for the parameters given by Equation (4-49) are listed in Table 4-3.

The values listed in Table 4-3 may be compared with those used for a matched-filter instrument (Table 4-2). For the selective chopper, which is a much simpler instrument, it is feasible to reduce the  $f$ -number from 4 to 1; also the instrument efficiency is increased from 0.02 to 0.05. Using the values listed in Table 4-3,  $\Delta S/N$  of about 2 is obtained from a one percent change in radiance between clean and polluted atmospheres.

Table 4-3. Parameters Specified for Selective Chopper  $\Delta S/N$  Calculation

Instrument f-number	$f/1$
Number of spectral lines	$n = 15$
Spectral half width of a line	$\Delta\lambda_\ell = 1.5 \times 10^{-4} \mu$
Detector area	$A_d = 6.25 \times 10^{-2} \text{ cm}^2$
Instrument efficiency	$\eta = 5 \times 10^{-2}$
Detector specific detectivity (InSb)	$D^* = 10^{11} \text{ cm-Hz}^{1/2}\text{-W}^{-1}$
Electronic band width	$\Delta f = 4.5 \text{ Hz}$
Clean atmosphere radiance ( $T_g = 300^\circ\text{K}$ )	$I = 1.5 \times 10^{-4} \text{ W-cm}^{-2}\text{-sr}^{-1}\text{-}\mu\text{m}^{-1}$

Of course, the selective chopper, being a high-spectral-resolution instrument, will operate using effectively larger values for the pollutant's absorption coefficient, and therefore larger changes in  $\Delta I/I$  will occur than for the lower-resolution matched-filter instrument.

#### 4.1.6 OPTICAL CORRELATION INSTRUMENT - FIBER-OPTICS FILTER TYPE

**4.1.6.1 Physical Principle.** The problem of remote sensing of small concentrations of gas spectroscopically ultimately reduces to the problem of obtaining a measurable signal related to the gas species of interest while rejecting signals from other gas species with overlapping spectra. Fiber-optics filtering (Reference 99) is based on prior knowledge of the shapes of both the background and source spectra. In the realm of conditions for which these spectral shapes remain unchanged, an instrument can be designed whose signal is related only to the spectrum of the gas of interest. This technique makes use of optical fibers in such a manner as to produce either a positive or a negative instrument transmission at a particular wavelength interval. The transmission as a function of wavelength is then adjusted, such that the product of the transmission with the background radiance is zero, while the product with the radiance related to the particular specie is maximized. The fact that the signal is related only to the species of interest is made possible by achieving a negative transmission.

Figure 4-12 is a schematic of a "fiber-optics filter" instrument. A spectrometer is used to obtain a spectrum of the radiation transmitted through the entrance slit. This spectrum, which includes structure associated with the particular gas of interest and structure associated with other molecules, is incident on the ends of the fiber optics arranged in columns as shown in the cross-section detail. Each column of the fibers is collected into a single bundle of fibers. Attenuation of the light being transmitted by a single bundle is effected by interrupting some fraction of the bundle with an

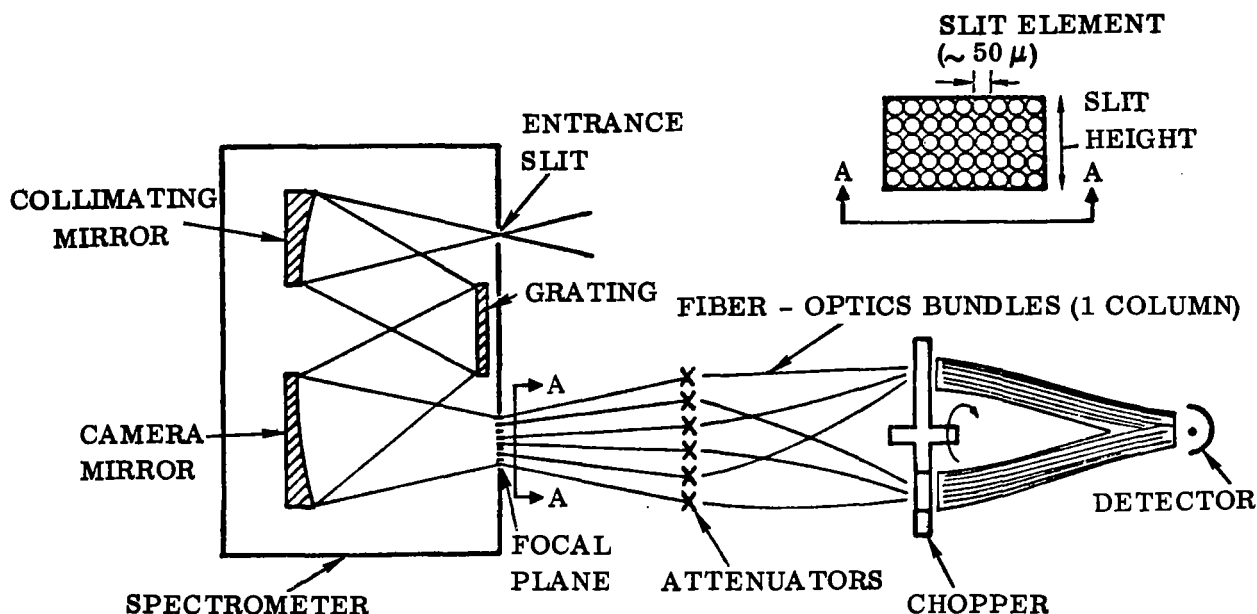


Figure 4-12. Schematic of Fiber-Optics Filter with Variable Transmission Resolution Elements

opaque object. The transmission can be reduced to zero by completely blocking a bundle. Following the attenuators the fiber bundles are collected into two groups. The light associated with the two groups of fiber bundles is chopped with 180° phase difference.

The resulting signal, capacitively coupled to eliminate the d.c. portion, is proportional to the difference between the two optical signals. A single detector is employed to eliminate relative drifts associated with systems using multiple detectors. The device thus acts like a variable-transmission filter (with spectral resolution elements corresponding to the fiber diameter) whose transmission can be varied from approximately +1 to -1.

This unique feature (transmission values adjustable between +1 and -1), makes it possible to design an instrument such that the signal is due almost entirely to the particular species of interest if the ratio of the source to background is known for each channel. A simple example for illustrative purposes is given here (Figure 4-13). A source  $I_S(\lambda)$  is postulated with an intensity 0.5 at A and 1.0 at B. The background  $I_{BG}(\lambda)$  consists of a number of spectral lines, two of which overlap  $I_S$  at A and B, but with intensities 1.0 and 0.5, respectively. A filter transmission function  $t(\lambda)$  is defined with a transmission of -0.5 at A and 1.0 at B and zero elsewhere. The integrated intensity  $I$  due to the source is then



$$I = \int_0^8 I_S(\lambda) t(\lambda) d\lambda = 0.5(-0.5) + 1.0(1.0) = 0.75$$

and due to the background is

$$I = \int_0^8 I_{BG}(\lambda) t(\lambda) d\lambda = 1.0(-0.5) + 0.5(1.0) = 0$$

This demonstrates the ability of fiber-optics filtering to suppress any linear combination of known background.

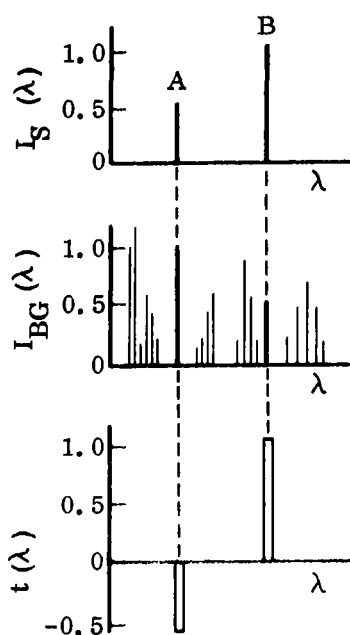


Figure 4-13. Postulated Source, Background and Transmission Functions

The spectral range of the device is, of course, limited by the transmission characteristics of the fiber optics. Glass fibers are suitable for the 0.4 to 2.0 $\mu$  region; arsenic trisulfide fibers are available for the 1 to 10 $\mu$  region. In the current development effort, plastic fibers with transmission in the 0.4 to 1.1 $\mu$  region were selected because of relative ease in the fabrication of ribbons.

A prototype instrument has been built to demonstrate the feasibility of this technique. A small Farrand monochromator with a dispersion of 110 Å/mm was employed. The exit slit was replaced with a stack of 20 ribbons composed of 75 $\mu$  diameter polyester fibers. The ribbons were made by pressing a strip of adhesive tape (25 $\mu$  thick) onto a single-filament array of fibers. With this arrangement, a spectral resolution of 11Å was theoretically possible. Actual resolution was on the order of 20 Å, being degraded somewhat by ribbon misalignment. Attenuation was provided by a simple arrangement of screws which could be interposed in a gap between the fiber bundles. A chopper wheel provided a square-wave modulation of approximately 600 Hz. Fiber optics were employed to recombine

the two beams after modulation. A photomultiplier was employed for detection. Figure 4-14 is a reproduction of an oscilloscope trace showing the signal from source only, background only, and source plus background, using a small mercury lamp as a source and tungsten lamp as a background. The intensity of the tungsten source, integrated over the spectral band corresponding to the 20 resolution elements, was about four times that of the mercury source. After filtering, the signal due to the tungsten is seen to be a d.c. level, while that of the mercury source is modulated at the chopping frequency.

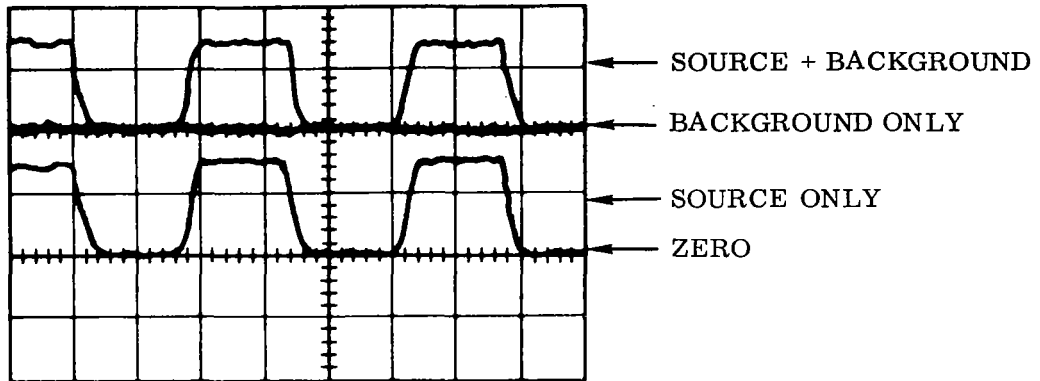


Figure 4-14. Oscilloscope Trace Illustrating Background Suppression

The following section discusses the theoretical development of an optimum filtering system.

4.1.6.2 Theory. The problem of finding the optimum filter for a given source function,  $S(\lambda)$ , and background function,  $B(\lambda)$ , can be reduced to a simple trial-and-error procedure by means of proofs which limit the possible choices for the optimum filter to a narrow class. For a discrete channel situation, source and background functions are defined by  $N$  values each:  $S_i$  and  $B_i$ , where  $i$  runs from 1 to  $N$ . The optimum filter  $T_i$  satisfies the conditions:

$$(1) \quad \left| \sum_{i=1}^N T_i S_i \right| = |S| = \text{maximum} \quad (4-50)$$

$$(2) \quad \sum_{i=1}^N T_i B_i = 0 \quad (4-51)$$

$$(3) \quad |T_i| \leq 1 \quad (4-52)$$

It can be easily shown that in the optimum filter, at most, one of the  $T_i$  may be less than 1 in absolute value. The argument, simply stated, is that if the optimum filter is assumed to have two  $|T_i| < 1$ , then it can be shown that the filter was not optimum after all: If two  $|T_i| < 1$ , then both are subject to arbitrary variations which will maintain condition (3) if the variations are all small enough; and will maintain condition (2) if the  $|T_i|$ 's are inversely proportional to the corresponding  $B_i$ 's; and yet will improve the maximum in (1).

Then the problem of finding the optimum filter reduces to finding which one of the  $N$   $T_i$ 's is less than unity in absolute value, and which of the remaining  $(N-1)$  are +1 (the

rest being - 1). The single  $T_i$  which is not either - 1 or + 1 must be found by trial-and-error (N trials), but the disposition of + 1's and - 1's among the remaining (N-1)  $T_i$ 's can be determined. Suppose that the  $j$ th  $T_i$  is less than 1 in absolute value,  $|T_j| < 1$ . Then the signs of the other  $T_i$  are the same as the signs of the quantities  $B_i S_j - B_j S_i$ . That is, if  $B_i/S_i > B_j/S_j$ , the  $T_i = + 1$ , and if  $B_i/S_i < B_j/S_j$ ,  $T_i = - 1$ . The proof of this, although somewhat lengthy, is simple in concept. It can be shown that if a filter which is supposed to be optimum does not have the same signs as  $B_i S_j - B_j S_i$ , then another filter,  $U_i$ , with the following properties can be constructed:  $\sum U_i S_i = \sum U_i B_i = 0$ , and the sign of  $U_i$  is the same as the sign of  $T_i$  (for  $i \neq j$ ). Now a new filter  $T_i' = T_i + \epsilon U_i$  can be formed. If  $\epsilon$ , a positive number, is small enough,  $|T_i'| < 1$ . But, because of the properties of  $U_i$ ,  $\sum T_i' S_i = \sum T_i S_i = |S|$ , and  $\sum T_i' B_i = 0$ . Finally, another new filter can be constructed such that  $T_i'' = T_i'/M$ , where  $M$  is the largest of the  $|T_i'|$  values. Now  $T_i''$  satisfies (2) and (3), but gives an improved maximum in (1). Then the optimum filter must have signs the same as  $B_i S_j - B_j S_i$ .

The process of finding the optimum filter would be as follows: Arrange the channels so that  $B_1/S_1 > B_2/S_2 - - - > B_N/S_N$ . Generate N filters by setting  $T_i = + 1$  for  $i < j$ ,  $T_i = - 1$  for  $i > j$  and calculate  $T_j$  from (2), for  $j = 1$  to  $N$ . The filter giving the largest  $|S|$  in (1) which does not conflict with (3), is the optimum.

**4.1.6.3 Concluding Remarks on Fiber-Optics Filtering.** So long as the shape of the background spectrum and the shape of the source spectrum remain the same, the signal output of the "fiber-optics filter" will be proportional to only the source. This can be seen by replacing  $S_i$  by  $C_S S_i$  and  $B_i$  by  $C_B B_i$  so that the conditions given by Equations (4-50) and (4-51) become respectively

$$C_S \sum_i S_i T_i = C_S S = S' \quad (4-53)$$

and (4-54)

$$C_B \sum_i B_i T_i = 0$$

Consideration is currently being given to the possibility of using the "fiber-optics technique" in conjunction with correlation techniques. In the ordinary correlation techniques, the transmission of the mask is limited to values between 0 and + 1. Two approaches are evident.

Using the fiber columns as slits, an instrument slit function correlating strongly with the spectrum of the species of interest can be produced. But now, one can vary the slit transmission between limiting values of + 1. By using a refractor plate to oscillate the spectrum over the fiber columns a modulated signal can be produced. The requirement now may be stated as:

$$\sum T_i (B_i' - B_i) = 0 \quad (4-55)$$

and

$$\Delta S = S' - S = \sum T_i (S_i' - S_i), \quad (4-56)$$

where  $B_i'$  and  $B_i$ , and  $S'$  and  $S$  have the same functional form, but are shifted with respect to each other, and  $\Delta S$  is to be maximized. This approach has the advantage over the usual correlation technique of being able to reduce the noise (apparent signal) caused by the background radiation. For example, if the composite spectrum of the gas of interest and the background structure are superimposed on a continuum background with a large slope, normal correlation techniques will produce a signal modulation which is related to the continuum. Fiber-optics correlation could be used to eliminate this type of noise. Other techniques are available for reducing this type of noise, but they may be more cumbersome. Their apparent disadvantage is that the modulated signal may be reduced from that attainable by the matched filter technique alone.

Another approach is to produce the correlation modulation by shifting between two independent sets of fibers. The problem now becomes

$$\sum_i B_i T_i = 0, \quad \sum_j B_j T_j = 0 \quad (4-57)$$

and

$$i \neq j$$

$$\sum_i S_i T_i = S, \quad \sum_j S_j T_j = S' \quad (4-58)$$

where  $\Delta S \equiv S' - S$  is to be a maximum. The necessary switching in channels could be carried out by mechanical switching of the attenuators.

#### 4.1.7 LASER PROBING OF POLLUTION

**4.1.7.1 Physical Principle.** In order to detect a pollutant with a laser probe, it is desirable that the laser wavelength coincide with an absorption line of the pollutant to be determined, and preferably not be absorbed by the clean atmosphere. The choice of such wavelengths is not simple, due to the fact that laser radiation is monochromatic and appears at specific wavelengths which cannot readily be changed. In addition, measured absorption spectra of the gases to be investigated are not always of high enough resolution to determine exact coincidence of the laser wavelength and an absorption line.

Laser probing techniques for satellite use could include a ground-based laser pointing at the satellite through the polluted atmosphere, or a satellite-carried laser pointing

down at the earth. The latter method is probably preferred to obtain most coverage of the earth. The laser radiation would be directed down, through the atmosphere and the polluted lower levels, to the earth's surface where it would be scattered. The backscattered radiation would again traverse the polluted and clean layers of the atmosphere and be detected on board the satellite.

Even assuming that the laser radiation is significantly absorbed by a particular pollutant, the interpretation of the backscattered signal will not be simple for the following reasons:

- a. The reflectivity of the earth's surface varies spectrally, spatially, and in its directional properties.
- b. Rayleigh scattering in the atmosphere may be closely allowed for, but aerosol and particle Mie scattering will be very difficult to determine.
- c. The laser beam will be considerably degraded by atmospheric turbulence effects.
- d. The radiance of the laser beam is inherently non-uniform over its cross section.

It may be possible to scan (by tuning) the laser wavelength across the absorption line, and use differencing to eliminate the above effects. It should be permissible to assume that over a small spectral range these effects do not change, whereas the pollutant absorption changes rapidly with wavelength over its absorption line.

The approximate power requirements for a satellite laser probing system may be estimated by considering Figure 4-15.

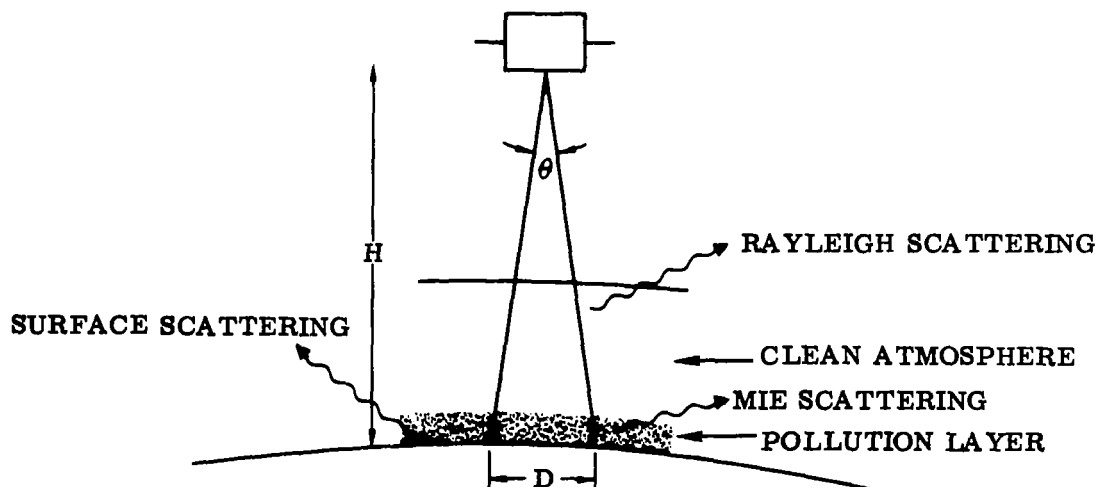


Figure 4-15. Laser Probe Schematic

If we neglect atmospheric attenuation and assume that the laser beam is of uniform intensity, then the irradiance  $I$  at the earth's surface is given by

$$I = \frac{P}{\pi \left(\frac{D}{2}\right)^2} \text{ w m}^{-2}, \quad (4-59)$$

where  $P$  is the laser output power and  $D$  is the beam diameter at the surface.

If the earth's surface is a perfect diffuse reflector, with reflectivity  $R$ , then the reflected power  $J$  is given by

$$J = \frac{IR}{\pi} = \frac{PR}{\pi \left(\frac{D}{2}\right)^2} \text{ w m}^{-2} \text{ sr}.$$

If the satellite detector, at height  $H$  above the earth, has a field-of-view matching the laser beam divergence and collecting optics area  $a$ , the available signal  $S$  (neglecting losses in the optical system) is given by

$$\begin{aligned} S &= \frac{Ja}{H^2} \cdot \pi \left(\frac{D}{2}\right)^2 \\ &= \frac{PRa}{\pi H^2} \text{ watts} . \end{aligned}$$

Now, if the atmospheric transmission due to scattering processes is  $\tau$  for the double atmospheric path,

$$S = \frac{PRa\tau}{\pi H^2} \text{ watts} \quad (4-60)$$

The following may be considered reasonable values for the parameters in Equation (4-60).

$$R = 0.15$$

$$a = 1 \text{ m}^2$$

$$H = 250 \text{ km}$$

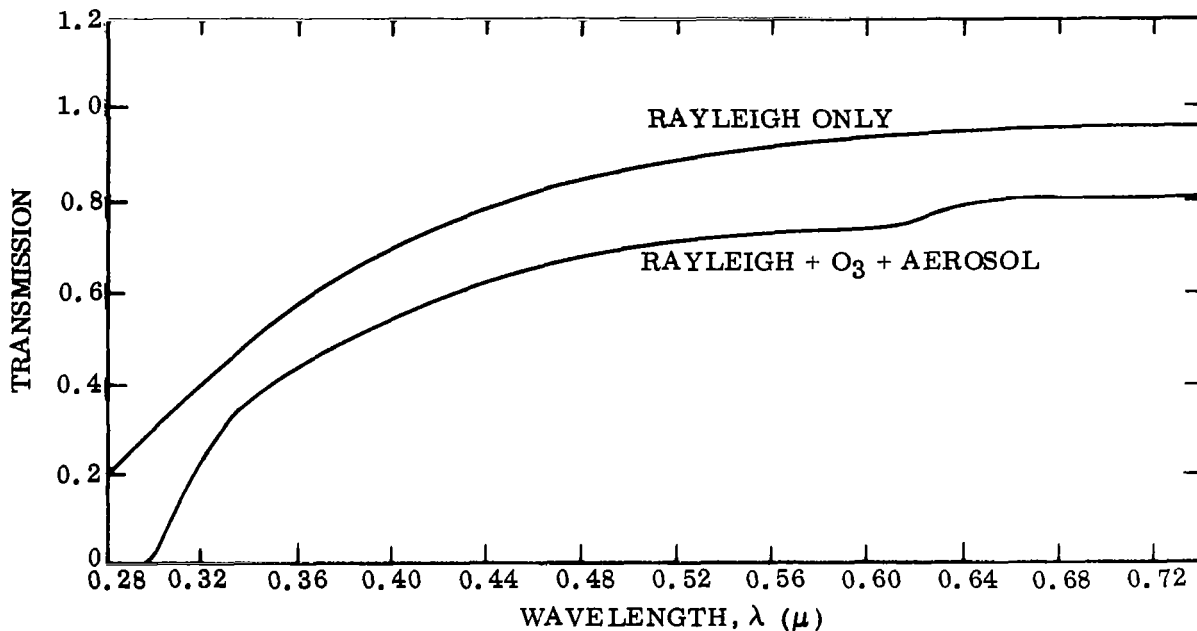


Figure 4-16. Single Pass Transmission Through Clean Atmosphere (Surface to Satellite) vs. Wavelength

$\tau$  depends on wavelength and on the aerosol content, but a value of 0.5 is representative of the visible region, as seen in Figure 4-16.

Thus  $S \approx 4 \times 10^{-13}$  P watts

This return signal must be considered in relation to the earth-atmosphere background. In the visible region, for  $R = 0.15$ , typical daytime background radiances are  $50\text{--}100 \text{ w m}^{-2} \mu^{-1} \text{sr}^{-1}$ , so that with a field of view of  $10^{-6} \text{ sr}$ , and a  $5 \text{ \AA}$  band pass, the background signal is  $2.5 \times 10^{-8}$  to  $5 \times 10^{-8}$  watts. Thus if P is 1.0 Mw,  $S = 4 \times 10^{-7}$  watts, and the signal to background in the visible region varies approximately between 8:1 and 15:1. This ratio might be improved by larger pulse power, smaller field-of-view or narrower spectral band pass. Of course, at night the background is probably negligible.

In the  $10\mu$  region, the earth-atmosphere background will not vary greatly between night and day, since it is due to thermal emission. A typical background radiance at  $10\mu$  is  $10 \text{ w m}^{-2} \mu^{-1} \text{ sr}^{-1}$ , so that with a field-of-view of  $10^{-6} \text{ sr}$ , and a  $0.1\mu$  band pass the background signal is  $10^{-6}$  watts. Assuming a signal return of  $4 \times 10^{-7}$  watts, the signal-to-background is less than one. If the field-of-view is reduced to  $10^{-7} \text{ sr}$ , and a filter of  $0.04\mu$  band pass, which is currently commercially available, is used, the signal-to-background is increased to 10:1.

The signal return depends on the product of the laser pulse power (P), the atmospheric transmission ( $\tau$ ), and the surface reflectivity (R). In the  $10\mu$  region,  $\tau$  is about 0.25 in the  $\text{O}_3$  bands and about 0.9 in the window region, assuming the laser can be tuned away from the atmospheric  $\text{CO}_2$  lines. Surface emissivities in this region are about 0.99, giving a surface reflectivity of about 0.01. Thus, to obtain the assumed signal return of  $4 \times 10^{-7}$  watts, pulses of 30 Mw in the  $\text{O}_3$  band, and about 8 Mw in the window region, are required. These powers are probably not attainable with the present state-of-the-art, particularly in the single-mode and tuned operation desired for this measurement.

**4.1.7.2 Accuracy Considerations.** Assuming that it is possible to design a system satisfying the requirements outlined above, where the background is negligible compared with the signal, the accuracy requirements of the system may be considered.

The return signal  $S_1$  at wavelength  $\lambda_1$  in the pollutant absorption band is given by

$$S_1 = B_1 + I_1 R_1 e^{-2(\alpha + \beta_1 + \gamma_1)} \quad (4-61)$$

where, at  $\lambda_1$ ,  $B_1$  is the background signal

$I_1$  is the laser output

$R_1$  is the surface reflectivity

$\alpha$  is the pollutant optical thickness

$\beta_1$  is the Rayleigh scattering optical thickness

$\gamma_1$  is the aerosol scattering and absorption optical thickness

At  $\lambda_2$ , which is outside the pollutant absorption band,

$$S_2 = B_2 + I_2 R_2 e^{-2(\beta_2 + \gamma_2)}$$



$B_1$  and  $B_2$  may be assumed to be negligible; if not, they must be measured, and  $R_1 = R_2$ ;  $\gamma_1 = \gamma_2$ .

Thus

$$\frac{S_1}{S_2} = \frac{I_1}{I_2} \frac{e^{-2(\alpha + \beta_1)}}{e^{-2\beta_2}} \quad (4-62)$$

$I_1$  is monitored at the laser source

$\beta_1$  and  $\beta_2$  may be calculated.

Thus  $\alpha$ , the optical thickness of the pollutant, may be determined.

If  $S_1, S_2, I_1$ , and  $I_2$  can each be measured with  $\pm 0.5$  percent error, and the errors in  $\beta_1$  and  $\beta_2$  are assumed negligible, a  $\pm 2$  percent error exists in  $e^{-2\alpha}$ , which leads to large errors in  $\alpha$ , since the optical thickness is generally very small. For example, if  $2\alpha = 0.1$ , which is close to the maximum value that might be reasonably expected under real conditions, then  $\pm 2$  percent error in  $e^{-2\alpha}$  gives  $\pm 20$  percent error in  $\alpha$ .

These measurement errors are optimistic and will not be readily reduced to improve the accuracy of determining the pollutant optical thickness. Some improvement may be obtained by averaging over many pulses, but since the satellite is moving at about 7 km/sec, the signal would be averaged over a sub-satellite path of considerable length, and with fluctuations in surface reflectivity, any accuracy improvement is doubtful.

In discussing accuracy, the wavelength jitter of the laser line must be considered. Thermal fluctuations, and mechanical and acoustical vibrations cause frequency instability (Reference 100) and hence, uncertainty in the precise wavelength of observation. This problem would be reduced by choosing, where possible, a laser with a broad line.

**4.1.7.3 Tuning of Lasers.** In order to probe the pollution layer it will be necessary to select lasers with single-mode operation at particular wavelengths, both coincident and noncoincident with an absorption line of the pollutants, and in an atmospheric window. It is unlikely that this will be possible without some tuning of the laser output.

Several techniques are currently available for tuning lasers. Small frequency shifts may be achieved by temperature control, mirror position control, and magnetic field effects. Larger changes are possible by Raman shifts of the laser frequency (Reference 101) although this is not continuous tuning and provides lasing only at discrete

wavelengths. Continuous tuning is possible in the region  $0.71$  to  $1.06\mu$  by using different polymethine dyes pumped by a Q-switched ruby laser (Reference 102).

Considerable attention has been given to tuning the  $\text{CO}_2$  laser, again over the discrete  $\text{CO}_2$  lasing lines. These techniques have included the use of a diffraction grating in place of a mirror (Reference 103), absorbing gas cells placed in the laser cavity (Reference 104), use of  $\text{CO}_2$  isotopes as the lasing gas (Reference 103), and pressure tuning (Reference 105).

With this variety of techniques it appears that lasers at suitable wavelengths may be chosen for pollution probing.

**4.1.7.4 Pulsing of Lasers.** In determining the pulsing requirements for a laser probing system, consideration will have to be given to the power output, the pulse duration, and the pulse repetition rate. The highest power possible is desired for accuracy in measuring the return signal. The pulse duration must be longer than tens of nanoseconds to be compatible with the response time of the detector. The pulse repetition rate should be high to reduce the ground area over which the signal is averaged.

Q-switching techniques for ruby and glass lasers are well established, but the pulse rates are low ( $\approx 10$  per second). Considerable progress is being made in pulsing  $\text{CO}_2$  lasers. Current techniques include the use of cells of gases, such as sulfur hexafluoride (Reference 106), hot  $\text{CO}_2$  (Reference 107), formic acid (Reference 107), or vinyl chloride (Reference 108) inserted in the lasing cavity; rotating a transparent plate inside the cavity (Reference 109), and high voltage transient pumping of the cavity (Reference 110).

**4.1.7.5 Summary.** It appears that with the present state-of-the art in lasers and detectors, it may in principle be possible to design a system to detect layers of pollution in the visible region, but not to measure the amount with high accuracy. It does not appear feasible to readily use a  $\text{CO}_2$  laser to probe in the  $10\mu$  region, due to the high earth-atmosphere background, and low return signals.

## 4.2 CONCLUSIONS

The criteria considered in the evaluation of instruments to detect air pollution from satellites are:

Sensitivity

Specificity

Required observation time

## Information content

### Complexity of the instrument

In general, the sensitivity, specificity, and information content should be high, the complexity should be low, and the observation time should be short.

A qualitative comparison of the instruments considered in passive systems is given in Table 4-4. In addition, active laser systems were investigated. It was found that it may, in principle, be possible to detect pollution in the visible, but not in the infrared with present state-of-the-art laser devices.

The results of the quantitative evaluation of the signal-to-noise ratios as a function of  $\Delta N_{\omega}$  is summarized in Figure 4-17 for the filter-wheel radiometer, polychromator-radiometer, scanning spectrometer, and the Michelson interferometer-spectrometer. For this comparison, the conditions for which the S/N were calculated were the same for the four instruments and are stated in Subsection 4.1.

Based on these criteria, the following conclusions are drawn:

- a. A high-resolution instrument with high sensitivity covering the infrared spectral region from  $3.5\mu$  to  $16\mu$  will have the greatest information content. Such an instrument is the Fourier transform interferometer-spectrometer. However, the present state-of-the-art is not sufficiently advanced to build an instrument for the present application.
- b. A high-resolution scanning spectrometer (grating, prism) does not possess the necessary sensitivity for the detection of pollutants.
- c. A low- to medium-resolution radiometer requires a difficult data reduction procedure to correct for atmospheric and other pollutant interference.
- d. Instruments based on optical correlation techniques (selective-chopper using absorption gas cells, and matched-filter) offer the greatest potential for immediate application.

Table 4-4. Qualitative Comparison Among Spectroscopic Instruments  
for the Detection of Pollutants from Satellites

Instrument	Sensitivity	Specificity	Complexity Of Instrum.	Observ. Time	Information Content	Remarks
Radiometer (filter wheel or many single filters)	Medium	Low	Low	Short	Medium	Limit $\Delta\omega \sim 3 \text{ cm}^{-1}$ ; many channels required
Radiometer (polychromator)	Low	High	Medium	Short	Medium	Assuming $\Delta\omega < 1 \text{ cm}^{-1}$
	Medium	Low		Short		Assuming $\Delta\omega > 1 \text{ cm}^{-1}$ ; Multiple detectors required
Scanning — Spectrometer	Low	High	Medium	Long	High	Assuming $\Delta\omega < \text{cm}^{-1}$
	Medium	Low		Medium		Assuming $\Delta\omega > \text{cm}^{-1}$
Optical Correlation Instrument	High	High	Medium	Short	Medium	Matched filter with multi- ple entrance slits and nondispersive
Interferometer — Spectrometer	High	High	High	Medium	High	Sampling time at least 10 sec; image motion compensation required; large information content for wide spectral interval

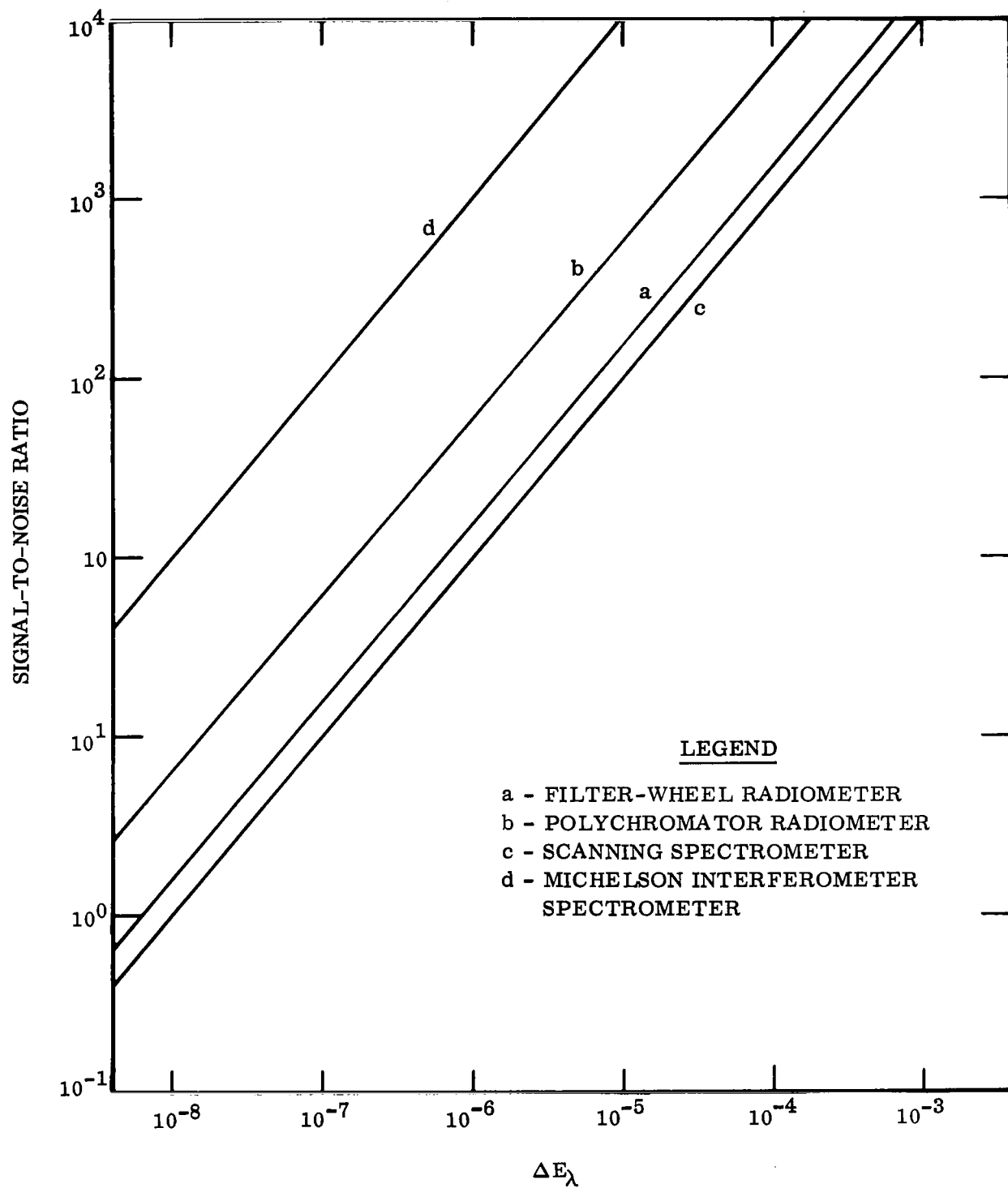


Figure 4-17. Signal-to-Noise Ratio as a Function of  $\Delta E_{\lambda}$

# 5

## RECOMMENDATIONS

The majority of the work described in this report is based upon low spectral resolution ( $0.1\mu$ , i.e.,  $100\text{ cm}^{-1}$  at  $3\mu$  and  $7\text{ cm}^{-1}$  at  $12.5\mu$ ). This is so because the high-resolution spectral characteristics of the pollutants and the atmosphere are not adequately known at the present time. Although a number of moderately high-resolution spectra ( $\Delta\omega \leq 1\text{ cm}^{-1}$ ) are available in the literature (see Tables 5-1 and 5-2), the necessary measurements to obtain absorption coefficients and fine structure parameters have not been made. These parameters are required to:

- a. Either calculate the spectral signature arising from a pollutant and its interaction with the atmosphere, as needed in the evaluation of spectroscopic instruments;
- b. Determine the actual concentration of pollutants from a measured spectrum, as needed in the remote sensing of air pollution.

In spite of this lack of basic information, the present study indicates that remote sensing of air pollution in the infrared is feasible. However, it is necessary to repeat the calculations of signal changes in high resolution before a satellite system can be designed. Without this knowledge, accurate determination of the pollution amount will be impossible by remote sensing.

In addition, the development of a prototype IR remote sensor should be pursued in order to ascertain the feasibility of the pollutant detection in the infrared under a variety of meteorological conditions. This should have high sensitivity and high specificity without being unduly complex and expensive. Such an instrument is one using optical correlation techniques.

Table 5-1. High Resolution Atmospheric Spectra

Range	Resolution	Type	Reference
2.8 - 23.7 $\mu$	0.1 $\text{cm}^{-1}$	Solar (from surface)	Migeotte et al (111)
8 - 13 $\mu$	0.3 $\text{cm}^{-1}$	Solar (surface)	Bignall et al (112)
7 - 400 $\mu$	0.5 $\text{cm}^{-1}$	Solar (5200m)	Farmer and Key (113)
1 - 6.5 $\mu$	0.5 - 1.0 $\text{cm}^{-1}$	Solar (aircraft)	Houghton et al (114)
6 - 20 $\mu$	1 $\text{cm}^{-1}$	Solar (balloon)	Murcray (115)
2.7 $\mu$ band	1 $\text{cm}^{-1}$	Solar (balloon)	Murcray et al (116)
4.3 $\mu$ band	1 $\text{cm}^{-1}$	Solar (balloon)	Kyle et al (117)
8 - 12 $\mu$	1 $\text{cm}^{-1}$	Emission (surface)	Convair (118)
8 - 12 $\mu$	1.5 $\text{cm}^{-1}$	Emission (surface)	Goddard SFC (119)
7.5 - 26 $\mu$	2 $\text{cm}^{-1}$	Emission (surface)	Bolle et al (120)
0.68 - 4.86 $\mu$	0.1 - 2 $\text{cm}^{-1}$	25 km horizontal	Streete et al (121)
2.05 and 2.7 $\mu$ CO <sub>2</sub>	Calculated		Calfee and Benedict(122)

Table 5-2. High Resolution Pollution Spectra

Species	Band	Resolution	Reference
CO	4.7 $\mu$	0.45 $\text{cm}^{-1}$	Calibration Tables (123)
CH <sub>4</sub>	3.3 $\mu$	0.65 $\text{cm}^{-1}$	Calibration Tables (123)
CH <sub>4</sub>	7.5 $\mu$	0.34 $\text{cm}^{-1}$	Calibration Tables (123)
NH <sub>3</sub>	10 $\mu$	0.5 $\text{cm}^{-1}$	Calibration Tables (123)
SO <sub>2</sub>	8.7 $\mu$	1 $\text{cm}^{-1}$	Hanst and Morreal (124)
C <sub>2</sub> H <sub>4</sub>	10.6 $\mu$	1 $\text{cm}^{-1}$	Hanst and Morreal (124)
CO	4.7 $\mu$	1 $\text{cm}^{-1}$	Hanst and Morreal (124)
NO	5.3 $\mu$	1 $\text{cm}^{-1}$	Hanst and Morreal (124)
NH <sub>3</sub>	10 $\mu$	1 $\text{cm}^{-1}$	Convair (118)
SO <sub>2</sub>	8.7 $\mu$	1 $\text{cm}^{-1}$	Convair (118)
C <sub>2</sub> H <sub>4</sub>	10.6 $\mu$	1 $\text{cm}^{-1}$	Convair (118)
NO <sub>2</sub>	6.3 $\mu$	1 $\text{cm}^{-1}$	Convair (118)
C <sub>6</sub> H <sub>6</sub>	9.7 $\mu$	1 $\text{cm}^{-1}$	Convair (118)
Acrolein	10.5 $\mu$	1 $\text{cm}^{-1}$	Convair (118)

# 6

## REFERENCES

1. L. S. Jaffe, J. Air Poll. Contr. Assoc. 18, 534, 1968.
2. J. V. Dave and P. M. Furukawa, "Scattered Radiation in the Ozone Absorption Bands at Selected Levels of a Terrestrial Rayleigh Atmosphere," Meteorological Monograph, Vol. 7, 1966.
3. A. E. S. Green, M. Griggs, Appl. Optics 2, 561, 1963.
4. R. H. Pierson, A. N. Fletcher, E. St. Clair Gantze, Anal. Chem. 28, 1218, 1956.
5. H. Nelburger, "What Factors Determine the Optimum Size Area for an Air Pollution Control Program," Conference on Air Pollution 3, 442, 1966.
6. A. J. Haagen - Smit, Ind. Eng. Chem. 44, 1342, 1952.
7. P. A. Leighton, W. A. Perkins, Air Pollution Foundation, Los Angeles, Rept. 14, March 1956.
8. P. A. Leighton, Photochemistry of Air Pollution, Academic Press, New York, 1961.
9. The Automobile and Air Pollution: Part II, U. S. Dept. of Commerce, Dec. 1967, p. 6.
10. CAMP, Washington, D. C., 1962-63, U. S. Dept. of HEW, Sept. 1966, p. 12.
11. C. I. Harding, T. R. Kelley, J. Air Poll. Cont. Ass. 17, 549, 1967.
12. D. H. Enhalt, J. Air Poll. Cont. Ass. 17, 518, 1967.
13. A. E. Bainbridge, L. E. Heidt, Tellus XVIII, 221, 1966.
14. Georgii, H. -W., Busch, E., & Weber, E., "Untersuchung über die zeitliche und räumliche Verteilung der Immissions-Konzentration des Kohlenmonoxid in Frankfurt." Berichte des Institutes für Meteorologie und Geophysik der Universität Frankfurt/Main, 1967.
15. Georgii, H. -W., Jost, D., & Schaefer, H. J., "Über die raumliche und zeitliche Verteilung von Schwefeldioxid und Sulfataerosolen in der unteren Troposphäre." Wissenschaftlicher Bericht. Forschungsvertrag T-483-J-203, 1968.
16. H. H. Slater, Nat. Air Poll. Control Adm., Private Communication.
17. A. R. Barringer, B. C. Newbury and A. J. Moffat, Proc. 5th Symp. Rem. Sens. of Environ. 123, 1968.



18. J. McDowall, Barringer Research Ltd., Private Communication.
19. R. A. McCormick, J. H. Ludwig, *Science* 156, 1358, 1967.
20. J. M. Mitchell, Jr., *Annal. New York Acad. Sci.* 95, 235, 1961.
21. C. E. Junge, *J. Meteorol.* 12, 13, 1955.
22. M. Corn, *Air Pollution I* (Ed. A. C. Stern), Academic Press, N.Y., 1968.
23. K. Bullrich, *Advances in Geophysics*, 10, 99, 1964.
24. C. W. Chagnon and C. E. Junge, *J. Meteorol.* 18, 746, 1961.
25. G. V. Rosenberg, *Soviet Physics Uspekhi* 3, 346, 1960.
26. D. Deirmendjian, *Appl. Optics* 3, 187, 1964.
27. J. M. Waldram, *Qu. Journ. Roy. Meteorol. Soc.* 71, 319, 1945.
28. A. T. Blanco and G. B. Hoidale, *Atmos. Sci. Lab., White Sands Missile Range, Rept. No. ECOM-5193*, 1968.
29. K. L. Coulson, *Planet. Space Sci.* 1, 265, 1959.
30. Z. Sekera and W. Viezee, *Rand Rept. R-389-PR*, 1961.
31. K. L. Coulson, *General Electric Rept. R64SD74*, 1964.
32. G. N. Plass and G. W. Kattawar, *Appl. Optics* 7, 1129, 1968.
33. G. W. Kattawar and G. N. Plass, *Appl. Optics*, 7, 1519, 1968.
34. W. E. K. Middleton, *Vision through the Atmosphere*, Univ. Toronto Press, 1952.
35. *Earth Photographs from Gemini III, IV, and V.*, Sci. & Tech. Info. Div., NASA, Washington, D. C., 1967.
36. D. Randerson, 1968 *J. Air Poll. Contr. Assoc.* 18, 249.
37. R. Frith, *Meteorological Satellites, Future Research Projects*, WMO Bulletin XI, 202, 1962.
38. A. E. S. Green, C. S. Lindenmeyer and M. Griggs, *J. Geophys. Res.* 69, 493, 1964.
39. A. S. Zachor, *J. Quant. Spectrosc. Rad. Trans.* I, 989, 1967.
40. D. Q. Wark, G. Yamamoto and J. H. Lienesch, *J. Atmos. Sci.* 19, 369, 1962, and *Weather Bureau Meteor. Satellite Lab. Report No. 10*, 1962.
41. M. Griggs and W. A. Marggraf, "Measurement of Cloud Reflectance Properties and Atmospheric Attenuation of Solar and Infrared Energy," Final Report, Contract AF19(628)-5517, Dec. 1967.

42. Handbook of Geophysics, Revised Edition, MacMillan Co., New York, 1960.
43. O. G. Sutton, Micrometeorology, McGraw-Hill, New York, 1953.
44. R. Geiger, The Climate Near the Ground, Harvard University Press, Cambridge, Mass., 1965.
45. M. N. Hill, ed., The Sea, Vol. I, Physical Oceanography, Interscience, New York, 1962.
46. H. H. Lettan and B. Davidson, eds., Exploring the Atmosphere's First Mile, Vols. I and II, Pergamon Press, New York, 1957.
47. R. G. Fleagle, J. Meteor, 13, 160, 1955.
48. F. S. Duckworth and J. S. Sandburg, Bul. Am. Meteor. Soc., 35, 198, 1954.
49. University of Michigan, NASA CR-87, pp. 141-151, Sept. 1966.
50. S. Twomey, Monthly Weather Review 94, 363, 1966.
51. J.C. Alishouse, L. J. Crone, H. E. Fleming, F.L. Van Cleef and, D. Q. Wark, Tellus 19, 1967.
52. O. N. Strand and E.R. Westwater, J. Assoc. Comp. Mach. 15, 100, 1968.
53. G. N. Plass, J. Opt. Soc. Am. 50, 868, 1960.
54. W. Malkmus, J. Opt. Soc. Am. 57, 323, 1967.
55. R. M. Goody, Atmospheric Radiation I. Theoretical Basis, Oxford, Clarendon Press, 1964.
56. J.A.L. Thomson, in "Proceedings of Specialist Conference on Molecular Radiation," (NASA TMX-53711), pp. 137-163, Oct. 6-7, 1967.
57. W. Malkmus and A. Thomson, J. Quant. Spectry. Radiative Transfer 2, 70, 1962.
58. C. D. Walshaw, Quart. J. Roy. Met. Soc. 83, 315, 1957.
59. D. E. Burch, D. Gryvnak, E. B. Singleton, W. L. France, and D. Williams, "Infrared Absorption by Carbon Dioxide, Water Vapor, and Minor Atmospheric Constituents," AFCRL-62-698, July 1962.
60. W. L. France and D. Williams, J. Opt. Soc. Am. 56, 70, 1966.
61. E. Finkman, A. Goldman, and U.P. Oppenheim, J. Opt. Soc. Am. 57, 1130, 1967.
62. Ya. I. Gerlovin and I. N. Orlova, Optics and Spectroscopy, 16, 9, 1964.
63. W. S. Benedict, R. Herman, G. E. Moore, and S. Silverman, Can. J. Phys. 34, 850, 1956.

64. A. Guttman, *J. Quant. Spectry. Radiative Transfer* 2, 1, 1962.
65. W. H. Conway, et al., Paper presented at 2nd Remote Sensing Symposium, University of Michigan, 1962.
66. R. S. Freund and W. Klemperer, *J. Chem. Phys.* 43, 2422, 1965.
67. O. R. Gilliam, C. M. Johnson, and W. Gordy, *Phys. Rev.* 78, 140, 1950.
68. B. Rosenblum, A. H. Nethercot, Jr., and C. H. Townes, *Phys. Rev.* 109, 400, 1958.
69. C. A. Burrus and W. Gordy, *Phys. Rev.* 92, 1437, 1953.
70. G. R. Bird et al., *J. Chem. Phys.* 40, 3378, 1964.
71. M. Saucho and M. D. Harmony, *J. Chem. Phys.* 45, 1812, 1966.
72. C. A. Burrus and W. Gordy, *Phys. Rev.* 92, 274, 1953.
73. R. Trambarulo, et al., *J. Chem. Phys.* 21, 851, 1953.
74. M. H. Sirvetz, *J. Chem. Phys.* 19, 938, 1952.
75. D. Kivelson, *J. Chem. Phys.* 22, 1733, 1954.
76. J. A. Roberts, et al., *J. Chem. Phys.* 43, 4337, 1965.
77. C. H. Townes and A. L. Schawlow, Microwave Spectroscopy, McGraw-Hill, New York, 1955.
78. General Dynamics/Convair Report, "Modeling of Microwave Radiometry for Determination of Ocean-Surface Features," Report No. GDC-PIN68-637, June 1968.
79. D. H. Staelin, Paper presented at the Electromagnetic Sensing Symposium, University of Miami, November 1965.
80. University of Michigan, NASA CR-588, Vol. III, Sept. 1966.
81. M. Dreyfus, D. Hilleary, Satellite Infrared Spectrometer, Aerospace Engineering, February 1962.
82. R. A. Hanel, L. Chaney, "The Infrared Interferometer Spectrometer Experiment (IRIS)," NASA X-650-64-204, July 1964; and NASA X-650-65-75, March 1965; and, "The Merits and Shortcomings of a Michelson-type Interferometer to Obtain the Vertical Temperatures and Humidity Profile," Application Satellites, Proceedings XVII th Intern. Astronautical Congress, Madrid, Spain, 1966; pp. 247.
83. A. G. Tescher, Pomona Division of General Dynamics, Private Communication .
84. D. M. Hunten, "Fourier Spectroscopy of Planets," *Science* 162, 313, 1968.

85. P. Fellgett, J. Physique, (France) 19, 187, 1958.
86. L. Mertz, Mem. Soc. Roy. Sci. de Liege 9, 120, 1964.
87. R. Beer, Applied Optics 6, 209, 1967.
88. J. and P. Connes, J. Opt. Soc. Am. 56, 896, 1966.
89. A. R. Barringer, J.P. Schock, Proc. 4th Symp. Rem. Sens. of Environ. 779, 1966.
90. D. T. Williams, B.L. Kolitz, Appl. Optics 7, 607, 1968.
91. P. H. VanCittert, "Effects of Slit Widths upon Distribution of Intensity in Spectral Lines," Zeitschrift for Physic 65, 547, 1930.
92. J. T. Houghton, N.D.P. Hughes, T.S. Moss and J. S. Seeley, Phil. Trans. Roy. Soc. London, 254, 47, 1961.
93. S. D. Smith, C. R. Pidgeon, "Infrared Spectra of Astronomical Bodies," Proc. XII Intern. Astrophys. Symp. Liege, June 24-26, 1963, p. 336. Also Private Communication, Goddard Space Flight Center.
94. R. Goody, JOSA 58, 900, 1968.
95. G. Peckham, C. D. Rodgers, J. T. Houghton, and S. D. Smith, Proceedings of the Symposium on Electromagnetic Sensing of the Earth from Satellites, University of Florida, Coral Gables, Fla., November 1965.
96. R. W. Astheiner, R. DeWaard, and E.A. Jackson, JOSA 51, 1386, 1961.
97. S. S. Penner, "Quantitative Molecular Spectroscopy and Gas Emissivities," p. 210 Addison-Wesley, Reading, Mass., 1959.
98. International Union of Pure and Applied Chemistry, "Tables of Wavelengths for the Calibration of Infra-Red Spectrometers," p. 580-581, Butterworth, Inc., Washington, D. C., 1961.
99. M. Dorian, C. B. Ludwig, M. L. Streiff, J.A.L. Thomson, "Remote Sensing," GDC-ERR-AN-1129, Convair, San Diego, California, December 1967.
100. C. Freed, IEEE, J. Qu. El. QE-4, 404-408, 1968.
101. S. F. Singer, Appl. Optics 7, 1125, 1968.
102. Y. Miyazoe and M. Maeda, Appl. Phys. Letters, 12, 206, 1968.
103. G.B. Jacobs and L. R. Snowman, IEEE, J. Qu. El. QE-3, 11, 603, 1967.
104. P. L. Hanst and J. A. Morreal, Presented at 61st Annual Meeting of Air Poll. Control. Assoc., St. Paul, Minnesota, June 23, 1968.
105. T. G. Roberts, G. J. Hutcheson, J. J. Ehrlich, W. C. Hales, and J. A. Barr, Jr., IEEE Qu-E, 11, 605, IEEE, 1967.

106. O. R. Wood and S. E. Schwarz, Appl. Phys. Letters 12, 263, 1968.
107. P. L. Hanst, J. A. Morreal, and W. J. Henson, Appl. Phys. Letters 12, 58, 1968.
108. J. T. Yardley, Appl. Phys. Letters, 12, 120, 1968.
109. A. J. Carswell and J. I. Wood, IEEE, J. Qu. El. QE-4, 294, 1968.
110. A. E. Hill, Appl. Phys. Letters 12, 324, 1968.
111. M. Migeotte, L. Neven, J. Swensson, 1956 Part I, 1957 Part II, Final Report AF61(514)-432.
112. K. Bignell, F. Saiedy, P. A. Sheppard, J. Opt. Soc. Am., 53, 466, 1963.
113. C. B. Farmer and P. J. Key, Appl. Opt. 4, 1051, 1965.
114. J. T. Houghton, N.D.P. Hughes, T. S. Moss and J. S. Seeley, Phil. Trans. Roy. Soc. London, 254, 47, 1961.
115. D. G. Murcay, 1968, Private Communication.
116. D. G. Murcay, F. M. Murcay and W. T. Williams, Appl. Opt. 6, 191, 1967.
117. T. G. Kyle, D. G. Murcay, F. M. Murcay, and W. J. Williams, J. Opt. Soc. Am. 55, 1421, 1965.
118. Convair - Space Sciences, unpublished.
119. Goddard SFC, 1968, Private Communication.
120. H. J. Bolle, G. Kuers, F. Moeller, H. Quenzel, Final Report AF61(052)-488, 1964.
121. J. L. Streete, J. H. Taylor, and S. L. Ball, Appl. Opt. 6, 489, 1967.
122. R. F. Calfee and W. S. Benedict, NBS Tech. Note 332, 1966.
123. Tables of Wavenumbers for the Calibration of Infrared Spectrometers, Butterworth Inc., Washington, 1961.
124. P. L. Hanst and J. A. Morreal, Presented at 61st Annual Meeting of Air Poll. Control Assoc., St. Paul, Minn., June 23, 1968.

## APPENDIX A

- Table A-1. Computed Relative and Absolute Intensities for Rayleigh Atmosphere ( $\theta = 0$ ,  $\theta_0 = 0$ )
- Table A-2. Computed Relative and Absolute Intensities for Rayleigh Atmosphere ( $\theta = 0$ ,  $\theta_0 = 30^\circ$ )
- Table A-3. Computed Relative and Absolute Intensities for Rayleigh Atmosphere ( $\theta = 0$ ,  $\theta_0 = 60^\circ$ )
- Table A-4. Computed Relative and Absolute Intensities for Rayleigh Atmosphere ( $\theta = 0$ ,  $\theta_0 = 75^\circ$ )
- Table A-5. Computed Relative and Absolute Intensities for Rayleigh Atmosphere ( $\theta = 0$ ,  $\theta_0 = 85^\circ$ )
- Table A-6. Absorption Coefficients for  $\text{SO}_2$ ,  $\text{CH}_4$ ,  $\text{NH}_3$ ,  $\text{CO}$ ,  $\text{HCl}$ ,  $\text{PAN}$ ,  $\text{C}_2\text{H}_4$ ,  $\text{C}_6\text{H}_6$ ,  $\text{NO}$ ,  $\text{O}_3$  and  $\text{NO}_2$  (at  $300^\circ\text{K}$  unless otherwise noted)

Table A-1. Computed Relative and Absolute Intensities for Rayleigh Atmosphere  
( $\theta = 0$ ,  $\theta_0 = 0$ )

THETA0= 0		THETA= 0				
LAMBDA	R=	0.00	.10	.20	.40	.80
2875	IS	0.	3.001E-17	6.103E-17	1.263E-16	2.716E-16
	IS/IA	0.	2.139E-14	4.350E-14	9.004E-14	1.938E-13
	IS+IA	1.403E-03	1.403E-03	1.403E-03	1.403E-03	1.403E-03
	INTENSITY	1.920E-05	1.920E-05	1.920E-05	1.920E-05	1.920E-05
2975	IS	0.	3.118E-06	6.427E-06	1.369E-05	3.150E-05
	IS/IA	0.	9.280E-04	1.913E-03	4.076E-03	9.376E-03
	IS+IA	3.360E-03	3.363E-03	3.366E-03	3.374E-03	3.392E-03
	INTENSITY	6.631E-05	6.637E-05	6.644E-05	6.658E-05	6.693E-05
3075	IS	0.	3.563E-03	7.418E-03	1.610E-02	3.936E-02
	IS/IA	0.	8.113E-02	1.689E-01	3.680E-01	8.961E-01
	IS+IA	4.392E-02	4.748E-02	5.134E-02	6.008E-02	8.328E-02
	INTENSITY	1.007E-03	1.088E-03	1.177E-03	1.377E-03	1.909E-03
3175	IS	0.	2.305E-02	4.813E-02	1.055E-01	2.615E-01
	IS/IA	0.	1.334E-01	2.785E-01	6.108E-01	1.513E+00
	IS+IA	1.728E-01	1.959E-01	2.209E-01	2.783E-01	4.343E-01
	INTENSITY	4.510E-03	5.112E-03	5.767E-03	7.265E-03	1.134E-02
3300	IS	0.	4.799E-02	1.001E-01	2.190E-01	5.391E-01
	IS/IA	0.	1.800E-01	3.753E-01	8.211E-01	2.021E+00
	IS+IA	2.667E-01	3.147E-01	3.668E-01	4.657E-01	8.058E-01
	INTENSITY	9.678E-03	1.142E-02	1.331E-02	1.762E-02	2.924E-02
3400	IS	0.	5.339E-02	1.110E-01	2.413E-01	5.835E-01
	IS/IA	0.	2.148E-01	4.468E-01	9.709E-01	2.348E+00
	IS+IA	2.485E-01	3.019E-01	3.595E-01	4.898E-01	8.320E-01
	INTENSITY	8.859E-03	1.076E-02	1.282E-02	1.740E-02	2.966E-02
3600	IS	0.	6.192E-02	1.281E-01	2.749E-01	6.442E-01
	IS/IA	0.	2.974E-01	6.151E-01	1.320E+00	3.094E+00
	IS+IA	2.082E-01	2.701E-01	3.363E-01	4.831E-01	8.524E-01
	INTENSITY	7.754E-03	1.006E-02	1.252E-02	1.799E-02	3.174E-02
4950	IS	0.	8.623E-02	1.746E-01	3.579E-01	7.535E-01
	IS/IA	0.	1.477E+00	2.990E+00	6.130E+00	1.291E+01
	IS+IA	5.638E-02	1.446E-01	2.329E-01	4.163E-01	8.119E-01
	INTENSITY	3.810E-03	9.436E-03	1.520E-02	2.710E-02	5.298E-02
5350	IS	0.	8.634E-02	1.743E-01	3.551E-01	7.378E-01
	IS/IA	0.	2.105E+00	4.248E+00	8.656E+00	1.799E+01
	IS+IA	4.102E-02	1.274E-01	2.153E-01	3.961E-01	7.788E-01
	INTENSITY	1.541E-03	4.784E-03	8.086E-03	1.486E-02	2.925E-02
5750	IS	0.	8.563E-02	1.725E-01	3.498E-01	7.201E-01
	IS/IA	0.	2.903E+00	5.846E+00	1.186E+01	2.441E+01
	IS+IA	2.950E-02	1.151E-01	2.020E-01	3.793E-01	7.496E-01
	INTENSITY	1.794E-03	7.000E-03	1.228E-02	2.306E-02	4.558E-02
6150	IS	0.	8.753E-02	1.760E-01	3.559E-01	7.280E-01
	IS/IA	0.	3.897E+00	7.837E+00	1.585E+01	3.241E+01
	IS+IA	2.246E-02	1.100E-01	1.985E-01	3.784E-01	7.504E-01
	INTENSITY	1.258E-03	6.162E-03	1.112E-02	2.120E-02	4.204E-02
6550	IS	0.	9.196E-02	1.847E-01	3.727E-01	7.587E-01
	IS/IA	0.	5.123E+00	1.029E+01	2.076E+01	4.227E+01
	IS+IA	1.795E-02	1.099E-01	2.027E-01	3.906E-01	7.766E-01
	INTENSITY	9.199E-04	5.633E-03	1.039E-02	2.002E-02	3.980E-02

Table A-2. Computed Relative and Absolute Intensities for Rayleigh Atmosphere  
( $\theta = 0$ ,  $\theta_0 = 30^\circ$ )

THETA0=30 LAMBDA R=		THETA= 0				
		0.00	.10	.20	.40	.80
2875	IS	0.	1.764E-18	3.587E-18	7.425E-18	1.596E-17
	IS/IA	0.	1.511E-15	3.074E-15	6.362E-15	1.368E-14
	IS+IA	1.167E-03	1.167E-03	1.167E-03	1.167E-03	1.167E-03
	INTENSITY	1.597E-05	1.597E-05	1.597E-05	1.597E-05	1.597E-05
2975	IS	0.	1.245E-06	2.566E-06	5.467E-06	1.258E-05
	IS/IA	0.	4.570E-04	9.419E-04	2.007E-03	4.617E-03
	IS+IA	2.724E-03	2.725E-03	2.727E-03	2.729E-03	2.737E-03
	INTENSITY	5.376E-05	5.378E-05	5.381E-05	5.387E-05	5.401E-05
3075	IS	0.	2.418E-03	5.034E-03	1.097E-02	2.670E-02
	IS/IA	0.	7.405E-02	1.542E-01	3.359E-01	8.179E-01
	IS+IA	3.265E-02	3.507E-02	3.768E-02	4.364E-02	5.935E-02
	INTENSITY	7.483E-04	8.037E-04	8.636E-04	9.990E-04	1.360E-03
3175	IS	0.	1.797E-02	3.753E-02	8.229E-02	2.039E-01
	IS/IA	0.	1.274E-01	2.680E-01	5.832E-01	1.445E+00
	IS+IA	1.411E-01	1.591E-01	1.786E-01	2.234E-01	3.450E-01
	INTENSITY	3.683E-03	4.152E-03	4.662E-03	5.831E-03	9.005E-03
3300	IS	0.	3.952E-02	8.243E-02	1.803E-01	4.439E-01
	IS/IA	0.	1.739E-01	3.626E-01	7.933E-01	1.953E+00
	IS+IA	2.273E-01	2.668E-01	3.097E-01	4.076E-01	6.712E-01
	INTENSITY	8.248E-03	9.682E-03	1.124E-02	1.479E-02	2.436E-02
3400	IS	0.	4.425E-02	9.203E-02	2.000E-01	4.837E-01
	IS/IA	0.	2.080E-01	4.327E-01	9.402E-01	2.274E+00
	IS+IA	2.127E-01	2.570E-01	3.047E-01	4.127E-01	6.964E-01
	INTENSITY	7.583E-03	9.161E-03	1.086E-02	1.471E-02	2.483E-02
3600	IS	0.	5.179E-02	1.071E-01	2.499E-01	5.389E-01
	IS/IA	0.	2.894E-01	5.985E-01	1.285E+00	3.010E+00
	IS+IA	1.790E-01	2.308E-01	2.861E-01	4.089E-01	7.179E-01
	INTENSITY	6.666E-03	8.595E-03	1.066E-02	1.523E-02	2.673E-02
4950	IS	0.	7.378E-02	1.494E-01	3.062E-01	6.447E-01
	IS/IA	0.	1.455E+00	2.945E+00	6.039E+00	1.271E+01
	IS+IA	5.071E-02	1.245E-01	2.001E-01	3.569E-01	6.954E-01
	INTENSITY	3.309E-03	8.123E-03	1.306E-02	2.329E-02	4.538E-02
5350	IS	0.	7.389E-02	1.491E-01	3.039E-01	6.314E-01
	IS/IA	0.	2.076E+00	4.190E+00	8.538E+00	1.774E+01
	IS+IA	3.559E-02	1.095E-01	1.847E-01	3.394E-01	6.670E-01
	INTENSITY	1.337E-03	4.112E-03	6.938E-03	1.275E-02	2.505E-02
5750	IS	0.	7.325E-02	1.475E-01	2.992E-01	6.180E-01
	IS/IA	0.	2.865E+00	5.769E+00	1.170E+01	2.409E+01
	IS+IA	2.557E-02	9.882E-02	1.731E-01	3.246E-01	6.415E-01
	INTENSITY	1.555E-03	6.008E-03	1.052E-02	1.975E-02	3.900E-02
6150	IS	0.	7.501E-02	1.508E-01	3.050E-01	6.238E-01
	IS/IA	0.	3.848E+00	7.739E+00	1.565E+01	3.200E+01
	IS+IA	1.949E-02	9.450E-02	1.703E-01	3.245E-01	6.433E-01
	INTENSITY	1.092E-03	5.294E-03	9.542E-03	1.818E-02	3.604E-02
6550	IS	0.	7.910E-02	1.589E-01	3.200E-01	6.526E-01
	IS/IA	0.	5.064E+00	1.017E+01	2.052E+01	4.178E+01
	IS+IA	1.562E-02	4.472E-02	1.745E-01	3.362E-01	6.682E-01
	INTENSITY	8.005E-04	4.854E-03	8.943E-03	1.723E-02	3.425E-02



**Table A-3. Computed Relative and Absolute Intensities for Rayleigh Atmosphere**  
( $\theta = 0, \theta_0 = 60^\circ$ )

THETA0=60 LAMBDA R=		THETA= 0				
		0.00	.10	.20	.40	.60
2875	IS	0.	4.668E-21	9.494E-21	1.965E-20	4.225E-20
	IS/IA	0.	7.019E-18	1.427E-17	2.955E-17	6.353E-17
	IS+IA	6.651E-04	6.651E-04	6.651E-04	6.651E-04	6.651E-04
	INTENSITY	9.103E-06	9.103E-06	9.103E-06	9.103E-06	9.103E-06
2975	IS	0.	1.690E-08	3.483E-08	7.421E-08	1.701E-07
	IS/IA	0.	1.157E-05	2.386E-05	5.083E-05	1.169E-04
	IS+IA	1.460E-03	1.460E-03	1.460E-03	1.460E-03	1.460E-03
	INTENSITY	2.881E-05	2.881E-05	2.881E-05	2.881E-05	2.882E-05
3075	IS	0.	4.137E-04	8.613E-04	1.870E-03	4.569E-03
	IS/IA	0.	4.028E-02	8.386E-02	1.821E-01	4.449E-01
	IS+IA	1.027E-02	1.068E-02	1.113E-02	1.215E-02	1.484E-02
	INTENSITY	2.354E-04	2.449E-04	2.551E-04	2.784E-04	3.401E-04
3175	IS	0.	6.257E-03	1.306E-02	2.865E-02	7.098E-02
	IS/IA	0.	9.400E-02	1.963E-01	4.304E-01	1.066E+00
	IS+IA	6.656E-02	7.282E-02	7.962E-02	9.521E-02	1.315E-01
	INTENSITY	1.737E-03	1.901E-03	2.078E-03	2.485E-03	3.590E-03
3300	IS	0.	1.604E-02	3.762E-02	8.230E-02	2.026E-01
	IS/IA	0.	1.347E-01	2.810E-01	6.146E-01	1.513E+00
	IS+IA	1.339E-01	1.519E-01	1.715E-01	2.162E-01	3.365E-01
	INTENSITY	4.859E-03	5.513E-03	6.224E-03	7.845E-03	1.221E-02
3400	IS	0.	2.079E-02	4.323E-02	9.394E-02	2.272E-01
	IS/IA	0.	1.619E-01	3.367E-01	7.316E-01	1.769E+00
	IS+IA	1.284E-01	1.492E-01	1.716E-01	2.223E-01	3.556E-01
	INTENSITY	4.576E-03	5.319E-03	6.119E-03	7.926E-03	1.268E-02
3600	IS	0.	2.531E-02	5.234E-02	1.124E-01	2.633E-01
	IS/IA	0.	2.264E-01	4.682E-01	1.005E+00	2.355E+00
	IS+IA	1.118E-01	1.371E-01	1.641E-01	2.242E-01	3.751E-01
	INTENSITY	4.164E-03	5.106E-03	6.113E-03	8.346E-03	1.397E-02
4950	IS	0.	3.998E-02	8.093E-02	1.659E-01	3.493E-01
	IS/IA	0.	1.161E+00	2.350E+00	4.818E+00	1.014E+01
	IS+IA	3.444E-02	7.442E-02	1.154E-01	2.004E-01	3.838E-01
	INTENSITY	2.247E-03	4.856E-03	7.528E-03	1.307E-02	2.504E-02
5350	IS	0.	4.004E-02	8.082E-02	1.641E-01	3.422E-01
	IS/IA	0.	1.659E+00	3.349E+00	6.824E+00	1.418E+01
	IS+IA	2.413E-02	6.417E-02	1.049E-01	1.888E-01	3.663E-01
	INTENSITY	9.063E-04	2.410E-03	3.942E-03	7.091E-03	1.376E-02
5750	IS	0.	3.955E-02	7.966E-02	1.616E-01	3.326E-01
	IS/IA	0.	2.292E+00	4.615E+00	9.362E+00	1.927E+01
	IS+IA	1.726E-02	5.681E-02	9.692E-02	1.788E-01	3.499E-01
	INTENSITY	1.049E-03	3.454E-03	5.893E-03	1.087E-02	2.127E-02
6150	IS	0.	4.088E-02	8.221E-02	1.662E-01	3.400E-01
	IS/IA	0.	3.085E+00	6.204E+00	1.255E+01	2.566E+01
	IS+IA	1.325E-02	5.413E-02	9.546E-02	1.795E-01	3.532E-01
	INTENSITY	7.423E-04	3.033E-03	5.348E-03	1.000E-02	1.979E-02
6550	IS	0.	4.401E-02	8.840E-02	1.784E-01	3.631E-01
	IS/IA	0.	4.067E+00	8.170E+00	1.648E+01	3.356E+01
	IS+IA	1.082E-02	5.483E-02	9.922E-02	1.892E-01	3.739E-01
	INTENSITY	5.545E-04	2.810E-03	5.085E-03	9.695E-03	1.916E-02

Table A-4. Computed Relative and Absolute Intensities for Rayleigh Atmosphere  
( $\theta = 0$ ,  $\theta_0 = 75^\circ$ )

THETA0=75 LAMBDA R=		THETA= 0				
		0.00	.10	.20	.40	.80
2875	IS	0.	1.905E-21	3.875E-21	8.021E-21	1.725E-20
	IS/IA	0.	4.661E-18	9.480E-18	1.962E-17	4.219E-17
	IS+IA	4.088E-04	4.088E-04	4.088E-04	4.088E-04	4.088E-04
	INTENSITY	5.595E-06	5.595E-06	5.595E-06	5.595E-06	5.595E-06
2975	IS	0.	1.367E-09	2.818E-09	6.003E-09	1.381E-08
	IS/IA	0.	1.570E-06	3.237E-06	6.897E-06	1.587E-05
	IS+IA	8.704E-04	8.704E-04	8.704E-04	8.704E-04	8.704E-04
	INTENSITY	1.718E-05	1.718E-05	1.718E-05	1.718E-05	1.718E-05
3075	IS	0.	3.062E-05	6.375E-05	1.389E-04	3.382E-04
	IS/IA	0.	1.053E-02	2.193E-02	4.778E-02	1.164E-01
	IS+IA	2.907E-03	2.938E-03	2.971E-03	3.046E-03	3.245E-03
	INTENSITY	6.662E-05	6.733E-05	6.808E-05	6.981E-05	7.438E-05
3175	IS	0.	1.435E-03	2.996E-03	6.570E-03	1.628E-02
	IS/IA	0.	5.974E-02	1.247E-01	2.735E-01	6.777E-01
	IS+IA	2.402E-02	2.545E-02	2.702E-02	3.059E-02	4.030E-02
	INTENSITY	6.270E-04	6.644E-04	7.052E-04	7.984E-04	1.052E-03
3300	IS	0.	6.709E-03	1.399E-02	3.061E-02	7.535E-02
	IS/IA	0.	9.292E-02	1.938E-01	4.240E-01	1.044E+00
	IS+IA	7.420E-02	7.891E-02	8.619E-02	1.028E-01	1.476E-01
	INTENSITY	2.620E-03	2.863E-03	3.128E-03	3.731E-03	5.354E-03
3400	IS	0.	7.995E-03	1.663E-02	3.613E-02	8.738E-02
	IS/IA	0.	1.099E-01	2.285E-01	4.966E-01	1.201E+00
	IS+IA	7.475E-02	8.074E-02	8.938E-02	1.089E-01	1.601E-01
	INTENSITY	2.594E-03	2.879E-03	3.186E-03	3.882E-03	5.709E-03
3600	IS	0.	1.016E-02	2.101E-02	4.509E-02	1.057E-01
	IS/IA	0.	1.491E-01	3.085E-01	6.621E-01	1.552E+00
	IS+IA	6.810E-02	7.826E-02	8.911E-02	1.132E-01	1.738E-01
	INTENSITY	2.536E-03	2.914E-03	3.319E-03	4.215E-03	6.471E-03
4950	IS	0.	1.822E-02	3.688E-02	7.561E-02	1.592E-01
	IS/IA	0.	7.058E-01	1.429E+00	2.929E+00	6.168E+00
	IS+IA	2.581E-02	4.403E-02	6.269E-02	1.014E-01	1.850E-01
	INTENSITY	1.684E-03	2.873E-03	4.091E-03	6.618E-03	1.207E-02
5350	IS	0.	1.814E-02	3.662E-02	7.462E-02	1.550E-01
	IS/IA	0.	1.002E+00	2.023E+00	4.122E+00	8.566E+00
	IS+IA	1.810E-02	3.624E-02	5.472E-02	9.272E-02	1.731E-01
	INTENSITY	6.798E-04	1.361E-03	2.055E-03	3.482E-03	6.503E-03
5750	IS	0.	1.774E-01	3.573E-01	7.248E-01	1.492E+00
	IS/IA	0.	1.379E+01	2.777E+01	5.632E+01	1.159E+02
	IS+IA	1.487E-02	1.903E-01	3.702E-01	7.377E-01	1.505E+00
	INTENSITY	7.825E-04	1.157E-02	2.251E-02	4.485E-02	9.150E-02
6150	IS	0.	1.868E-02	3.757E-02	7.597E-02	1.554E-01
	IS/IA	0.	1.857E+00	3.735E+00	7.552E+00	1.544E+01
	IS+IA	1.006E-02	2.874E-02	4.763E-02	8.003E-02	1.654E-01
	INTENSITY	5.636E-04	1.610E-03	2.668E-03	4.820E-03	9.268E-03
6550	IS	0.	2.105E-02	4.229E-02	8.531E-02	1.737E-01
	IS/IA	0.	2.457E+00	4.935E+00	9.950E+00	2.027E+01
	IS+IA	8.569E-03	2.962E-02	5.085E-02	9.388E-02	1.822E-01
	INTENSITY	4.391E-04	1.518E-03	2.608E-03	4.811E-03	9.340E-03

Table A-5. Computed Relative and Absolute Intensities for Rayleigh Atmosphere  
( $\theta = 0$ ,  $\theta_0 = 85^\circ$ )

THEIA0=85 LAMBDA R=		THETA= 0				
		0.00	.10	.20	.40	.80
2875	IS	0.	7.476E-22	1.520E-21	3.147E-21	6.767E-21
	IS/IA	0.	3.663E-18	7.449E-18	1.542E-17	3.315E-17
	IS+IA	2.041E-04	2.041E-04	2.041E-04	2.041E-04	2.041E-04
	INTENSITY	2.794E-06	2.794E-06	2.794E-06	2.794E-06	2.794E-06
2975	IS	0.	5.011E-10	1.033E-09	2.201E-09	5.062E-09
	IS/IA	0.	1.170E-06	2.411E-06	5.137E-06	1.182E-05
	IS+IA	4.284E-04	4.284E-04	4.284E-04	4.284E-04	4.284E-04
	INTENSITY	8.455E-06	8.455E-06	8.455E-06	8.455E-06	8.455E-06
3075	IS	0.	3.085E-06	6.423E-06	1.399E-05	3.408E-05
	IS/IA	0.	3.141E-03	6.541E-03	1.425E-02	3.470E-02
	IS+IA	9.820E-04	9.851E-04	9.884E-04	9.960E-04	1.016E-03
	INTENSITY	2.251E-05	2.258E-05	2.265E-05	2.283E-05	2.329E-05
3175	IS	0.	1.145E-04	2.392E-04	5.245E-04	1.299E-03
	IS/IA	0.	3.137E-02	6.549E-02	1.430E-01	3.558E-01
	IS+IA	3.652E-03	3.767E-03	3.891E-03	4.176E-03	4.951E-03
	INTENSITY	9.532E-05	9.831E-05	1.016E-04	1.090E-04	1.292E-04
3300	IS	0.	1.412E-03	2.944E-03	6.441E-03	1.586E-02
	IS/IA	0.	6.619E-02	1.380E-01	3.020E-01	7.434E-01
	IS+IA	2.133E-02	2.274E-02	2.427E-02	2.777E-02	3.719E-02
	INTENSITY	7.740E-04	8.252E-04	8.809E-04	1.008E-03	1.349E-03
3400	IS	0.	1.807E-03	3.758E-03	8.160E-03	1.975E-02
	IS/IA	0.	7.670E-02	1.595E-01	3.466E-01	8.383E-01
	IS+IA	2.356E-02	2.537E-02	2.732E-02	3.173E-02	4.331E-02
	INTENSITY	8.399E-04	9.044E-04	9.739E-04	1.131E-03	1.544E-03
3600	IS	0.	2.440E-03	5.046E-03	1.083E-02	2.538E-02
	IS/IA	0.	9.748E-02	2.016E-01	4.328E-01	1.014E+00
	IS+IA	2.503E-02	2.747E-02	3.008E-02	3.586E-02	5.041E-02
	INTENSITY	9.322E-04	1.023E-03	1.120E-03	1.336E-03	1.878E-03
4950	IS	0.	4.273E-03	8.650E-03	1.773E-02	3.734E-02
	IS/IA	0.	2.885E-01	5.841E-01	1.197E+00	2.521E+00
	IS+IA	1.481E-02	1.908E-02	2.346E-02	3.254E-02	5.215E-02
	INTENSITY	9.664E-04	1.245E-03	1.531E-03	2.124E-03	3.403E-03
5350	IS	0.	3.925E-03	7.923E-03	1.614E-02	3.354E-02
	IS/IA	0.	3.822E-01	7.715E-01	1.574E+00	3.266E+00
	IS+IA	1.027E-02	1.420E-02	1.819E-02	2.641E-02	4.361E-02
	INTENSITY	3.857E-04	5.332E-04	6.833E-04	9.921E-04	1.646E-03
5750	IS	0.	3.553E-03	7.155E-03	1.451E-02	2.988E-02
	IS/IA	0.	5.021E-01	1.011E+00	2.051E+00	4.223E+00
	IS+IA	7.075E-03	1.063E-02	1.423E-02	2.154E-02	3.645E-02
	INTENSITY	4.301E-04	6.461E-04	8.651E-04	1.312E-03	2.246E-03
6150	IS	0.	3.941E-03	7.926E-03	1.603E-02	3.278E-02
	IS/IA	0.	6.640E-01	1.335E+00	2.700E+00	5.522E+00
	IS+IA	5.936E-03	9.877E-03	1.366E-02	2.190E-02	3.871E-02
	INTENSITY	3.325E-04	5.534E-04	7.766E-04	1.230E-03	2.169E-03
6550	IS	0.	5.239E-03	1.052E-02	2.123E-02	4.322E-02
	IS/IA	0.	8.794E-01	1.766E+00	3.564E+00	7.258E+00
	IS+IA	5.957E-03	1.120E-02	1.648E-02	2.719E-02	4.918E-02
	INTENSITY	3.053E-04	5.738E-04	8.440E-04	1.393E-03	2.520E-03

**Table A-6. Absorption Coefficients for SO<sub>2</sub>, CH<sub>4</sub>, NH<sub>3</sub>, CO, HCl, PAN  
C<sub>2</sub>H<sub>4</sub>, C<sub>6</sub>H<sub>6</sub>, NO, O<sub>3</sub> and NO<sub>2</sub>**

**SO<sub>2</sub> - SULFUR DIOXIDE**

1/CM	MICRON	K(300°K) (atm <sup>-1</sup> cm <sup>-1</sup> )			
1000.	10.000	.381E-02	1314.	7.610	.246E 00
1031.	9.700	.416E-02	1325.	7.550	.195E 01
1042.	9.600	.631E-02	1333.	7.500	.366E 01
1053.	9.500	.121E-01	1341.	7.455	.443E 01
1064.	9.400	.244E-01	1351.	7.400	.379E 01
1075.	9.300	.592E-01	1352.	7.395	.555E 01
1087.	9.200	.212E 00	1370.	7.300	.205E 01
1099.	9.100	.763E 00	1389.	7.200	.143E 00
1111.	9.000	.251E 01	1404.	7.125	.264E-01
1124.	8.900	.659E 01	1429.	7.000	.323E-01
1139.	8.783	.121E 02	1449.	6.900	.353E-01
1163.	8.600	.290E 01	1471.	6.800	.304E-01
1164.	8.592	.172E 02	1493.	6.700	.157E-01
1176.	8.500	.936E 01	1504.	6.650	.122E-01
1190.	8.400	.293E 01	1515.	6.600	.989E-02
1205.	8.300	.107E 01	1527.	6.550	.762E-02
1220.	8.200	.231E 00	1541.	6.489	.412E-01
1235.	8.100	.649E-01	1563.	6.400	.804E-02
1250.	8.000	.136E-01	1575.	6.350	.573E-02
1266.	7.900	.607E-02	1587.	6.300	.673E-02
1282.	7.800	.668E-02	1613.	6.200	.940E-02
1249.	7.700	.205E-01	1639.	6.100	.103E-01
1316.	7.600	.891E 00	1667.	6.000	.757E-02
1333.	7.500	.387E 02	2700.	3.704	.150E-01
1342.	7.450	.124E 03	2800.	3.571	.400E-01
1351.	7.400	.149E 03	2850.	3.509	.720E-01
1356.	7.375	.141E 03	2885.	3.466	.152E 00
1361.	7.350	.248E 03	2900.	3.446	.253E 00
1371.	7.295	.395E 02	2915.	3.431	.400E 00
1374.	7.276	.218E 03	2925.	3.419	.570E 00
1389.	7.200	.712E 02	2940.	3.401	.900E 00
1408.	7.100	.600E-01	2957.	3.382	.100E 01
1429.	7.000	.869E-02	2975.	3.361	.860E 00
2390.	4.184	.198E-02	2985.	3.350	.670E 00
2439.	4.100	.972E-02	2993.	3.341	.442E 00
2469.	4.050	.916E-01	3000.	3.333	.750E 00
2484.	4.026	.526E 00	3010.	3.322	.267E 01
2500.	4.000	.408E 00	3020.	3.311	.400E 01
2532.	3.950	.916E-01	3030.	3.300	.930E 00
2564.	3.900	.198E-02	3037.	3.293	.505E 00
			3050.	3.279	.900E 00
			3060.	3.268	.114E 01
			3075.	3.252	.135E 01
			3086.	3.240	.140E 01
			3095.	3.231	.137E 01
			3100.	3.226	.131E 01
			3110.	3.215	.110E 01
			3125.	3.200	.740E 00
			3150.	3.175	.262E 00
			3160.	3.164	.150E 00
			3175.	3.150	.680E-01
			3200.	3.125	.100E-01
			4082.	2.450	.143E-01
			4132.	2.420	.312E-01
			4153.	2.408	.545E-01
			4172.	2.397	.901E-01
			4186.	2.389	.124E 00
			4195.	2.384	.183E 00
			4203.	2.379	.249E 00
			4209.	2.376	.305E 00
			4227.	2.366	.422E 00

**CH<sub>4</sub> - METHANE**

1/CM	MICRON	K (300°K) (atm <sup>-1</sup> cm <sup>-1</sup> )
1195.	8.368	.857E-01
1216.	8.223	.420E 00
1234.	8.105	.133E 01
1246.	8.026	.322E 01
1250.	8.000	.101E 01
1256.	7.960	.201E 01
1263.	7.915	.485E 01
1266.	7.900	.322E 01
1277.	7.828	.121E 01
1288.	7.762	.209E 01
1293.	7.736	.734E 01
1299.	7.697	.946E 01
1305.	7.664	.689E 00

**Table A-6. Absorption Coefficients for SO<sub>2</sub>, CH<sub>4</sub>, NH<sub>3</sub>, CO, HCl, PAN, C<sub>2</sub>H<sub>4</sub>, C<sub>6</sub>H<sub>6</sub>, NO, O<sub>3</sub> and NO<sub>2</sub>, Contd.**

4294.	2.329	.305E 00	1418.	7.050	.221E-01
4354.	2.297	.249E 00	1439.	6.950	.274E-01
4390.	2.278	.183E 00	1449.	6.900	.471E-01
4435.	2.255	.124E 00	1471.	6.800	.131E 00
4456.	2.244	.901E-01	1493.	6.700	.390E 00
4496.	2.224	.545E-01	1515.	6.600	.578E 00
4498.	2.223	.312E-01	1538.	6.500	.673E 00
4552.	2.197	.143E-01	1563.	6.400	.578E 00

**NH<sub>3</sub> - AMMONIA**

1/CM	MICRON	K(300°K) (atm <sup>-1</sup> cm <sup>-1</sup> )
667.	15.000	.102E-01
676.	14.800	.161E-01
685.	14.600	.216E-01
694.	14.400	.294E-01
704.	14.200	.398E-01
714.	14.000	.532E-01
725.	13.800	.721E-01
735.	13.600	.107E 00
746.	13.400	.162E 00
758.	13.200	.258E 00
769.	13.000	.345E 00
781.	12.800	.432E 00
794.	12.600	.555E 00
806.	12.400	.623E 00
820.	12.200	.696E 00
833.	12.000	.745E 00
847.	11.800	.795E 00
862.	11.600	.715E 00
877.	11.400	.641E 00
893.	11.200	.491E 00
909.	11.000	.491E 00
917.	10.900	.142E 01
926.	10.800	.538E 01
929.	10.760	.296E 02
935.	10.700	.237E 01
943.	10.610	.158E 00
950.	10.526	.776E 00
953.	10.490	.324E 00
962.	10.400	.504E 01
964.	10.370	.407E 02
971.	10.300	.536E 00
980.	10.200	.426E-01
990.	10.100	.230E 00
1000.	10.000	.378E 00
1020.	9.800	.765E 00
1042.	9.600	.913E 00
1064.	9.400	.913E 00
1087.	9.200	.848E 00
1111.	9.000	.668E 00
1149.	8.700	.346E 00
1163.	8.600	.236E 00
1190.	8.400	.987E-01
1220.	8.200	.368E-01
1250.	8.000	.120E-01
1282.	7.800	.669E-02
1316.	7.600	.477E-02
1351.	7.400	.477E-02
1389.	7.200	.948E-02

1599.	6.253	.170E 00
1632.	6.129	.751E 00
1667.	6.000	.182E 00
1681.	5.950	.190E 00
1695.	5.900	.301E 00
1740.	5.747	.470E 00
1754.	5.700	.449E 00
1786.	5.600	.205E 00
1818.	5.500	.734E-01
1852.	5.400	.213E-01
1887.	5.300	.896E-02
1923.	5.200	.359E-02
1961.	5.100	.324E-02
2000.	5.000	.290E-02

**CO - CARBON MONOXIDE**

1/CM	MICRON	K(300°K) (atm <sup>-1</sup> cm <sup>-1</sup> )	K(600°K) (atm <sup>-1</sup> cm <sup>-1</sup> )
1400.	7.142	.000E-32	.849E-30
1425.	7.017	.000E-32	.430E-24
1450.	6.896	.000E-32	.860E-24
1475.	6.779	.000E-32	.129E-23
1500.	6.666	.000E-32	.172E-23
1525.	6.557	.000E-32	.110E-21
1550.	6.451	.000E-32	.219E-21
1575.	6.349	.000E-32	.328E-18
1600.	6.250	.000E-32	.655E-18
1625.	6.153	.000E-32	.110E-15
1650.	6.060	.000E-32	.219E-15
1675.	5.970	.000E-32	.491E-13
1700.	5.882	.100E-26	.980E-13
1725.	5.797	.355E-22	.549E-10
1750.	5.714	.711E-22	.109E-09
1775.	5.633	.130E-17	.232E-08
1800.	5.555	.260E-17	.454E-08
1825.	5.479	.226E-13	.112E-06
1850.	5.405	.453E-13	.219E-06
1875.	5.333	.166E-09	.226E-04
1900.	5.263	.331E-09	.455E-04
1925.	5.194	.437E-06	.110E-02
1950.	5.128	.873E-06	.215E-02
1975.	5.063	.334E-03	.279E-01
2000.	5.000	.667E-03	.537E-01
2025.	4.938	.879E-02	.219E-01
2050.	4.878	.107E 00	.581E 00
2075.	4.819	.109E 00	.109E 01
2100.	4.761	.205E 01	.184E 01
2125.	4.705	.241E 01	.109E 01
2150.	4.651	.120E 01	.630E 00
2175.	4.597	.338E 01	.242E 01
2200.	4.545	.147E 01	.219E 01
2225.	4.494	.139E 00	.871E 00

**Table A-6. Absorption Coefficients for SO<sub>2</sub>, CH<sub>4</sub>, NH<sub>3</sub>, CO, HCl, PAN, C<sub>2</sub>H<sub>4</sub>, C<sub>6</sub>H<sub>6</sub>, NO, O<sub>3</sub> and NO<sub>2</sub>, Contd.**

2250.	4.444	.233E-02	.139E-00	787.	12.700	.448E+02
2275.	4.395	.379E-05	.693E-02	793.	12.600	.790E+02
2300.	4.347	.178E-09	.595E-04	800.	12.500	.296E+02
2325.	4.301	.121E-16	.207E-07	806.	12.400	.106E+02
2350.	4.255	.109E-21	.967E-16	811.	12.330	.965E+01

**HCl - HYDROGEN CHLORIDE**

1/CM	MICRON	K(300°K) (atm <sup>-1</sup> cm <sup>-1</sup> )	K(600°K) (atm <sup>-1</sup> cm <sup>-1</sup> )
2200.	4.545	.000E-32	.562E-06
2225.	4.494	.000E-32	.431E-05
2250.	4.444	.000E-32	.806E-05
2275.	4.395	.000E-32	.118E-04
2300.	4.347	.000E-32	.155E-04
2325.	4.301	.000E-32	.918E-04
2350.	4.255	.000E-32	.168E-03
2375.	4.210	.000E-32	.244E-03
2400.	4.166	.722E-07	.320E-03
2425.	4.123	.451E-05	.139E-02
2450.	4.081	.896E-05	.247E-02
2475.	4.040	.134E-04	.354E-02
2500.	4.000	.178E-04	.462E-02
2525.	3.960	.112E-03	.140E-01
2550.	3.921	.207E-03	.235E-01
2575.	3.883	.105E-02	.330E-01
2600.	3.846	.191E-02	.424E-01
2625.	3.809	.767E-02	.852E-01
2650.	3.773	.134E-01	.127E-00
2675.	3.738	.411E-01	.170E-00
2700.	3.703	.688E-01	.213E-00
2725.	3.669	.154E-00	.280E-00
2750.	3.636	.240E-00	.348E-00
2775.	3.603	.375E-00	.380E-00
2800.	3.571	.509E-00	.412E-00
2825.	3.539	.566E-00	.370E-00
2850.	3.508	.465E-00	.260E-00
2875.	3.478	.168E-00	.867E-01
2900.	3.448	.258E-00	.129E-00
2925.	3.418	.644E-00	.339E-00
2950.	3.389	.815E-00	.493E-00
2975.	3.361	.720E-00	.535E-00
3000.	3.333	.469E-00	.515E-00
3025.	3.305	.272E-00	.386E-00
3050.	3.278	.756E-01	.257E-00
3075.	3.252	.390E-01	.156E-00
3100.	3.225	.240E-02	.547E-01
3125.	3.200	.120E-02	.289E-01
3150.	3.174	.596E-05	.320E-02
3175.	3.149	.298E-05	.160E-02
3200.	3.125	.693E-10	.129E-04

**PAN - PEROXYACETYL NITRATE**

1/CM	MICRON	K(300°) (atm <sup>-1</sup> cm <sup>-1</sup> )
757.	13.200	.683E+00
763.	13.100	.131E+01
769.	13.002	.228E+01
775.	12.900	.416E+01
781.	12.800	.117E+02

819.	12.200	.124E+02
826.	12.100	.990E+01
833.	12.000	.868E+01
840.	11.900	.496E+01
847.	11.800	.826E+00
1111.	9.000	.630E+00
1123.	8.900	.119E+01
1136.	8.800	.777E+01
1149.	8.700	.462E+02
1165.	8.580	.138E+03
1176.	8.500	.428E+02
1190.	8.400	.138E+01
1204.	8.300	.119E+01
1250.	8.000	.239E+01
1265.	7.900	.144E+02
1283.	7.790	.978E+02
1298.	7.700	.546E+02
1315.	7.600	.153E+02
1333.	7.500	.113E+02

**C<sub>2</sub>H<sub>4</sub> - ETHYLENE**

1/CM	MICRON	K(300°) (atm <sup>-1</sup> cm <sup>-1</sup> )
813.	12.300	.828E+00
819.	12.200	.969E+00
826.	12.100	.142E+01
833.	12.000	.289E+01
840.	11.900	.517E+01
847.	11.800	.899E+01
854.	11.700	.138E+02
862.	11.600	.208E+02
869.	11.500	.293E+02
877.	11.400	.404E+02
884.	11.300	.460E+02
892.	11.200	.549E+02
900.	11.100	.612E+02
909.	11.000	.657E+02
917.	10.900	.702E+02
925.	10.800	.854E+02
934.	10.700	.109E+03
943.	10.600	.261E+03
946.	10.563	.731E+03
952.	10.500	.226E+03
955.	10.468	.182E+03
961.	10.400	.101E+03
970.	10.300	.872E+02
980.	10.200	.778E+02
990.	10.100	.717E+02
1000.	10.000	.633E+02
1010.	9.900	.552E+02
1020.	9.800	.430E+02
1030.	9.700	.279E+02
1041.	9.600	.172E+02
1052.	9.500	.114E+02
1063.	9.400	.792E+01

**Table A-6. Absorption Coefficients for SO<sub>2</sub>, CH<sub>4</sub>, NH<sub>3</sub>, CO, HCl, PAN, C<sub>2</sub>H<sub>4</sub>, C<sub>6</sub>H<sub>6</sub>, NO, O<sub>3</sub> and NO<sub>2</sub>, Contd.**

1075.	9.300	.406E+01	1675.	5.970	.320E-07	.181E-02
1086.	9.200	.255E+01	1700.	5.882	.124E-05	.130E-02
1098.	9.100	.176E+01	1725.	5.797	.354E-04	.479E-02
1111.	9.000	.828E+00	1750.	5.714	.711E-03	.273E-01
1123.	8.900	.567E+00	1775.	5.633	.952E-02	.916E-01
1136.	8.800	.393E+00	1800.	5.555	.786E-01	.234E 00
1149.	8.700	.329E+00	1825.	5.479	.355E 00	.420E 00
2939.	3.402	.352E+01	1850.	5.405	.684E 00	.433E 00
3022.	3.308	.184E+02	1875.	5.333	.539E-01	.400E-01
3108.	3.217	.303E+02	1900.	5.263	.926E 00	.562E 00
3158.	3.166	.184E+02	1925.	5.194	.485E 00	.621E 00
3187.	3.137	.352E+01	1950.	5.128	.408E-01	.243E 00
			1975.	5.063	.318E-03	.281E-01
			2000.	5.000	.482E-01	.466E-03
			2025.	4.936	.442E-15	.718E-07

**C<sub>6</sub>H<sub>6</sub> - BENZENE**

1/CM	MICRON	K(300°K) (atm <sup>-1</sup> cm <sup>-1</sup> )
1007.	9.923	.923E+00
1013.	9.867	.471E+01
1018.	9.821	.150E+02
1023.	9.773	.226E+02
1029.	9.712	.183E+02
1035.	9.658	.464E+02
1036.	9.648	.590E+02
1038.	9.629	.464E+02
1040.	9.610	.150E+02
1042.	9.588	.905E+01
1046.	9.559	.150E+02
1049.	9.524	.188E+02
1053.	9.490	.150E+02
1059.	9.437	.471E+01
1064.	9.397	.923E+00
3011.	3.321	.923E+00
3033.	3.300	.471E+01
3037.	3.292	.150E+02
3042.	3.287	.464E+02
3058.	3.270	.170E+03
3124.	3.201	.464E+02
3139.	3.185	.150E+02
3147.	3.177	.471E+01
3150.	3.174	.923E+00

**O<sub>3</sub> - OZONE**

1/CM	MICRON	K(300°K) (atm <sup>-1</sup> cm <sup>-1</sup> )
1006.	9.940	.235E+01
1010.	9.900	.345E+01
1017.	9.830	.500E+01
1024.	9.770	.615E+01
1028.	9.722	.915E+01
1036.	9.650	.585E+01
1043.	9.590	.405E+01
1049.	9.530	.790E+01
1054.	9.490	.450E+01
1057.	9.460	.865E+01
1063.	9.400	.405E+01

**NO<sub>2</sub> - NITROGEN DIOXIDE**

1/CM	MICRON	K(300°K) (atm <sup>-1</sup> cm <sup>-1</sup> )
1563.	6.400	.210E+02
1587.	6.300	.110E+03
1620.	6.171	.295E+03
1639.	6.100	.218E+03
1667.	6.000	.362E+01
2778.	3.600	.857E-02
2857.	3.500	.111E+00
2890.	3.460	.382E+01
2941.	3.400	.210E+01
2985.	3.350	.389E+00
3030.	3.300	.367E-01
3125.	3.200	.123E-01
3226.	3.100	.960E-02

**NO - NITRIC OXIDE**

1/CM	MICRON	K(300°K) (atm <sup>-1</sup> cm <sup>-1</sup> )	K (600°K) (atm <sup>-1</sup> cm <sup>-1</sup> )
1300.	7.692	.000E-32	.614E-20
1325.	7.547	.000E-32	.882E-18
1350.	7.407	.000E-32	.175E-17
1375.	7.272	.000E-32	.362E-15
1400.	7.142	.000E-32	.723E-15
1425.	7.017	.000E-32	.899E-13
1450.	6.896	.000E-32	.179E-12
1475.	6.779	.000E-32	.172E-10
1500.	6.666	.417E-21	.343E-10
1525.	6.557	.494E-17	.246E-08
1550.	6.451	.988E-17	.488E-08
1575.	6.349	.591E-13	.248E-06
1600.	6.250	.118E-12	.491E-06
1625.	6.153	.962E-11	.378E-05
1650.	6.060	.627E-09	.327E-04

Table A-6. Absorption Coefficients for SO<sub>2</sub>, CH<sub>4</sub>, NH<sub>3</sub>, CO, HCl, PAN, C<sub>2</sub>H<sub>4</sub>, C<sub>6</sub>H<sub>6</sub>, NO, O<sub>3</sub> and NO<sub>2</sub>, Contd.

HF - HYDROGEN FLUORIDE

1/CM	MICRON	K(300°K) (atm <sup>-1</sup> cm <sup>-1</sup> )	K(600°K) (atm <sup>-1</sup> cm <sup>-1</sup> )
3000.	3.333	.112E-12	.684E-06
3025.	3.305	.266E-09	.115E-04
3050.	3.276	.532E-09	.224E-04
3075.	3.252	.799E-09	.333E-04
3100.	3.225	.106E-08	.441E-04
3125.	3.200	.133E-08	.550E-04
3150.	3.174	.159E-08	.659E-04
3175.	3.149	.186E-08	.768E-04
3200.	3.125	.213E-08	.877E-04
3225.	3.100	.237E-08	.985E-04
3250.	3.076	.274E-08	.140E-02
3275.	3.053	.411E-08	.218E-02
3300.	3.030	.549E-08	.287E-02
3325.	3.007	.686E-08	.357E-02
3350.	2.985	.823E-08	.427E-02
3375.	2.962	.961E-08	.497E-02
3400.	2.941	.109E-07	.566E-02
3425.	2.919	.126E-07	.636E-02
3450.	2.898	.152E-07	.705E-02
3475.	2.877	.178E-07	.774E-02
3500.	2.857	.204E-07	.844E-02
3525.	2.836	.229E-07	.913E-02
3550.	2.816	.255E-07	.982E-02
3575.	2.797	.281E-07	.105E-01
3600.	2.777	.306E-07	.112E-01
3625.	2.758	.332E-07	.119E-01
3650.	2.739	.358E-07	.126E-01
3675.	2.721	.384E-07	.133E-01
3700.	2.702	.410E-07	.140E-01
3725.	2.684	.436E-07	.147E-01
3750.	2.666	.462E-07	.154E-01
3775.	2.649	.488E-07	.161E-01
3800.	2.631	.514E-07	.168E-01
3825.	2.614	.540E-07	.175E-01
3850.	2.597	.566E-07	.182E-01
3875.	2.580	.592E-07	.189E-01
3900.	2.564	.618E-07	.196E-01
3925.	2.547	.644E-07	.203E-01
3950.	2.531	.670E-07	.210E-01
3975.	2.515	.696E-07	.217E-01
4000.	2.500	.722E-07	.224E-01
4025.	2.484	.748E-07	.231E-01
4050.	2.469	.774E-07	.238E-01
4075.	2.453	.800E-07	.245E-01
4100.	2.439	.826E-07	.252E-01
4125.	2.424	.852E-07	.259E-01
4150.	2.409	.878E-07	.266E-01
4175.	2.395	.904E-07	.273E-01
4200.	2.380	.930E-07	.280E-01
4225.	2.366	.956E-07	.287E-01
4250.	2.352	.982E-07	.294E-01
4275.	2.339	.1008E-06	.301E-01
4300.	2.325	.1034E-06	.308E-01
4325.	2.312	.1060E-06	.315E-01
4350.	2.298	.1086E-06	.322E-01
4375.	2.285	.1112E-06	.329E-01
4400.	2.272	.1138E-06	.336E-01